

DISS. ETH No. 19239

**INVESTIGATION OF COMPOUND SEMICONDUCTORS AS  
BUFFER-LAYER IN THIN FILM SOLAR CELLS**

A dissertation submitted to  
ETH ZURICH

for the degree of  
DOCTOR OF SCIENCES

presented by  
STEPHAN FRIEDRICH BUECHELER  
Dipl. Phys. ETH Zurich  
born on May 12th, 1977  
citizen of Germany

Accepted on the recommendation of:  
Prof. Dr. Danilo Pescia, examiner  
Prof. Dr. Ayodhya N. Tiwari, coexaminer  
Prof. Dr. Marc Burgelman, coexaminer

Zürich, 2010



# Contents

<b>Abstract</b>	<b>v</b>
<b>Zusammenfassung (Abstract in German)</b>	<b>ix</b>
<b>1 Introduction</b>	<b>1</b>
1.1 General introduction . . . . .	1
1.2 Chalcopyrite thin film solar cells . . . . .	1
1.2.1 Molybdenum Back Contact . . . . .	3
1.2.2 CIGS Absorber . . . . .	3
1.2.3 Buffer layer . . . . .	3
1.2.4 Front contact and Ni-Al Grid . . . . .	4
1.3 Aim of this thesis . . . . .	4
1.4 Buffer layers . . . . .	5
1.4.1 Suitable buffer layer materials . . . . .	6
1.4.1.1 CdS buffer layer . . . . .	7
1.4.1.2 Indium(III)sulfide buffer layer . . . . .	7
1.4.2 Buffer layer deposition methods . . . . .	8
1.4.2.1 Chemical bath deposition . . . . .	8
1.4.2.2 Ultrasonic spray pyrolysis of compound semiconductors . . . . .	9
<b>2 Methods of characterization and interpretation</b>	<b>13</b>
2.1 Material characterization . . . . .	13
2.1.1 X-ray diffraction . . . . .	13
2.1.2 Electron microscopy . . . . .	14
2.1.2.1 Scanning electron microscopy . . . . .	14
2.1.2.2 Transmission electron microscopy . . . . .	14
2.1.3 X-ray photoelectron spectroscopy . . . . .	15
2.1.4 Ion spectroscopy . . . . .	16
2.1.5 NIR-UV spectroscopy . . . . .	16
2.1.6 Thickness measurement . . . . .	17

---

2.2	Device characterization and interpretation . . . . .	17
2.2.1	Current voltage characteristics . . . . .	18
2.2.1.1	Recombination mechanisms . . . . .	20
2.2.1.2	Jsc-Voc theory . . . . .	23
2.2.1.3	Measurement equipment . . . . .	25
2.2.2	Spectral response . . . . .	26
2.2.2.1	Measurement equipment . . . . .	27
2.2.3	Capacitance measurements . . . . .	27
2.2.3.1	Capacitance voltage measurement . . . . .	27
2.2.3.2	Capacitance frequency spectroscopy . . . . .	28
<b>3</b>	<b>Growth mechanism and layer properties</b>	<b>31</b>
3.1	Transport of precursor solution . . . . .	31
3.2	Chemical precursors in solution . . . . .	32
3.3	Chemical reaction and mechanism . . . . .	32
3.4	Growth kinetics . . . . .	35
3.5	Layer properties . . . . .	38
3.5.1	Crystal structure . . . . .	38
3.5.2	Morphology . . . . .	41
3.5.3	Chemical composition . . . . .	50
3.5.4	Optical properties and band gap considerations . . . . .	52
3.6	Summary and conclusion . . . . .	59
<b>4</b>	<b>Application in CIGS thin film solar cells</b>	<b>61</b>
4.1	Morphology and interdiffusion in CIGS devices . . . . .	61
4.2	Interface formation . . . . .	65
4.3	Photovoltaic properties with CIGS absorbers . . . . .	71
4.3.1	Effect of oxygen at the CIGS surface . . . . .	71
4.3.2	Impact of absorber copper excess . . . . .	72
4.3.3	Impact of absorber surface modifications . . . . .	77
4.3.4	Performance versus gallium content and air annealing effects . . . . .	83
4.3.5	Partial electrolyte treatment . . . . .	97
4.4	Summary and conclusion . . . . .	99
<b>5</b>	<b>Application in CIGSSe thin film solar cells</b>	<b>103</b>
5.1	Morphology and interdiffusion in CIGSSe devices . . . . .	104
5.2	Photovoltaic properties with CIGSSe absorbers . . . . .	106
5.2.1	Impact of the deposition temperature . . . . .	106
5.2.2	Influence of the solvent and additives . . . . .	107

---

5.2.3	Impact of the In to S ratio in the solution . . . . .	111
5.2.4	Impact of device light soaking and annealing . . . . .	112
5.2.4.1	Light soaking . . . . .	112
5.2.4.2	Device annealing . . . . .	113
5.3	Performance with reference to CdS buffer layer . . . . .	114
5.3.1	Definition of the CdS reference . . . . .	114
5.3.2	PV performance . . . . .	117
5.4	Summary and conclusion . . . . .	118
<b>6</b>	<b>Other alternative buffer layers</b>	<b>121</b>
6.1	Deposition of ZnS films . . . . .	121
6.2	Photovoltaic performance with ZnS buffer layer . . . . .	123
6.3	Summary and conclusion . . . . .	127
<b>7</b>	<b>Outlook and closing remarks</b>	<b>129</b>
	<b>Acknowledgment</b>	<b>131</b>
	<b>Abbreviations and Symbols</b>	<b>133</b>
	<b>Curriculum Vitae</b>	<b>137</b>
	<b>Publications</b>	<b>139</b>



# Abstract

In the scope of this thesis the substitution of suitable compound semiconductors for the commonly used CdS as buffer layer in Cu(In,Ga)Se<sub>2</sub> based thin film solar cells is studied. An ultrasonic spray pyrolysis (USP) method is developed which allows conformal coverage of complex surfaces with compact thin layers. This is a low-cost and large area deposition method, applicable for in-line roll-to-roll manufacturing.

The growth mechanism and layer properties of USP-In<sub>2</sub>S<sub>3</sub> layers is presented in dependence of the deposition parameters. A chemical reaction equation and a possible mechanism for the formation of In<sub>2</sub>S<sub>3</sub> layers from solution droplets containing InCl<sub>3</sub> and thiourea precursors is proposed. The mechanism can be described as a mixture of particle deposition with subsequent chemical conversion into In<sub>2</sub>S<sub>3</sub> (indirect process) and chemical vapor deposition (direct process). From analyzing the deposition process versus time it can be concluded that particle deposition is the dominant growth mechanism.

The growth kinetics for a given solvent are mainly influence by the substrate temperature and the relative and absolute precursor concentration. Homogeneous and compact In<sub>2</sub>S<sub>3</sub> layers with continuous substrate coverage are obtained from methanol or acetone based solutions with InCl<sub>3</sub> and TU precursors at a deposition temperature of 200 °C. Polycrystalline layers are grown from solutions with sulfur excess whereas sulfur deficient solutions yield amorphous or nanocrystalline films. Impurities of extrinsic elements such as chlorine and oxygen can be minimized by increasing the temperature and amount of sulfur excess in the solution.

An indirect energy band gap of 2.01 eV is found for USP-In<sub>2</sub>S<sub>3</sub> layers on silicon and SLG substrate. Even though the derived band gap of the USP-In<sub>2</sub>S<sub>3</sub> layer is smaller than band gap of CdS, a gain in the current density can be expected due to the lower absorption coefficient.

The application of USP-In<sub>2</sub>S<sub>3</sub> as buffer layer is investigated on Cu(In,Ga)Se<sub>2</sub> absorbers grown by a 3-stage co-evaporation process. With ultrasonic spray pyrolysis it is possible to grow stoichiometric tetragonal-In<sub>2</sub>S<sub>3</sub> layers with low impurity concentration on CIGS absorbers with conformal substrate coverage. A microcrystalline In<sub>2</sub>S<sub>3</sub> structure is favorable for buffer layer application to avoid spikes which could lead to deteriorate ZnO.

With increasing deposition temperature an increased copper concentration in the buffer layer was found and simultaneously an upwards shift of the valence band maximum was observed. This confirms that copper incorporation rather than sodium incorporation dominates the modifications of the electronic properties of In<sub>2</sub>S<sub>3</sub> deposited on CIGS absorbers. The application of the spray deposition temperature profile to the absorber layer before

CBD-CdS deposition showed that the elevated temperature necessary for the deposition of USP-In<sub>2</sub>S<sub>3</sub> amplifies oxygenation of the CIGS surface, i.e. selenium vacancies are filled with oxygen and the type inversion of the CIGS surface is reduced. Minimizing the oxygenation of the CIGS surface is mandatory in order to achieve highly efficient solar cells. The degree of copper excess in the 2<sup>nd</sup> stage of the absorber deposition has a direct influence on the performance of the CIGS solar cells with USP-In<sub>2</sub>S<sub>3</sub> buffer layer. The copper excess affects predominantly the fill factor. For CIGS samples with 20% or higher copper excess a fill factor higher than 65% was not achieved. Decreasing the copper excess to 10% and below resulted in a significant increase of the fill factor. Modifications of absorber finishing showed that copper-poor grow conditions are necessary in order to minimize recombination losses of CIGS solar cells with USP-In<sub>2</sub>S<sub>3</sub> buffer layers. Also the reduction of gallium concentration towards the surface of the absorber proved to be necessary for good device performance.

The variation of the gallium content in CIGS layers grown with minimum copper excess and copper-poor finish revealed a change of the dominant recombination mechanism for a [Ga]/[III] ratio between 0.22 and 0.23. Since the change from SCR dominated to interface dominated recombination happens between [Ga]/[III] ratio between 0.22-0.23 it can be concluded that a cliff in the conduction band forms for  $[Ga]/[III] \geq 0.23$ .

A significant increase of the  $V_{OC}$  and the FF is observed for CIGS solar cells with USP-In<sub>2</sub>S<sub>3</sub> buffer layer after device annealing at 200 °C in air. This improvement results from an increase of the activation energy caused by a band gap widening of the surface region of the absorber due to copper depletion.

Highest total area efficiency of 13.4% was achieved with USP-In<sub>2</sub>S<sub>3</sub> buffer layer on a CIGS absorber with [Ga]/[III] ratio of 0.14 and a gallium finish. However, the procedure of the gallium finish failed in terms of reproducibility. Minimum copper excess, copper-poor finish and gallium reduction in the 3<sup>rd</sup> stage proved to be a CIGS absorber deposition procedure yielding reproducible results with USP-In<sub>2</sub>S<sub>3</sub> buffer layer. With this process highest total area efficiency of 13.1% was achieved corresponding to 13.7% of the CBD-CdS reference device. With the application of a MgF<sub>2</sub> anti-reflection coating, the total area efficiency of this CIGS solar cells is increased to 14.2% and the active area efficiency is 15.0%.

Sulfur containing Cu(In,Ga)(S,Se)<sub>2</sub> (CIGSSe) absorbers grown by rapid thermal processing are also investigated for possible application of USP-In<sub>2</sub>S<sub>3</sub> as buffer layer. Those absorbers have a higher surface roughness. With the USP method is possible to cover those rough surfaces with a compact In<sub>2</sub>S<sub>3</sub> layer. Even though the CIGSSe absorbers are extremely copper-poor, copper diffusion from the absorber into the buffer layer is detected with XPS depth profiling. After device annealing at 200 °C for 5 min the width of the In<sub>2</sub>S<sub>3</sub> region in the XPS depth profile is decreased indicating a reconstruction of the interface region due to provided thermal energy during the annealing treatment.

Variation of sulfur deficiency in the precursor solution is a tool for the optical absorption properties of the In<sub>2</sub>S<sub>3</sub> buffer layer by introducing chlorine. Furthermore, reflection losses can be reduced with this parameter. Sulfur excess variation mainly influences the layer growth and absorber surface by adding more sulfur. Best cell efficiency of 12.4% was obtained with a CIGSSe absorber and USP-In<sub>2</sub>S<sub>3</sub> buffer layer sprayed with sulfur excess.



With USP method stoichiometric ZnS layers can be grown from zinc chloride and thiorea precursors dissolved in acetone. Chlorine impurities are found in the sprayed ZnS layers. The amount of chlorine impurity decreases with increasing deposition temperature and increasing amount of sulfur available during reaction. The same behavior was also observed for chlorine impurities in USP-In<sub>2</sub>S<sub>3</sub> layers.

A significant increase of all PV parameters of CIGSSe solar cells with USP-ZnS buffer layer is observed after device annealing in air at 200 °C. The effect of device annealing on the PV performance can be divided into two steps irrespective of the ZnS deposition temperature and layer thickness. In a first step the  $V_{OC}$  and FF considerably increase after 20 min of accumulated annealing time. In a second step a further increase in the  $V_{OC}$  is observed along with a significant increase in the  $J_{SC}$  after 60 min of accumulated annealing time caused by a modification of the optical properties of the ZnO-ZnS layer stack.

Highest total area efficiency of 10.8% is obtained with USP-ZnS buffer layer on CIGSSe absorbers, however with major losses in  $V_{OC}$  and FF compared to the CdS reference with and efficiency of 11.4%. The losses result from an unfavorable band alignment of the ZnO/ZnS/CIGSSe stack. Partial substitution of oxygen for the sulfur in ZnS should yield an optimized band alignment and thus improve the device performance.



# Zusammenfassung (Abstract in German)

Im Rahmen dieser Dissertation wurde die Verwendung von geeigneten Verbindungshalbleitern als n-Typ Pufferschichten, allen voran  $\text{In}_2\text{S}_3$ , in  $\text{Cu}(\text{In,Ga})\text{Se}_2$  basierten Dünnschicht-solarzellen untersucht. Ziel ist es nicht nur das üblicherweise verwendete CdS als Pufferschicht zu ersetzen, sondern auch eine alternative zum Abscheideverfahren im chemischen Bad zu finden. Hierfür wurde ein Methode der Ultraschall Sprühpyrolyse (USP) entwickelt, die es erlaubt kompakte dünne Schichten auf komplexen Oberflächen abzuscheiden. Die Entwickelte USP Methode ist kostengünstig, anwendbar auf grossen Flächen und geeignet für lineare Rollendeposition.

Die Wachstumsmechanismen und Eigenschaften von USP- $\text{In}_2\text{S}_3$  Schichten werden in Abhängigkeit zu den Wachstumsparametern dargestellt. Für die Bildung von  $\text{In}_2\text{S}_3$  Schichten aus Lösungsmitteltröpfchen, die  $\text{InCl}_3$  und Thioharnstoff (TU) als Ausgangsstoffe enthalten, wird eine chemische Reaktionsgleichung und ein möglicher Reaktionsmechanismus aufgestellt. Das Wachstum der  $\text{In}_2\text{S}_3$  Schichten wird hauptsächlich beeinflusst durch die Proben temperatur, das Lösungsmittel und die relative bzw. absolute Konzentration der chemischen Ausgangsstoffe. Homogene und kompakte  $\text{In}_2\text{S}_3$  Schichten mit kontinuierlicher Probenabdeckung werden erhalten mit  $\text{InCl}_3$  und TU gelöst in Methanol oder Aceton bei einer Proben temperatur von  $200^\circ\text{C}$ . Diese Schichten wachsen polykristallin, falls die Lösung Schwefel im Überfluss enthält. Aus Schwefelarmen Lösungen erhält man amorphe oder nanokristalline Schichten. Verunreinigungen durch Fremdatome wie Chlor oder Sauerstoff können minimiert werden indem die Temperatur der Probe und/oder der Schwefelüberschuss erhöht werden.

Für USP- $\text{In}_2\text{S}_3$  Schichten sowohl auf Kalknatronglas (Fensterglas) als auch auf Silizium Wafern wurde eine indirekte Bandlücke von  $2.01\text{ eV}$  bestimmt. Obwohl diese Bandlücke kleiner ist als die des zu ersetzenden Materials CdS (direkt  $2.4\text{ eV}$ ), wird eine Steigerung der Stromdichte in der Solarzelle erwartet, da der Absorptionskoeffizient im Material mit indirekter Bandlücke kleiner ist.

Die Anwendung von USP- $\text{In}_2\text{S}_3$  als Pufferschicht wurde untersucht auf  $\text{Cu}(\text{In,Ga})\text{Se}_2$  Absorbermaterial, das mit einem 3-Stufen Koverdampfungsprozess der einzelnen Elemente gewachsen wurde. Mit der entwickelten USP Methode ist es möglich stöchiometrische, tetragonale  $\text{In}_2\text{S}_3$  Schichten mit geringer Verunreinigung und kompakter Abdeckung auf den CIGS Absorbern zu wachsen. Aufgrund der Proben temperatur von  $200^\circ\text{C}$  diffundieren geringe Mengen Kupfer aus dem Absorber in die  $\text{In}_2\text{S}_3$  Schicht. Diese Kupferdiffusion nimmt mit steigender Proben temperatur zu und mit steigender Kupferkonzentration im  $\text{In}_2\text{S}_3$  wird eine Aufwärtsverschiebung des Valenzbandes beobachtet.

Es hat sich herausgestellt, dass die CIGS Zusammensetzung, welche optimale Ergebnisse mit CdS als Pufferschicht liefert, für die Verwendung von  $\text{In}_2\text{S}_3$  als Pufferschicht angepasst werden muss. Das Mass des Kupferüberschusses in der 2. Stufe des Absorber Wachstums hat einen direkten Einfluss auf die Leistung der CIGS Solarzellen mit USP- $\text{In}_2\text{S}_3$  Pufferschichten. Der Kupferüberschuss beeinflusst besonders den Füllfaktor der Diodenkennlinie. Mit CIGS Proben, die einen Kupferüberschuss von 20% oder mehr in der 2. Stufe hatten, wurde ein maximaler Füllfaktor von nur 65% erreicht. Änderungen in der 3. Stufe zeigten, dass eine kupferarme Endzusammensetzung des CIGS notwendig ist um Rekombinationsverluste in der Solarzelle mit USP- $\text{In}_2\text{S}_3$  Pufferschicht zu minimieren. Es hat sich auch herausgestellt, dass der Galliumgehalt in der Oberflächenregion reduziert werden muss um einen hohen Wirkungsgrad zu erzielen.

Eine Variation des Galliumgehalts in CIGS, das mit minimalem Kupferüberschuss und einem kupferarmem Endgehalt gewachsen wurde, zeigt eine Änderung des dominanten Rekombinationsmechanismus ein  $[\text{Ga}]/[\text{III}]$  Verhältnis zwischen 0.22 und 0.23. Dies deutet auf die Bildung eines negativen Valenzbandversatzes zwischen Puffer- und Absorberschicht für  $[\text{Ga}]/[\text{III}] \geq 0.23$  hin.

Ein deutlicher Anstieg der Leerlaufspannung und des Füllfaktors der CIGS Solarzellen mit USP- $\text{In}_2\text{S}_3$  Pufferschichten wird beobachtet nach einem Tempern der fertigen Zelle bei 200 °C in Luft. Diese Leistungsverbesserung basiert auf einem Anstieg der Aktivierungsenergie von der Sättigungsstromdichte, der wiederum auf eine Aufweitung der Bandlücke des Absorbers durch Kupferverarmung in der Oberflächenregion zurückgeführt werden kann. Der höchste Wirkungsgrad von 13.4% einer CIGS Solarzelle mit USP- $\text{In}_2\text{S}_3$  Pufferschicht wurde erreicht mit einem  $[\text{Ga}]/[\text{III}]$  Verhältnis von 0.14 und einem Gallium "Finish". Die Methode des Gallium "Finish" erwies sich allerdings als nicht reproduzierbar. Mit minimalem Kupferüberschuss in der 2. Stufe, Kupferarmer Endzusammensetzung und reduziertem Gallium Gehalt in der 3. Stufe konnten hingegen reproduzierbare Resultate mit USP- $\text{In}_2\text{S}_3$  Pufferschichten erzielt werden. Dieser Prozess ergab einem maximalen Wirkungsgrad von 13.1% (mit der entsprechenden CdS Referenz wurden 13.7% erreicht). Das zusätzliche Aufbringen einer  $\text{MgF}_2$  Antireflexionsschicht steigerte den Wirkungsgrad auf 14.2%, was einer Effizienz von 15% der aktiven Fläche entspricht.

USP- $\text{In}_2\text{S}_3$  Pufferschichten wurde auch mit schwefelhaltigen  $\text{Cu}(\text{In,Ga})(\text{S,Se})_2$  (CIGSSe) Absorbern getestet. Die CIGSSe Absorber werden mithilfe eines beschleunigten thermischen Verfahrens hergestellt, was eine grössere Oberflächenrauigkeit zur Folge hat. Mit der entwickelten USP Methode ist es möglich auch diese rauen Oberflächen mit einer kompakten durchgehenden  $\text{In}_2\text{S}_3$  Schicht zu bedecken. Obwohl die CIGSSe Absorber extrem kupferarm sind, wurde auch hier Kupferdiffusion vom Absorber in die USP- $\text{In}_2\text{S}_3$  Pufferschicht mit XPS Tiefenprofilen nachgewiesen. Mit den schwefelhaltigen CIGSSe Absorbern wurde ein Wirkungsgrad von 12.4% erreicht bei entsprechenden 10.3% der CdS Referenzzelle.

Neben den  $\text{In}_2\text{S}_3$  Schichten wurden auch ZnS Schichten als mögliche Pufferschichten in CIGSSe Solarzellen untersucht. Stöchiometrische ZnS Schichten können mit der USP Methode aus  $\text{ZnCl}_2$  und Thioharnstoff als Ausgangsstoffe gelöst in Azeton gewachsen

werden. Analog zu den Beobachtungen bei  $\text{In}_2\text{S}_3$  können Chlor Verunreinigungen auch im ZnS durch anheben der Proben temperatur oder des Schwefelgehalts in der Lösung verringert werden.

Die Leistung von CIGSSe Solarzellen mit USP-ZnS Pufferschicht verbessert sich erheblich mit einem Temperprozess der fertigen Zelle bei  $200\text{ }^\circ\text{C}$ . Dieser Effekt lässt sich unabhängig von der ZnS Depositionstemperatur und Schichtdicke in zwei Schritte unterteilen. In einem ersten Schritt steigen  $V_{\text{OC}}$  und FF stark an, was auf eine verringerte Elektron-Loch-Recombination hinweist. In einem zweiten Schritt nach 20 min akkumulierter Temperatur wird ein weiterer Anstieg des  $V_{\text{OC}}$  zusammen mit einem starken Anstieg des  $J_{\text{SC}}$  beobachtet, was auf Veränderungen der optischen Eigenschaften der ZnS Schicht hindeutet. Mit USP-ZnS Pufferschichten auf CIGSSe Absorbern wurde ein maximaler Wirkungsgrad von 10.8% erreicht, mit einem deutlichen Anstieg in der Stromdichte aber mit bedeutenden Verlusten in  $V_{\text{OC}}$  und FF im Vergleich zur CdS Referenzsolarzelle (11.4%). Die Verluste ergeben sich durch ein unvorteilhafte Ausrichtungen der Valenz- und Leitungsbänder. Ein teilweises Ersetzen der Schwefelatome durch Sauerstoff im ZnS sollte die Ausrichtungen der Bänder verbessern und damit auch die Leistung der Solarzelle.



# 1 Introduction

## 1.1 General introduction

The increasing global energy demand and the predicted severe climate changes places the development of secure, sustainable, reliable and competitive energy sources on topmost priority. The most abundant energy source available on earth is the irradiation from the sun. This suggests itself the development of a cost-effective technology for direct conversion of the solar irradiation in electricity, the most valuable form of energy. In order to meet this goal, thin film photovoltaics on the basis of solid state semiconductors are a promising solution (see for instance [1]). Polycrystalline CdTe and Cu(In,Ga)(S,Se)<sub>2</sub> thin film solar cells have emerged as the most promising options for highly-efficient and cost-effective solar electricity generation with high potential of reaching grid parity in numerous countries. In this thesis the focus is put on the investigation of thin film solar cells with Cu(In,Ga)(S,Se)<sub>2</sub> absorber material.

## 1.2 Chalcopyrite thin film solar cells

Highest cell efficiency of 20.0% is achieved with a Cu(In,Ga)Se<sub>2</sub> absorber in combination with a CdS n-type semiconductor grown by chemical bath deposition (CBD) [2, 3]. However, the properties of the CBD deposition technique and of the material CdS have several disadvantages which will be discussed within this thesis. The development of a Cd-free buffer layer with superior properties to CdS and of an alternative deposition procedure are among major objectives in the field chalcopyrite thin film solar cell research and production implementation.

The alloy Cu(In,Ga)(S,Se)<sub>2</sub> is a group I-III-VI<sub>2</sub> p-type semiconductor with adjustable energy band gap  $E_g$ . The crystalline structure of the chalcopyrite is shown in figure 1.1a. Changing the ratio of the group III elements In and Ga in the compound changes the energy band gap from 1.01 eV (CuInSe<sub>2</sub>) to 1.68 eV (CuGaSe<sub>2</sub>). The band gap can also be engineered by changing the ratio of the group VI elements S and Se from 1.01 eV (CuInSe<sub>2</sub>) to 1.53 eV (CuInS<sub>2</sub>) or from 1.68 eV (CuGaSe<sub>2</sub>) to 2.43 eV (CuGaS<sub>2</sub>) [4]. The band gap engineering potential of the chalcopyrite compound with the mentioned elements is summarized in figure 1.1b.

In this work  $\text{Cu(In,Ga)Se}_2$  (CIGS) absorber layers with different ratios of the group three elements and  $\text{Cu(In,Ga)(S,Se)}_2$  (CIGSSe) alloys are investigated. In the following the abbreviation CIGS is also used for the general description of solar cells based on  $\text{Cu(In,Ga)(S,Se)}_2$  alloys. Whenever absorbers containing sulfur are used in this work the abbreviation CIGSSe is used.

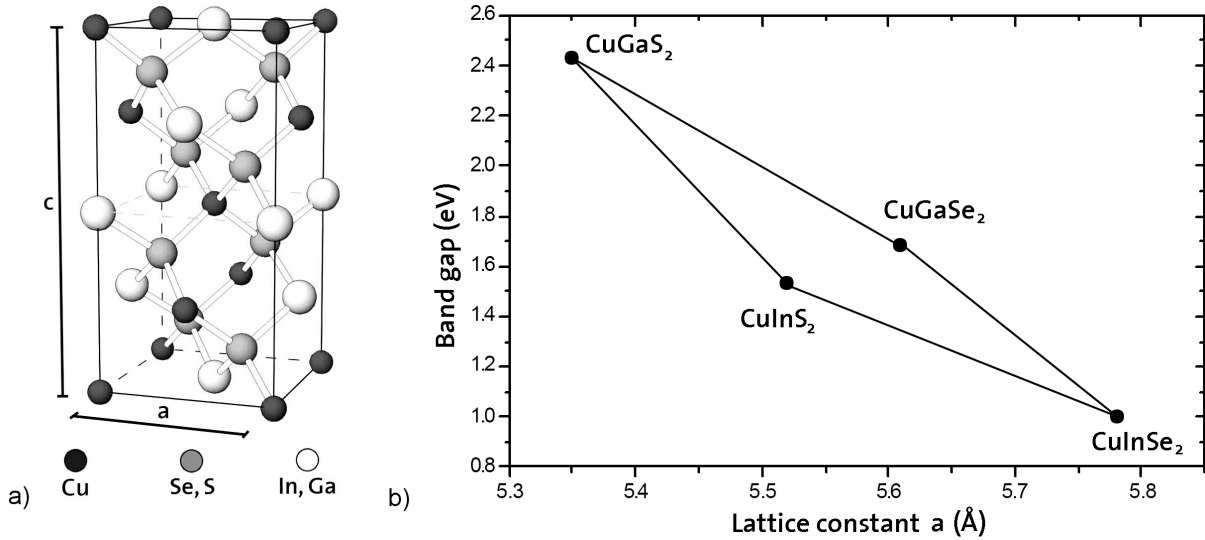


**Figure 1.1:** a) Unit cell of chalcopyrite structure ( $\alpha$ -phase) with lattice constants  $a$  and  $c$ , named after the mineral Chalcopyrite ( $\text{CuFeS}_2$ ). Cation and Anion arrangements are the same as in the Zincblende mineral ( $\text{ZnSe}$ ) and the basic atom arrangement corresponds to the diamond crystal structure. b) Band gap and lattice constants range for chalcopyrite compounds [5].

The absorption coefficient of the CIGS alloys is in the order of  $10^5 \text{ cm}^{-1}$  for photons with energy above the energy band gap. In figure 1.2 absorption coefficients of commonly used absorber materials for photovoltaic (PV) applications are compared. Alloying the  $\text{CuInSe}_2$  with gallium shifts the absorption edge to higher energy but no change in the absorption coefficient for photons with  $E > E_g$  is observed.

Due to the high absorption coefficient of the chalcopyrite compound a layer thickness of 1.5 to 2  $\mu\text{m}$  is sufficient for PV applications. For the application in thin film solar cells a n-type semiconductor is deposited onto the p-type CIGS absorber layer for the formation of a pn junction. The pn junction is sandwiched between an electrical front and back contact. In this work molybdenum is used as electrical back contact and a bilayer of aluminum doped zinc oxide (AZO) and intrinsic zinc oxide (i-ZnO) as electrical front contact. The deposition processes of these layers is described in the following sections.



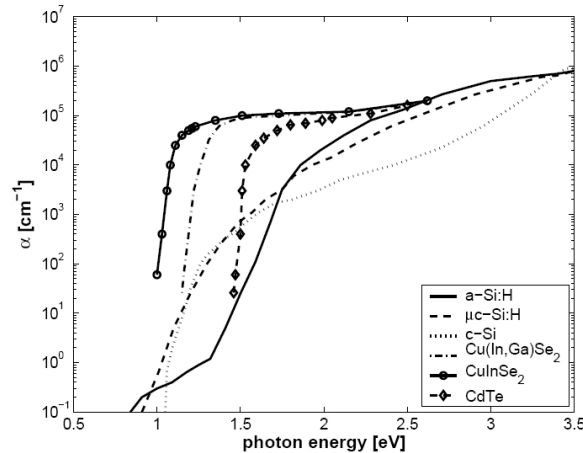


**Figure 1.2:** *The optical absorption coefficient  $\alpha$  versus incident photon energy spectra of light absorbing materials used in solar cells (from [6]).*

### 1.2.1 Molybdenum Back Contact

Molybdenum is commonly used as back contact for CIGS solar cells as it forms a low-resistive and ohmic contact to the absorber by a thin  $\text{MoSe}_2$  interlayer [7]. Usually Mo is deposited by DC-magnetron sputtering or by electron-beam evaporation. For the CIGS cells investigated in this work, Mo is deposited by DC-magnetron sputtering in argon from a metallic Mo target 200 mm in diameter on a  $5 \times 5 \text{ cm}^2$  soda lime glass (SLG) substrate. A bilayer of Mo is used as back contact. First, a thinner layer at high sputter power (typically 100 nm, 2 kW) for achieving good adhesion to the substrate, and immediately after that a thicker layer at low sputter power (typically 850 nm, 0.3 kW) is deposited.

### 1.2.2 CIGS Absorber

The sulfur free CIGS absorber is grown with a modified 3-stage process where the elements are co-evaporated and Se is provided in excess. In the first stage an  $(\text{In,Ga})_2\text{Se}_3$  precursor layer is deposited at a substrate temperature of  $400^\circ\text{C}$ . Secondly, Cu and Se are co-deposited at a substrate temperature of  $580^\circ\text{C}$  until the layer composition is Cu rich. In the third stage, In, Ga and Se are co-evaporated at the same substrate temperature until the desired Cu deficiency of the film is reached. For further information see [8].

### 1.2.3 Buffer layer

The buffer layer provides the n-type counterpart to the p-type absorber for forming the pn-junction. Since the buffer layer is the main topic of this thesis it is discussed separately in section 1.4.

### 1.2.4 Front contact and Ni-Al Grid

The front contact of the devices processed during this work is a stack of two layers, an intrinsic zinc oxide (i-ZnO) buffer layer and an aluminum doped zinc oxide (AZO) front contact layer. Both layers are deposited by radio frequency (RF) sputtering at a frequency of 13.56 MHz. The i-ZnO layer is sputtered in an argon and oxygen atmosphere from a 4-inch ceramic ZnO target at a sputter power of 150 W. The typical thickness of the applied i-ZnO layer is 50 nm. This layer has a high resistivity and transmission. The AZO layer is sputtered from a 4-inch ceramic ZnO target doped with 2 wt.% Al<sub>2</sub>O<sub>3</sub>. The optimum thickness of the AZO layer is determined by a trade-off between transparency and conductivity. Here a thickness of approximately 250 nm is deposited at a sputter power of 200 W with pure argon as working gas. Such bilayers exhibit a sheet resistance of about 20  $\Omega_{\square}$  measured on a soda lime glass dummy.

Additional current collection is supported by a metal grid applied onto the front contact. For this a 50 nm thick nickel and a 2  $\mu\text{m}$  thick aluminum bilayer is deposited by electron-beam evaporation of elemental Ni and Al through aperture masks. The purpose of the Ni is to prevent the formation of a resistive Al<sub>2</sub>O<sub>3</sub> barrier.

## 1.3 Aim of this thesis

The aim of this thesis is the substitution of a suitable compound semiconductor for the commonly used CdS as buffer layer in CIGS based thin film solar cells. The challenge is to develop a low-cost deposition method which allows conformal coverage of complex surfaces with thin layers suitable for the deposition of alternative buffer layer materials. Next to cost-efficiency and conformal coverage, the requirements for the deposition technique are in-line compatibility and scalability.

A further and very important aim of this thesis is to understand the interface formation between the alternative buffer and the CIGS absorber layers. This understanding will provide the foundation for further efficiency improvements and therefore cost reductions with the objective of sustainable and cost-efficient solar electricity production.

## 1.4 Buffer layers

Chalcopyrite thin film solar cells are n-on-p heterojunction devices. In case of CIGS based solar cells the junction is formed between a p-type  $\text{CuIn}_{1-x}\text{Ga}_x\text{Se}_{2-2z}\text{S}_{2z}$  compound semiconductor and a  $n^+$ -type window layer stack. This is an one-sided abrupt junction resulting in an almost complete shift of the depletion region into the p-type absorber material. Photons with energy above the energy band gap of the n-type semiconductor stack are absorbed in the window material. Carriers generated within the diffusion length from the junction in the window material will be collected and contribute to the photocurrent. However, because of the high recombination rate in the window layer and the asymmetric depletion region across the junction, most of the carriers generated in the window material are lost. To improve the performance of such devices it is essential to reduce the parasitic light absorption in the window material.

For optimum flow of minority charge carriers across the junction a continuous band alignment is desired. In heterojunction devices the p-n junction partners most often have different energy band gaps resulting in energy band discontinuities. In n-on-p heterojunction devices the band offset in the conduction band between the p-type absorber and the n-type window material should be small in order to prevent a barrier formation for photo-generated electrons [9].

Due to the polycrystalline nature of the p- and n-type layers in the CIGS thin film solar cell, defects at the interface are unavoidable. The defects at the junction originate from crystallographic point defects due to non-stoichiometry of the semiconductors at the interface [10]. These defects influence the potential distribution at the junction and can add additional transport paths for charge carrier tunneling and recombination [9].

The requirements for the n-type window stack can be summarized as follows (cf. [9–11]):

- Sufficiently large band gap and negligible absorption of light with energy below the energy band gap of the window material in order to reduce parasitic absorption losses.
- Conduction band offset  $\Delta E_C$  should be small; a negative  $\Delta E_C$  enhances interface recombination of electron hole pairs and a positive  $\Delta E_C$  forms a potential barrier for electrons.
- Formation of no or only minimum number of interface traps (deep-defects) at the junction. A large interface trap density increases the recombination velocity at the interface.
- Fermi level close to the conduction band in order to reach a high built in potential and high recombination barrier for holes at the interface.
- High conductivity for efficient electron transport from the heterojunction to an external circuit.

In state-of-the-art CIGS based solar cells a stack of three layers is used to meet the above mentioned requirements of the window material. The stack is composed of a transparent conductive oxide (TCO) layer a highly transparent and resistive (HTR) oxide layer and a buffer layer. In this work aluminum doped ZnO (AZO) was used as TCO material. The AZO layer is highly n-type doped and provides high conductivity for lateral electron transport.

Intrinsic ZnO (i-ZnO) is applied as HTR layer to limit electrical losses at local shunts and grain boundaries. Rau et al. developed a model in 2001 with which the beneficial effect of the i-ZnO layer in polycrystalline CIGS based solar cells can be explained by the conduction band offset at the HTR-buffer interface enabling self-limitation of electrical losses due to electrical potential differences between the n-type window material and the single grains in the CIGS absorber [12]. The offset barrier limits current flowing into the diodes with poor quality and thus improves the performance of parallel connected diodes.

Both AZO and i-ZnO are high band gap materials with low parasitic absorption losses, however, with an unfavorable conduction band offset if directly applied onto the absorber layer. In order to improve the band alignment between the n-type window material and the p-type absorber layer a thin buffer layer is introduced. An additional requirement for the buffer layer material is the reduction of the interface trap (deep-defect) density.

### 1.4.1 Suitable buffer layer materials

Even though highest efficiency of chalcopyrite based solar cells is achieved with CBD-CdS buffer layer there are several reasons to substitute the deposition method as well as the material.

The high absorption coefficient ( $10^5 \text{ cm}^{-1}$ ) and relatively low energy band gap (2.4 eV) of CdS limits the spectral response of the device in the low wavelength region ( $<520 \text{ nm}$ ). In order to overcome this limitation a buffer layer material with higher energy band gap and/or lower absorption coefficient is required. Most promising materials are  $\text{In}_2\text{S}_3$ ,  $\text{Zn}(\text{O},\text{S})$  and  $(\text{Zn},\text{Mg})\text{O}$ . Table 1.1 shows a selection of such alternative buffers on CIGS and CIGSSe absorber layers.

The chemical bath deposition is a batch to batch process and therefore difficult to implement in an in-line (or even roll-to-roll) production line. Furthermore, it is a wet chemical method which requires substrate drying for the subsequent vacuum-based front contact deposition. During the CBD process Cd-ion containing waste accumulates which has to be extensively decontaminated or recycled. An substituting deposition technique should be compatible with in-line processing. Possible methods are atomic layer deposition (ALD), ion layer gas reaction (ILGAR), sputtering and thermal evaporation (PVD), and ultrasonic spray pyrolysis (USP). See table 1.1 for a selection of results of these methods.

**Table 1.1:** Selection of buffer layer materials for CIGS thin film solar cells. A more detailed summary can be found in [13]. Efficiency values with \* correspond to cells with  $MgF_2$  anti-reflection coating.

Buffer layer	Deposition	Absorber	Efficiency [%]	Ref.
CdS	CBD	Cu(In,Ga)Se <sub>2</sub>	20.0	[2]
In <sub>2</sub> S <sub>3</sub>	co-evap.		13.3	[14]
	compound-evap.		15.2	[15]
	reactive sputtered		11.1	[16]
	ceramic sputtered		13.3	[17]
	ALD		16.4	[18]
Zn(O,S)	USP		13.4	[19]
	CBD		18.5	[20]
(Zn,Mg)O	ALD		18.5*	[21]
	ALD		18.1*	[22]
In <sub>2</sub> S <sub>3</sub>	ILGAR	Cu(In,Ga)(S,Se) <sub>2</sub>	14.7	[23]
	USP		12.4	[24]
Zn(O,S)	CBD		14.9	[25]
(Zn,Mg)O	sputtered		13.1	[26]

Naghavi et al. recently reviewed the materials and deposition methods for buffer layers in chalcopyrite thin film solar cells [13]. In the following the materials and methods used in this thesis are described in more detail.

#### 1.4.1.1 CdS buffer layer

The compound CdS is a II-VI semiconductor with intrinsic n-type conductivity. The band gap of CdS is 2.4 eV [27]. Crystalline CdS occurs in the cubic zincblende and the hexagonal wurtzite structure [28]. The transition of the energy band gap is allowed direct and the absorption coefficient is  $>10^5 \text{ cm}^{-1}$  for  $E > E_g$ .

#### 1.4.1.2 Indium(III)sulfide buffer layer

The binary alloy In<sub>2</sub>S<sub>3</sub> is a III-VI n-type semiconductor and a prospect substitute of the CdS buffer layer in CIGS solar cells. The reported values for the band gap energy vary from 1.98 eV to 3.7 eV [29, 30] depending on the deposition method. The nomenclature of the different phases of In<sub>2</sub>S<sub>3</sub> is not consistent in literature. Here the definition of C.E.T. White and H. Okamoto is taken as reference [31]. When referring to In<sub>2</sub>S<sub>3</sub> it is distinguished between three phases. The nomenclature  $\alpha$ -,  $\beta$ - and  $\gamma$ -phase are assigned to the occurring phases in the order of ascending temperature at 60 at.% S (see figure 1.3).

The tetragonal  $\alpha$ -In<sub>2</sub>S<sub>3</sub> phase changes to the cubic  $\beta$ -In<sub>2</sub>S<sub>3</sub> phase at a temperature of 414 °C and is stable up to 750 °C where the transition to the hexagonal  $\gamma$ -In<sub>2</sub>S<sub>3</sub> phase takes place. The melting point of  $\gamma$ -In<sub>2</sub>S<sub>3</sub> is 1090 °C. On the slightly In rich side also

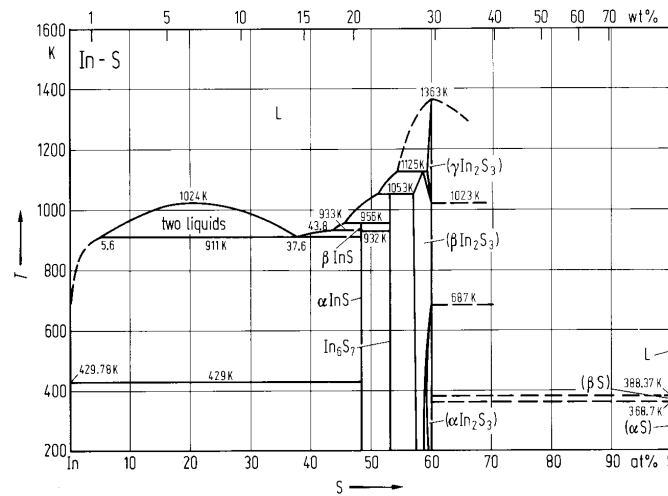


**Figure 1.3:** *Equilibrium phase diagram of the binary alloy In-S (figure from [32]).*

$\beta$ - $\text{In}_2\text{S}_3$  is stable at room temperature. This phase was previously also called  $\text{In}_{2.8}\text{S}_4$  [33]. The crystal structures of various  $\text{In}_x\text{S}_y$  phases are listed in table 1.2.

**Table 1.2:** *The crystal structure of various  $\text{In}_x\text{S}_y$  phases according to [31].*

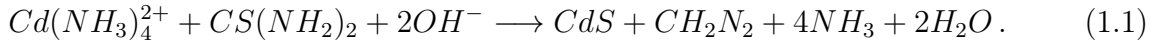
Phase	Structure	Composition [at.%]	lattice parameters [nm]			angle [ $^\circ$ ]	Reference
			a	b	c		
$\alpha$ -InS	orth	50	0.4442	1.0642	0.3939	-	[34]
$\text{In}_6\text{S}_7$	mon	53.8	0.9090	0.3887	1.7705	108.2	[35]
$\alpha$ - $\text{In}_2\text{S}_3$	tetr	60	0.761		0.3224	-	[36]
$\beta$ - $\text{In}_2\text{S}_3$	cub	57.5	1.0717			-	[37]
$\beta$ - $\text{In}_2\text{S}_3$	cub	60	1.074			-	[38]

## 1.4.2 Buffer layer deposition methods

Several techniques are investigated and used for the deposition of thin buffer layers on the chalcopyrite absorber. The variety of techniques are reviewed by Siebentritt [39], Hariskos et al. [40], and more recently by Naghavi et al. [13]. In the following only the deposition methods used during this work are described.

### 1.4.2.1 Chemical bath deposition

Solar cells with Chemical bath deposited CdS as buffer layer yield the highest efficiencies so far. An important side effect of the CBD technique is the etching of the absorber surface in the bath before the CdS film growth [41] and the recovery of the surface inversion [42]. The CdS film growth in the solution can be described by the chemical reaction



The reaction can be divided in three steps [43]. First, the growth rate remains low and nucleation goes on. In the second step, the CdS film begins to grow at more or less constant rate which is supposed to be an ion-by-ion deposition process where the  $Cd^{2+}$  and the  $S^{2-}$  ions react with the surface of the growing layer. The resulting layer is compact, adherent and reflecting. During the third step, an agglomeration of colloids and larger particles from the solution takes place, resulting in a powdery, poorly adhering layer.

The following recipe is used for the chemical bath deposition of CdS on the cells processed during this work. Cadmium acetate ( $Cd(CH_3COO)_2$ ), thiourea ( $CS(NH_2)_2$ ) and ammonia ( $NH_3$ ) are dissolved in high-purity water ( $\approx 18 M\Omega cm$ ). The samples processed up to the absorber layer are put into the solution and heated in a water bath to 65-70 °C while the solution is mixed permanently by a magnetic stirrer. After about 15 min of deposition a 50-60 nm thick CdS layer is formed. More informations about the process during CBD can be found in [43].

#### 1.4.2.2 Ultrasonic spray pyrolysis of compound semiconductors

Spray pyrolysis is a low cost, non-vacuum deposition technique broadly used in research and industry for nano-scale powder synthesizing, surface etching and coating. The method was first described by Camberlin and Skarman in 1966 [44]. It can be categorized by the droplet formation method between the pneumatic-, electrostatic- or ultrasonic-spray pyrolysis approaches. In this work an ultrasonic atomizer was used for the droplet formation. With this technique, small droplets (with diameter smaller than 5  $\mu m$ ) can be produced with a uniform and narrow size distribution. These small droplets can be transferred to the substrate with little momentum, thus minimizing possible bounce and impact effects on the surface, making this technique suitable for coating sensitive surfaces [45].

An ultrasonic spray pyrolysis (USP) system consists of an ultrasonic atomizer, a droplet transport system and a heating area for substrate material. For this work we used a chamber-based ultrasonic atomizer, where the droplets are generated from a liquid solution in a chamber sitting above oscillating piezo crystals schematically shown in figure 1.4.

From this chamber, the droplets are transferred with nitrogen carrier gas into a funnel. The funnel is kept very close to the heated substrate, creating an almost closed deposition area above the substrate surface which is important to prevent surface oxidation of the sample. Before every deposition run the system is vented with nitrogen in order to decrease the oxygen content in the reaction area. The reaction area is kept at normal atmospheric pressure.

The droplet diameter  $d$  produced by the nebulizer described above can be estimated by Lang's correlation assuming that the majority of the droplets are formed by capillary wave mechanisms [46]. It was found by Lang that the mean droplet diameter (in cm) is

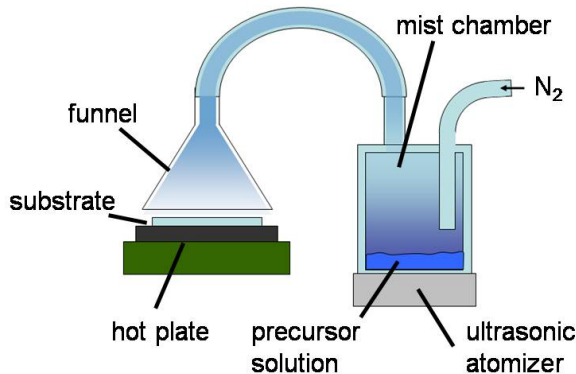


**Figure 1.4:** Schematic setup of the ultrasonic spray pyrolysis system used in this work

a constant fraction of the capillary wavelength in the exciting frequency range between 10 and 800  $kHz$ :

$$d = 0.34 \left( \frac{8\pi\sigma}{\rho f^2} \right)^{1/3}, \quad (1.2)$$

where 0.34 is the empirically found constant fraction,  $\sigma$  is the surface tension of the solvent ( $mN/m$ ),  $\rho$  the density of the solvent ( $g/ml$ ) and  $f$  is the excitation frequency ( $Hz$ ). It was found later, that the fraction of 0.34 is also valid for excitation frequencies in the  $MHz$  range (e.g. [47, 48]). The excitation frequency in the used setup is 1.7  $MHz$ . Table 1.3 shows the expected droplet mean diameters for commonly used solvents, as calculated through Lang's correlation.

**Table 1.3:** Overview of possible solvents with respective surface tension  $\sigma$ , density  $\rho$ , calculated droplet diameters  $d$  at 1.7  $MHz$  excitation frequency, vapor pressure  $VP$  at  $200^\circ C$ , donor number, dielectric constant and boiling point  $BP$  [49, 50]. \* Ethylene glycol monobutyl ether; \*\* at  $171^\circ C$ .

Solvent	$\sigma$ [mN/m]	$\rho$ [g/ml]	$d$ [ $\mu m$ ]	$VP$ [mbar]	Donor number	Dielectric constant	$BP$ [ $^\circ C$ ]
Methanol	22.5	0.788	2.1	37726	17.0	32.6	64.7
Ethanol	22.32	0.798	2.1	30994	19.0	24.3	78.4
Acetone	25.2	0.798	2.2	25710	17.0	20.7	56.5
Acetonitrile	19.1	0.786	2.0	16300	14.1	36.2	81.8
Water	71.98	0.997	3.0	15549	18.0	78.5	100
EB*	32	0.90	2.3	1013**	--	--	171

The surface temperature of the substrate is determined by calibration measurements previously to the layer deposition and correlated to the temperature of the hot plate which is measured with a thermocouple directly at the backside of the substrate. For the temperature calibration a spray deposition run with same deposition parameters was performed



---

with a thermocouple attached to the surface of an dummy sample (same configuration and structure as later used for the layer deposition). A constant ratio between the temperature of the hot plate at the back of the sample which is continuously monitored and the surface temperature was determined depending on the substrate material and configuration.



## 2 Methods of characterization and interpretation

### 2.1 Material characterization

#### 2.1.1 X-ray diffraction

The diffraction of photons is used to investigate the crystal structure of thin layers on SLG substrates. Monochromatic X-rays pointed to the sample. The diffraction angle and the intensity of the reflected radiation are measured. In a crystalline structure intensity peaks appear at defined diffraction angles according to Bragg's law

$$2 d \sin\Theta = n \lambda, \quad (2.1)$$

where  $d$  is the distance between the crystal planes,  $\Theta$  is the diffraction angle and  $\lambda$  is the wavelength of the incident x-ray radiation. These peaks are characteristic for a certain material and the crystalline orientation of the grains in a polycrystalline layer.

The preferential orientation of a certain crystal plane (hkl) in a polycrystalline layer can be derived by using the texture coefficient [51]

$$TC_{(hkl)} = \frac{I_{(hkl)}/I_{(hkl)}^0}{\frac{1}{N} \sum_N I_{(hkl)}/I_{(hkl)}^0}, \quad (2.2)$$

where  $N$  is the number of reflections considered in the analysis,  $I_{(hkl)}$  is the intensity of a peak in the measured spectrum for the (hkl) plane and  $I_{(hkl)}^0$  is the intensity of the according peak taken from completely random orientated powder of the same material [52]. A value of 1 for the texture coefficient represents random orientation while for preferential orientation the value deviate from one. In order to analyze the preferential orientation of the whole sample the standard deviation  $\sigma$  of all  $TC_{(hkl)}$  values as compared to randomly orientation is used and derived by

$$\sigma = \sqrt{\frac{\sum_N (TC_{(hkl)} - 1)^2}{N}}. \quad (2.3)$$

The values of  $\sigma$  can be used to compare the degree of orientation between different samples. A value 0 means completely random orientation of the grains in the sample.

The average grain size of the crystals in a polycrystalline thin layer can be derived with the Debye-Scherrer formula

$$D = \frac{0.9 \cdot \lambda}{\Delta\theta \cdot \cos\theta}, \quad (2.4)$$

where  $D$  is the diameter of the grains in nm,  $\lambda$  the wavelength of the used X-rays in nm,  $\Delta\theta$  the FWHM of the intensity peak in radian and  $\theta$  the position of the peak maximum.

The XRD measurements were performed with a Siemens Kristalloflex and Diffraktometer D5000. In this setup a copper filament emits Cu-K $\alpha$  radiation with characteristic wavelength of 1.5406 Å. For the accomplished measurements the acceleration voltage is set to 40 kV and the filament current to 30 mA.

## 2.1.2 Electron microscopy

### 2.1.2.1 Scanning electron microscopy

High resolution scanning electron microscopy (SEM) images of the thin semiconductor layers were obtained with a Leo SEM 1530 operated at accelerating voltage between 3 and 5 kV. For cross section images, the samples were cleaved by breaking the supporting substrate. Non-conductive samples were coated with a thin platinum layer (approx. 5 nm thick) deposited by DC-sputtering. The conductivity from the coated surface or cross section was established with conductive silver paste.

The chemical composition of the thin films was measured with a Jeol JSM-5400 equipped with an energy dispersive x-ray spectrometer (EDX) from Tracor Northern with Flextran software. For the analytical measurements the microscope was operated at 20 kV acceleration voltage in fast scanning TV mode.

### 2.1.2.2 Transmission electron microscopy

For transmission electron microscopy (TEM) the samples were prepared with the conventional XTEM-preparation method. The sample to be investigated is cut in 2 mm wide stripes and the multilayer structure is sandwiched between the substrate and an additional silicon dummy. The Si-solar cell-glass stack is implemented in a copper or stainless steel tube and bonded with a vacuum compatible epoxy. After drying, the tube is cut into wafers. The wafers are first mechanically polished with wet grinding paper and dimple grinder and subsequently by ion milling until the region of interest approaches a thickness below 10 nm. The preparation procedure is described in more detail in [53].

The cross-section samples were investigated with a Tecnai F30ST (FEI) transmission electron microscope running at 300 kV accelerating voltage and a point to point resolution of

0.19 nm. The TEM was operated by Elisabeth Mueller at the Electron Microscopy Center, ETH Zuerich.

The high angular annular dark field detector (HAADF) was used for scanning TEM (STEM) images. For this imaging technique the electron beam is highly focused and scans over the sample area. In a homogeneous, defect-free material the brightness increases for thick areas and heavier atomic species. The intensity of the signal has a linear dependency on the sample thickness and an almost square one from the atomic number  $Z$ . Therefore, this technique is also called  $Z$ -contrast imaging.

Also in the scanning mode the chemical composition of the sample was investigated with EDX. With this chemical composition mapping of the cross-section was possible. However, this method only allows for qualitative and not quantitative analysis. The detected signal is highly thickness dependent due to re-absorption of x-rays and re-emission of x-rays with other characteristic energy. Additionally, no calibration measurement of a calibration sample with a well known composition and thickness was possible.

### 2.1.3 X-ray photoelectron spectroscopy

X-ray photoelectron spectroscopy (XPS) is a useful tool for the investigation of elemental composition chemical condition of the elements at the surface of the sample. The measurements were performed with a PHI-Quantum 2000 "imaging XPS". The depth resolution of the used method is 2-3 nm and the detection limit is typically 0.1-1 at%. The elements in the sample were excited with Aluminum- $K\alpha$  radiation ( $h\nu=1486.6$  eV). The work function ( $\phi$ ) of the system during the measurements was 3.7 eV. With this the binding energy ( $E_{BE}$ ) which is characteristic for the elements can be calculated from the detected kinetic energy ( $E_{kin}$ ) of the emitted electrons with

$$E_{BE} = E_{phot} - E_{kin} - \phi, \quad (2.5)$$

where  $E_{phot}$  is the energy of the exiting radiation.

For compositional depth-profiling the sample can be alternately etched by argon ion bombardment and analyzed with XPS. Samples were etched with 4 kV Ar-ions which corresponds to a etching rate of 18.8 nm/min of  $\text{SiO}_2$  and 16.8 nm/min of  $\text{Ta}_2\text{O}_5$  determined by calibration measurements. For thin layers 2 kV Ar-ions were used for the etching which corresponds to one third of the etching rate compared to the 4 kV Ar-ions.

XPS measurements of semiconductors and insulators can cause charging of the sample which causes an error in the energy scale. For the compensation of possible charging electron- and ion-neutralizer were active during all measurements.

### 2.1.4 Ion spectroscopy

Rutherford backscattering spectroscopy (RBS) and elastic recoil detection analysis (ERDA) are characterization methods to determine absolute elemental compositions and impurity concentrations. For both methods a 6 MV tandem accelerator was used, located at the ETH Laboratory for Ion Beam Physics and operated by Dr. Max Doebeli.

Helium ions with kinetic energy of 2 MeV are accelerated to the sample and backscattered particles are detected with a silicon detector in used the RBS setup. The incident He ions are elastically scattered at atom nuclei in the sample and lose energy mainly by the interaction with free or bound electrons. The energy of the backscattered ions is detected. This energy is a function of the mass and the position of the elements in the sample and therefore allows an elemental depth profiling. The resolution of such depth profiling is between 0.5 and 10 nm close to the sample surface. The composition and the layer thickness of thin layers can be determined with an error below 1%.

For the elemental analysis of sprayed compound semiconductors thin layers were deposited on (111) oriented silicon wafers. This allowed an exact analysis of elements heavier than the silicon substrate. The disadvantage of the RBS method is the accuracy limit for light elements, especially impurities of oxygen, nitrogen or carbon. Those impurities can be detected with high accuracy by ERDA measurements. ERDA is based on the same principle as RBS, however, the recoiled target atoms are detected instead of the backscattered He-ions.

In the used ERDA setup  $^{127}\text{I}$ -ions are accelerated towards the sample with kinetic energy of 12 MeV. The recoiled target atoms are detected with a combination of a time-of-flight spectrometer and a gas ionization chamber. A detailed description can be found in [54].

### 2.1.5 NIR-UV spectroscopy

The optical properties of the thin films were investigated with a UV-160 Shimadzu spectrometer in the wavelength range of 300-1100 nm. This spectrometer is a dual beam device and allows for direct comparison to a reference configuration.

Additionally, a UV-3600 spectrometer with integrating sphere was used in order to measure the total transmittance, specular reflectance, and global reflectance. With the used integrating sphere measurements in the wavelength range between 220 and 2600 nm are possible.

### 2.1.6 Thickness measurement

The layer thickness of thin films on supporting substrate was measured with a DEKTAC 3030 from Veeco Instruments Inc. Best reliability and reproducibility of the thickness measurement of sprayed layers was obtained by post-deposition etching of the layer in concentrated HCl. For this the sprayed films was partially covered with polyimide tape. After etching, the tape was removed and residuals of the glue were dissolved in acetone. This procedure resulted in a sharp step profile of the thickness and allowed thickness measurements below 30 nm.

## 2.2 Device characterization and interpretation

The electronic transport in CIGS thin film solar cells is commonly described by the single diode model [55]:

$$J = J_0 \left( e^{\frac{q(V-JR_s)}{AkT}} - 1 \right) + \frac{V - JR_s}{R_p} - J_{Ph}, \quad (2.6)$$

where  $J_0$  is the saturation and  $J_{Ph}$  the photogenerated current density. The expression  $kT$  is the thermal energy where  $k$  is the Boltzmann constant and  $T$  the absolute temperature. The diode ideality factor  $A$ , the series resistance  $R_s$  and parallel resistance  $R_p$  account for non-ideal behavior of the device. The equivalent circuit is shown in figure 2.1.

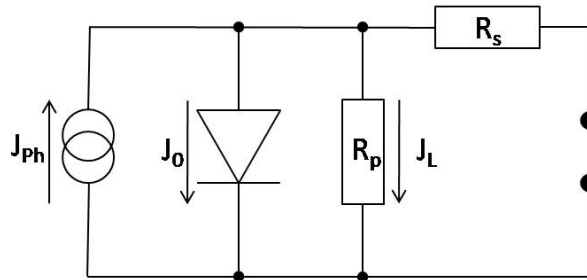


**Figure 2.1:** Equivalent circuit of the single diode model. The photogenerated current density  $J_{Ph}$  is indicated by a current source. In parallel to the current source but with inverted direction there is the saturation current density of the diode  $J_0$  and the leakage current density  $J_L$  indicated by a diode and a resistor connected in parallel. The resistor  $R_s$  represents the resistive losses in the device.

The series resistance in this model is composed of in plane resistances in the electrical front and back contact, contact resistances between the layers, and resistances for current transport through the intrinsic zinc oxide layer, the buffer layer and the quasi neutral region (QNR) in the absorber material. For achieving high efficiency the series resistance has to be minimized.

The parallel resistance, also called shunt resistance, represents current leakage of the diode at applied bias voltage. This is mainly caused by shunts through the cell due to crystal damages at the p-n junction and metalization spikes at the junction. The parallel resistance has to be maximized for high efficiency devices.

In the following sections characterization and interpretation methods of the heterojunction device are discussed.

### 2.2.1 Current voltage characteristics

The basic electrical parameter are measured by current voltage characteristics. Four terminal contacting method is used to eliminate contact resistances made at the electrical front and back contact. A bias voltage is applied to the solar cell and the current is measured. If the device is illuminated a diode characteristic shifted on the y-axis by short circuit current is expected. Figure 2.2 shows a typical current voltage characteristic of a CIGS device.

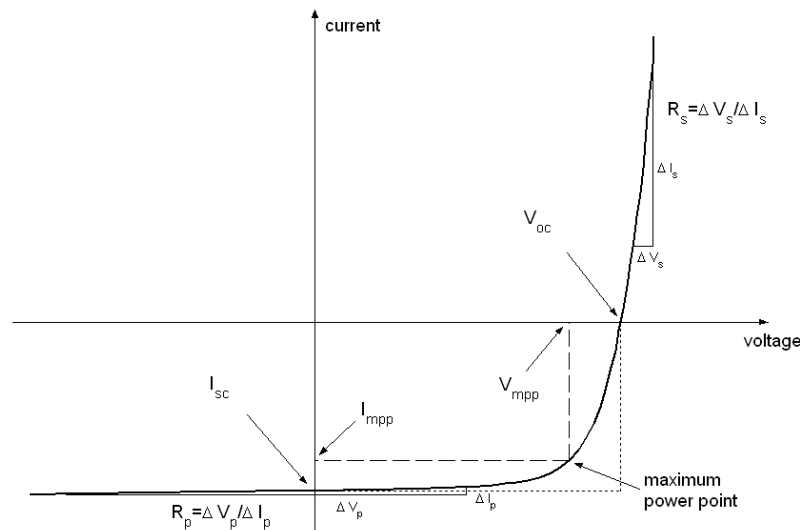


**Figure 2.2:** *Current voltage characteristics of a CIGS solar cell.*

The electrical parameter indicated in figure 2.2 are the open circuit voltage  $V_{OC}$ , the short circuit current  $I_{SC}$ , the fill factor  $FF$  and the series and parallel resistances. Also indicated is the maximum power point of the device. The maximum power point ( $P_{MPP}$ ) is derived by curve sketching of the function  $P(V)=I*V$ .

With the maximum power point, the fill factor is defined as:



$$FF = \frac{P_{MPP}}{V_{OC}J_{SC}} = \frac{V_{MPP}J_{MPP}}{V_{OC}J_{SC}}. \quad (2.7)$$

The fill factor is a measure of the squareness of the I-V characteristics and is always below unity. The value  $J_{SC}$  is the short circuit current density of the device. An empirical formula for the fill factor was found by Green [56]:

$$FF_0 = \frac{v_{OC} - \ln(v_{OC} + 0.72)}{v_{OC} + 1}, \quad (2.8)$$

where  $v_{OC}$  is given by  $v_{OC} = qV_{OC}/AkT$  as a function of the ideality factor A. Including the series and parallel resistances this expression expands to [55]:

$$FF = FF_0(1 - r_s) \left( 1 - \frac{(v_{OC} + 0.7) FF_0(1 - r_s)}{v_{OC} r_p} \right), \quad (2.9)$$

where  $r_s$  and  $r_p$  are normalized by  $r_{s(p)} = R_{s(p)}J_{SC}/V_{OC}$ . The fill factor depends on the series and parallel resistances as well as on the diode ideality factor. These dependencies are illustrated in figure 2.3.

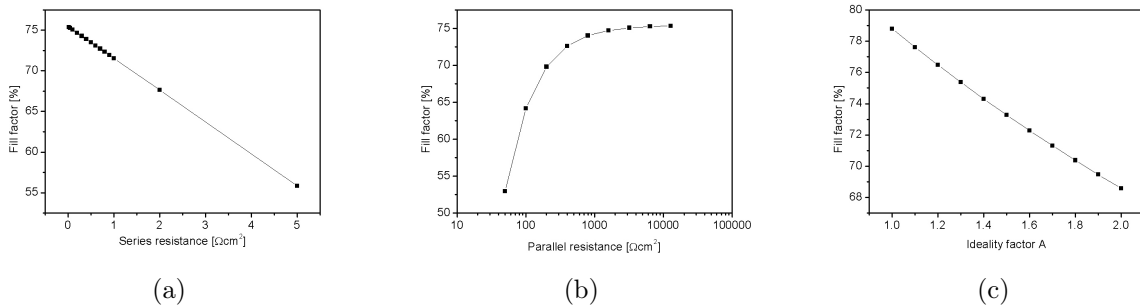


**Figure 2.3:** Dependency of the fill factor on the series resistance (a), parallel resistance (b) and ideality factor (c) as derived from equation 2.9.

The short circuit current density of a CIGS device depends on the one hand on optical losses due to reflection at interfaces, parasitic absorption, shadowing effect of grids, and absorption coefficient of the absorber. On the other hand there are also electrical losses since not all electron-hole pairs contribute to the  $J_{SC}$ .

The open circuit voltage of the device can be derived from 2.6 and approximated by

$$V_{OC} \approx \frac{AkT}{q} \ln \left( \frac{J_{Ph}}{J_0} \right), \quad (2.10)$$

if the parallel resistance is sufficiently large ( $V_{OC}/R_p \ll 1$ ). In order to maximize the device open circuit voltage, the saturation current  $J_0$  has to be small, i.e., recombination mechanisms have to be minimized. The recombination mechanisms will be discussed in more detail in section 2.2.1.1.

The design of an efficient CIGS solar cell can be summarized in the following goals:

- maximum absorption of photons in the p-type CIGS;
- minimum recombination of generated electron-hole pairs;
- $R_s \rightarrow 0$  and  $R_p \rightarrow \infty$ ;
- ideality factor close to unity.

An important parameter of photovoltaic devices is the conversion efficiency  $\eta$  of the incoming light to electricity. This is given by the ratio of maximum power point ( $P_{MPP}$ ) to the power of the incident irradiation ( $P_i$ ):

$$\eta = \frac{P_{MPP}}{P_i} 100\% = FF \frac{V_{OC} J_{SC}}{P_i} 100\%. \quad (2.11)$$

The incident irradiation power is given in  $\text{W}/\text{m}^2$ . Since the electrical device parameter  $V_{OC}$ ,  $J_{SC}$  and  $FF$  depend considerably on the external parameters device temperature, irradiation intensity and spectrum, standard test conditions (STC) were defined in order to obtain comparable values. The STC specify an intensity of  $100 \text{ mW}/\text{cm}^2$  with AM1.5G spectrum and a constant device temperature of  $25^\circ\text{C}$ . More details can be found in the international standards IEC 60904-1 ed2.0 and IEC 60904-3 ed2.0.

### 2.2.1.1 Recombination mechanisms

Not all generated electron-hole pairs contribute to the device current in a real solar cell. Among the several possible recombination mechanism the non-radiative was found to be the main limitation of the  $V_{OC}$  in CIGS solar cells (e.g. [57]). A detailed description of the recombination theory can be found in [55, 57, 58]. In the non-radiative recombination there are basically three different paths for the electrons and holes to recombine in the heterojunction. Figure 2.4 shows a simplified band diagram of a CIGS device. The arrows illustrate the possible recombination paths: (A) in the quasi neutral region (QNR) of the absorber, (B) in the space charge region (SCR) and (C) at the buffer-absorber interface.

In order to understand the device properties it is important to identify the dominant recombination mechanism which limits the performance. The dominant recombination current can be written as [55]:

$$J_{rec} = J_0 \left( e^{\frac{qV}{AkT}} - 1 \right) = J_{00} e^{\frac{-E_a}{AkT}} \left( e^{\frac{qV}{AkT}} - 1 \right). \quad (2.12)$$

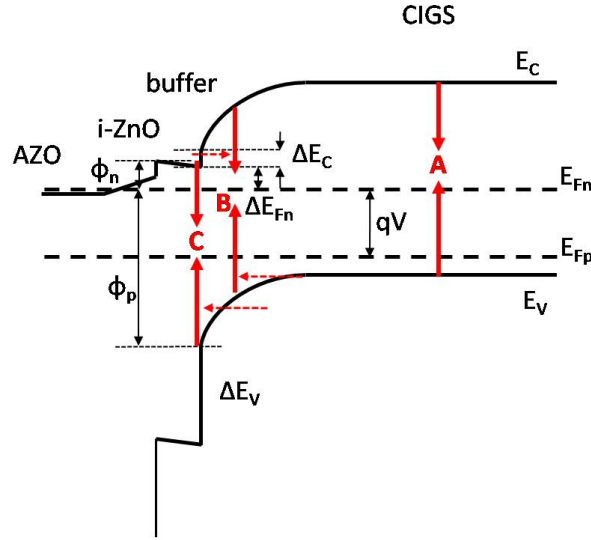


**Figure 2.4:** Band diagram of a ZnO/buffer/CIGS heterojunction under applied bias voltage. The red arrows indicate the three relevant recombination mechanisms: (A) in the quasi neutral region of the bulk, (B) in the space charge region and (C) at the buffer-absorber interface. The band diagram is drawn with a negative conduction band offset (cliff) at the buffer-absorber interface which is likely for  $In_2S_3$  buffer layers. Not shown are possible interface states.

Here  $J_{00}$  is an only weekly temperature dependent pre-factor,  $E_a$  is the activation energy of the saturation current and  $A$  is again the ideality factor. At open circuit voltage the recombination current density exactly compensates the short circuit current density. By combining equation 2.6 and 2.12 one finds

$$V_{OC} = \frac{E_a}{q} - \frac{AkT}{q} \ln \left( \frac{J_{00}}{J_{SC}} \right), \quad (2.13)$$

under the assumption that  $V_{OC} > 3AkT/q$ , where  $3AkT/q \approx A * 78 \text{ mV}$  at RT. With this assumption only the exponential term has to be considered in equation 2.12. Since the recombination paths A-C are parallel, only the dominant mechanism can be evaluated. The recombination mechanisms A-C are discussed in detail in ref [55] and only summarized here:

### Recombination in the QNR

If the dominating path is the recombination in the bulk of the absorber the upper limit of the  $V_{OC}$  is basically given by the band gap of the absorber, the shallow acceptor density and the diffusion properties of the minority carriers. In the QNR recombination limit one finds [55]:

$$V_{OC} = \frac{E_g}{q} - \frac{kT}{q} \ln \left( \frac{qD_e N_C N_V}{J_{SC} L_e N_a} \right), \quad (2.14)$$

where  $D_e$  is the diffusion constant and  $L_e$  the diffusion length of electrons,  $N_{C(V)}$  the effective density of state in the conduction (valence) band of the absorber, and  $N_a$  the acceptor density.

### Recombination in the SCR

The limitation of the  $V_{OC}$  if recombination in the space charge region is dominant can be written as:

$$V_{OC} = \frac{E_g}{q} - \frac{2kT}{q} \ln \left( \frac{kTD_e\pi/2\sqrt{N_C N_V}}{J_{SC} L_e^2 E_{max}} \right). \quad (2.15)$$

Here  $E_{max}$  is the electric field given by  $E_{max} = \sqrt{2qN_a V_{bm}/\epsilon_s}$ , where  $V_{bm}$  is the band bending and  $\epsilon_s$  the dielectric constant of the absorber. Rau et al. showed that in both regimes, the QNR and the SCR dominated recombination, an increase of the doping density  $N_a$  by one order of magnitude yields an increase of 60 mV in the  $V_{OC}$  [55].

### Recombination at the interface

Under the assumption that the recombination centers at the interface are not too close to the conduction band, i.e. the recombination rate is dominated by the concentration of free holes at the interface, the  $V_{OC}$  can be written as

$$V_{OC} = \frac{\phi_p^f}{q} - \frac{AkT}{q} \ln \left( \frac{qS_p N_V}{J_{SC}} \right), \quad (2.16)$$

where  $S_p$  is the surface recombination velocity and  $\phi_p^f$  the corrected barrier height for holes at zero bias (cf. fig. 2.4):

$$\phi_p^f = A \cdot \phi_p^0. \quad (2.17)$$

Equation 2.13 shows a linear dependency of the  $V_{OC}$  and the temperature of the solar cell if the ideality factor  $A$  is only weakly dependent on the temperature. In that case an extrapolation to zero Kelvin of the  $V_{OC}$  versus the temperature plot yields the activation energy  $E_a$ . Depending on the dominant recombination mechanism, this activation energy either equals the band gap of the absorber in case of dominant QNR or SCR recombination (cf. equ. 2.14 and 2.15) or it equals the corrected barrier height for holes at the buffer absorber interface (equ. 2.16).

The saturation current  $J_0$  and the diode ideality factor  $A$  can be derived from J-V measurements in the dark. A detailed discussion can be found in [59]. In case of dark J-V measurements the photocurrent in equation 2.6 is zero and if  $R_s/R_p \ll 1$  holds, then equation 2.6 can be rewritten as

$$V = \frac{AkT}{q} * (\ln J - \ln J_0) + JR_s, \quad (2.18)$$

or

$$\ln J = \frac{q}{AkT}(V - JR_s) + \ln J_0. \quad (2.19)$$

A semilogarithmic plot of  $J$  versus  $(V - JR_s)$  yields the diode ideality factor  $A$  from the slope and the saturation current  $J_0$  from the axis intercept. However, this method is heavily influenced by the series resistance in the CIGS solar cells resulting in complications when calculating the ideality factor and saturation current [57]. A method which allows the calculation of the ideality factor and the saturation current in devices with non negligible series resistance is described in the following section.

### 2.2.1.2 Jsc-Voc theory

In this section a possibility for deriving the diode ideality factor and the saturation current in the presence of series resistance is described following reference [60]. The idea is to measure the  $V_{OC}$  and  $J_{SC}$  at varying illumination intensities. Starting from equation 2.6 for short circuit conditions the expression

$$-J_{SC} = J_0 \left( e^{\frac{qJ_{SC}R_s}{AkT}} - 1 \right) + \frac{J_{SC}R_s}{R_p} - J_{Ph}, \quad (2.20)$$

is valid and for open circuit conditions equation 2.6 changes to

$$J_{Ph} = J_0 \left( e^{\frac{qV_{OC}}{AkT}} - 1 \right) + \frac{V_{OC}}{R_p}. \quad (2.21)$$

If the series resistance is small compared to  $V_{OC}/J_{SC}$ , then the exponential term approaches unity in equation 2.20 and if further  $R_s/R_p \ll 1$  is valid (parallel resistance sufficiently large) then the short circuit current  $J_{SC}$  equals the photogenerated current density  $J_{Ph}$ . In that case  $J_{Ph}$  can be substituted by  $J_{SC}$  in equation 2.21 yielding a diode equation without the contribution of the series resistance.

The diode parameters can be extracted from equation 2.21 in a semilogarithmic plot. From the slope the ideality factor can be obtained if the temperature is known and the intercept with the y-axis yields the saturation current.

### Temperature dependence of the ideality factor

The  $J_{SC}$ - $V_{OC}$  measurement can be done at different temperatures, i.e. the temperature

dependence of the ideality factor can be investigated. From equation 2.14 it can be seen that the ideality factor should be unity and not change with temperature in case recombination in the QNR is dominant. Due to the thin absorber layer in CIGS devices SRC recombination is usually the dominant recombination mechanism. In that case the ideality factor should be two (see equ. 2.15). However, in most cases an ideality factor close to 1.5 or below is observed for high efficiency devices at room temperature [57].

Walter et al. explained the deviation of the ideality factor from two at room temperature with a model based on an exponential distribution of trap states in the band gap [61]. The expression for the inverse ideality factor based on this model can be written as

$$\frac{1}{A} = \frac{1}{2} \left( 1 + \frac{T}{T^*} \right), \quad (2.22)$$

where  $kT^*$  is the characteristic energy of the distribution. In this model  $A$  approaches 2 for  $T \rightarrow 0$  K. However, values above two can not be explained by this model. Rau proposed a model which also accounts for tunneling enhancement of SCR recombination (see dashed arrows pointing to path B in figure 2.4). In that case equation 2.22 extends to

$$\frac{1}{A} = \frac{1}{2} \left( 1 + \frac{T}{T^*} - \frac{E_{00}^2}{3(kT)^2} \right), \quad (2.23)$$

where  $E_{00} = q\hbar/2 * \sqrt{N_a/m^*\epsilon_s}$  is the characteristic tunneling energy depending on the acceptor concentration  $N_a$  and the dielectric constant  $\epsilon_s$  of the semiconductor [62]. This equation is valid for the whole temperature range and can describe ideality factors above two. The extra term in equation 2.23 describes the tunneling enhanced recombination via midgap states.

An ideality factor  $A = (1 + N_a/N_d)$  is expected for interface recombination [63]. If tunneling enhances the interface recombination it can be described using the thermionic field emission theory of Schottky contacts described by Padovani and Stratton [62]. In that case it is assumed that the number of electrons at the interface exceeds the number of free holes which would be the case for a negative conduction band alignment (cliff) between the absorber and buffer layer as indicated in figure 2.4. A detailed description can be found in [64]. The temperature dependence of the ideality factor in case of tunneling enhanced interface recombination is given by

$$A = \frac{E_{00}}{kT} \coth \left( \frac{E_{00}}{kT} \right). \quad (2.24)$$

Again  $E_{00}$  is the characteristic tunneling energy as described above.

If the dominant recombination is tunneling enhanced either in SCR or at the interface, then the ideality factor strongly depends on the temperature and an extrapolation of the activation energy from equations 2.15 and 2.16 is difficult. A rearrangement of equation 2.12 yields

$$A \ln J_0 = -\frac{E_a}{kT} + A \ln J_{00}. \quad (2.25)$$

With this equation the activation energy  $E_a$  can be calculated also for a temperature dependent ideality factor by a modified Arrhenius plot (the slope of  $A \ln J_0$  vs.  $1/T$ ). Analog to the extrapolation of equations 2.15 and 2.16 the activation energy from the Arrhenius plot equals the band gap in case of SCR dominated recombination and in case of interface recombination it equals the corrected barrier height for holes at the interface. Table 2.1 summarizes the expected values for the activation energy and ideality factor for the relevant recombination mechanisms.

**Table 2.1:** Summary of the relevant recombination mechanisms in CIGS-based thin film solar cells.

Recombination path	Ideality factor $A(T)$	$E_a$ from Arrhenius plot	$qV_{OC}(T \rightarrow 0)$
QNR	1	$E_g$	$E_g$
SCR	$\left(\frac{1}{2} \left(1 + \frac{T}{T^*}\right)\right)^{-1}$	$E_g$	$E_g$
tunneling enhanced			
SCR	$\left(\frac{1}{2} \left(1 + \frac{T}{T^*} - \frac{E_{00}^2}{3(kT)^2}\right)\right)^{-1}$	$E_g$	–
Interface	$1 + \frac{N_a}{N_d}$	$\phi_p^f$	$\phi_p^f$
tunneling enhanced			
interface	$\frac{E_{00}}{kT} \coth\left(\frac{E_{00}}{kT}\right)$	$\phi_p^f$	–

### 2.2.1.3 Measurement equipment

Current voltage characteristics are measured using a Keithley 2400 source meeter. The device is contacted with Kelvin probe contacts in the four terminal configuration. A varying voltage bias between -700 and 850 mV is applied to the cell whilst simultaneously measuring the current. For illuminated J-V measurements the device is illuminated using 1200 W metal halide lamp behind a UV filter. The intensity of the sun simulator is adjusted to 100 mW/cm<sup>2</sup> at the measurements position with a mono crystalline silicon reference solar cell manufactured and calibrated by ISE Freiburg. The temperature of the device under

test is kept constant at 25 °C with a peltier cooling system.

For temperature dependent measurements a cryostat was designed and built in the scope of this thesis. The sample is mounted on a copper plate inside a vacuum chamber. The copper plate is cooled with a continuous flow of liquid nitrogen and the temperature is adjusted with heating cartridges inside the copper plate and controlled with a Tecon controller. The temperature is measured with a surface thermocouple on a dummy sample which is exposed to the same conditions as the sample under test. Electrical contacts to the solar cell are made using Kelvin probe contacts in the four terminal configuration. With this setup the temperature can be varied between 100 and 370 K.

The vacuum chamber is equipped with a side glass for device illumination. An halogen light source is installed for the cell illumination. The illumination intensity can be varied with two sets of neutral density filters placed in two sequenced filter wheels controlled by a home made computer software. In order to prevent temperature instabilities during the measurements with high illumination intensities a glass coated with a highly doped tin oxide layer is placed in front of the light source. The cut-off wavelength of that filter is sufficiently larger than the wavelength corresponding to the band gap of the absorber in the device under test.

$J_{SC}$  and  $V_{OC}$  sets are measured varying illumination intensities in the above mentioned temperature range with a Keithley 2400 source meeter. The software for the temperature dependent measurements was developed in house during the master thesis of Fabian Pianezzi [65]. Simultaneously dark J-V measurements are performed in the same temperature range.

## 2.2.2 Spectral response

The response of a solar cell to the various wavelengths of the illumination spectrum is measured with the so called spectral response or quantum efficiency measurement. Quantum efficiency (QE) here means the ratio of the number of extracted charge carriers to the number of incident photons per wavelength. In QE it is distinguished between external QE (EQE) and internal QE (IQE). The EQE includes electrical and optical losses whereas the IQE is corrected for the optical losses. The IQE can be calculated from the EQE if the reflectance and transmission of the finished solar cell is known:

$$IQE(\lambda) = \frac{EQE(\lambda)}{1 - R(\lambda) - T(\lambda)} \approx \frac{EQE(\lambda)}{1 - R(\lambda)}. \quad (2.26)$$

The approximation is valid, if the absorber layer thickness is sufficient to absorb all incident photons with  $E > E_g$ . The IQE is a tool to distinguish between wavelength dependent optical and electrical losses.



If absolute EQE can be measured the EQE spectra can be used to calculate the short circuit current density  $J_{SC}$  of the device under a given illumination spectra [66]:

$$J_{SC} = q \int_0^{\infty} EQE(\lambda)\phi(\lambda)d\lambda, \quad (2.27)$$

where  $q$  is the elemental charge and  $\phi(\lambda)$  the number of incident photons per unit area and time. Due to the spectral mismatch of most solar simulator this gives a more accurate value of the  $J_{SC}$  than the J-V measurement.

The band gap of the absorber can be calculated from the QE spectra. Close to the absorption edge of the absorber the quantum efficiency is proportional to the absorption coefficient which in turn is proportional to  $\sqrt{h\nu - E_g}$  for a direct band gap semiconductor. Therefore, plotting  $(QE \cdot h\nu)^2$  versus the photon energy  $h\nu$  a linear extrapolation of the absorption edge yields the band gap of the CIGS absorber. In case of a graded band gap the determined value from QE is equal to the minimum band gap of the absorber.

### 2.2.2.1 Measurement equipment

The QE measurements were done using a 900 W halogen lamp, a beam chopper running at 360 Hz, and a dual grating image monochromator. Before each QE measurement the monochromatic beam was calibrated with a silicon reference solar cell produced and calibrated at ISE Freiburg. The beam size was adjusted such that illumination area is smaller than the cell area for both, the reference cell and the device under test. A white light bias is applied during all measurements in order to put the device into operating conditions. The solar cell is contacted at the front and back contact with the two terminal method. With a lock-in amplifier the AC fraction with the same frequency as the beam chopper is separated from the DC offset, amplified and transferred to the computer software for evaluation. During the complete measurement the device under test is kept at 25 °C using a peltier cooling and heating element. This measurement procedure yields absolute QE spectra.

## 2.2.3 Capacitance measurements

Capacitance measurements are a further powerful tool for the characterization of the pn junction in thin film solar cells. The depletion region of the pn junction forms a capacitance which is defined as  $C \equiv dQ_c/dV$ , where  $dQ_c$  is the evanescent increase of the charge per unit area with the evanescent change of the applied voltage  $dV$  [9].

### 2.2.3.1 Capacitance voltage measurement

Capacitance voltage (C-V) measurements are used to determine the apparent shallow doping concentration in the semiconductor. For an one-sided abrupt  $n^+p$ -junction the

doping concentration can be written as [9]:

$$N_a(x) = -\frac{2}{A_0^2 q \epsilon_s \epsilon_0} \frac{dV}{d(1/C^2)}, \quad (2.28)$$

where  $x=A_0\epsilon_s\epsilon_0/C$  is the apparent profiling depth,  $A_0$  the device area,  $\epsilon_s$  the dielectric constant of the semiconductor,  $\epsilon_0$  the permittivity of the vacuum, and  $N_a$  is the apparent shallow doping concentration of the junction partner with lower doping concentration. This measurement yields an apparent doping concentration profile since the position  $x$  does not reflect a real position in the heterojunction. The doping concentration can be obtained by plotting  $1/C^2$  vs.  $V$ . This plot is also known as Mott-Schottky plot. The local slope is inversely proportional to the doping density at the apparent position  $x$  away from the junction and the intersection with the  $x$ -axis gives the built in voltage of the junction ( $V_{bi}$ ). Assuming a plate type capacitor, the width  $W(V)=\epsilon_s\epsilon_0A_0/C(V)$  of the capacitor corresponds to the width of the SCR. A detailed description of C-V analysis can be found in standard textbooks (see [67]).

C-V measurements were performed using an Hewlett-Packard HP4192A LCR bridge at Electronics and Information Systems (ELIS), Universiteit Gent and using an Agilent E4980A impedance analyzer at Empa. In both systems the samples were mounted in a cryostat and the temperature was varied between 100 and 360 K. Before cooling the sample was kept in dark for more than one hour at 300 K in order to reach a relaxed state. The voltage in the C-V sweep was varied between -1.5 and 0.5 V and measurements were taken for  $10^3$ ,  $10^4$  and  $10^5$  Hz.

### 2.2.3.2 Capacitance frequency spectroscopy

Admittance spectroscopy (C-f) can be used to characterize defect levels in the semiconductors in a  $n^+p$  configuration. A detailed summary with application to CIGS based solar cells of this method was given by Walter et al. [68]. Walter et al. showed that the energy distribution of defects  $N_t(E_\omega)$  in the assumption of parabolic bands can be written as

$$N_t(E_\omega) = -\frac{V_{bi}^2}{w [qV_{bi} - (E_{fn\infty} - E_\omega)]} \frac{dC}{d\omega} \frac{\omega}{kT}, \quad (2.29)$$

where  $E_{fn\infty}$  is the energy position of the Fermi level with respect to the valence band edge in the  $n$ -type semiconductor and  $\omega$  is the angular frequency of the ac signal;  $\omega = \omega_0$  is the maximum frequency for which a defect at an energy  $E_\omega$  can be charged and discharged and therefore contributes to the junction capacitance. The frequency is given by  $\omega = 2\nu_0 \exp(-E_\omega/kT) V_{bi}$ , where  $\nu_0$  is the attempt to escape frequency. The attempt to escape frequency can be obtained from an Arrhenius plot of the maxima of  $\omega dC/d\omega$  vs  $\omega$ . The intersect of the Arrhenius plot with the frequency axis yields the attempt to escape frequency, which is usually in the order of  $10^{11} \text{ s}^{-1}$ . With the correct attempt to escape

frequency a plot of  $N_t(E_\omega)$  vs the energy difference determined for different temperatures should result in overlapping peaks. The built in voltage  $V_{bi}$  of the pn junction and the depletion width  $w$  can be calculated from the C-V measurements and only influence the height of the density of states but not the energy position.

C-f measurements were performed using an Hewlett-Packard HP4192A LCR bridge at Electronics and Information Systems (ELIS), Universiteit Gent and using an Agilent E4980A impedance analyzer at Empa. In both systems the samples were mounted in a cryostat and the temperature was varied between 100 and 360 K. Before cooling the sample was kept in dark for more than one hour at 300 K in order to reach a relaxed state. For samples measured at ELIS the frequency was varied between 10 and  $10^7$  Hz whereas a frequency range of 100 Hz - 2 MHz was used for measurements at Empa.



# 3 Growth mechanism and layer properties

This chapter is in part based on the following publications:

S. Buecheler, R.L. Sauaia, D. Corica, C. Fella, R. Verma, A. Chirila, Y.E. Romanyuk and A.N. Tiwari, "Deposition process of ultrasonically sprayed  $\text{In}_2\text{S}_3$  buffer layers for  $\text{Cu}(\text{In,Ga})\text{Se}_2$  thin film solar cells", *Proc. 24th European Photovoltaic Solar Energy Conference and Exhibition*, Hamburg, Germany, 2009

D. Corica, S. Buecheler, D. Guettler, A. Chirila, S. Seyrling, R. Verma and A.N. Tiwari, "Indium Sulfide Buffer Layer for  $\text{Cu}(\text{In,Ga})\text{Se}_2$  Thin-Film Solar Cells Deposited by Ultrasonic Spray Pyrolysis", *Proc. 23rd European Photovoltaic Solar Energy Conference and Exhibition*, Valencia, Spain, Sept 1-5, 2008.

S. Buecheler, D. Corica, D. Guettler, A. Chirila, R. Verma, U. Müller, T.P. Niesen, J. Palm, A.N. Tiwari, "Ultrasonically sprayed indium sulfide buffer layers for  $\text{Cu}(\text{In,Ga})(\text{S,Se})_2$  thin-film solar cells", *Thin Solid Films*, Volume **517**, Issue 7, 2 February 2009, Pages 2312-2315.

For the deposition of  $\text{In}_2\text{S}_3$  layers, an ultrasonic spray pyrolysis system as described in section 1.4.2.2 was developed and analyzed. Indium(III)chloride ( $\text{InCl}_3$ ) and thiourea ( $\text{CS}(\text{NH}_2)_2$ ) hereafter called TU were identified as best suitable precursor chemicals. Among the possible solvents, methanol, ethanol, acetone, acetonitrile and water were investigated during this work. If not otherwise mentioned, the standard solution for the  $\text{In}_2\text{S}_3$  deposition is 0.02 M  $\text{InCl}_3$  and 0.03 M TU dissolved in methanol or acetone. The solution was prepared always directly before the deposition run in order to avoid the formation of possible precipitation.

## 3.1 Transport of precursor solution

The theoretically derived droplet sizes for various solvents are given in table 1.3. In order to investigate the droplet size experimentally, a saturated solution with methanol as solvent was sprayed for several seconds onto a glass substrate at room temperature. Immediately after the deposition, the sample was inspected under a light microscope. Droplets

with diameters between 0.9 and 5.2  $\mu\text{m}$  were found on the sample surface showing good agreement with the calculated mean diameter from Lang's correlation (see table 1.3).

In the standard deposition process, the concentrations of the precursor salts in the solvent are 0.02 M for  $\text{InCl}_3$  and 0.03 M for TU. For such diluted solution, the vapor pressure of the solvent is initially relevant for the evaporation of the droplet. However, if the droplet starts evaporating, the precursor concentrations increase and the solvent vapor pressure over the droplet decreases. This effect is counteracted by the increase in vapor pressure of the solvent due to increased droplet curvature [69].

Considering the high vapor pressures of the used organic solvents at the deposition temperature (table 1.3) and the small droplet size ( $< 5 \mu\text{m}$ ), rapid and complete solvent evaporation above the substrate surface can be assumed (cf. [69]). This assumption of complete solvent evaporation before reaching the substrate surface is confirmed by scanning electron microscopy (SEM) of USP- $\text{In}_2\text{S}_3$  layers deposited with the described method. Figure 3.1 (a)-(d) shows the surface morphology of an 80 nm thick USP- $\text{In}_2\text{S}_3$  layer deposited on glass substrate. An homogeneous layer formation is visible without any evidence of droplet patterns.

If the droplets with diameter in the order of 2  $\mu\text{m}$  reach the surface in a wet state, a circular pattern in the deposited layer is visible (fig. 3.1 (e)-(g)). The shown  $\text{In}_2\text{S}_3$  layer in figure 3.1 (e)-(g) was sprayed with a commercially available ultrasonic spray system in which the droplets are formed directly at the tip of the nozzle. In this spray setup no or only partial evaporation of the solvent occurs during the transport of the droplets from the nozzle to the heated substrate. The droplets reach the surface in a wet state forming a distinct 'droplet' pattern in the layer. The growth mechanism of this later method was describe in details by D. Beckel [70].

## 3.2 Chemical precursors in solution

The precursor solution for the USP deposition process is prepared by dissolving  $\text{InCl}_3$  and TU in an organic solvent. A formation of an In(III) complex with the solvent or the TU molecules is very likely [71]. It was found experimentally by Carty and Tuck [72] that TU binds to In via an S atom forming the complex  $\text{In}(\text{CS}(\text{NH}_2)_2)_3\text{Cl}_3$  (hereafter called  $\text{InTU}_3\text{Cl}_3$ ) with coordination number 6 in solution. This complex can be crystallized and it decomposes at 180 °C.

## 3.3 Chemical reaction and mechanism

Starting from the chemical precursors  $\text{InCl}_3$  and TU, the following chemical equation for the formation of  $\text{In}_2\text{S}_3$  is conceivable:

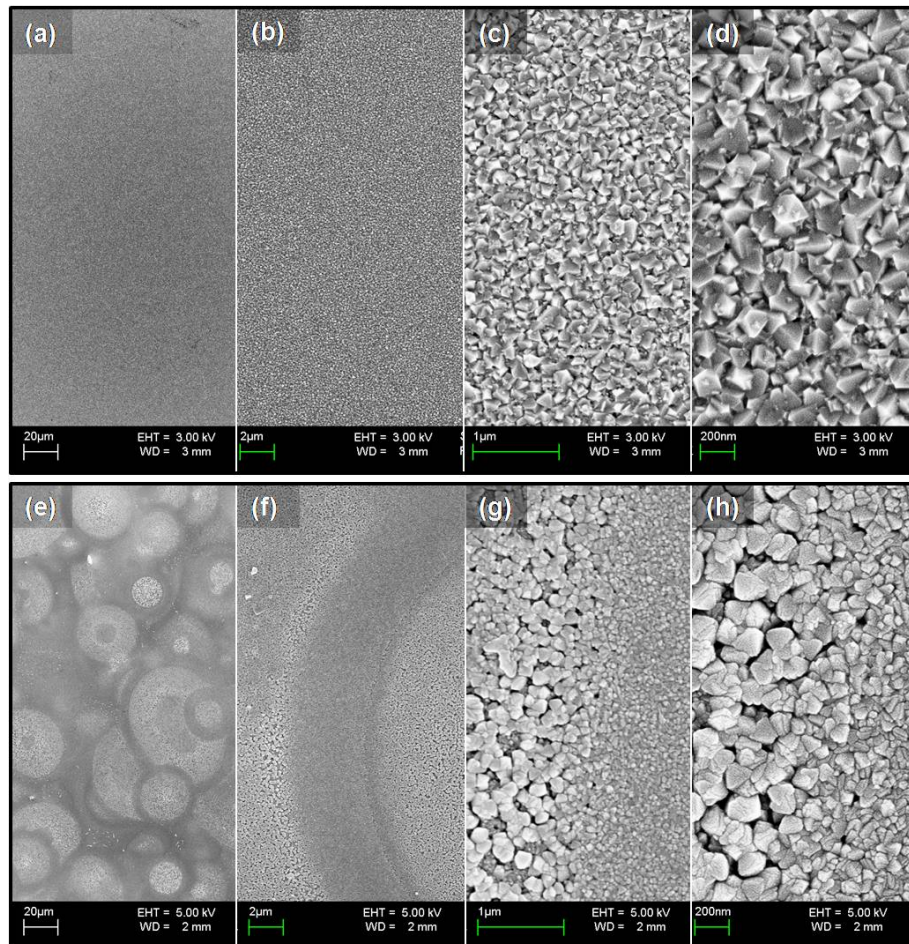
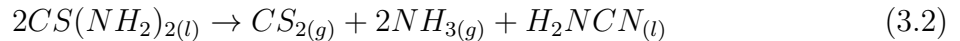


**Figure 3.1:** Surface morphology of sprayed  $In_2S_3$  layers on glass substrate. (a)-(d): SEM images of an  $In_2S_3$  layer sprayed with the ultrasonic spray pyrolysis system developed during this work and described in section 1.4.2.2. (e)-(h): SEM images of an  $In_2S_3$  layer deposited with a commercially available ultrasonic spray system in which the droplets are formed directly at the tip of the nozzle.



The change of Gibbs free energy of this reaction is positive when calculated for a closed system at 200 °C surface temperature, indicating that the equilibrium is on the precursor side of the equation. However, the setup used for the In<sub>2</sub>S<sub>3</sub> layer deposition is not closed. Volatile products can leave the system, shifting the equilibrium towards the product side of the equation.

A possible mechanism for the proposed reaction is the formation of the InTU<sub>3</sub>Cl<sub>3</sub> complex introduced in section 3.2. During the rapid evaporation of the solvent in the droplet, the complex already starts to decompose leaving fragments of elemental In, InCl and InCl<sub>2</sub>. Such fragments were experimentally detected by mass spectroscopy attached to a tube furnace in which the layer deposition was simulated with standard precursor solution. The fraction of the complex, which is not decomposed during solvent evaporation, as well as TU which is not bound to In, thermally decomposes when reaching the surface area with temperature above 180 °C [73]. The decomposition products of TU are:



The gaseous CS<sub>2</sub> is a reactive endothermic compound which further reacts with InCl<sub>x</sub> fragments forming In<sub>2</sub>S<sub>3</sub>.

Studies on impurity concentrations by Rutherford backscattering spectrometry and elastic recoil detection analysis of the final In<sub>2</sub>S<sub>3</sub> layer deposited on (111) orientated Si wafer showed that a high content of Cl is present in the layer if the TU to InCl<sub>3</sub> molar ratio is smaller than 3:2 in the precursor solution [74]. The chemical composition is described in more detail in section 3.5.3. The chlorine impurity in the layer originates from InCl<sub>3</sub> residuals incorporated into its structure. If TU is provided in excess for the chemical reaction described in equation 3.1, the Cl impurity is reduced below 1 at% and further minimized if the molar ratio of InCl<sub>3</sub> to TU is 1:3 or lower which amplifies the probability of complex formation in the solution.

This indicates that InTU<sub>3</sub>Cl<sub>3</sub> complexes more likely decompose into InCl<sub>x</sub> fragments (x<3) and decomposition products of TU, yielding In<sub>2</sub>S<sub>3(s)</sub>, HCl<sub>(g)</sub>, H<sub>2</sub>NCN<sub>(l)</sub> and NH<sub>3(g)</sub>. In a side reaction NH<sub>3</sub> and HCl form NH<sub>4</sub>Cl, which was detected on the system funnel as a condensed white powder. At least in principle, the excess of TU can also help in shifting the reaction equilibrium towards the product side of the chemical equation.

From the collected evidences, the mechanism of the In<sub>2</sub>S<sub>3</sub> formation can be described by a mixture of particle (not decomposed InTU<sub>3</sub>Cl<sub>3</sub> complex) and vapor deposition (InCl<sub>x</sub> fragments and CS<sub>2</sub> from the decomposition of the complex during rapid solvent evaporation). This conclusion is confirmed by SEM analysis of spray sequences shown in figure 3.2.



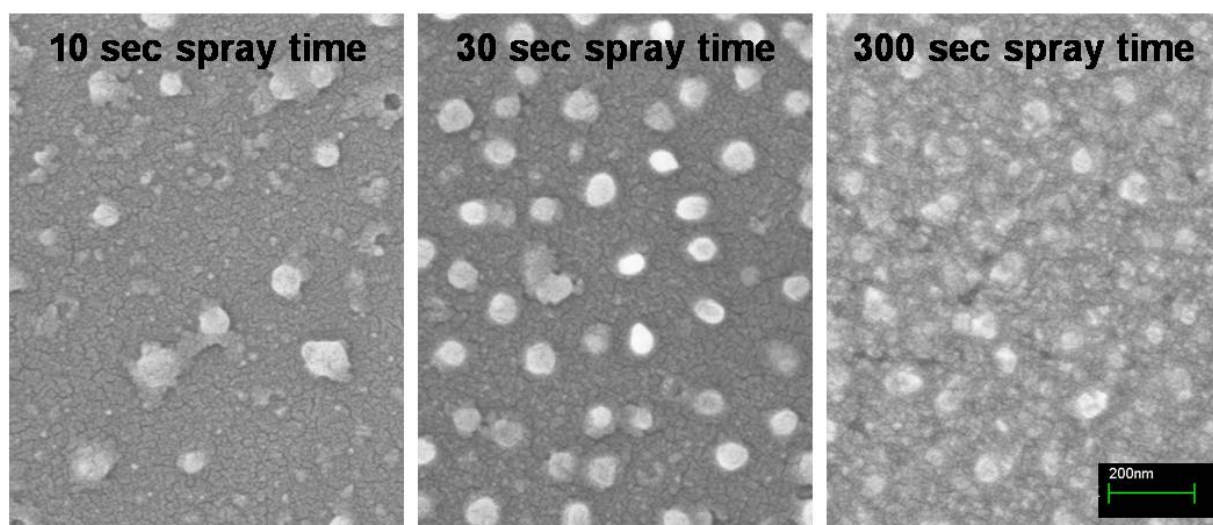


**Figure 3.2:** *Time series of USP deposition on glass substrate at a surface temperature of 200 °C.*

In a time variation, the precursor solution was sprayed onto glass substrates at 200 °C surface temperature. After 30 seconds spray time some particles are visible on the surface which might be an agglomeration of  $\text{In}_2\text{S}_3$  originating from the decomposition of  $\text{InTU}_3\text{Cl}_3$  complex particles. The particle coverage increases with increasing spray time, as can be seen in figure 3.2. Simultaneously, new small particles are formed whereas already existing ones grow in size. This effect can be explained by the vapor deposition of  $\text{In}_2\text{S}_3$  formed through the reaction between  $\text{InCl}_x$  fragments and  $\text{CS}_2$ .

The decomposition product cyanamide ( $\text{H}_2\text{NCN}$ ), which is in liquid phase on the substrate surface, may increase the surface mobility, leading to coalescence of small agglomerations to  $\text{In}_2\text{S}_3$  crystals. The image series (a)-(d) in figure 3.1 shows an 80 nm thick  $\text{In}_2\text{S}_3$  layer. A dense polycrystalline structure is visible with grain sizes of up to 100 nm in diameter. Since no significant carbon impurity is detected in the finished structure (shown in section 3.5.3), it can be concluded that the liquid cyanamide does not remain in the layer. Either it gathers into droplets on the surface and is removed by a subsequent water rinsing step or it reacts with fragments of the solvent or traces of oxygen and leaves the system as volatile products.

### 3.4 Growth kinetics

The growth kinetic, layer morphology, crystal structure, chemical composition and optical properties of thin films deposited by USP depend on the spray parameters. The main parameters affecting the above mentioned properties are the surface temperature, the absolute and relative precursor concentrations and the solvent properties. The impact of those parameters is presented in this and the following sections.

In the used USP system the feed rate and the kinetic energy of the droplets are coupled by the carrier gas flow rate. A high kinetic energy of the droplets results in a high bounce rate on the substrate surface which reduces the growth rate significantly. However, droplets were produced in excess in this system, i.e. the growth kinetics are not limited by the droplet feed rate. Therefore, for all experiments the flow rate of the carrier gas was set such that the bounce effect was minimized.

For studying the growth rate a number of experiments were performed, varying only one parameter (surface temperature  $T_S$ , absolute and relative precursor concentrations) in one series and keeping all others constant. The thicknesses of the sprayed films were measured with a stylus profilometer DEKTAK 3030. As expected an increase of the growth rate with increasing absolute concentration of the precursors in the solution is observed.

The growth rate of  $\text{In}_2\text{S}_3$  layers was investigated at different surface temperatures of the substrate (see fig. 3.3a). For substrate surface temperatures of  $180^\circ\text{C}$  and below segregation of white particles and no layer growth is observed. As described in section 3.2 a minimum temperature of  $180^\circ\text{C}$  is required for decomposition of the precursors and initiating the chemical reaction. For surface temperatures above  $180^\circ\text{C}$  a continuous layer with yellow to orange color is obtained. An increase of the growth rate was observed with increasing temperature. This is an additional indication that the solution droplets do not reach the surface in a wet state, since for droplet deposition the growth rate is expected to decrease with increasing temperature [69]. An increase in growth rate with increasing substrate temperature is commonly observed with chemical vapor deposition approaches.

Figure 3.3b shows that the layer growth rate also depends on the precursor ratio. The growth rate is cut in half if the In to S ratio is changed from sulfur deficiency (1:1) to sulfur excess (1:4). As it will be shown in section 3.5.3 the  $\text{In}_2\text{S}_3$  layers sprayed with sulfur deficiency contain chlorine impurities of about 20 at%. Most likely these impurities are  $\text{InCl}_x$  molecules incorporated as nano-sized crystals in the  $\text{In}_2\text{S}_3$  matrix. The density of all  $\text{InCl}_x$  crystals is smaller than the density of  $\text{In}_2\text{S}_3$  [75, 76]. Assuming that the number of In atoms does not change, the difference in the density explains a reduction of the growth rate with reduced chlorine incorporation, i.e., from In/S ratio of 1:1 to 1:2. A further reduction of the growth rate can be explained by a shift of the dominant deposition mechanism from particle deposition to vapor phase deposition.

It can be summarized that the growth rate increases with rising substrate temperature and increasing indium concentration in the precursor solution and it decreases with increasing sulfur excess.

Figure 3.4 shows the growth rate determined by profilometry versus inverse temperature in a semi logarithmic plot. The slope of the linear fit is the activation energy of the chemical reaction, which is 54 kJ/mol. This activation energy represents contributions from enthalpies of melting and decomposition of both TU and the  $\text{InTU}_3\text{Cl}_3$  complex.

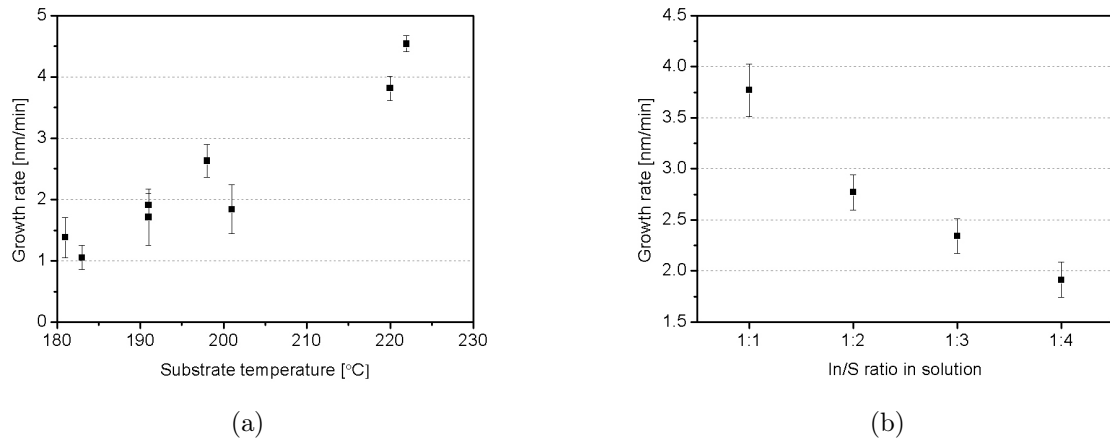


**Figure 3.3:** Growth rate of sprayed  $In_2S_3$  layers deposited on soda lime glass at different deposition temperatures and with varying In/S ratio.

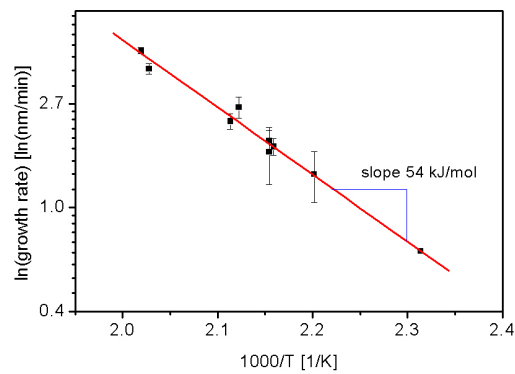


**Figure 3.4:** Arrhenius plot of the growth rate of  $In_2S_3$  layers on glass substrate.

## 3.5 Layer properties

### 3.5.1 Crystal structure

#### *Effect of substrate temperature*

X-ray diffraction (XRD) measurements were used to examine the crystalline structure of indium sulfide layers deposited at surface temperatures between 190 °C and 230 °C (figure 3.5). The spraying time was set to 35 min in order to obtain a layer sufficiently thick for XRD measurements. For the investigated temperature region all layers show polycrystalline structures.

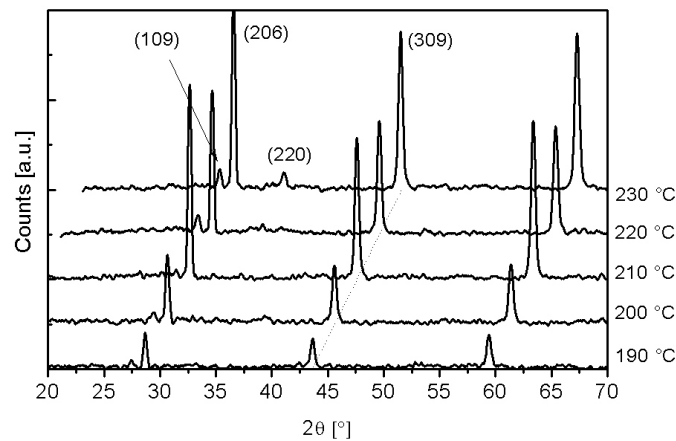


**Figure 3.5:** XRD measurement of indium sulfide layers at different substrate temperatures. For better clarity an offset in  $x$ - and  $y$ -axis is applied. The dotted line indicate the position of the (309) peak. The peaks coincide with the data for  $\text{In}_2\text{S}_3$  powder and are indexed according to [77].

The obtained peak positions match to the crystal plane distances  $d_{(hkl)}$  of  $\text{In}_2\text{S}_3$ . Thus the crystalline grains in the sprayed layer can be clearly identified with the  $\text{In}_2\text{S}_3$  compound. However, it is difficult to distinguish between the tetragonal  $\alpha$ - and the cubic  $\beta$ - $\text{In}_2\text{S}_3$  phase with XRD only (the definition of the phases can be found in section 1.4.1.2). The diffraction angles of these phases are close together [77, 78]. The XRD pattern of both phases show a peak at a diffraction angle of  $2\Theta=33^\circ$  and  $2\Theta=48^\circ$  of similar intensity when randomly oriented. Since these peaks do not appear in the measured pattern, the orientation of the crystalline grains in the grown layer is not randomly distributed. Assuming the layer consists only of the tetragonal  $\alpha$ - $\text{In}_2\text{S}_3$  phase, then the preferential orientation can be identified by calculating the texture coefficient (see section 2.1.1). In table 3.1 the derived values are summarized.

All the layers sprayed at different substrate temperatures show a clear preferential orien-

tation in the [103] direction. There is no or very little detection of crystals grown in the other indicated directions.

**Table 3.1:** *Texture coefficient (TC) and standard deviation  $\sigma$  of TC for the indium sulfide layers obtained by USP with varying substrate temperature  $T_s$ . In the bottom line the average grain size  $D$  in the layers is shown derived by the Debye-Scherrer formula.*

(hkl)	190 °C	200 °C	210 °C	220 °C	230 °C
116	0.04	0.11	0.02	0.07	0.03
109	0.1	0.07	0.02	0.07	0.05
206	4.78	4.71	4.98	4.78	4.81
220	0.02	0.05	0.01	0.06	0.08
309	1.05	1.05	0.96	1.0	1.02
400	0.01	0.01	0.01	0.02	0.01
$\sigma$	1.53	1.50	1.59	1.52	1.53
$D$ [nm]	20	20	22	21	21

Furthermore, the standard deviation  $\sigma$  of these layers is approximately the same, i.e. the overall preferential orientation in the indium sulfide film does not change with varying substrate temperature between 190 °C and 230 °C. The crystal size of the film calculated from the (206) peak using the Debye-Scherrer formula is approximately 20 nm for all deposition temperatures.

#### *Effect of In/S ratio in the solution*

The XRD pattern of the layers sprayed for 35 min with varying In/S ratio in the precursor solution from 1:1 to 1:4 is shown in figure 3.6.

The indium sulfide films sprayed with an excess of sulfur in the precursor solution show the crystalline structure of  $\text{In}_2\text{S}_3$  whereas the intensity of the peaks as well as the overall preferential orientation of the films decrease with increasing sulfur ratio in the solution.

The differences in the signal intensity can be attributed to different layer thicknesses, as measurements with a stylus profilometer revealed a dependence of the layer growth rate on the precursor ratio (see also section 3.4). The inset in figure 3.6 shows that the growth rate decreases with the relative increase of sulfur in the precursor solution. The XRD measurement of the layer sprayed with an In to S ratio of 1:1 does not show any distinct peak. Either the grain size in the layer is too small to be detected or sulfur deficiency prevents nucleation for crystalline growth resulting in amorphous films. In the polycrystalline layers [103] is the preferred growth direction of the crystals (see table 3.2). The decrease of  $\sigma$  with increasing sulfur excess indicates a decrease of preferential orientation. A small decrease in average grain size  $D$  is also observed with increasing sulfur amount.

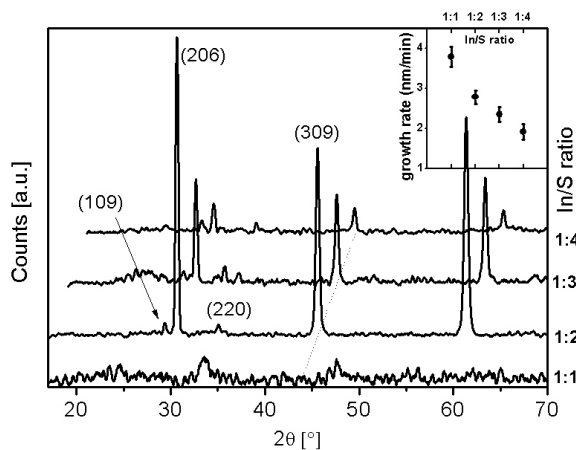


**Figure 3.6:** XRD pattern and growth rate of USP- $\text{In}_2\text{S}_3$  on SLG as a function of the In/S ratio in the precursor solution deposited at  $200^\circ\text{C}$ . For better clarity an offset in  $x$ - and  $y$ -axis is applied. The dotted line indicate the position of the (309) peak.

**Table 3.2:** Texture coefficient (TC) and standard deviation  $\sigma$  of TC for the indium sulfide layers obtained by USP with varying In/S ratios in the precursor solution. For In/S=1:1 no crystalline structure was detected. In the bottom line the average grain size  $D$  in the layers is shown derived by the Debye-Scherrer formula.

(hkl)	1:1	1:2	1:3	1:4
116	-	0.01	0.08	0.49
109	-	0.02	0.04	0.18
206	-	5.09	4.57	4.10
220	-	0.04	0.07	0.28
309	-	0.85	1.03	0.90
400	-	0.0	0.03	0.06
$\sigma$	-	1.62	1.50	1.29
$D$ [nm]	-	23	21	19

### 3.5.2 Morphology

With the developed ultrasonic spray pyrolysis method homogeneous  $\text{In}_2\text{S}_3$  can be deposited on substrates with an area up to  $10 \times 10 \text{ cm}^2$ . The morphology and the microstructure, however, depend on the deposition parameters. In this section the effect of various solvent, relative and absolute precursor concentration, and additives on the morphology and microstructure are discussed.

Figure 3.7 shows the surface morphology of  $\text{In}_2\text{S}_3$  layers sprayed on soda lime glass using different solvents for the precursor transport. Important parameters of a solvent used in the investigated USP system are the dielectric constant and the donor number for the solubility of the precursors, the density and surface tension for the size of the generated droplets, and the boiling point for the evaporation of the droplets at a certain substrate temperature. These parameters are summarized in table 1.3.

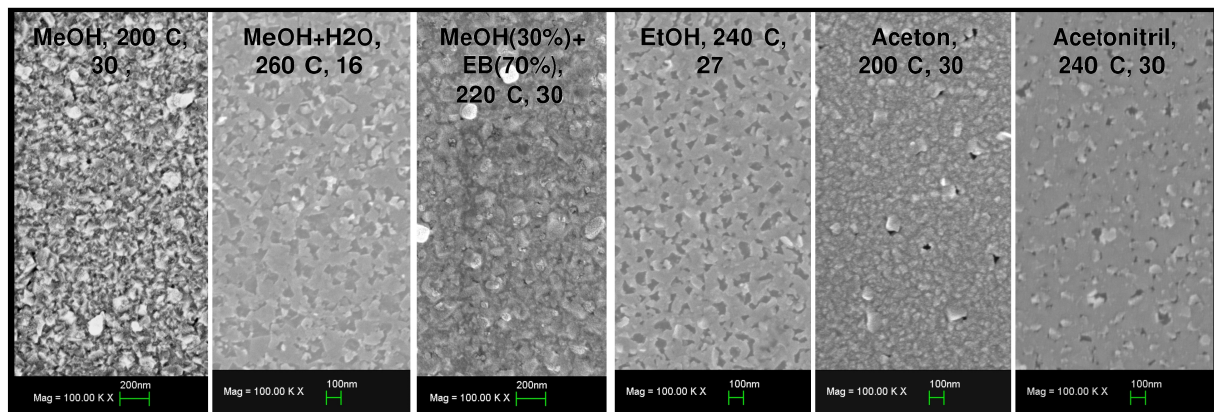


**Figure 3.7:** Surface morphology of  $\text{In}_2\text{S}_3$  layers on soda lime glass substrate sprayed using different solvents as labeled in the image. Given are also the temperature of the substrate and the deposition time.

The layer sprayed with pure methanol as solvent shows a polycrystalline film with homogeneous coverage of the sample surface (see also fig. 3.1). The crystal size is estimated to be in the order of 20-100 nm corresponding to the value derived with the Debye-Scherrer formula (equ. 2.4) from XRD measurement of layers deposited with similar spray parameters. The grains form a compact structure and no voids are visible.

The  $\text{In}_2\text{S}_3$  thin films deposited using a mixed solvent of 50 vol% methanol and 50 vol% water do not show a compact growth. The substrate temperature was adjusted in this experiment such that the ratio of the substrate temperature to the boiling point of the mixed solvent is the same as for pure methanol solution. A high density of voids is visible in the deposited layer. This microstructure is not suitable for an application of such films as buffer layers since a continuous coverage of the absorber is not obtained.

A solution mixed from 30 vol% methanol and 70 vol% ethylene glycol monobutyl ether (EB) yield a compact layer of microcrystalline or amorphous material. Energy dispersive x-ray measurement of such layers showed a chlorine concentration in the order of 10 at%.  $\text{In}_2\text{S}_3$  layers sprayed with the same parameters but a pure methanol solvent have a chlorine impurity in the order of 1 at% (see section 3.5.3). The mechanism of layer formation spraying from the methanol-EB mixture with high solvent boiling point in the investigated USP system might be as follows: the droplets reach the substrate surface without solvent evaporation due to the significantly reduced ratio between substrate temperature ( $T_s$ ) and solvent boiling point ( $T_{\text{sbp}}$ ). The value  $T_s/T_{\text{sbp}}$  in this experiment was engineered such that it lies in the range for compact amorphous layer formation as described by D. Beckel [70]. The microstructure and morphology of such layers are suitable for the application as buffer layers, however, reproducibility proved to be a problem.

The  $\text{In}_2\text{S}_3$  layers sprayed from an ethanol solution have similar microstructure as the layers deposited from the methanol-water mixture. The density of voids is too high for an application as buffer layer.

When acetone is used as solvent, a compact and homogeneous polycrystalline  $\text{In}_2\text{S}_3$  is obtained and only few voids are found. The chlorine impurity in these layers is below 1 at% as determined from RBS measurements on silicon substrate. The boiling point of acetone is slightly below the one of methanol. The chemical mechanism for the layer formation from acetone solutions can be assumed to be as described in section 3.3. The morphology and microstructure of the  $\text{In}_2\text{S}_3$  deposited with acetone as solvent meet the requirements for an application as buffer layer.

Similar layers can be obtained with acetonitrile as solvent. However, in order to guarantee complete solvent evaporation before the droplets reach the substrate, the substrate temperature has to be increased to 240 °C. A possible application will be discussed in section 5.2.

Figure 3.8 shows the surface morphology of  $\text{In}_2\text{S}_3$  layers deposited on soda lime glass with  $\text{InCl}_3$  concentration of 0.01 mol/l dissolved in methanol and In/S ratio variations (1:1, 1:2, 1:3, 1:4) in the solution at a substrate temperature of 200 °C for 35 min. It can be seen that the morphology and microstructure depends on the precursor ratio. The SEM images of layers deposited with ratio variation confirm the results from XRD measurements presented in section 3.5.1. For sulfur deficient conditions (In/S=1:1) amorphous or microcrystalline layers are obtained; in case of sulfur excess (1:2, 1:3, 1:4) polycrystalline layers are formed with grain size in the order of 100 nm.

This effect is observed irrespective of the crystalline characteristic of the underlying substrate. Figure 3.9 shows sprayed  $\text{In}_2\text{S}_3$  layers on silicon wafers. Also here amorphous or microcrystalline structure is visible for sulfur deficiency and polycrystalline layer formation is observed if sulfur is supplied in excess.



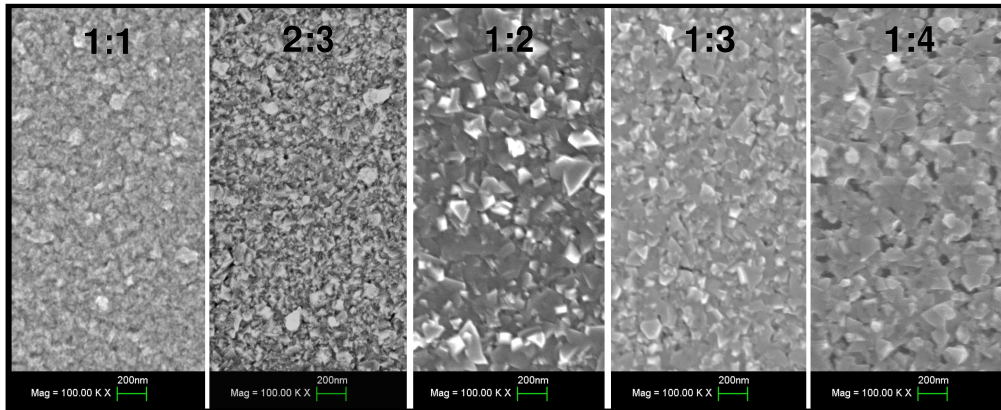


**Figure 3.8:** *Surface morphology of  $In_2S_3$  layers on soda lime glass substrate sprayed using different indium to sulfur ratios in the precursor solution as labeled in the image.*

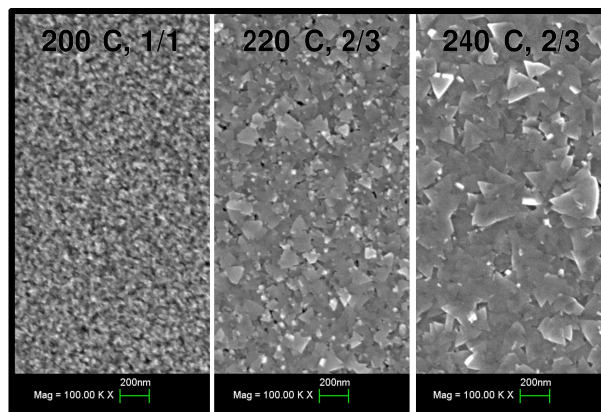


**Figure 3.9:** *Surface morphology of  $In_2S_3$  layers on silicon wafers sprayed using indium to sulfur ratio of 1:1 and 2:3 in the precursor solution.*

$\text{In}_2\text{S}_3$  layers deposited with varying absolute precursor concentration are shown in figure 3.10. The layers were sprayed with  $\text{InCl}_3$  of 0.02, 0.04, and 0.08 mol/l keeping a constant precursor ratio of  $\text{In}/\text{S}=2:3$  at 200 °C substrate temperature for 30 min. Irrespective of the precursor concentration all films show a polycrystalline homogeneous structure. As mentioned in the previous section, the growth rate increases with the absolute precursor concentration in the investigated range. The measured thicknesses for the layers are  $43\pm 2$ ,  $89\pm 2$ , and  $101\pm 0$  nm, respectively. Spraying with  $\text{InCl}_3$  concentration of 0.02 mol/l on soda lime glass yields maximum grain size of 100 nm. The maximum grain size increases to 200 nm with increased  $\text{InCl}_3$  concentration to 0.04 mol/l. If the concentration is increased to 0.08 mol/l no further growth of the grains is observed. However, the amount of small grains in the inter spaces increases. This suggests a limitation of the maximum grain size to twice the thickness of the layer.

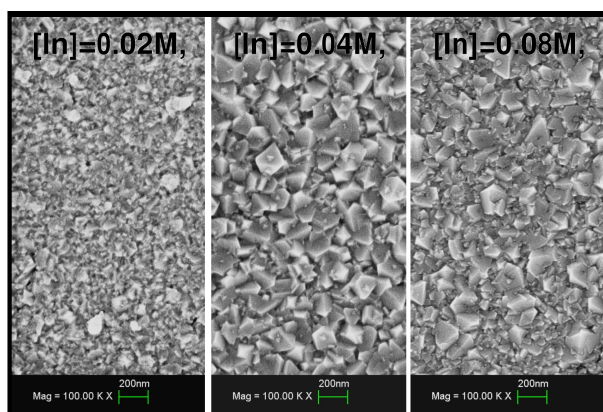


**Figure 3.10:** Surface morphology of  $\text{In}_2\text{S}_3$  layers on soda lime glass substrate sprayed using different absolute precursor concentrations as labeled in the image. The  $\text{In}/\text{S}$  ratio was constant at 2:3.

Oxygen at the interface between the absorber and buffer layers is not desired. This will be discussed in more detail in section 4.2. Additives such as citric acid can reduce oxygenation during the deposition process. Figure 3.11 shows the effect of citric acid added to the precursor and/or pre-spray solution on the microstructure and morphology of  $\text{In}_2\text{S}_3$  layers on soda lime glass substrates. The investigated combinations are given in table 3.3.

If a high citric acid concentration both in the pre-spray and precursor solution is used (sample A) a extremely thin and inhomogeneous layer with several cracks and agglomeration of bigger particles is obtained. Citric acid has metal-chelating properties which might result in the formation of a soluble complex with indium. This might reduce the available indium atoms for the reaction with sulfur to  $\text{In}_2\text{S}_3$ .

Layers sprayed with no citric acid only available in the pre-spray solution and not in the precursor solution show a compact microstructure. Also the formation of bigger particles embedded in the compact  $\text{In}_2\text{S}_3$  layer is observed. The density of the larger particles increases if citric acid is also added to the precursor solution in diluted concentration.

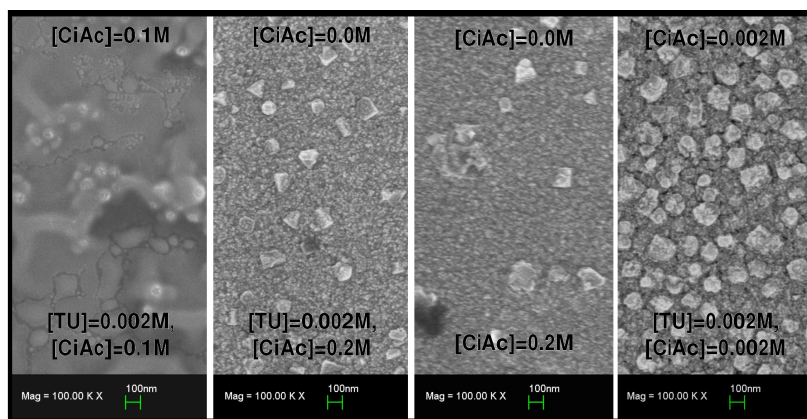


**Figure 3.11:** Surface morphology of  $In_2S_3$  layers on soda lime glass substrate sprayed using different citric acid combinations. The values displayed at the bottom of the images are the compositions of the pre-spray solution and the values at the top are the concentration of citric acid during the growth of the layer in the precursor solution (see also table 3.3.)

The concentration of citric acid was reduced by two orders of magnitude compared to the concentration used for the layer at the very left in figure 3.11. The effect of the additive citric acid on the PV properties will be discussed in section 5.2.

**Table 3.3:** Concentration of citric acid in the pre-spray and precursor solution used for the antioxidant investigation. The precursor concentration for all samples was 0.02 mol/l  $InCl_3$  and 0.03 mol/l TU in acetone. The acetone based pre-spray solution for layers A,B and D contained additionally 0.002 mol/l TU.

Layer	pre-spray Citric Acid [mol/l]	pre-spray TU [mol/l]	precursor solution Citric Acid [mol/l]
A	0.1	0.002	0.1
B	0.2	0.002	0.0
C	0.2	0.0	0.0
D	0.002	0.002	0.002

The morphology and microstructure of  $In_2S_3$  layers discussed so far were all deposited on glass or silicon substrates with smooth surfaces. The CIGS layers, however, have rough and complex surfaces. The left hand side of figure 3.12 shows the bare surface of  $Cu(In,Ga)Se_2$  deposited by a three stage process. The polycrystalline nature of the layer is visible with grain sizes up to one micron. The SEM image shows grains with different orientations. The  $Cu(In,Ga)Se_2$  layers grown by the used three stage process are (220)/(204)-textured films but also orientations along (002) and (112) are present [8]. The (220)/(204) notation is commonly used for the peak obtained from the overlapping (220) and (204) reflections. It was shown theoretically by Zhang et al. [79] and experimentally by Siebentritt et al. [80] that {112} facets are the most stable surface of the  $Cu(In,Ga)Se_2$  grains.

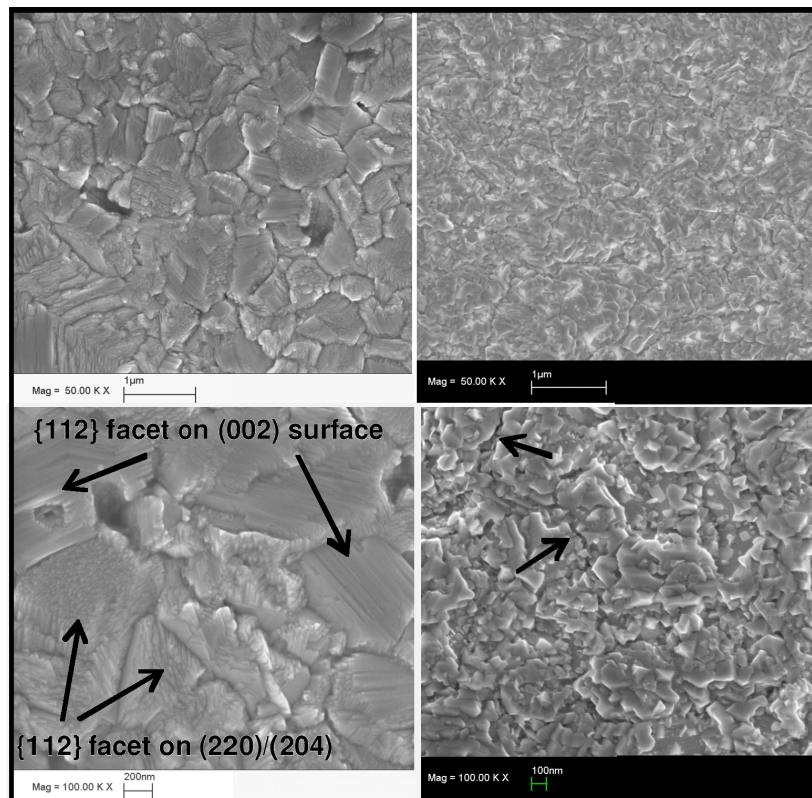


**Figure 3.12:** In the SEM images on the left hand side the bare CIGS surface is shown. In the lower image the  $\{112\}$  facets on the (002) and (220)/(204) surfaces are indicated. The images on the right hand side show the coverage of the CIGS surface with the USP-In<sub>2</sub>S<sub>3</sub> buffer layer.

The formation of these facets can be seen on the bare surface of the  $\text{Cu}(\text{In,Ga})\text{Se}_2$  for different orientations in figure 3.12. The  $\{112\}$  facets on the (002) surfaces form elongated ripples. On the (220)/(204) grains the  $\{112\}$  facets form rough surfaces with ledges up to 100 nm high [81].

On the right hand side of figure 3.12 a CIGS layer covered with a sprayed  $\text{In}_2\text{S}_3$  film is presented. The  $\text{In}_2\text{S}_3$  was deposited from a methanol solution with In/S ratio of 2:3 at a deposition temperature of 200 °C. The  $\{112\}$  facets of the CIGS grains are not visible any more but the polycrystalline nature of the  $\text{In}_2\text{S}_3$  layer is observed. Micro-cracks are spotted in the  $\text{In}_2\text{S}_3$  layer indicated by the arrows on the right hand side of figure 3.12. These micro-cracks are most likely formed at complex grain boundaries of the underlying CIGS grains.

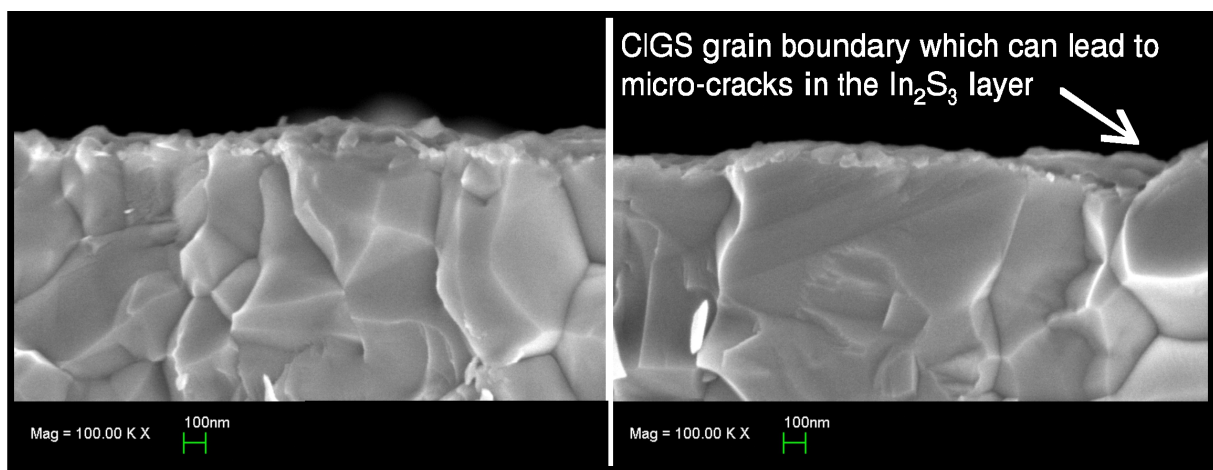


**Figure 3.13:** SEM cross-section images of the CIGS/USP- $\text{In}_2\text{S}_3$  layer stack. The  $\text{In}_2\text{S}_3$  layer is approximately 50 nm thick and continuously covers the CIGS surface.

The cross-section of the  $\text{Cu}(\text{In,Ga})\text{Se}_2/\text{In}_2\text{S}_3$  stack is shown in figure 3.13. The two images are SEM micrographs of the cross-section at two different locations of the same sample shown in figure 3.12. The  $\text{In}_2\text{S}_3$  deposited by ultrasonic spray pyrolysis forms a homogeneous and continuous layer with conformal coverage on the CIGS grains. The thickness of the sprayed  $\text{In}_2\text{S}_3$  layer is approximately 50 nm. Micro-cracks are not visible in the cross-section of the  $\text{Cu}(\text{In,Ga})\text{Se}_2/\text{In}_2\text{S}_3$  stack. In the image on the right a complex CIGS grain boundary which might induce micro-cracks in the  $\text{In}_2\text{S}_3$  layer is indicated by the white arrow.

Left hand side of figure 3.14 shows the bare surface of  $\text{Cu}(\text{In,Ga})(\text{Se,S})_2$  layers deposited by sputtering of metallic precursors with subsequent rapid thermal processing. The roughness of the layers is significantly higher compared to the three stage  $\text{Cu}(\text{In,Ga})\text{Se}_2$  described before. Deep valleys are visible between the grains and also crystals with (112) surface are present. The surface roughness of the  $\text{Cu}(\text{In,Ga})(\text{Se,S})_2$  layer was investigated with AFM. Figure 3.15 shows a AFM scan over a  $10 \times 10 \mu\text{m}^2$  area on a bare CIGSSe surface.

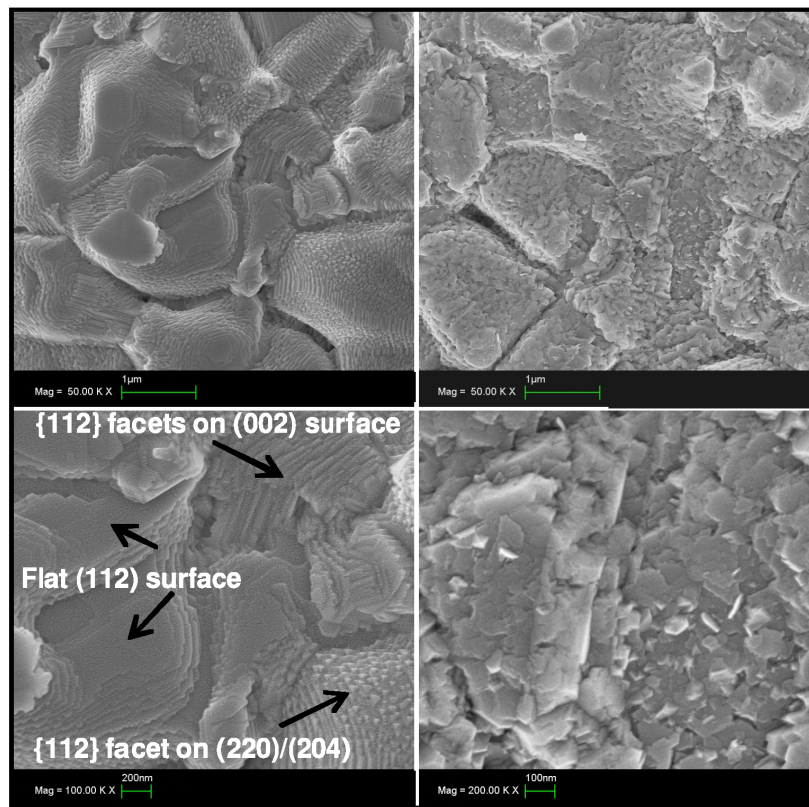


**Figure 3.14:** In the SEM images on the left hand side the bare CIGSSe surface is shown. In the lower image the {112} facets on the (112), (002) and (220)/(204) surfaces are indicated. The images on the right hand side show the coverage of the CIGSSe surface with the USP-In<sub>2</sub>S<sub>3</sub> buffer layer. The distinct microstructure of the In<sub>2</sub>S<sub>3</sub> layer is clearly visible.

The average roughness on this area is 126 nm and the root mean square 155 nm. The average grain size is 2-3  $\mu\text{m}$ . The two other AFM scans show a CIGSSe grain before and after USP- $\text{In}_2\text{S}_3$  deposition. The grain size of the  $\text{In}_2\text{S}_3$  on the CIGSSe is determined by AFM to be 20-60 nm.

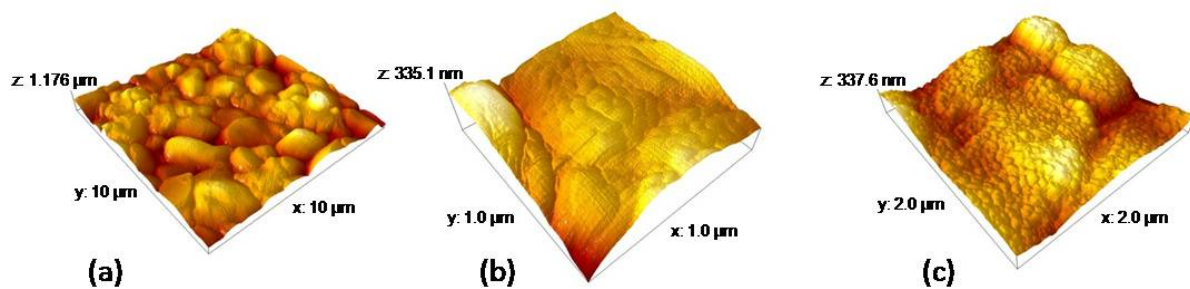


**Figure 3.15:** AFM images of the bare CIGSSe absorber surface in (a) and (b); the AFM image in (c) shows the grains of an  $\text{In}_2\text{S}_3$  layer on top of a single CIGSSe grain.

The rough surface of the  $\text{Cu}(\text{In,Ga})(\text{Se,S})_2$  layer is continuously covered with USP- $\text{In}_2\text{S}_3$  as shown on the right hand side of figure 3.14. The  $\text{In}_2\text{S}_3$  layer was sprayed from a methanol based solution with In/S ratio of 1:3 at a substrate temperature of 200  $^\circ\text{C}$ . The microstructure of the polycrystalline  $\text{In}_2\text{S}_3$  can be found also in the deep valleys between the CIGSSe grains, however, the formation of micro-cracks can not be excluded along grain boundaries of the CIGSSe.

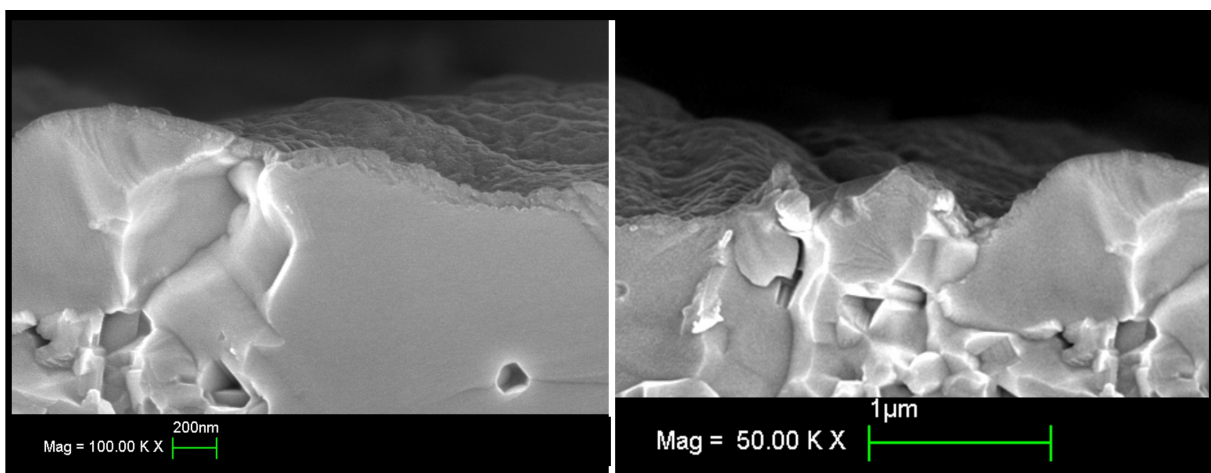


**Figure 3.16:** SEM cross-section images of the CIGSSe/USP- $\text{In}_2\text{S}_3$  layer stack. The  $\text{In}_2\text{S}_3$  layer is approximately 50 nm thick and continuously covers the CIGSSe surface. The image on the right hand side points out the pronounced surface roughness of the CIGSSe absorber.

Conformal coverage of the  $\text{Cu}(\text{In,Ga})(\text{Se,S})_2$  absorber with USP- $\text{In}_2\text{S}_3$  is verified by the cross-section image shown in figure 3.16. The layer thickness also in this case is about 50

nm.

From the morphology and microstructure analysis it can be concluded that the USP method is suitable for the deposition of compact and continuous  $\text{In}_2\text{S}_3$  layers on the rough CIGS and CIGSSe surfaces using the appropriate deposition parameters.

### 3.5.3 Chemical composition

To learn more about the effect of the relative sulfur amount in the solution on the layer properties, the chemical composition of indium sulfide layers sprayed for 20 min at 200 °C with an  $\text{InCl}_3$  concentration of 0.01 mol/l and an indium to sulfur ratio of 1:1 and 1:3 was analyzed by XPS (figure 3.17).

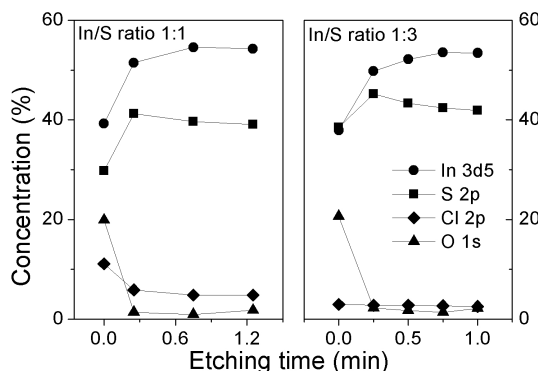


**Figure 3.17:** Elemental concentration depth profile as obtained from XPS measurements. Layers were grown with In to S ratio of 1:1 and 1:3 in the precursor solution. The etching rate was estimated to be 30 nm/min.

On the surface of the both samples a high concentration of oxygen was detected which originates from surface oxidation during air exposure. These layers were etched with 2 keV argon ions for measuring depth profiles of elements. After etching the measured oxygen concentration decreases significantly during the first sputtering step and stays almost constant throughout the remainder of the depth profile in both films. Also chlorine was detected in both layers, but the Cl concentration is almost doubled in the layer sprayed with 1:1 ratio compared to the layer sprayed with In/S ratio of 1:3. However, the analyzing technique does not allow a conclusion on the quantitative atomic concentration, as the corresponding sputter yield of the elements in these layers is not known. Especially the chlorine and sulfur are prone to depletion at the surface due to the Ar-ion sputtering.

More quantitative information about the chemical composition of the sprayed films was therefore obtained from Rutherford backscattering spectroscopy (RBS). For this purpose layers were grown on Si (111) wafers. As expected from the XPS results, the films deposited



with sulfur deficiency in the precursor solution with respect to stoichiometric  $\text{In}_2\text{S}_3$  show a high chlorine peak (figure 3.18).

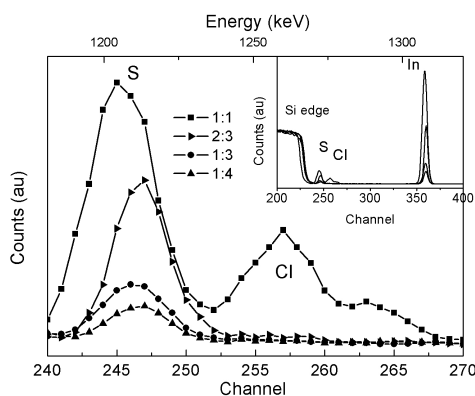


**Figure 3.18:** Rutherford backscattering spectrum of  $\text{In}_2\text{S}_3$  sprayed from solutions with different In to S ratio.

The atomic concentrations of the elements calculated from RBS spectra are summarized in Figure 3.19. In layers sprayed from solutions with In to S ratio of 1:1 high chlorine concentrations of 20 at% deposited at 200 °C, 16 at% at 220 °C and 13 at% at 240 °C were found.

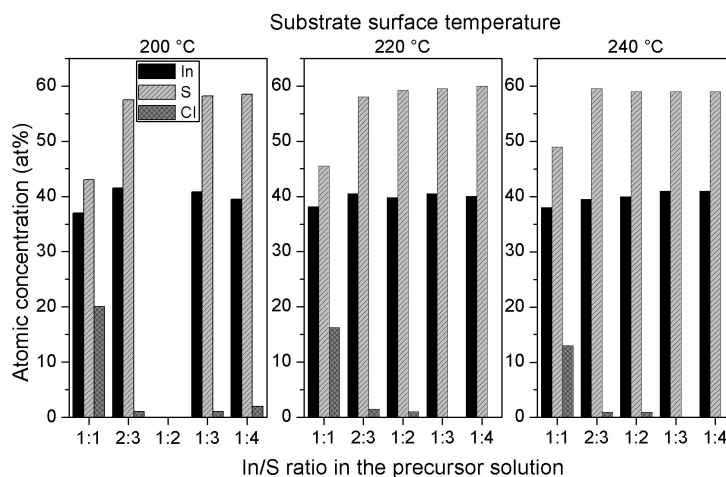


**Figure 3.19:** Composition of layers on (111)-Si deposited at different temperatures using solutions of different In/S precursor ratios as derived from RBS measurements.

Two effects can be noted here: (i) the chlorine concentration decreases with increasing deposition temperature and with increasing sulfur content in the solution; (ii) with stoichiometric concentration or sulfur excess in the solution the chlorine concentration drops below 1 at%. A dependency on temperature can not be observed in this case. Apart from the expected In, S and Cl no other elements were detected in these layers. In all these

layers  $40\pm 1$  at% of indium and  $60\pm 1$  at% of sulfur were measured.

The concentrations of the different elements detected by elastic recoil detection analysis (ERDA) measurements are shown in figure 3.20. Again sprayed indium sulfide films with different In/S ratio in the precursor solution deposited at substrate temperatures of  $200\text{ }^\circ\text{C}$  and  $240\text{ }^\circ\text{C}$  were analyzed. In all samples Cl, O, N, and C impurities were found, whereas the impurity concentration decreases with increasing substrate temperature and degree of sulfur excess in the solution. Analogue to the RBS analysis, ERDA measurements confirm that only the layers sprayed with S deficiency have significant chlorine impurities.

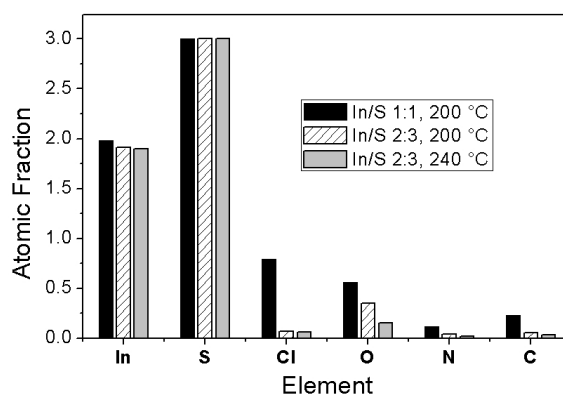


**Figure 3.20:** Composition of layers on (111)-Si substrate deposited at different surface temperatures using solution of different In/S ratios as derived from ERDA measurements.

### 3.5.4 Optical properties and band gap considerations

Since most of the generated charge carriers in the n-type buffer layer in CIGS thin film solar cells are lost, a key requirement of the buffer layer is a low optical absorption over a wide spectrum. The commonly used CdS buffer layer has a direct optical band gap with high absorption coefficient. In order to improve the current density of the device, any material which replaces the CdS must have a higher optical band gap and/or a lower absorption coefficient. Figure 3.21a shows the transmission and reflection of USP-In<sub>2</sub>S<sub>3</sub> layers deposited at different substrate temperatures from a methanol solution with 0.02 mol/L InCl<sub>3</sub>, an In/S ratio of 2:3. The deposition was aborted after 15 min and 20 sec.

Within the investigated temperature range, it can be assumed that the temperature only affects the layer growth rate, i.e. for constant deposition time, the thickness is varied. A decrease of the transmission is observed over the whole wavelength range with increasing substrate temperature. The reduced transmission is mainly caused by a high reflection of the In<sub>2</sub>S<sub>3</sub> layer. The reflection increases above 20% and the peak shifts towards higher wavelengths. In figure 3.21b the transmission is corrected for the reflection. In this plot the effect of increased absorption as a function of the layer thickness is visible. The thickness increases from  $21\pm 5$  nm to  $69\pm 2$  nm from  $181$  to  $222\text{ }^\circ\text{C}$  deposition temperature. The

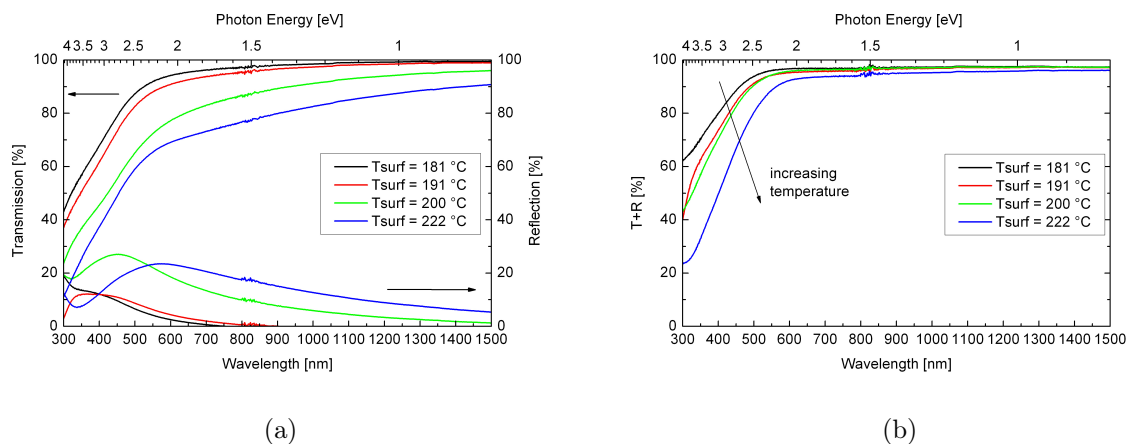


**Figure 3.21:** Optical transmission and reflection of sprayed indium sulfide films on glass substrate with a variation of the substrate surface temperature  $T_s$ : (a) Transmission and reflection spectra, (b) sum of the transmission and reflection ( $T+R=1-\text{Absorption}$ ). The data were already corrected for the glass substrate. Spray parameters were: 0.02 mol/L  $\text{InCl}_3$  and 0.03 mol/L thiourea, In/S ratio was equal to 2/3, 15'20" spray time (4 cycles).

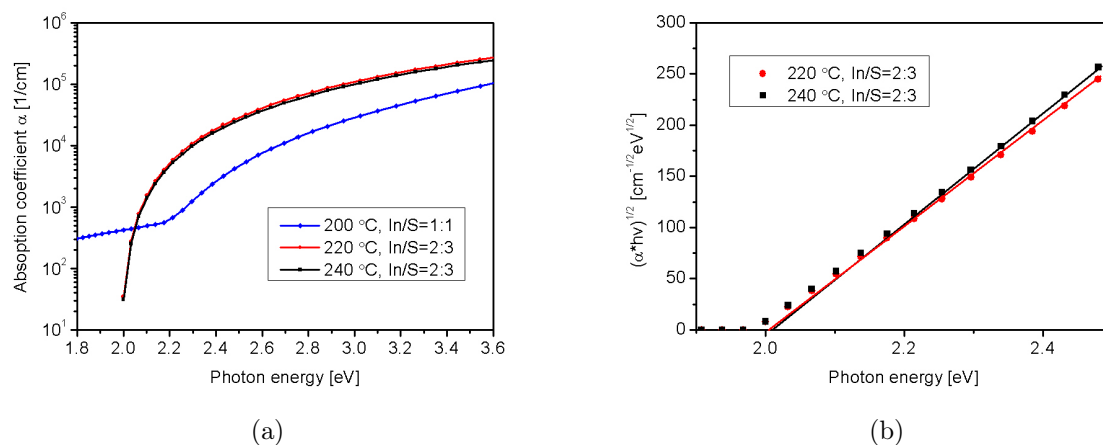
transmission (of the light entering the layer) of the 69 nm thick layer in the wavelength region of 650-1200 nm is between 93-96%.

Figure 3.22a shows the absorption coefficient of USP- $\text{In}_2\text{S}_3$  deposited on silicon wafer at 200 °C with In/S ratio of 1:1 and at 220 °C and 240 °C with In/S ratio of 2:3 in the precursor solution. From the extinction coefficient  $k$  which is measured by ellipsometry, the absorption coefficient  $\alpha$  is calculated with [9]

$$\alpha = \frac{4\pi k}{\lambda}, \quad (3.3)$$

where  $\lambda$  is the wavelength of the photons. The absorption coefficient of the samples deposited with an In/S ratio of 2:3 coincide over the whole spectrum. The absorption coefficient increases for photons with energies above 2 eV and reaches values of  $10^5 \text{ cm}^{-1}$  only above 3 eV. The curve for the USP- $\text{In}_2\text{S}_3$  layer deposited with In/S ratio of 1:1 has a completely different shape. As shown in the previous section this layer has high chlorine impurities of about 20 at%. This completely changes the absorption characteristics. The absorption coefficient is significantly smaller than that of pure  $\text{In}_2\text{S}_3$  layers.

The transmission of USP- $\text{In}_2\text{S}_3$  layers deposited with In/S ratio of 1:1 and 1:2 is shown in figure 3.23. The layer with high chlorine impurity (In/S ratio 1:1) has not only a higher transmission over the whole wavelength region but also the absorption edge is shifted to lower wavelengths. The effect of the precursor ratio on the device performance is discussed in section 5.2.



**Figure 3.22:** (a) Absorption coefficient of USP- $\text{In}_2\text{S}_3$  thin layers deposited with In/S ratio of 1:1 at 200 °C and with 2:3 ratio at 220 °C and 240 °C on silicon wafers. (b) Extrapolation of the function  $(\alpha \cdot hv)^{1/2}$  versus  $h\nu$  to determine the optical band gap of the  $\text{In}_2\text{S}_3$  thin films.

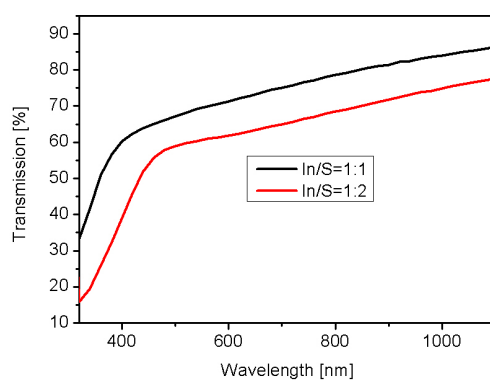


**Figure 3.23:** Transmission of USP- $\text{In}_2\text{S}_3$  layers deposited with different precursor ratios. The thickness of both layers is estimated from SEM images to be approximately 60 nm.

In order to determine the optical band gap as well as to distinguish between direct and indirect transition the following model was applied to the absorption coefficient [82]:

$$\alpha(h\nu) = \frac{A(h\nu - E_g)^m}{h\nu}, \quad (3.4)$$

where A and m are constants,  $h\nu$  the photon energy and  $E_g$  the energy band gap. The constant m equals 1/2 and 3/2 for direct allowed and direct forbidden transition [9]. For allowed indirect transition m equals 2. The modeling of the absorption coefficient from the layers sprayed with In/S ratio of 2:3 yields a value for m close to 2. This suggests that the energy band gap of USP-In<sub>2</sub>S<sub>3</sub> is indirect. Knowing the value of m, the band gap can be determined by an linear extrapolation of  $(\alpha h\nu)^{1/2}$  to zero. Figure 3.22b shows the linear extrapolation of the function  $(\alpha h\nu)^{1/2}$  for USP-In<sub>2</sub>S<sub>3</sub> layers deposited on silicon wafers at 220 °C and 240 °C from a methanol based solution with In/S ratio of 2:3. The determined band gap for the two layers is between 2.00 and 2.01 eV. This corresponds well with values reported in literature for stoichiometric In<sub>2</sub>S<sub>3</sub> thin layers. Barreau et al. reported a indirect band gap of 2.01 eV for In<sub>2</sub>S<sub>3</sub> layers deposited by co-evaporation of indium and sulfur on Na free corning glass. They determined the band gap from transmission and reflection measurements of In<sub>2</sub>S<sub>3</sub> carefully selected for stoichiometry. Barreau et al. also calculated the band structure of In<sub>2</sub>S<sub>3</sub> using density functional theory and found an allowed indirect transition [30]. An indirect band gap of 2.2 eV was calculated for In<sub>2</sub>S<sub>3</sub> layers deposited by spray ion layer gas reaction (spray-ILGAR) by Allsop et al. [83]. Sterner et al. found an indirect band gap of 2.1 eV for In<sub>2</sub>S<sub>3</sub> layers deposited by atomic layer deposition [84].

However, there are also values reported in literature which differ significantly from the 2.0-2.01 eV found in this study. Recently, a review on properties of In<sub>2</sub>S<sub>3</sub> deposited by different techniques was composed by N. Barreau [85]. Band gap values for In<sub>2</sub>S<sub>3</sub> were reported between 2.0 and 3.7 eV. Barreau attributes the large variations of the band gap values to changes of the stoichiometry and incorporation of extrinsic atoms such as oxygen, sodium, and copper. Density functional theory calculations suggest that the sulfur strongly influences the width and the nature of the band gap in In<sub>2</sub>S<sub>3</sub> since the top of the valence band is mainly composed of sulfur p orbitals [30]. Oxygen can substitute sulfur atoms compressing the lattice resulting in a band gap widening as shown by Robles et al. [86]. Sodium and/or copper can occupy the vacancies and substitute indium on the tetragonal sites of the spinel like structured In<sub>2</sub>S<sub>3</sub>. The sodium was found to widen the band gap [87] and copper reduces the band gap value [88]. The band gap of In<sub>2</sub>S<sub>3</sub> is also discussed in section 4.2 in view of interface formation with the Cu(In,Ga)Se<sub>2</sub>.

Figure 3.24a shows the absorption coefficient of USP-In<sub>2</sub>S<sub>3</sub> layers deposited on soda lime glass at different substrate temperatures from a methanol solution and In/S ratio of 2:3 for 60 min. The absorption coefficient is calculated from transmission and reflection measurements using the following equation [82]:

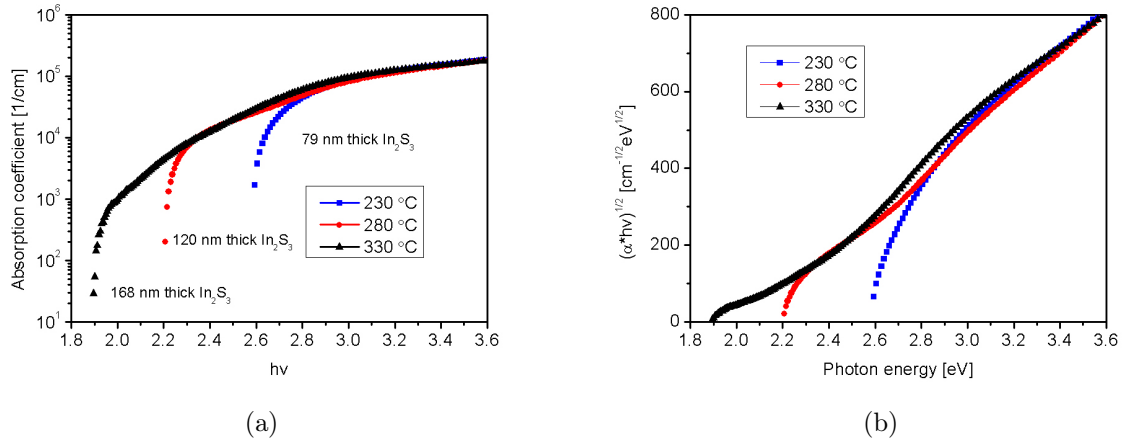


**Figure 3.24:** (a) Absorption coefficient of USP- $\text{In}_2\text{S}_3$  thin layers deposited with In/S ratio of 2:3 at 230 °C, 280 °C and 240 °C on soda lime glass. The deposition was terminated after 60 minutes. (b) The function  $(\alpha h\nu)^{1/2}$  plotted versus  $h\nu$  for the USP- $\text{In}_2\text{S}_3$  thin films deposited at different temperatures.

$$\alpha = -\frac{1}{t} \ln \left( \frac{T}{(1-R)^2} \right), \quad (3.5)$$

where  $t$  is the layer thickness. The transmission  $T$  and reflection  $R$  take values between zero to one.

For photon energies above 2.9 eV the three curves coincide reaching an absorption of  $1.5 \cdot 10^5 \text{ cm}^{-1}$  at 3.4 eV. Depending on the deposition temperature the curves decline at different energies. The temperature has a major impact on the layer thickness, but also on interdiffusion of elements from the glass substrate to the  $\text{In}_2\text{S}_3$  and the formation of different phases. The absorption coefficient of the layer sprayed at 330 °C forms an upper envelop for the three curves. Figure 3.24b shows the function  $(\alpha h\nu)^{1/2}$  plotted versus the photon energy. The shape of the curves for the investigated temperatures region differs especially in the lower energy part. For 280 °C and 330 °C the curves exhibit two linear regions. The extrapolation of the linear regions to zero is shown in figure 3.25 for the different temperatures. For all layers the extrapolation coincide linear region yield energy values close to the value found on silicon wafers by ellipsometry; 1.98 eV, 2.00 eV, and 2.06 eV is found for 230 °C, 280 °C, and 330 °C, respectively. For the two higher temperatures an additional value of 2.21 eV and 2.17 eV is determined (fig. 3.25b+c).

The used substrate material soda lime glass has a  $\text{Na}_2\text{O}$  content of more than 10%. Diffusion of sodium into the  $\text{In}_2\text{S}_3$  is very likely since sodium is a highly mobile element. Both the incorporation of sodium into the spinel-type  $\text{In}_2\text{S}_3$  structure and the formation of the  $\text{NaIn}_5\text{S}_8$  phase results in an increased band gap value [87, 89]. An increase of the temperature enhances the diffusion of Na and phase transformation. The appearance of

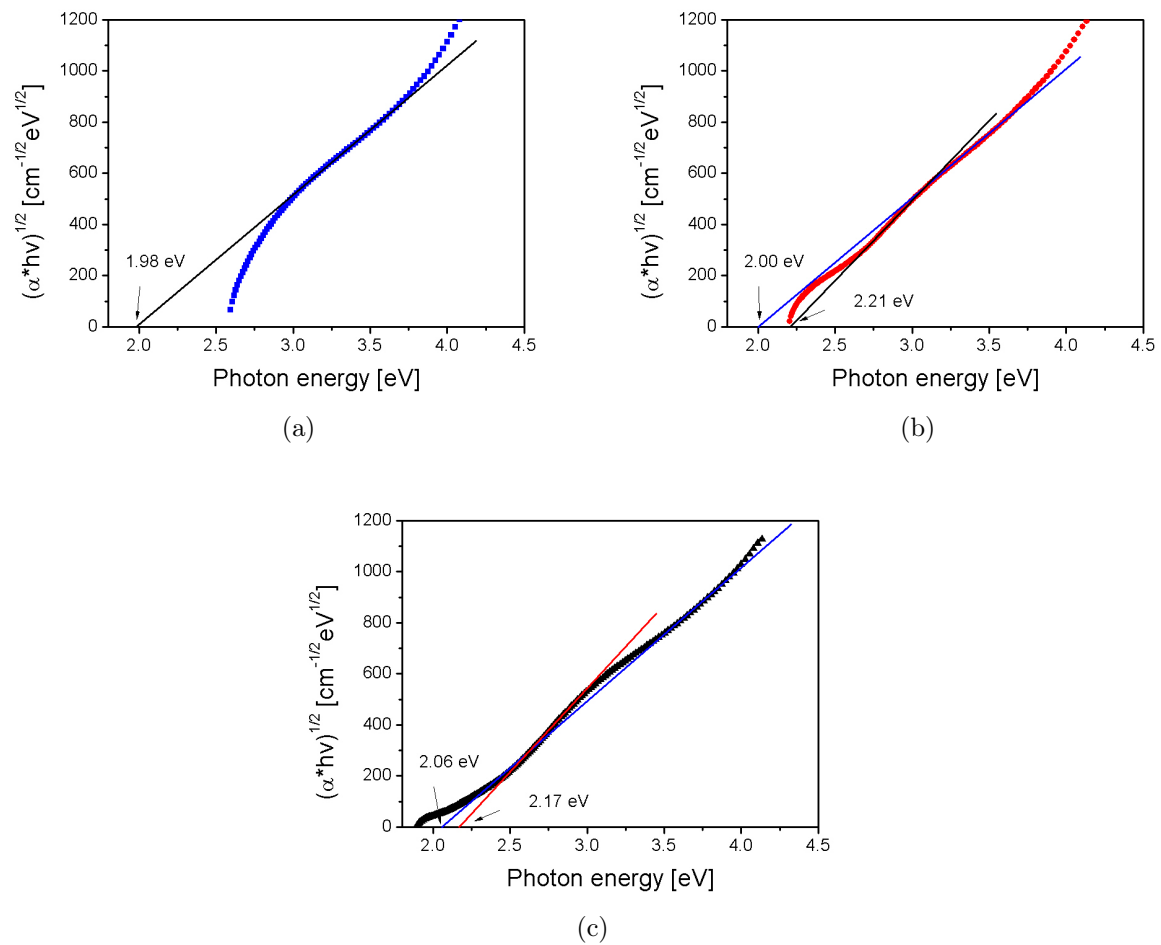


**Figure 3.25:** Extrapolation of the linear part of the function  $(\alpha h\nu)^{1/2}$  vs.  $h\nu$  to determine the energy band gap of the thin layer. (a)  $\text{In}_2\text{S}_3$  deposited at  $230^\circ\text{C}$  on soda lime glass with thickness of 79 nm; (b) 120 nm thick  $\text{In}_2\text{S}_3$  layer deposited at  $280^\circ\text{C}$ ; (c) 168 nm thick  $\text{In}_2\text{S}_3$  layer deposited at  $330^\circ\text{C}$ . The function  $(\alpha h\nu)^{1/2}$  of the layers deposited at  $280^\circ\text{C}$  and  $330^\circ\text{C}$  show two linear regions.

the second band gap value for higher deposition temperatures indicate the coexistence of  $\text{In}_2\text{S}_3$  and a sodium containing phase in the thin layer. This could be either a solid solution of two phases or the formation of a stacked bi-layer. It should be noted here that this does not happen at  $230^\circ\text{C}$  deposition temperature. Therefore, it is assumed that the above described band gap widening due to sodium diffusion does not happen in the  $\text{In}_2\text{S}_3$  layer deposited on the CIGS.

The determined band gap for the USP- $\text{In}_2\text{S}_3$  layer of close to 2.0 eV is smaller than the value of 2.4 eV for commonly used CdS buffer layers. The expected parasitic losses would be higher, however, the transition at 2.0 eV is indirect for  $\text{In}_2\text{S}_3$ , resulting in a lower absorption coefficient. Figure 3.26a compares the absorption coefficient of USP- $\text{In}_2\text{S}_3$  and CdS. The absorption coefficient for CdS was taken from SCAPS (original data from [90]) and for USP- $\text{In}_2\text{S}_3$  from figure 3.22. The absorption in CdS increases rapidly for photons with energy higher than 2.4 eV. The increase of the absorption in  $\text{In}_2\text{S}_3$  increases more gradually due to the indirect nature of the band gap. Between 2.4 and 3.0 eV the absorption in CdS is higher than in the  $\text{In}_2\text{S}_3$  layer.

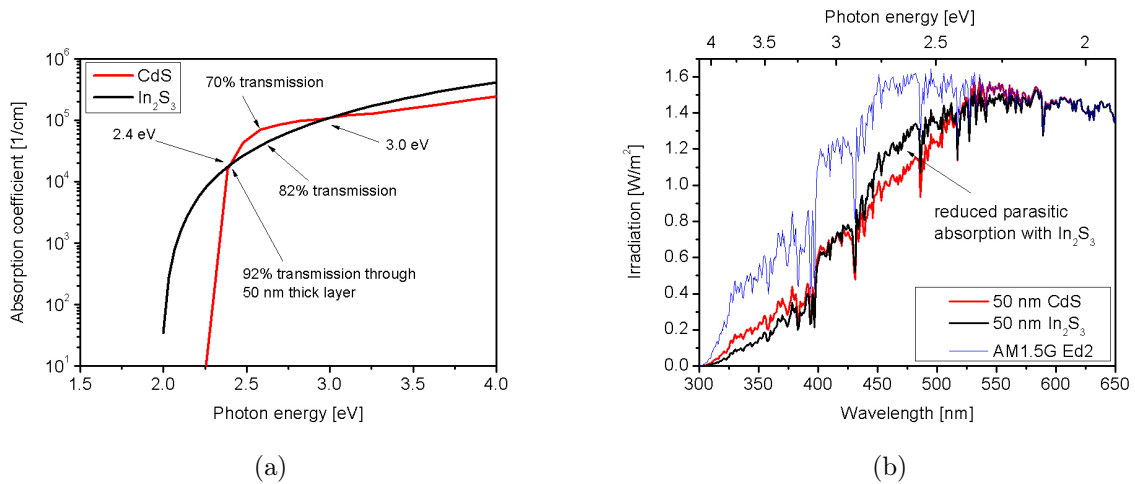


**Figure 3.26:** (a) Absorption coefficient of CdS and  $\text{In}_2\text{S}_3$  thin layers. (b) Calculated solar irradiance after passing 50 nm thick CdS and USP- $\text{In}_2\text{S}_3$ .

Figure 3.26b shows the transmitted irradiance of the AM1.5G Ed2 spectrum through 50 nm thick layers of CdS and  $\text{In}_2\text{S}_3$  [91]. The irradiance was calculated using Lambert's law of absorption which can be written as

$$I(t) = I_0 e^{(-\alpha t)}, \quad (3.6)$$

where  $I_0$  is the irradiance from AM1.5G Ed2 spectrum. Reflection is neglected in this calculation, since reflection losses can be minimized using appropriate anti-reflection coatings for the two materials. The plotted transmission in figure 3.26b shows that an increase in current density can be expected if USP- $\text{In}_2\text{S}_3$  is substituted for the commonly used CdS



as buffer layer in CIGS based thin film solar cells.

### 3.6 Summary and conclusion

In this chapter the growth mechanism and layer properties of USP-In<sub>2</sub>S<sub>3</sub> layers is presented. A chemical reaction equation and a possible mechanism for the formation of In<sub>2</sub>S<sub>3</sub> layers from solution droplets containing InCl<sub>3</sub> and thiourea precursors is proposed. The mechanism can be described as a mixture of particle deposition with subsequent chemical conversion into In<sub>2</sub>S<sub>3</sub> (indirect process) and chemical vapor deposition (direct process). From analyzing the deposition process versus time it can be concluded that particle deposition is the dominant growth mechanism.

The growth kinetics for a given solvent are mainly influence by the substrate temperature and the relative and absolute precursor concentration. Homogeneous and compact In<sub>2</sub>S<sub>3</sub> layers with continuous substrate coverage are obtained from methanol or acetone based solutions with InCl<sub>3</sub> and TU precursors at a deposition temperature of 200 °C. Polycrystalline layers are grown from solutions with sulfur whereas sulfur deficient solutions yield amorphous or nanocrystalline films. Impurities of extrinsic elements such as chlorine and oxygen can be minimized by increasing the temperature and amount of sulfur excess in the solution.

An indirect energy band gap of 2.01 eV is found for USP-In<sub>2</sub>S<sub>3</sub> layers on silicon and SLG substrate. Even though the derived band gap of the USP-In<sub>2</sub>S<sub>3</sub> layer is smaller than band gap of CdS, a gain in the current density can be expected due to the lower absorption coefficient.



## 4 Application in CIGS thin film solar cells

This chapter is in part based on the following publications:

S. Buecheler, F. Pianezzi, C. Fella, A. Chirila, K. Decock, M. Burgelman and A.N. Tiwari, "Interface formation between  $\text{CuIn}_{1-x}\text{Ga}_x\text{Se}_2$  absorber and  $\text{In}_2\text{S}_3$  buffer layer", submitted to *Thin Solid Films*, Special Issue, Proc. of E-MRS Spring Meeting 2010, accepted for publication.

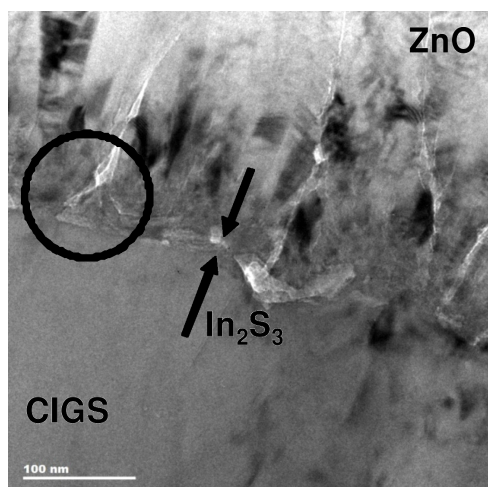
S. Buecheler, D. Corica, A. Chirila, D. Güttler, F. Pianezzi, R. Verma, K. Decock and A.N. Tiwari, "Influence of the absorber composition in  $\text{CuIn}_{1-x}\text{Ga}_x\text{Se}_2$  solar cells with sprayed  $\text{In}_2\text{S}_3$  buffer layers on the dominant recombination mechanism", *Proc. 24th European Photovoltaic Solar Energy Conference and Exhibition*, Hamburg, Germany, 2009

D. Corica, S. Buecheler, D. Guettler, A. Chirila, S. Seyrling, R. Verma and A.N. Tiwari, "Indium Sulfide Buffer Layer for  $\text{Cu}(\text{In,Ga})\text{Se}_2$  Thin-Film Solar Cells Deposited by Ultrasonic Spray Pyrolysis", *Proc. 23rd European Photovoltaic Solar Energy Conference and Exhibition*, Valencia, Spain, Sept 1-5, 2008.

### 4.1 Morphology and interdiffusion in CIGS devices

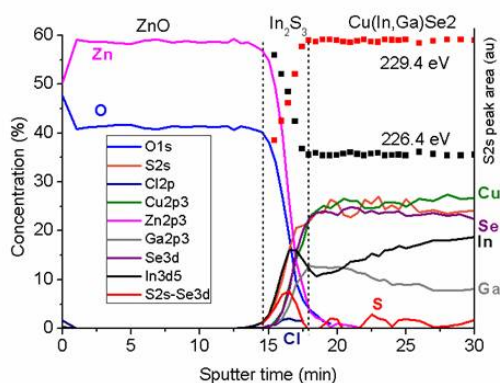
In this section the microstructure of the USP- $\text{In}_2\text{S}_3$  layer in the finished device structure and elemental interdiffusion properties at the front contact - buffer layer - absorber interfaces are discussed.

Figure 4.1 shows a conventional TEM image of AZO/i-ZnO/ $\text{In}_2\text{S}_3$ / $\text{Cu}(\text{In,Ga})\text{Se}_2$  interfaces. Indicated by arrows the  $\text{In}_2\text{S}_3$  layer is visible. With TEM polycrystalline phases in the sprayed layer could not be explicitly identified. This might originate from the destructive sample preparation method. The average layer thickness is 30 nm, however, there are regions where  $\text{In}_2\text{S}_3$  spikes are formed (see circle in fig. 4.1). These spikes affect the ZnO layer growth adversely. A gap between the columnar ZnO grains arises, starting at the peak of the  $\text{In}_2\text{S}_3$  spike. This could lead to reduced in plane conductivity of the ZnO and to long term performance stability problems, if the device is not perfectly encapsulated.



**Figure 4.1:** : Conventional TEM image of ZnO- $\text{In}_2\text{S}_3$ - $\text{Cu}(\text{In},\text{Ga})\text{Se}_2$  interface. The  $\text{In}_2\text{S}_3$  layer was sprayed with indium to sulfur ratio of 1:3 at  $200^\circ\text{C}$  surface temperature. The arrows mark the  $\text{In}_2\text{S}_3$  layer and the circle highlights an  $\text{In}_2\text{S}_3$  spike as origin of a inter-grain gap in the ZnO front contact.

Figure 4.2 shows the elemental depth profile as obtained by XPS of a  $\text{Cu}(\text{In},\text{Ga})\text{Se}_2$  based solar cell with USP- $\text{In}_2\text{S}_3$  buffer layer. Clear sulfur and indium peaks are visible in the  $\text{In}_2\text{S}_3$  region, both starting at the same sputter depth. Also chlorine impurity is measured throughout the whole  $\text{In}_2\text{S}_3$  region. No distinct copper diffusion is detected in this measurement as the copper and selenium signals start together.



**Figure 4.2:** Elemental depth profile as obtained with XPS measurements including step-wise Ar etching from a  $\text{Cu}(\text{In},\text{Ga})\text{Se}_2$  based solar cell with USP- $\text{In}_2\text{S}_3$  buffer layer.

To get more information on the elemental interdiffusion with higher resolution, elemental mapping of the front contact - buffer - absorber interfaces were gathered with energy dispersive X-ray analysis (EDX) in scanning TEM mode. Figure 4.3 shows the elemental distribution map of  $\text{Cu}(\text{In},\text{Ga})\text{Se}_2$  based solar cells with USP- $\text{In}_2\text{S}_3$  buffer layer at the cross section of the ZnO/ $\text{In}_2\text{S}_3$ / $\text{Cu}(\text{In},\text{Ga})\text{Se}_2$  interfaces. After deposition of the indium sulfide

buffer layer on the CIGS/Mo/SLG stack of the sample shown in Figure 4.3b, a chemical surface treatment was applied (also referred to as partial electrolyte Cd treatment). For this purpose, the  $\text{In}_2\text{S}_3/\text{CIGS}/\text{Mo}/\text{SLG}$  layer stack was immersed in an aqueous solution containing 0.0018 mol/L cadmium acetate, 1.32 mol/L ammonia, and 0.02 mol/L thiourea for two minutes, whereas the bath was heated from room temperature to 45 °C.

On the left hand side the cross section of the heterostructures in scanning TEM (STEM) mode are illustrated. The elemental mapping areas are indicated with the red rectangle helping to define the transitions from one layer to the next. The Ga and Se maps overlap perfectly with each other and correspond well with the CIGS border shown in the STEM image, i.e., diffusion of gallium and selenium into the  $\text{In}_2\text{S}_3$  layer is below detection limit. The same is true for the zinc of the ZnO layer<sup>1</sup>. Hence, the interface of the buffer layer to the absorber is defined by gallium and selenium and to the front contact by the zinc signal.

The sulfur maps perfectly fit into the defined abrupt interfaces. The indium map of both samples has homogeneous intensity in the CIGS region and increased intensity in the  $\text{In}_2\text{S}_3$  layer which was already seen in the depth profile obtained with XPS. However, contrarily to the XPS results a clear copper diffusion from the absorber into the  $\text{In}_2\text{S}_3$  is visible in both samples.

The tetragonal  $\text{In}_2\text{S}_3$ , which is formed by the USP method, has a spinel-like structure with many cationic vacancies. It is very likely that these vacancies are partly filled with copper ions from the absorber during the  $\text{In}_2\text{S}_3$  deposition, which in turn increases the copper vacancies at the absorber surface.

The efficiency of the solar cell shown in Figure 4.3a is below 4% (see also [74]). Applying the abovementioned chemical surface treatment after the buffer deposition can have two effects: (i) a very thin CdS layer is formed on top of the  $\text{In}_2\text{S}_3$  surface, reducing acceptor-like defect states at the interface to the front contact [10, 92, 93]; (ii) cadmium ions diffuse through the  $\text{In}_2\text{S}_3$  layer into the absorber and filling the emerged copper vacancies, which leads to a surface type-inversion and with it to an improved band alignment [94]. Both effects contribute to higher expected cell efficiency.

The device shown in Figure 4.3b has 10% efficiency, mainly due to increased fill factor and current density. The corresponding CBD-CdS reference on this absorber was 12.5%. The photovoltaic properties of CIGS based devices with and without the partial electrolyte Cd treatment are discussed in more detail in section 4.3.5. In the sample, which was treated in the Cd solution, neither in the bulk material nor at the buffer layer interfaces any Cd could be detected with EDX and EELS within the detection limits.

The elemental map of oxygen in Figure 4.3a shows some intensity in the buffer and absorber regions. This is most probably caused by oxidation effects due to elevated temperature of

---

<sup>1</sup>The areas with low signal in the Ga, Se and Zn maps originate from the three dimensional shape of the interfaces.

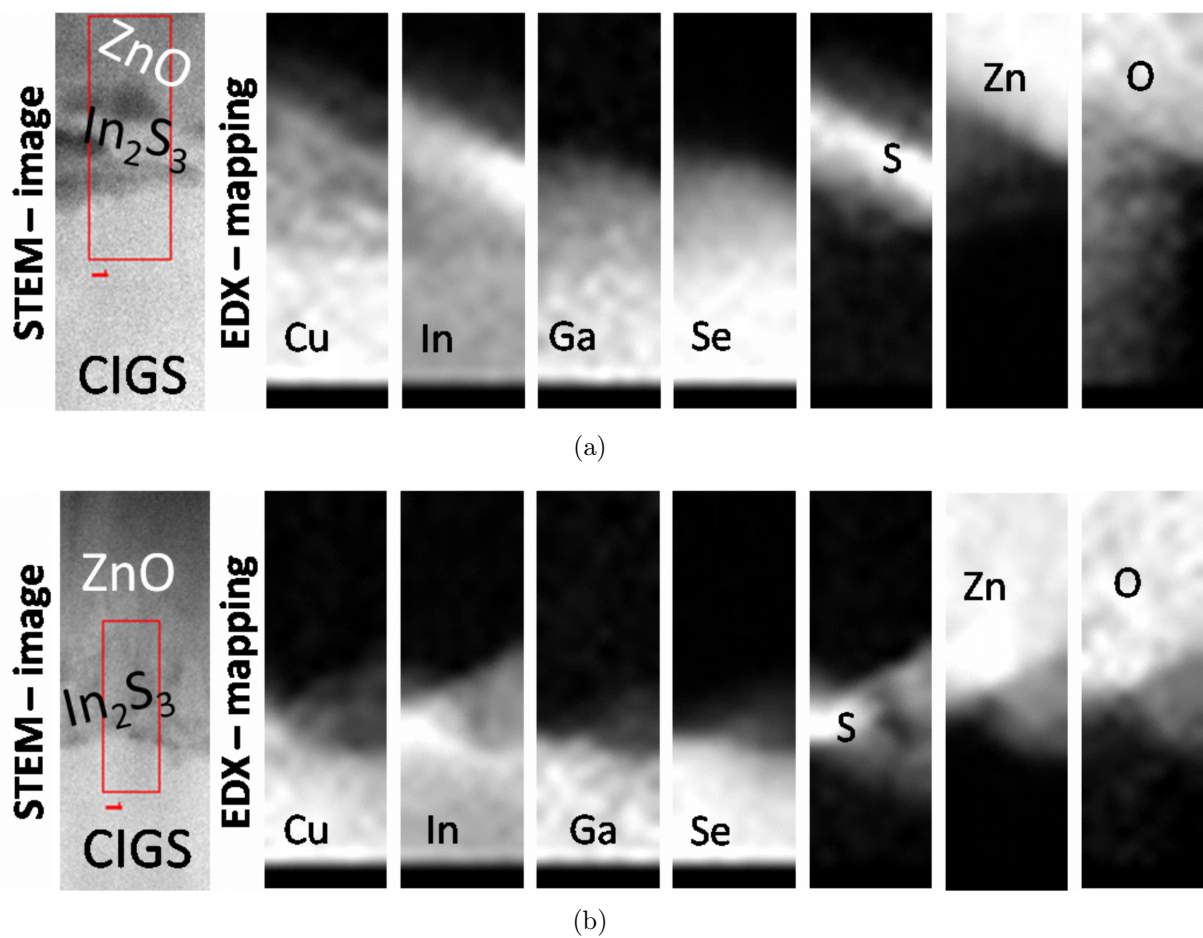


**Figure 4.3:** STEM analysis with a high angular annular dark field detector on the left hand side and elemental mapping by EDX at the ZnO/In<sub>2</sub>S<sub>3</sub>/Cu(In,Ga)Se<sub>2</sub> interfaces of an as deposited sample (a) and a sample with chemically treated In<sub>2</sub>S<sub>3</sub> surface (b).

the absorber at the grain boundaries during the heating up period for the spray deposition and some oxygen impurity incorporation into the  $\text{In}_2\text{S}_3$  during deposition. The same oxygen amount is expected for the sample shown in Figure 4.3b, the lack of oxygen signal in the buffer and absorber region probably results from an unfavorable sample orientation (no grain boundaries are visible) and a larger TEM sample thickness.

With ultrasonic spray pyrolysis it is possible to grow stoichiometric tetragonal- $\text{In}_2\text{S}_3$  layers with low impurity concentration and conformal substrate coverage. A microcrystalline  $\text{In}_2\text{S}_3$  structure is favorable for buffer layer application to avoid spikes which could lead to deteriorate ZnO. Copper diffusion into the  $\text{In}_2\text{S}_3$  layer already during deposition was observed, irrespective of the investigated absorber type.

## 4.2 Interface formation

In the previous section the diffusion of Cu from the  $\text{Cu}(\text{In,Ga})\text{Se}_2$  into the  $\text{In}_2\text{S}_3$  buffer layer was described qualitatively. For a detailed analysis of the elemental interdiffusion first the bare surface of  $\text{Cu}(\text{In,Ga})\text{Se}_2$  absorber layers with two different  $[\text{Ga}]/[\text{III}]$  and  $[\text{Cu}]/[\text{III}]$  ratios<sup>2</sup> were investigated with XPS followed by an analysis of the elemental composition after the deposition of thin  $\text{In}_2\text{S}_3$  at different substrate temperatures. The XPS spectra of the  $\text{Cu}(\text{In,Ga})\text{Se}_2$  surface are shown in figure 4.4 and the calculated surface composition is given in table 4.1.

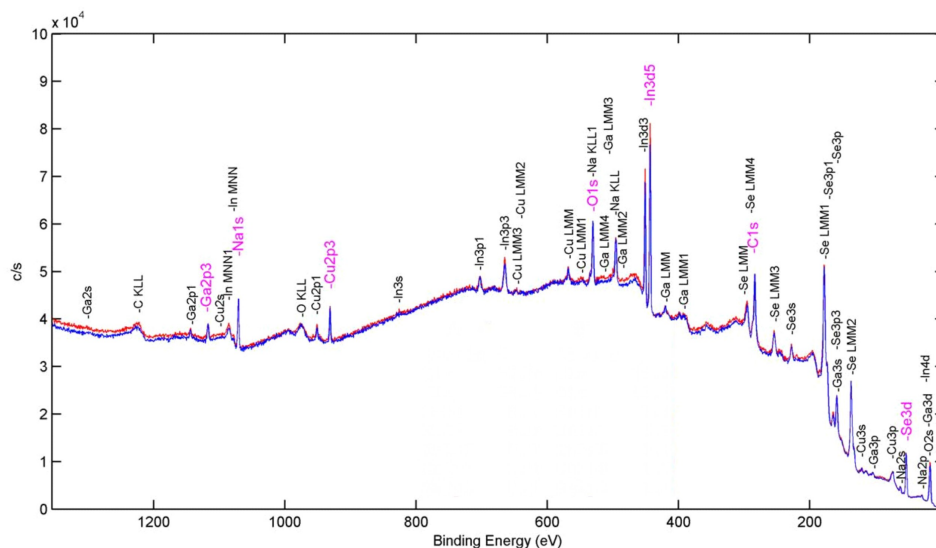


**Figure 4.4:** XPS spectra of the CIGS absorbers A and B.

The chemical shift analysis of the O1s peak is difficult because it is overlapped by the Na KLL1 Auger line at 532 eV. In the following it is assumed that the detected carbon and oxygen are adsorptions on the surface and are not chemically bound to the absorber.

<sup>2</sup>Here  $[\text{III}]$  represents the sum of the group 3 elements  $[\text{Ga}]+[\text{In}]$ .

**Table 4.1:** Surface composition of bare  $\text{Cu}(\text{In},\text{Ga})\text{Se}_2$  absorber layers determined from XPS measurements. Values are given in at% and normalized for 100 at%

	Cu $2p_3$	In $3d_5$	Ga $2p_3$	Se $3d$	Na $1s$	Cu/(III) surface	Ga/(III) XPS	Cu/(III) bulk	Ga/(III) EDX
A	8.7	26.7	4.4	33.3	26.9	28.1	14.1	89.5	23.8
B	9.4	24.9	6.0	33.1	26.7	30.4	19.3	85.9	25.8

However, an oxide formation, especially  $\text{InO}_x$ , can not be excluded.

On the surface of both absorbers a high concentration of Na was identified. The absorbers were grown on a Mo coated soda-lime glass (SLG) in a high temperature process. The Na diffuses from the SLG through the Mo back contact into the absorber during the growth and segregates on the absorber surface. The effect of Na on the absorber growth and its properties is out of scope of this thesis and can be found elsewhere [8, 57, 95]. However, it should be noted that there is Na present during the spray deposition of the buffer layer.

The ratio of  $[\text{Cu}]/[\text{III}]$  was determined to be 0.28 and 0.3 for the two samples which is very close to the commonly reported  $[\text{Cu}]/[\text{III}]$  of 0.33 ratio on the surface of  $\text{Cu}(\text{In},\text{Ga})\text{Se}_2$  semiconductors. This observation was previously identified as the formation of a  $\text{Cu}(\text{In},\text{Ga})_3\text{Se}_5$  surface layer [96], which was also called ordered vacancy compound (OVC) [97]. In 1999 Herberholz et al. developed a model for the near surface region of free  $\text{Cu}(\text{In},\text{Ga})\text{Se}_2$  absorbers [98]. They proposed a metal terminated ( $\{112\}$  plane) crystal surface with net positive surface charge due to the absence of Se bounds. They further concluded that this positive surface charge leads to the observed band bending and is a driving force for copper migration from the surface into the bulk. Partially, the copper vacancies ( $\text{V}_{\text{Cu}}^-$ ) are occupied by In ions ( $\text{In}_{\text{Cu}}^{2+}$ ) creating charge compensating defect complexes  $(2\text{V}_{\text{Cu}}^- + \text{In}_{\text{Cu}}^{2+})^0$ . Using first principle calculations of bulk  $\text{CuInSe}_2$  Zhang et al. showed that the formation of such  $(2\text{V}_{\text{Cu}}^- + \text{In}_{\text{Cu}}^{2+})^0$  complexes is energetically favored due to low formation energies. The rearrangement of In in the surface region of the absorber, leading to the formation of the  $(2\text{V}_{\text{Cu}}^- + \text{In}_{\text{Cu}}^{2+})^0$  complexes, were proposed to be the major structural element of the ordered defect compound (ODC) [99]. Niemegeers et al. included the ODC layer between the absorber and buffer in a model for electronic transport properties [100]. In the simulation of the device in SCAPS-1D [101] they used the bulk properties of  $\text{Cu}(\text{In},\text{Ga})_3\text{Se}_5$  for the modeling parameters of the ODC layer and assumed a layer thickness of 15 nm. The developed model consistently explains both the measured AC and DC transport properties of  $\text{Cu}(\text{In},\text{Ga})\text{Se}_2$  devices with CdS buffer layer.

More recently Moenig et al. re-investigated the  $\text{Cu}(\text{In},\text{Ga})\text{Se}_2$  surface by hard X-ray photoelectron spectroscopy (HAX-PES) at the BESSY synchrotron in Berlin [102]. With HAX-PES the variable photon energy of the exciting synchrotron radiation can be used to control the information depth. On  $\text{Cu}(\text{In},\text{Ga})\text{Se}_2$  layers grown under Cu-poor conditions they found a completely Cu depleted surface in sub-nanometer scale. This result supports



the surface reconstruction model which was theoretically described by Zhang et al. [79]. Moenig et al. also showed that a surface ratio of  $[Cu]/[III] \approx 0.33$  measured with conventional XPS can be explained with the surface reconstruction model assuming a bilayer structure. The bilayer consists of a completely Cu depleted surface layer in sub-nano scale on top of the bulk  $Cu(In,Ga)Se_2$  material [102].

Based on these argumentations and the XPS measurements of the bare surface of the  $Cu(In,Ga)Se_2$  (see table 4.1) a completely Cu depleted metal terminated surface layer with net positive surface charge is assumed. In this Cu depleted surface layer copper vacancies and indium on copper antisites form  $(2V_{Cu}^- + In_{Cu}^{2+})^0$  defect clusters.

In order to investigate the interdiffusion of elements across the absorber-buffer interface and the phase formation in the buffer layer,  $In_2S_3$  layers were sprayed on the absorbers A and B at 200 °C surface temperature with a precursor ratio of  $In/S=2:3$ . Additionally,  $In_2S_3$  layers were deposited onto absorber A at 220 °C, 250 °C and 300 °C to explore the effect of additional heat energy.

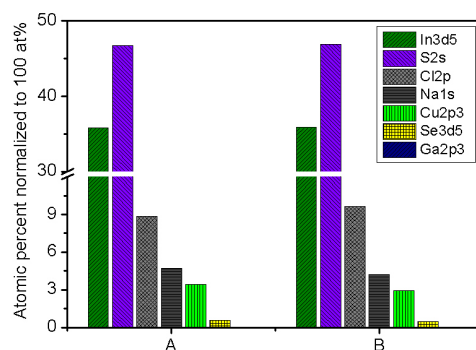


**Figure 4.5:** Elemental composition of  $In_2S_3$  layer sprayed at 200 °C onto  $Cu(In,Ga)Se_2$  absorbers A and B. The atomic concentration was calculated from XPS measurements assuming that the carbon and oxygen is only adsorbed on the surface.

Figure 4.5 shows the elemental composition of the  $In_2S_3$  deposited on the two absorbers A and B. The composition of the two samples on the different absorbers is almost identical. For both samples chlorine concentrations of approximately 9at% were calculated from the XPS spectra. This result disagrees with the findings described in section 3.5.3. There the chlorine impurity in  $In_2S_3$  deposited by USP at 200 °C substrate surface temperature and a precursor ratio of  $In/S=2:3$  was determined from RBS measurements to be below 1at%. The samples for the RBS measurement were prepared on silicon wafer, i.e. no sodium was present during the growth. However, there is a significant amount of Na present during the  $In_2S_3$  deposition on the  $Cu(In,Ga)Se_2$  absorber as shown in table 4.1. The high chlorine concentration on the surface of the  $In_2S_3/Cu(In,Ga)Se_2$  structure can be at least partially explained by the formation of solid NaCl during the  $In_2S_3$  deposition which is then incor-

porated into the buffer layer structure.

Irrespective of the surface composition of the absorber approximately 3 at% Cu content was found on the surface of the sprayed  $\text{In}_2\text{S}_3$  layer.  $\text{In}_2\text{S}_3$  layers crystallize in the spinel-type structure with vacancies on the tetraedral sites. The formula for the vacancy containing crystal structure can be written as  $(\text{In}_{16})_{\text{Oh}}(\text{In}_{16/3}\square_{8/3})_{\text{Td}}\text{S}_{32}$ , where  $\square$  represents the vacancies and Oh and Td the octahedral and tetraedral sites, respectively [103]. Copper (and/or sodium) that diffuses into the spinel-type  $\text{In}_2\text{S}_3$  can occupy the cationic vacancies. It is assumed that two-third of the incorporated copper (sodium) atoms fill vacancies and the other third substitutes In on tetraedral sites in order to keep charge neutrality. This assumption leads to the formula  $(\text{In}_{16})_{\text{Oh}}(\text{In}_{(16-\alpha)/3}\text{M}_{\alpha}\square_{(8-2\alpha)/3})_{\text{Td}}\text{S}_{32}$ , with  $\alpha \leq 4$  and M stands for Cu or Na [104].

Incorporation of Cu into  $\text{In}_2\text{S}_3$  affects the electronic properties of the thin layer. Barreau et al. reported a linear decrease of the indirect band gap as well as a decrease of the carrier concentration with increasing Cu content [88]. From XPS measurements and calculations using density-functional theory, Guillot-Deudon et al. conclude that the  $\text{Cu}3d$  orbital appears at the top of the valence band and thus decreases the energy band gap. The lower conduction band states were found to remain unchanged in that work. Therefore, the energy band gap of  $\text{In}_2\text{S}_3$  deposited onto  $\text{Cu}(\text{In,Ga})\text{Se}_2$  is expected to be smaller than that of pure  $\text{In}_2\text{S}_3$  due to copper incorporation into the spinel structure. The band gap of  $\text{In}_2\text{S}_3$ , however, also depends on impurities of third elements such as sodium and oxygen. Barreau et al. found that the substitution of oxygen for sulfur in  $\text{In}_2\text{S}_3$  increases the conduction band minimum position and with this the energy band gap [105].

Also the incorporation of sodium in the  $(\text{In}_{16})_{\text{Oh}}(\text{In}_{(16-\alpha)/3}\text{M}_{\alpha}\square_{(8-2\alpha)/3})_{\text{Td}}\text{S}_{32}$  structure was found to increase the energy band gap mainly by shifting the valence band maximum downwards [87, 104, 106]. For both, incorporation of oxygen and sodium an improved n-type character of the  $\text{In}_2\text{S}_3$  material by improving the electrical conductivity was reported [85]. As shown in figure 3.20 and 4.5 oxygen as well as sodium are present in the sprayed  $\text{In}_2\text{S}_3$  layer. The present oxygen might at least partially substitute sulfur and the sodium might not only form NaCl with the chlorine from the precursor but also partially fill the vacancies in the spinel structure. Both impurities at least slightly counteract the electrical conductivity and energy band gap decrease due to Cu insertion. However, an increase of the band gap of the  $\text{In}_2\text{S}_3$  deposited on glass was only observed for temperatures  $>230^\circ\text{C}$  (cf. fig. 3.25). Therefore, no significant band gap widening of the  $\text{In}_2\text{S}_3$  layer on the CIGS absorber due to sodium incorporation is expected.

Figure 4.6a shows calculated elemental composition from XPS measurements of In and S as well as of impurities Cl, Na, Cu, Se and Ga in  $\text{In}_2\text{S}_3$  sprayed at  $200^\circ\text{C}$ ,  $220^\circ\text{C}$ ,  $250^\circ\text{C}$  and  $300^\circ\text{C}$  surface temperature onto absorber A. The copper concentration in the  $\text{In}_2\text{S}_3$  layer clearly increases with increasing surface temperature. Due to the positive elemental charges at the surface of the  $\text{Cu}(\text{In,Ga})\text{Se}_2$  the diffusion of copper into the buffer layer would not be expected, however, the chemical potential difference and the high density of

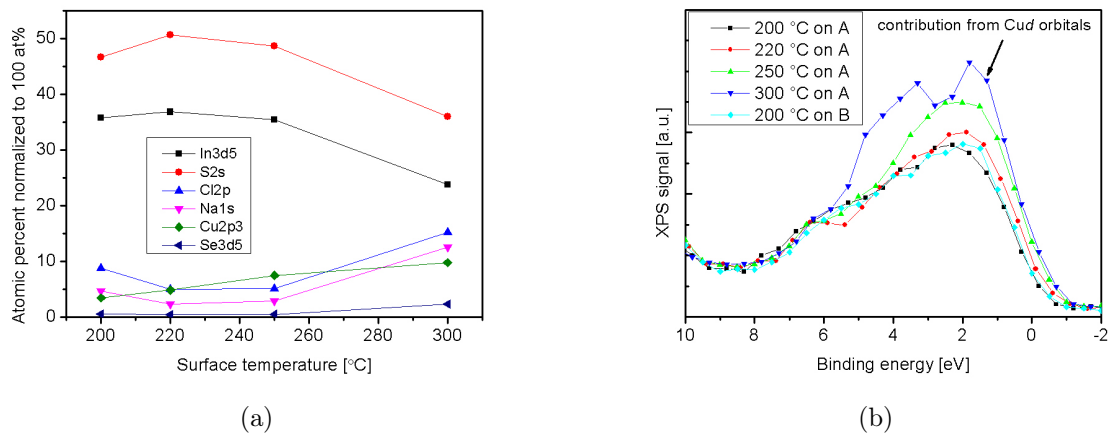


**Figure 4.6:** (a) Surface composition of  $\text{In}_2\text{S}_3$  layers deposited on CIGS absorber A at different substrate temperatures. (b) Valence band edge of  $\text{In}_2\text{S}_3$  layers on absorbers A and B. The spectra are normalized to the  $\text{In}4d$  peak at 17.3 eV.

cationic vacancies in the spinel-type  $\text{In}_2\text{S}_3$  are the driving force for the interdiffusion. This driving force increases with increasing heat energy.

The valence band edge of  $\text{In}_2\text{S}_3$  sprayed at different substrate temperatures on the absorbers A and B is shown in figure 4.6b. The  $\text{In}4d$  level was used as energy reference. It was found that the  $\text{In}4d$  orbitals do not participate in chemical bonding and therefore no chemical shift of the binding energy is expected in the investigated compounds [107–109]. For the  $\text{In}4d$  level 17.3 eV was used as reference value [107]. The valence band edge of the investigated  $\text{In}_2\text{S}_3$  layers shifts upwards with increasing substrate deposition temperature. Also the shape of the valence band changes with increasing deposition temperature. Such change of the shape was identified by Guillot-Deudon et al. as the contribution from  $\text{Cu}d$  orbitals [104]. This confirms that rather the effect of Cu incorporation than Na incorporation dominates the changes of the electronic properties in the  $\text{In}_2\text{S}_3$  layers on the  $\text{Cu}(\text{In},\text{Ga})\text{Se}_2$  absorbers.

Figure 4.7a shows the Cu concentration as calculated for the Cu-In-S system. Also shown in figure 4.7a are the Cu concentration regions for different phases in the Cu-In-S system as taken from the tentative phase diagram shown in figure 4.7b [110]. From the phase diagram of the quasibinary system it can be assumed that already for low Cu concentrations the  $\text{In}_2\text{S}_3$  and  $\text{CuIn}_5\text{S}_8$  phases coexist. However, it was found by Abou-Ras that the phase transformation from  $\text{In}_2\text{S}_3$  to  $\text{CuIn}_5\text{S}_8$  not only requires the appropriate Cu concentration but also an activation temperature of approximately 250 °C [53]. He observed a similar temperature dependency of the Cu diffusion across the buffer-absorber interface with  $\text{In}_2\text{S}_3$  grown by atomic layer deposition (ALD) [53]. Abou-Ras et al. also found an orientation relationship between the {112} plane in  $\text{Cu}(\text{In},\text{Ga})\text{Se}_2$  and the {103} plane in  $\text{In}_2\text{S}_3$  for a sample with ALD- $\text{In}_2\text{S}_3$  deposited at 210 °C [111]. This relationship was not there if the  $\text{In}_2\text{S}_3$  buffer layer was deposited at 240 °C instead the formation of an

interface layer was observed. The author identified the interface layer as  $\text{CuIn}_5\text{S}_8$  using high resolution TEM (HR-TEM) [53]. Abou-Ras et al. also investigated the crystalline structure at the interface of  $\text{Cu}(\text{In,Ga})\text{Se}_2$  with  $\text{In}_2\text{S}_3$  deposited by sputtering [112] and thermal compound-evaporation [113]. For all analyzed interfaces he found the formation of the  $\text{CuIn}_5\text{S}_8$  phase at deposition temperatures around or above  $250^\circ\text{C}$  and concluded that the phase transformation only occurs if both, enough Cu and heat energy are available [53].

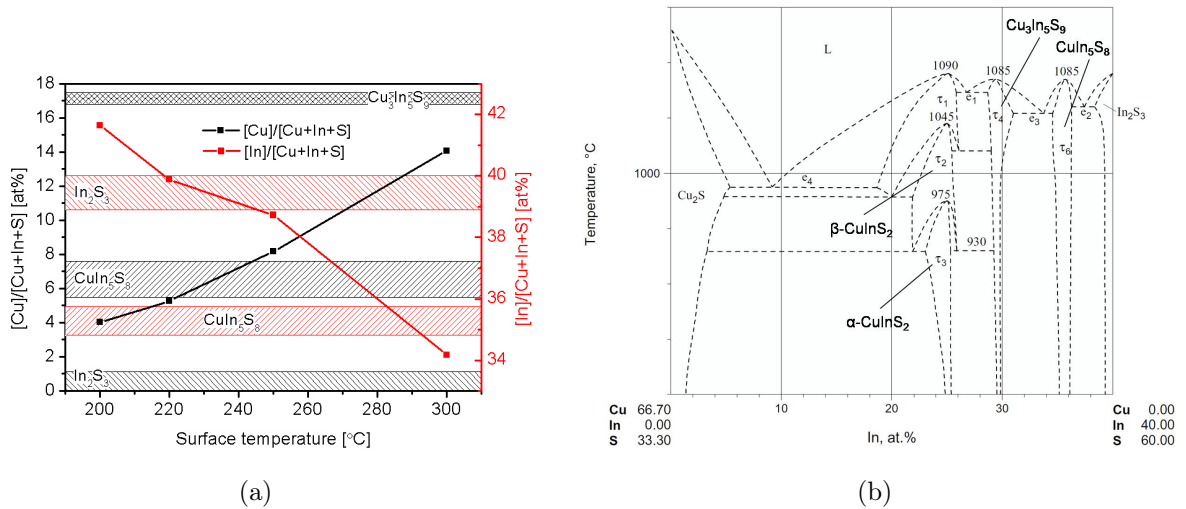


**Figure 4.7:** (a) Copper and indium content in the  $\text{In}_2\text{S}_3$  layers deposited on CIGS absorbers at different substrate temperatures. Also shown are the compositional regions of single phase existence for  $\text{In}_2\text{S}_3$ ,  $\text{CuIn}_5\text{S}_8$  and  $\text{Cu}_3\text{In}_5\text{S}_9$  the tentative phase diagram of the  $\text{Cu}_2\text{S}$ - $\text{In}_2\text{S}_3$  quasibinary system (b). The diagram is taken from ref [110].

Barreau et al. investigated copper containing  $\text{In}_2\text{S}_3$  layers deposited by sequential co-evaporation of indium-sulfur and copper-sulfur with varying copper concentrations at a substrate temperature of  $200^\circ\text{C}$ . They reported that the system consists of single phase  $\text{In}_2\text{S}_3$  if  $\alpha \leq 4$  in  $(\text{In}_{16})_{\text{Oh}}(\text{In}_{(16-\alpha)/3}\text{Cu}_{\alpha}\square_{(8-2\alpha)/3})_{\text{Td}}\text{S}_{32}$ , i.e. the copper content lies between the  $\text{In}_2\text{S}_3$  and  $\text{CuIn}_5\text{S}_8$  in the phase diagram (fig 4.7) [88]. This agrees with the findings of Abou-Ras [53]. From XRD measurements Barreau et al. concluded that the Cu is homogeneously distributed in the whole film and the presence of Cu yields reduced lattice parameters and observed the formation of a secondary phase which was identified as  $\text{CuInS}_2$  if the Cu concentration exceeds the stoichiometry of  $\text{CuIn}_5\text{S}_8$ .

Following these argumentations it is assumed that the  $\text{In}_2\text{S}_3$  deposited at  $200^\circ\text{C}$  and  $220^\circ\text{C}$  onto the  $\text{Cu}(\text{In,Ga})\text{Se}_2$  is tetragonal  $\text{In}_2\text{S}_3$  single phase with Cu impurities on the cationic vacancies and partially substituting In on tetrahedral sites in the spinel-type structure. For  $\text{In}_2\text{S}_3$  deposited at substrate temperatures of  $250^\circ\text{C}$  and above it is assumed that the  $\text{In}_2\text{S}_3$  and  $\text{CuIn}_5\text{S}_8$  phases coexist.

## 4.3 Photovoltaic properties with CIGS absorbers

### 4.3.1 Effect of oxygen at the CIGS surface

With ultrasonic spray pyrolysis a deposition temperature of about 200 °C is necessary to grow In<sub>2</sub>S<sub>3</sub> films as buffer layers in Cu(In,Ga)Se<sub>2</sub> thin film solar cells. For the deposition of the In<sub>2</sub>S<sub>3</sub> layer the Cu(In,Ga)Se<sub>2</sub> absorber is heated to 200 °C in nitrogen ambient, however, still containing a considerable amount of oxygen. As described in section 4.2 the energetically favored surface of Cu(In,Ga)Se<sub>2</sub> is the metal terminated, completely Cu depleted {112} plane with positive charges due to selenium vacancies ( $V_{Se}$ ). At the grain boundaries it is necessary to passivate these charges in order to reduce grain boundary recombinations [114]. Oxygenation assisted by Na is reported to be the major passivation mechanism at the Cu(In,Ga)Se<sub>2</sub> grain boundaries [115]. At the Cu(In,Ga)Se<sub>2</sub> surface, however, the passivation of the positive charges is not desired since it would reduce the type inversion of the surface [42]. In Cu(In,Ga)Se<sub>2</sub> devices with CBD-CdS buffer layer it is believed that the CBD treatment restores the positive surface charges of the absorber which were passivated due to oxygenation after air exposure [115]. It is also believed that the wet CBD treatment does not penetrate deep into the absorber layer and therefore leaves the positive charges at the grain boundaries passivated.

In order to investigate the effect of heating to 200 °C in nitrogen ambient with a considerable amount of oxygen on the interface properties, the heating cycle of a spray procedure was simulated with a standard Cu(In,Ga)Se<sub>2</sub> absorber prior to CBD-CdS deposition. The temperature of the bare absorber was ramped up to 200 °C in 25 min. After the temperature was stabilized at 200 °C the heating power was switched off and the sample remained on the heating plate until it reached room temperature again. Subsequently, the device was finished with standard CBD-CdS, ZnO bilayer and Ni/Al grid. The photovoltaic (PV) parameters are listed in table 4.2 and compared to a standard reference sample with absorber from the same CIGS deposition run. The annealing treatment is detrimental for all PV parameters. The average  $V_{OC}$  decreases by 80 mV and the average FF by 15% absolut.

**Table 4.2:** Average and best cell PV parameters solar cells with CdS buffer layer on CIGS absorbers. The effect of absorber heating and spraying of a water-thiourea-ammonia solution during heating was tested.

Sample		$\eta$ [%]	$V_{OC}$ [mV]	$J_{SC}$ [mA/cm <sup>2</sup> ]	FF [%]	$R_p$ [ $\Omega$ cm <sup>2</sup> ]
not annealed	average	11.6 ± 0.7	615 ± 16	27.9 ± 0.4	66 ± 3	1339 ± 136
	best cell	12.6	642	28.8	68	1264
annealed w/o spray	average	8.2 ± 0.7	536 ± 38	26.8 ± 0.4	51 ± 3	745 ± 73
	best cell	9.1	618	26.5	56	651
annealed w. spray	average	11.3 ± 0.6	612 ± 28	27.3 ± 1.1	66 ± 4	1612 ± 511
	best cell	12.1	645	26.2	72	2328

Kronik et al. proposed the following model for the mechanism of restoring the positive surface charges during CBD [115]: Oxygen partially fills selenium vacancies during air exposure of the absorber. Each oxygen atom which occupies a  $V_{Se}$  converts a double donor into an acceptor. For a complete compensation of the positive surface charges not all  $V_{Se}$  must be occupied by oxygen. During the chemical bath deposition the oxygen atoms are replaced by sulfur atoms or dissolved by ammonia. They further assumed that the  $S_{Se}$  defects are electrically neutral, since the electronegativities of S and Se are much closer than O and Se. Based on that Kronik et al. concluded that for every surface oxygen atom which is replaced by sulfur, the interface will acquire a net positive charge due to the remaining selenium vacancies.

With this mechanism the described observations can be explained. During the annealing the oxygenation of the  $Cu(In,Ga)Se_2$  surface is amplified, i.e., more selenium vacancies are filled with oxygen. The conditions of the CBD treatment, however, remain the same. Compared to the un-treated sample more  $O_{Se}$  remain on the surface and the positive charge density at the buffer-absorber interface is reduced. The conduction band at the interface is shifted away from the Fermi level resulting in a reduced recombination barrier for holes at the interface. This increased recombination can explain the reduced  $V_{OC}$ .

In another experiment an aqueous solution with 0.02 mol/l thiourea and 1.42 mol/l ammonia was sprayed during the complete annealing. The annealing procedure and device finishing was exactly the same as described above and also the absorber was from the same CIGS deposition run. In table 4.2 the PV parameters are displayed. All parameters are comparable to the reference sample. Enhanced surface oxygenation is prevented due to the availability of sulfur atoms during the treatment. Following the mechanism postulated by Kronik et al. [115], the presence of sulfur can have two effects: (i) sulfur fills selenium vacancies and with this prevents oxygen from occupying additional  $V_{Se}$ ; (ii) sulfur replaces already during the annealing treatment  $O_{Se}$  and with this increases the net positive surface charge.

Based on these findings, either a solution containing thiourea was sprayed during the heating phase or the absorbers were not preheated but directly put onto the heated hot plate with the precursor spray already running.

### 4.3.2 Impact of absorber copper excess

The efficiencies of CIGS solar cells with  $In_2S_3$  buffer layers deposited by ultrasonic spray pyrolysis are still far from those obtained with CdS buffer layer. It is therefore important to understand the limitations of the CIGS- $In_2S_3$  system in a photovoltaic device. This section gives insights into the dependence of the PV performance on the Cu excess of such solar cells.

Absorbers with a modified 2<sup>nd</sup> stage were investigated where the time of the 2<sup>nd</sup> stage after

reaching the stoichiometric point was varied. The percentage value of the Cu excess represents the time how long the second stage was retarded beyond the stoichiometric point of the  $\text{CuIn}_{1-x}\text{Ga}_x\text{Se}_2$  phase and thus determines the amount of  $\text{Cu}_x\text{Se}$  phases present at the end of the 2<sup>nd</sup> stage. The stoichiometric point was identified with the end point detection method. The time of the 3<sup>rd</sup> stage was then adapted to reach a Cu poor final composition of  $[\text{Cu}]/[\text{III}]=0.85$ . For this work the Cu excess was varied between minimum Cu excess and 25%, whereas minimum of Cu excess means that the 3<sup>rd</sup> stage was started immediately after the stoichiometric point was detected. The process is described in more details in [8, 116]. The ratio  $x=[\text{Ga}]/[\text{III}]$  of the absorber was varied by changing the evaporation rates of In and Ga in the 3<sup>rd</sup> stage.

Before buffer layer deposition, the surface of the absorber was rinsed with double deionized high-purity water and etched in an aqueous solution of  $\text{NH}_4\text{OH}$  (1mol/l) for 2 min at room temperature in order to remove excess sodium compounds and oxides on the absorber surface and obtain similar initial conditions for the buffer layer deposition.

The energy band gap values of the  $\text{CuIn}_{1-x}\text{Ga}_x\text{Se}_2$  absorbers as measured with external quantum efficiency are correlated in figure 4.8 with the bulk ratio of  $x=[\text{Ga}]/[\text{III}]$  determined by EDX. The different symbols in the plot represent a variation of Cu excess in the second deposition stage.

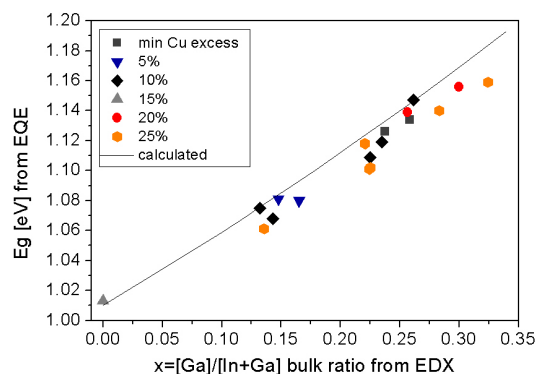


**Figure 4.8:** Energy band gap value  $E_g^{EQE}$  of  $\text{CuIn}_{1-x}\text{Ga}_x\text{Se}_2$  absorbers as determined from EQE versus average bulk composition measured with EDX.

Our standard absorbers for solar cells with CdS buffer layer deposited by chemical bath deposition (CBD) are grown with 25% Cu excess and Ga content of  $x=0.3$ . Secondary ion mass spectroscopy (SIMS) depth profiles of such absorbers reveal a double grading of the energy band gap due to a Ga dip approximately 500 nm below the surface [116]. The band gap value measured by EQE correlates with the absorption coefficient of the absorber and therefore (if the Ga dip is not buried too deep in the absorber) with the minimum band gap of the grading in the absorber (see also [117]). The information depth of the composition measurement with EDX at an acceleration voltage of 20 kV is in the order of the absorber thickness and therefore yields a value close to the average over the

depth profile.

The solid line in figure 4.8 shows the energy band gap dependence of the absorber on the x ratio as calculated with:

$$E_g^{CuIn_{1-x}Ga_xSe_2} = E_g^{CuInSe_2}(1-x) + E_g^{CuGaSe_2}x - bx(1-x) \quad (4.1)$$

where b is the bowing coefficient which describes the deviation from the linear behavior [118, 119]. Here, the bowing coefficient was assumed to be 0.20 eV, the energy band gap of CIS as 1.01 eV and of CGS as 1.68 eV.

The measured energy band gap values from EQE of the  $CuIn_{1-x}Ga_xSe_2$  absorbers are consistent with the values determined with the calculation above inserting averaged x ratios (solid line in fig. 4.8 assuming b to be 0.20 eV). In the following the energy band gap value  $E_g^{EQE}$  will be used as reference value.

Plotting the solar cell conversion efficiency versus  $E_g^{EQE}$  reveals a strong dependence of the solar cell performance on the x ratio of the absorber as well as on the amount of Cu excess during the deposition process (fig. 4.9). Taking only the values of samples with minimum Cu excess up to 10% into account, an efficiency peak of about 13% is observed at 1.12 eV ( $x=0.24$ ). For samples with higher Cu excess lower efficiencies were obtained with an optimum value at 1.12 eV.

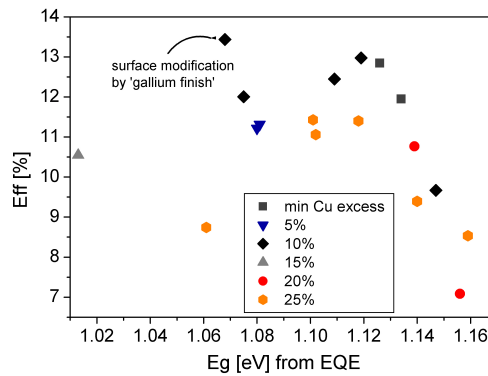


**Figure 4.9:** Solar cell conversion efficiency versus energy band gap determined by EQE. The different symbols represent samples with different Cu excess during the 2<sup>nd</sup> stage.

In the investigated range of the ratio x no significant deviation from the expected dependence of the  $J_{SC}$  and the  $V_{OC}$  (fig. 4.10a) on the band gap of the absorber is observed.

An exception is the sample with 10% Cu excess and a measured  $E_g^{EQE}$  of 1.07 eV. The surface of that absorber was modified by depositing a few Å of Ga in absence of In flux at



the end of the growth process. With this modification the  $V_{OC}$  was significantly increased and a device efficiency of 13.4% was obtained.

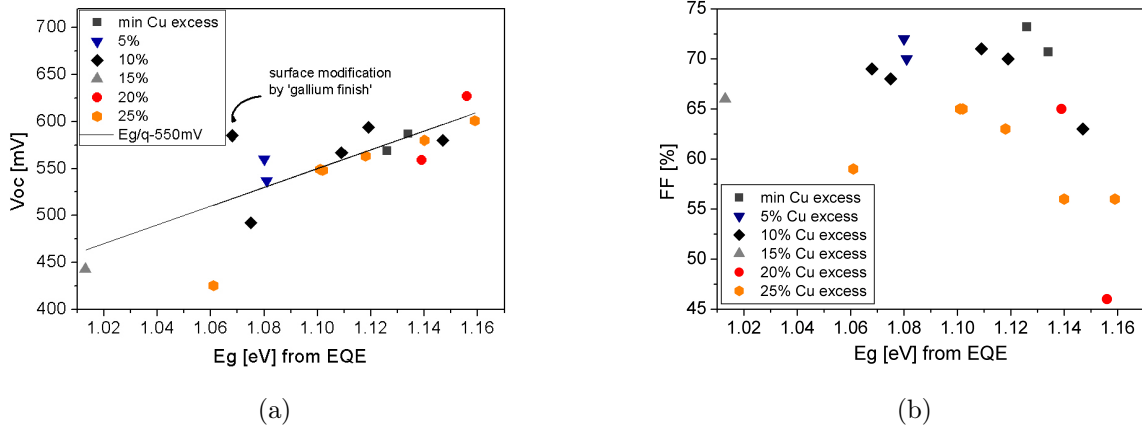


**Figure 4.10:** (a) Open circuit voltage versus the absorber's band gap. (b) Fill factor of CIGS solar cells with  $In_2S_3$  buffer layer in dependence of the band gap determined by EQE in the absorber.

The fill factors (FF) of the  $CuIn_{1-x}Ga_xSe_2$  solar cells with different  $x$  ratios are shown in figure 4.10b. It is clearly visible that the dependence of the efficiency on the Ga concentration originates from the FF behavior. A similar behavior of the fill factor and the efficiency of  $CuIn_{1-x}Ga_xSe_2$  solar cells with different Ga content and co-evaporated  $In_2S_3$  buffer layer was observed by Jacob et al. [120]. They found a FF and efficiency maximum at an  $x$  ratio of 0.24.

Temperature dependent  $J_{SC}V_{OC}$  measurements of devices grown with 10% Cu excess were performed (black diamonds in the figures) in order to analyze the dominant recombination mechanism in  $CuIn_{1-x}Ga_xSe_2$  solar cells with sprayed  $In_2S_3$  buffer layer. The activation energy  $E_a$  was determined from the slope in a modified Arrhenius plot by plotting  $A \cdot \ln(J_0)$  against the inverse temperature  $1/T$  [57].

In table 4.3 the calculated activation energies  $E_a$  of solar cells grown with 10% Cu excess are compared to the energy band gap values  $E_g^{EQE}$  of the absorber. The energy difference  $\Delta E = E_a - E_g^{EQE}$  increases with increasing  $x$  ratio.

The ideality factor at room temperature is also given in table 4.3 and the temperature dependence is shown in figure 4.11. For the samples with  $E_g^{EQE}$  of 1.11 eV and 1.12 eV a large negative  $\Delta E$  and a strong temperature dependence of  $A$  are observed.

In the single diode model three main recombination mechanisms are possible [57]: (i) if recombination in the quasi neutral region (QNR) is dominant, then the ideality factor is

**Table 4.3:** Gallium concentration as measure with EDX and energy band gap value measured with EQE of solar cells grown with 10% Cu excess are compared to the activation energy determined from the modified Arrhenius plot. The ideality factor at 300 K is also given. The absorber surface of the sample marked with \* was modified with a Ga finish. The values of the samples with dominant recombination in the interface region are in italics and the corresponding corrected barrier height for the holes at the interface  $\phi_p^f$  is in bold.

[Ga]/[III]	$E_g^{EQE}$ [eV]	$E_a \pm 0.03$ [eV]	$\Delta E$ [meV]	A at 300K
0.14*	1.07	1.05	-20	1.9
0.13	1.08	1.01	-70	1.9
<i>0.23</i>	<i>1.11</i>	<b>0.96</b>	-150	1.9
<i>0.24</i>	<i>1.12</i>	<b>0.96</b>	-160	1.5
	$E_g^{min}$	$E_g^{minSCR}$		
		OR $\phi_p^f$		

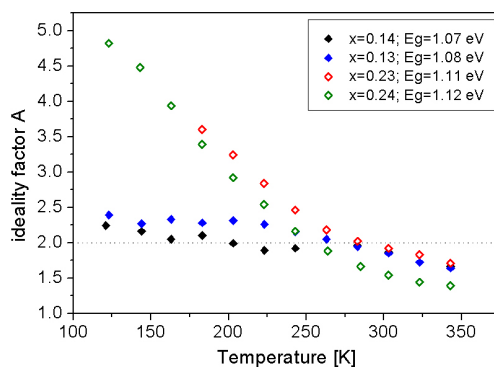


**Figure 4.11:** Temperature dependence of the ideality factor.

close to unity and the activation energy is equal the absorber's band gap; (ii) if recombination in the space charge region (SCR) is dominant, then the activation energy is also close to the absorbers band gap and the ideality factor is equal to 2, however, in CIGS solar cells an A value around 1.5 is generally observed with a temperature dependence due to trap states in the SCR and tunneling of electrons and holes [58]; (iii) dominant recombination at the interface is distinguished by an activation energy equal to the interface barrier height for holes and an ideality factor between 1 and 2, which increases above 2 if recombination is enhanced due to tunneling of holes in the conduction band. The recombination theory is described in more detail in section 2.2.1.1.

For the sample with  $x=0.14$  and  $x=0.13$  the activation energy is very close to the band gap measured with EQE. Therefore one would expect the dominant recombination in the SCR. The measured activation energy of the samples with  $x=0.23$  and  $x=0.24$  is the corrected barrier height for holes at the absorber-buffer interface. For those samples interface recombination is the dominant mechanism most likely due to the formation of a cliff in the conduction band alignment at the interface. The recombination mechanism is enhanced for the samples with  $x=0.23$  ( $E_g^{EQE}=1.11$  eV) and  $x=0.24$  ( $E_g^{EQE}=1.12$  eV) by tunneling of holes in the valence band into the interface, indicated by the strong temperature dependence of the ideality factor (fig. 4.11).

The degree of Cu excess in the 2<sup>nd</sup> stage has a direct influence on the device performance of solar cells with USP-In<sub>2</sub>S<sub>3</sub> buffer layers. These devices show a better performance if the Cu excess is reduced towards a minimum. The effect is predominantly visible in the fill factor of the solar cells. Therefore, minimum copper excess was identified as standard parameter for further investigations.

### 4.3.3 Impact of absorber surface modifications

In this section the influence of the CIGS surface modifications in terms of [Ga]/[III] and [Cu]/[III] ratio at the surface and the selenium finishing of the absorber on the device performance and the diode quality are discussed. Results are partially gathered during the diploma thesis of Carolin Fella [121].

Table 4.4 gives an overview of the samples used in this investigation. The absorbers were grown with minimum Cu excess in the 2<sup>nd</sup> stage on molybdenum coated soda lime glass as described in section 1.2. Also shown in table 4.4 are the [Ga]/[III] and [Cu]/[III] ratios as determined from X-ray fluorescence (XRF) measurements.

Sample a is the standard reference sample with reduced gallium content. With sample b and c the influence of selenium finish is investigated by modifying the availability of selenium during the cooling phase of the absorber after deposition. In case of sample b, the selenium source was closed and switched off at 250 °C substrate temperature while the Se source was already switched off at 580 °C for sample c. For samples d-i the selenium was

**Table 4.4:** Overview of the samples with different surface modifications of the absorber.

Sample	Surface modification	remark	[Ga]/[III]	[Cu]/[III]
a	no	reference	0.24	0.9
b	Se off at 250 °C		0.25	0.88
c	Se off at 580 °C		0.25	0.87
d	Ga ramp		0.23	0.87
e	no	half Ga flux in 3 <sup>rd</sup>	0.22	0.86
f	Ga finish	half Ga flux in 3 <sup>rd</sup>	0.21	0.84
g	In finish	half Ga flux in 3 <sup>rd</sup>	0.23	0.86
h	Cu-poor	half Ga flux in 3 <sup>rd</sup>	0.23	0.8
i	Cu-rich	half Ga flux in 3 <sup>rd</sup>	0.25	0.93

switched off at 250 °C substrate temperature. For sample d the gallium flux was ramped down in the 3<sup>rd</sup> stage while keeping the indium flux constant.

Half but constant gallium flux in the 3<sup>rd</sup> stage was used for samples e-i. No additional surface treatment was applied to sample e. For sample f, the indium source was closed before the gallium source and vice versa for sample g. The influence of the copper content was investigated with sample h and i. Sample h was prepared with Cu-poor absorber finish and sample i with Cu-rich finish. The expression Cu-rich is used in this work for  $[\text{Cu}]/[\text{III}] \geq 0.9$ .

In<sub>2</sub>S<sub>3</sub> was deposited on the absorber at 200 °C surface temperature using 0.02 mol/l InCl<sub>3</sub> and an In/S ratio of 2:3 dissolved in acetone. The absorbers were put directly into the solution saturated ambient below the funnel on the preheated hot-plate. The deposition was terminated after 15 minutes. A CBD-CdS reference sample was also prepared for all modifications except for sample b and c where the absorber delaminated during the CBD process.

Figure 4.12 illustrates the open circuit voltage and the fill factor of the samples a-i with USP-In<sub>2</sub>S<sub>3</sub> buffer layer. Except for samples a, g and i, the V<sub>OC</sub> follows the expected increase with the gallium content indicated by the dashed line. The band gap which is the basis of the dashed line is calculated from the average gallium content using equation 4.1. The band gap is divided by the elemental charge and shifted down by 620 mV in order to meet the scale. The samples which deviate from the expected increase of the V<sub>OC</sub> are the reference sample a, the sample g with indium finish, and the Cu-rich sample i. Even though the V<sub>OC</sub> of the other sample follow the expected increase with increasing gallium content, the values are about 100 mV below the CBD-CdS reference devices.

The fill factor of the reference sample a is with 62.4% the lowest in this investigation (see fig. 4.12b). An increased amount of selenium available during the cooling phase of the absorber b has a positive effect on the FF of the device (compare sample b and c). Also

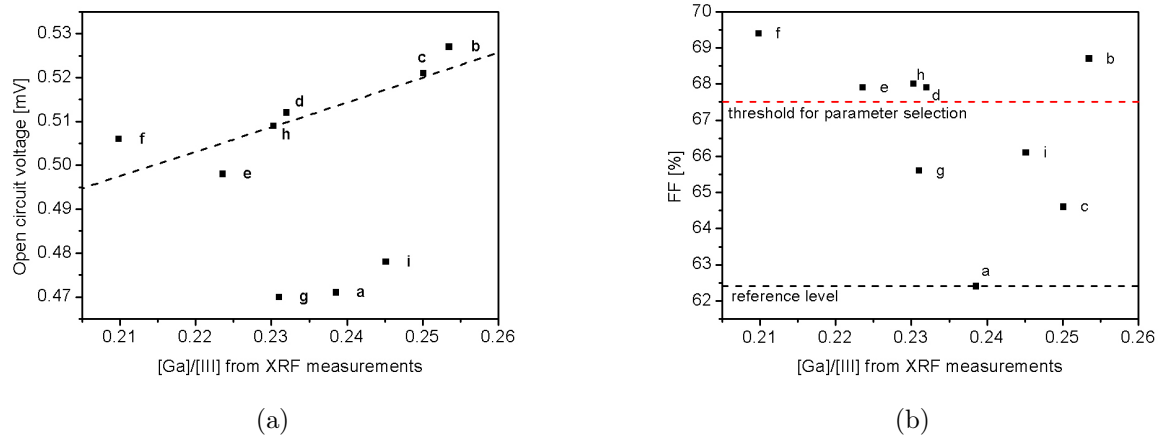


**Figure 4.12:** Open circuit voltage (a) and fill factor (b) for the nine investigated samples with USP- $\text{In}_2\text{S}_3$  buffer layer plotted against the gallium content of the absorber.

the modification of the gallium flux in the 3<sup>rd</sup> stage of sample d and e has a positive effect on the FF (compare sample d and e with a). An additional In finish in sample g decreases the FF whereas an additional Ga finish in sample f further increases the FF (compare sample f and g with e). Preparation of the absorber in Cu-rich conditions as in sample i has a detrimental effect on the FF whereas a Cu-poor condition as in sample h does not affect the FF (compare sample h and i with e). It has to be noted here that the effect of surface modification is overlapped by the effect of gallium content in some cases. The effect of the gallium content will be described and discussed in section 4.3.4.

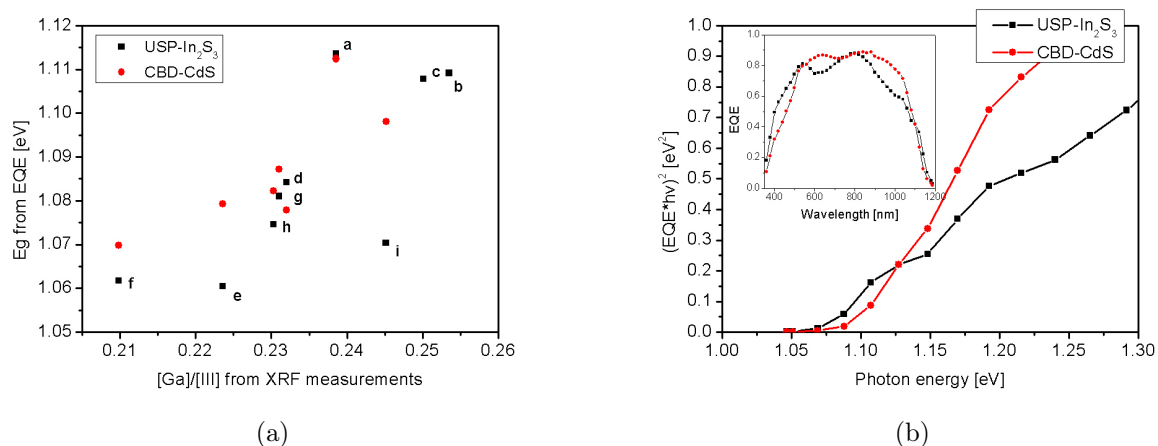


**Figure 4.13:** (a) Energy band gap derived from EQE of CIGS devices with different surface modifications of the absorber. (b) Determination of the minimum energy band gap of Cu-rich CIGS solar cells with USP- $\text{In}_2\text{S}_3$  and CBD-CdS buffer layer. The inset of (b) shows the external quantum efficiency of those two devices.

In figure 4.13a the minimum band gap of the absorbers derived from external quantum efficiency measurements is plotted against the gallium content measured with x-ray fluorescence spectroscopy (XRF). The composition measured with XRF is an averaged composition over the whole absorber thickness. Except for the sample d with the Ga ramp in the 3<sup>rd</sup> stage, the minimum band gap of the absorber with In<sub>2</sub>S<sub>3</sub> buffer is always below the value of the reference with CdS buffer layer. The correlation shows that the samples e and i with In<sub>2</sub>S<sub>3</sub> buffer layer and the sample a for both buffer layers depart from the general trend. For samples e and i the difference of the minimum band gap of the device with In<sub>2</sub>S<sub>3</sub> and CdS buffer layer is 0.02 and 0.03 eV, respectively. The difference in the minimum band gap for the Cu-rich sample i is also shown in figure 4.13b. There  $(EQE \cdot h\nu)^2$  is plotted against the photon energy. The extrapolation of the two curves in the figure close to the absorption edge result in the above mentioned difference. This difference is also visible in the EQE plot in the inset of figure 4.13b.

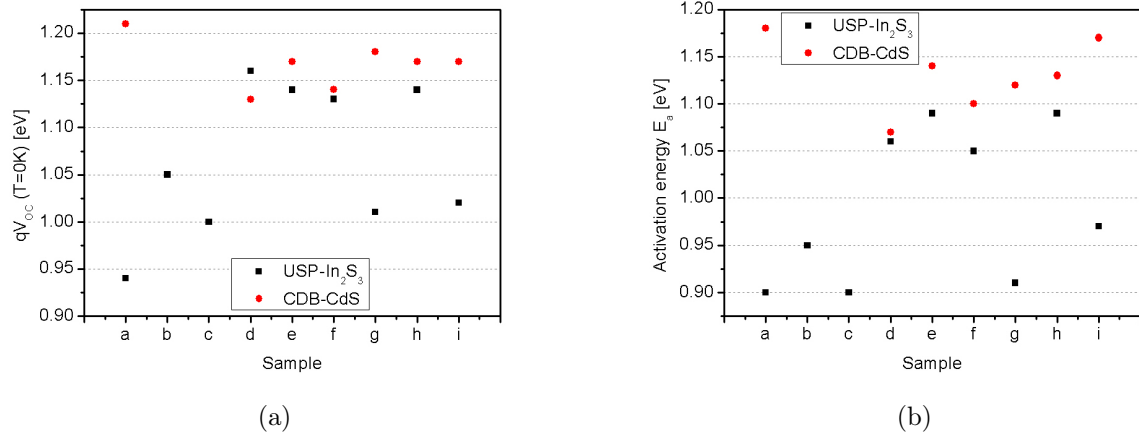


**Figure 4.14:** (a)  $V_{OC}$  extrapolated to  $T=0$  K and (b) activation energy  $E_a$  for samples with different surface modifications of the absorber.

The difference in the open circuit voltage of the solar cells with USP-In<sub>2</sub>S<sub>3</sub> and the reference CBD-CdS buffer layer indicates different recombination losses. In order to investigate the dominant recombination mechanism the temperature dependency of the  $V_{OC}$  was measured and evaluated according to equation 2.14-2.16. The extrapolation of  $qV_{OC}$  to  $T=0$  K is shown in figure 4.14a.

Since the ideality factor of the samples with USP-In<sub>2</sub>S<sub>3</sub> buffer layer is not constant with temperature (see fig. 4.15), the activation energy of the recombination current was also derived from equation 2.25. The derived values are presented in figure 4.14b.

Large differences of the  $qV_{OC}(T \rightarrow 0 K)$  and  $E_a$  values are observed for the samples a, g and i between the solar cells with USP-In<sub>2</sub>S<sub>3</sub> and the reference CBD-CdS buffer layer. These are the same samples where the  $V_{OC}$  deviates from the general trend in figure 4.12a. In these cases the activation energy of the recombination current in the cells with USP-In<sub>2</sub>S<sub>3</sub>

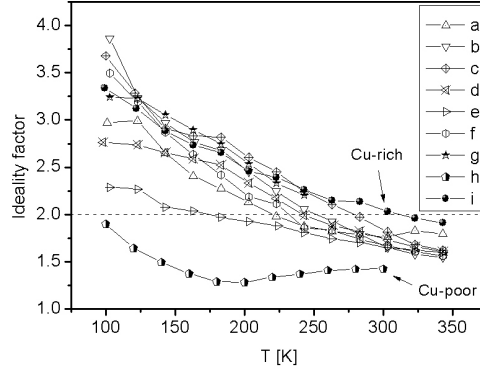


**Figure 4.15:** Ideality factor of the samples a-i with USP-In<sub>2</sub>S<sub>3</sub> buffer layer as a function of the temperature.

buffer layer equals the corrected barrier height for holes at the interface (see equ. 2.17, fig. 2.4 and tab. 4.5) and interface recombination is the dominant loss for the  $V_{OC}$ . The same applies to sample b and c where the measured activation energy has a similar value. For all samples with dominant interface recombination, the barrier height for holes at the interface at zero bias  $\phi_p^0$  is close to 0.5 eV (cf. equ. 2.17), which indicates an only weakly inverted surface of the absorber.

**Table 4.5:** Overview of the of the absorber's band gap, the activation energy and the diode ideality factor of the samples with different surface modifications of the absorber. The values of the samples with dominant recombination in the interface region are in italics and the corresponding corrected barrier height for the holes at the interface  $\phi_p^f$  is in bold.

Sample	$E_g^{XRF}$ [eV]	$E_g^{EQE}$ [eV]	$qV_{OC}(0K)$ [eV]	$E_a^{J_{sc}V_{oc}}$ [eV]	$E_a^{dark}$ [eV]	$A$	$E_a^{J_{sc}V_{oc}}$ CdS [eV]
a	<i>1.13</i>	<i>1.11</i>	<i>0.94</i>	<b>0.90</b>	<i>0.93</i>	<i>1.76</i>	1.18
b	<i>1.14</i>	<i>1.11</i>	<i>1.05</i>	<b>0.95</b>	<i>1.02</i>	<i>1.65</i>	
c	<i>1.14</i>	<i>1.11</i>	<i>1.00</i>	<b>0.90</b>	<i>0.97</i>	<i>1.81</i>	
d	1.13	1.08	1.16	1.06	1.10	1.73	1.07
e	1.13	1.06	1.14	1.09	1.13	1.65	1.14
f	1.12	1.06	1.13	1.05	1.13	1.67	1.10
g	<i>1.13</i>	<i>1.08</i>	<i>1.01</i>	<b>0.91</b>	<i>1.00</i>	–	1.12
h	1.13	1.07	1.14	1.09	1.19	1.42	1.13
i	<i>1.14</i>	<i>1.07</i>	<i>1.02</i>	<b>0.97</b>	<i>1.15</i>	<i>2.03</i>	1.17
	$E_g^{average}$	$E_g^{min}$		$E_g^{minSCR}$ or $\phi_p^f$			$E_g^{minSCR}$

For the samples d, e, f, and h the difference in the activation energy between the cells with USP-In<sub>2</sub>S<sub>3</sub> and the CBD-CdS reference is considerably smaller. The calculated ac-

tivation energy is close to the minimum band gap of the absorber as derived from EQE measurements. Thus, the losses of the device voltage are dominated by charge carrier recombination in the SCR. Furthermore, the smaller activation energy as compared to the CdS reference cells indicate a broadening of the SCR. The SCR of the cells with USP-In<sub>2</sub>S<sub>3</sub> buffer layer increases such that the band gap minimum of the absorber lies within the SCR.

With this the deviation from the general trend of the  $V_{OC}$  of sample a, g and i can be explained by amplified interface recombination. However, this does not explain the overall difference of about 100 mV in the  $V_{OC}$  to the CdS reference cells of the samples with dominant recombination in the SCR. Equation 2.15, which is valid for SCR dominated recombination, shows that the main parameter influencing the  $V_{OC}$  in this regime are the diffusion constant  $D_e$  and length  $L_e$  of the minority carriers, the band bending  $V_{bm}$  and the shallow acceptor density  $N_a$ .

The samples a, d, h and i were selected in order to investigate the apparent shallow doping concentration of CIGS absorbers with USP-In<sub>2</sub>S<sub>3</sub> buffer layer. Figure 4.16 shows the doping density in the CIGS absorber as derived from capacitance voltage measurements. The figure shows the lower envelope of apparent doping densities measured at temperatures between 100 and 360 K. For all samples the doping concentration of  $1\text{-}3 \cdot 10^{15} \text{ cm}^{-3}$  is rather low. As described in section 2.2.1.1 a change in the doping concentration  $N_a$  by one order of magnitude results in change of 60 mV in the  $V_{OC}$ . Therefore, the overall lower doping concentration in the devices with USP-In<sub>2</sub>S<sub>3</sub> buffer layer could result in reduced open circuit voltage. This will be discussed in more detail in following subsection.

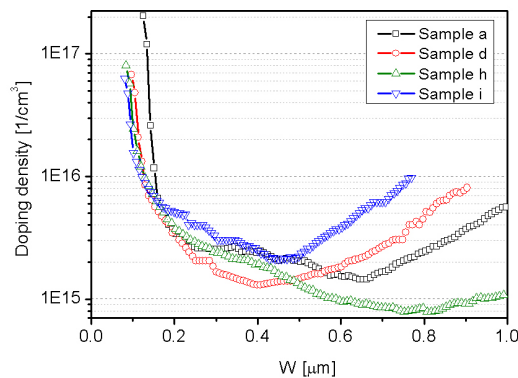


**Figure 4.16:** Doping density of the samples a, d, h and i with USP-In<sub>2</sub>S<sub>3</sub> buffer layer. Plotted is the lower envelope of measured apparent doping densities at temperatures between 100 and 360 K. The measurements were performed at 300 kHz.

The main processing difference between USP and CBD is the heating of the absorber to 200 °C during the USP deposition. Even though the ambient is saturated with nitrogen carrier gas and the vapor from the solution droplets, there still is a considerable amount of oxygen available. Following the description in section 4.3.1 this means that oxygen



partially fills the selenium vacancies on the surface of the absorber. This has two main effects: (i) Reduced number of positive charges at the surface. This explains the only weakly inverted surface of the absorber as mentioned above. (ii) The oxygenation enhances the copper diffusion away from the surface. This mechanism was described by Rau et al. [42]. They proposed that the In-O bond is highly polarized due to the large difference in the electronegativity of the two elements. This increases the positive charge of the In atom and therefore also the ionic nature of the In-Se bond resulting in a more negatively charged Se atom. The increased negative charge of the Se atom weakens the next Cu-Se covalent bond, increasing the probability that the Cu ion is released. The main dopant for  $N_a$  in the CIGS semiconductor are copper vacancies  $V_{Cu}$  [122]. The released copper ions from the surface region diffuse into the bulk of the absorber where they either eliminate the  $V_{Cu}$  or directly compensate the acceptor density. The diffusion of only a fraction of one monolayer of Cu atoms is sufficient to reduce the effective acceptor density by one order of magnitude [42].

The results show, that the amount of copper in the absorber has a strong impact on the recombination mechanism (sample h compared to i). Also a reduction of the band gap towards the surface of the absorber is important in order to minimize the interface recombination in CIGS solar cells with USP-In<sub>2</sub>S<sub>3</sub> buffer layer (sample a-c compared to d-i). The influence of the gallium content on the device performance and diode quality is investigated in more detail in the next section.

#### 4.3.4 Performance versus gallium content and air annealing effects

The PV performance of CuIn<sub>1-x</sub>Ga<sub>x</sub>Se<sub>2</sub> solar cells with USP-In<sub>2</sub>S<sub>3</sub> buffer layers as a function of the gallium content in the absorber layer is presented and compared to CBD-CdS reference devices on the same absorber. Results of this section are partially gathered during the diploma thesis of Carolin Fella [121].

Based on the findings described in the previous sections the following parameters for the absorber layer deposition were chosen: modified 3-stage process with min Cu excess in the 2<sup>nd</sup> stage. Substrate temperature for all samples was close to 600 °C. No indium or gallium finish was applied, i.e., both sources were closed simultaneously. Selenium was switched off at 280 °C substrate temperature during cool down. The gallium content was varied by changing the gallium flux in the 1<sup>st</sup> stage. The gallium flux in the 3<sup>rd</sup> stage was always adjusted to half of the flux in the 1<sup>st</sup> stage. In table 4.6 the [Ga]/[III] and [Cu]/[III] values as measured with XRF of the eight investigated samples are summarized.

The [Ga]/[III] ratio varies from 0.33 to 0.12 for the samples 1-8. For all samples the [Cu]/[III] ratio was kept constant around 0.80, fulfilling the Cu-poor requirement. Since XRF was used for concentration measurement, the ratios given in table 4.6 are average values over the whole absorber thickness.

**Table 4.6:**  $[Ga]/[III]$  and  $[Cu]/[III]$  values of the  $CuIn_{1-x}Ga_xSe_2$  absorbers as measured with XRF of the eight investigated samples are summarized

Sample	$[Ga]/[III]$	$[Cu]/[III]$
1	0.33	0.83
2	0.28	0.81
3	0.25	0.82
4	0.23	0.80
5	0.22	0.81
6	0.19	0.84
7	0.16	0.80
8	0.12	0.79

Figure 4.17 shows the PV parameter versus the  $[Ga]/[III]$  ratio of the samples 1-8 with USP- $In_2S_3$  buffer layer and the corresponding CdS reference. The  $V_{OC}$  of the CdS reference samples shows the expected increase with increasing gallium content. In contrary the  $V_{OC}$  of the as deposited cells with USP- $In_2S_3$  first increases until a  $[Ga]/[III]$  ratio of 0.22 is reached and for further increase of gallium content it drops again and remains constant around 500 mV. This is indicated by the two black dashed lines which are the linear fits in the two gallium regions in figure 4.17a. At the lowest gallium content this means already a difference of 40 mV to the CdS reference which increases to 140 mV for the highest gallium content. The finished device with USP- $In_2S_3$  buffer layer was annealed in air at 200 °C for up to 130 minutes accumulated time. The effect of the annealing on the  $V_{OC}$  of the device is shown in figure 4.17a. After 40 min of annealing the  $V_{OC}$  of the samples with  $[Ga]/[III] \geq 0.23$  increases and the values follow the same dependency on the gallium content as the  $V_{OC}$  of the samples with lower gallium content. With further annealing the  $V_{OC}$  is shifted to higher values for all  $[Ga]/[III]$  ratios, however, the dependency on the gallium content does not change. With this, the difference to the CdS reference samples is reduced to 30 mV for the lowest gallium concentration and to 80 mV for the highest concentration. This change in the  $V_{OC}$  points to a modification in the doping concentration and/or recombination mechanism induced by air annealing of the finished device.

There are only small differences in the current density between the cells with USP- $In_2S_3$  and the CdS references. The expected gain with  $In_2S_3$  buffer layer is not visible in the curves in figure 4.17. The samples were produced without anti-reflection coating. This is illustrated in figure 4.18 where the external quantum efficiency curves of the devices with the different buffer layers are compared. The pronounced valleys in the spectra of the devices with  $In_2S_3$  buffer layer indicate high reflection losses. In the shown spectra the gain in the low wavelength region of the cells with  $In_2S_3$  buffer layer is clearly visible. In figure 4.19 the EQE of the  $In_2S_3$  buffered cells is corrected for reflection losses by dividing the EQE by  $(1-R)$ . In this case R is the reflection of the finished device measured before the deposition of the grid lines. This shows that with appropriate AR-coating the ex-

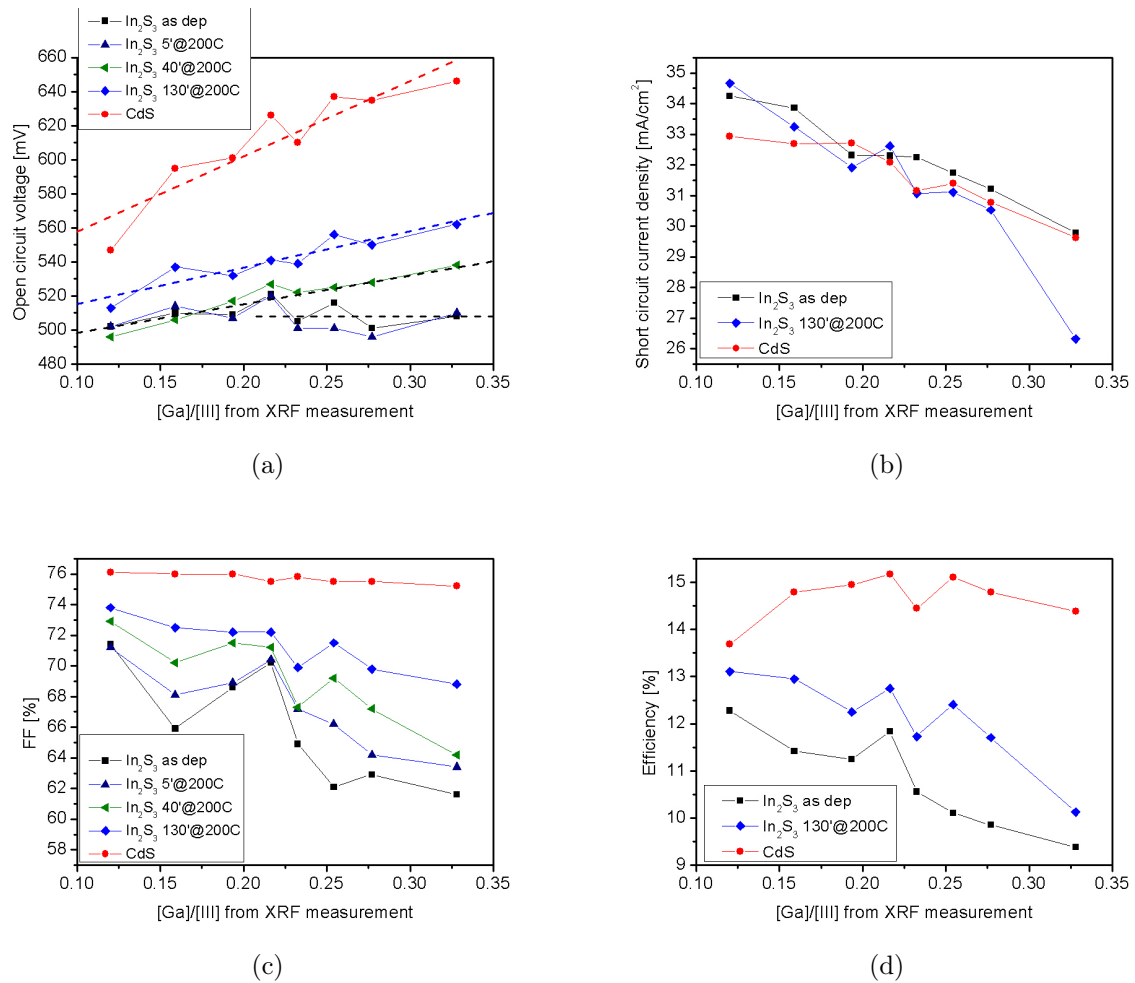


**Figure 4.17:** PV parameter of  $\text{CuIn}_{1-x}\text{Ga}_x\text{Se}_2$  solar cells versus the gallium content  $x = [\text{Ga}]/[\text{III}]$  for devices with  $\text{In}_2\text{S}_3$  buffer layer and CdS references.

pected increase in current density can be obtained (cf. section 3.5.4). With annealing an decrease in the current density is observed for the samples with  $[\text{Ga}]/[\text{III}] \geq 0.23$  (fig. 4.17b).

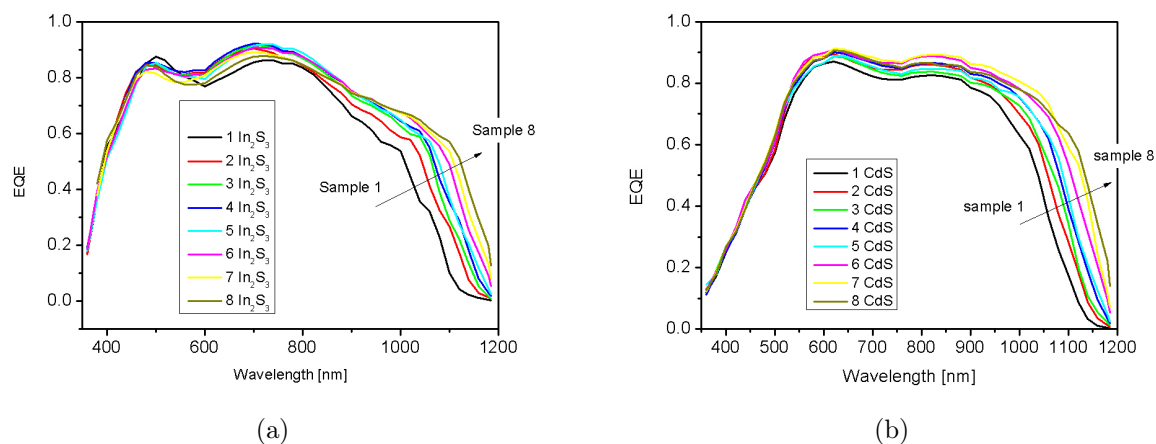


**Figure 4.18:** External quantum efficiency of  $\text{CuIn}_{1-x}\text{Ga}_x\text{Se}_2$  solar cells with USP  $\text{In}_2\text{S}_3$  buffer layer in (a) and with CBD-CdS buffer layer in (b).

The fill factor (fig. 4.17c) of the as deposited solar cells with USP- $\text{In}_2\text{S}_3$  buffer layers show a general decrease with increasing gallium content in the absorber with two deviations (sample 5 and 7). With annealing the deviation levels out, the slope of the decrease is reduced and shifted to higher values. The FF of the annealed devices approach the values of the CdS reference samples. For the lowest gallium content the difference is reduced to 2% absolute whereas a difference of 6% absolute is measured for the highest gallium content.

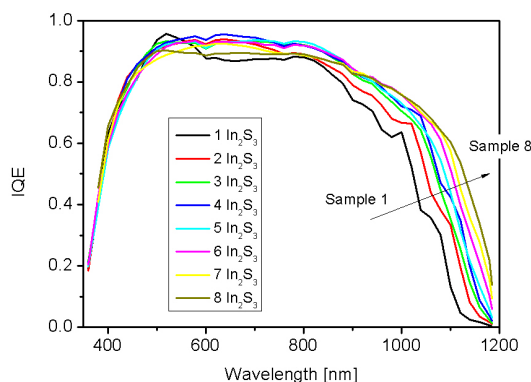


**Figure 4.19:** Internal quantum efficiency of  $\text{CuIn}_{1-x}\text{Ga}_x\text{Se}_2$  solar cells with USP- $\text{In}_2\text{S}_3$  buffer layer.

Finally, the combination of the described  $V_{\text{OC}}$ ,  $J_{\text{SC}}$  and FF yield the conversion efficiency

shown in figure 4.17d. A decrease of the efficiency with increasing gallium content is observed for the as deposited devices with USP-In<sub>2</sub>S<sub>3</sub> buffer layers given by the behavior of the J<sub>SC</sub> and FF. The efficiency values increase with the air annealing treatment at 200 °C for 130 min, irrespective of the gallium content. The highest efficiency of 13.1% is obtained for a [Ga]/[III] ratio of 0.12. For this ratio the CBD-CdS reference cell showed an efficiency of 13.7%, i.e. the cell with USP-In<sub>2</sub>S<sub>3</sub> buffer layer reaches 96% of the CBD-CdS reference cell. The highest efficiency of 15.2% of the CBD-CdS reference devices is obtained for a [Ga]/[III] ratio of 0.22. For this ratio only an efficiency of 12.7% is measured for the cell with USP-In<sub>2</sub>S<sub>3</sub> buffer layer, i.e. only 84% of the reference value is achieved.

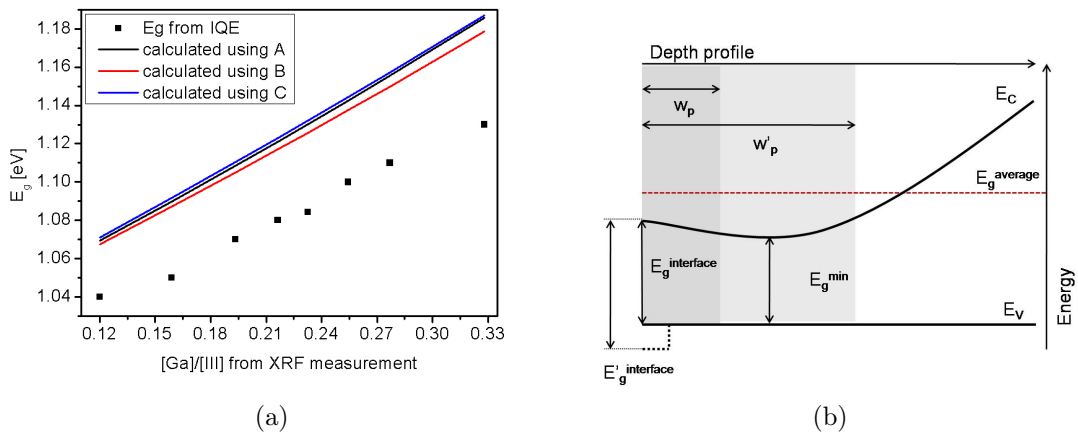


**Figure 4.20:** (a) Energy band gap of the  $\text{CuIn}_{1-x}\text{Ga}_x\text{Se}_2$  absorber plotted versus the gallium content  $x=[\text{Ga}]/[\text{III}]$ . The squares are band gap values derived from linear extrapolation of  $(\text{IQE} \cdot h\nu)^2$  versus  $h\nu$ . The lines are values calculated from XRF measurements using an interpolation between the band gap values of the pure semiconductors  $\text{CuInSe}_2$  and  $\text{CuGaSe}_2$  based on equation 4.1 for A, on reference [120] for B and, [8] for C. (b) Sketch of the double grading of the band gap estimated from the evaporation profile. Indicated are the average, minimum, and interface band gap as well as the expansion of the SCR into the absorber for two different doping concentrations.

Figure 4.20a shows the band gap of the absorber determined from the IQE shown in figure 4.19 plotted against the [Ga]/[III] ratio from XRF measurements. Also shown in figure 4.20a are the calculated band gap values based on XRF measurements using three different approaches. For the curve A, the equation 4.1 was used whereas the curves B and C are based on the references [120] and [8], respectively. The calculated band gap values from XRF more or less coincide, the values determined from the IQE measurement, however, are 0.04 to 0.06 eV below the values from XRF. Since the XRF signals are superpositions of all atoms throughout the whole layer thickness it yields an average composition and therefore the calculated band gap value from XRF data represents the average band gap of the absorber layer. This is indicated in figure 4.20b with the dashed line in the profile. In contrary, the band gap value derived from IQE measurements yields the minimum band gap of the absorber under the assumption that a significant amount

of photons reach the position of the minimum band gap. The minimum band gap is also indicated in figure 4.20b. Not known with these measurements is the band gap of the absorber close to the surface region which is important for the  $V_{OC}$  and the analysis of recombination mechanisms of the device. Since the CIGS samples are grown with minimum copper excess in the 2<sup>nd</sup> stage, the gallium dip and therefore the minimum band gap is expected close to the surface of the absorber. Additionally, the gallium ratio on the 3<sup>rd</sup> stage was reduced by a factor of 2. Thus, only a small increase of the minimum band gap towards the surface of the CIGS is expected. This consideration does not include a possible band gap widening due to copper depletion indicated as  $E_g^{interface}$  in figure 4.20b [123].

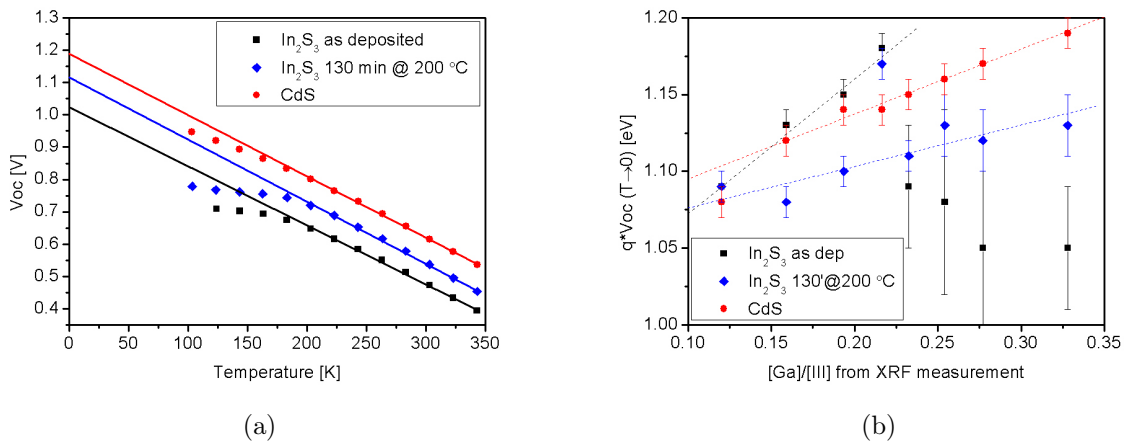


**Figure 4.21:** (a) Plot of open circuit voltage as a function of the cell temperature for the  $CuIn_{1-x}Ga_xSe_2$  sample with the highest Ga content in this series. Shown is the  $V_{OC}$  for cells with USP- $In_2S_3$  before and after annealing and the CdS reference. The linear part of each curve is extrapolated to  $T=0K$ . (b) Summary of  $q*V_{OC}$  values derived as described in subfigure (a) for all  $CuIn_{1-x}Ga_xSe_2$  absorbers investigated in this series. The error bars originate from standard deviation of an average value for different illumination intensities.

The  $V_{OC}$  values as a function of the temperature of the sample 1 with USP- $In_2S_3$  buffer before and after annealing and of the CBD-CdS reference sample are shown in figure 4.21a. In the range between 200 and 340 K a linear dependency between the  $V_{OC}$  and the temperature is observed for all three samples. An extrapolation of the linear part yields three almost parallel lines with an intersect at the  $V_{OC}$  of 1.05 eV for the as deposited and 1.13 eV for the annealed device with USP- $In_2S_3$  buffer, and 1.19 eV for the CBD-CdS reference.

The measurements as described in figure 4.21a are performed at different illumination intensities. For each intensity the linear part of the curve is extrapolated to zero Kelvin the average value for all illumination intensities is given in figure 4.21b and the error bars are given by the standard deviation. Figure 4.21b summarizes the  $qV_{OC}$  values for all samples 1-8. The black squares represent the as deposited, the blue diamonds the annealed devices with USP- $In_2S_3$  buffer layer, and the red circles the CBD-CdS references.

The  $qV_{OC}$  values of the CdS reference samples show the expected increase with increasing gallium content. Also the values of the as deposited samples with  $In_2S_3$  buffer first increase up to a  $[Ga]/[III]$  ratio of 0.22. For  $[Ga]/[III] \geq 0.23$  the  $qV_{OC}$  value is significantly reduced and shows a high standard deviation. A further increase can not be observed anymore. After air annealing of the finished device at  $200^\circ C$  for 130 min two effects on the dependency of the  $qV_{OC}$  values on the  $[Ga]/[III]$  ratio are found: (i) the slope of the increase up to a  $[Ga]/[III]$  ratio of 0.22 is reduced; (ii) the  $qV_{OC}$  values of the samples with  $[Ga]/[III] \geq 0.23$  increase with simultaneous decrease of the standard deviation and they show the same dependency as the samples described in (i). An exception is sample 5 with a  $[Ga]/[III]$  ratio of 0.22 where the  $qV_{OC}$  value is above the CdS reference and does not change with annealing.

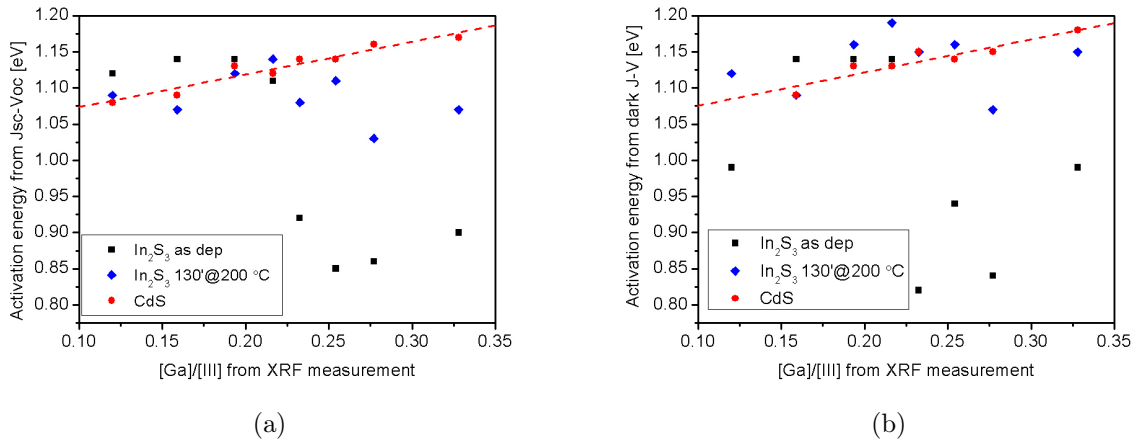


**Figure 4.22:** (a) Activation energy  $E_a$  from  $J_{SC}V_{OC}$  measurements of  $CuIn_{1-x}Ga_xSe_2$  solar cells with USP- $In_2S_3$  buffer layer before and after an annealing treatment. Also shown are the activation energies of the reference samples with CBD-CdS buffer layer. (b) Activation energy of the same samples but determined from dark J-V measurements.

In order to confirm the observations described above and shown in figure 4.21 and to investigate the effect of illumination the activation energy for the saturation current is derived from temperature dependent J-V measurements in dark and under illumination. The results of the activation energies under illumination without the effect of series resistance derived using the  $J_{SC}V_{OC}$  theory are shown in figure 4.22a as a function of the gallium content (cf. section 2.2.1.2). The activation energy of the as deposited devices with USP- $In_2S_3$  buffer layer follow the trend given by the CdS references up to a  $[Ga]/[III]$  ratio of 0.22. Again here a considerable decrease of the activation energy for  $[Ga]/[III] \geq 0.23$  is found. With annealing no significant change is observed up to  $[Ga]/[III]=0.22$ . For  $[Ga]/[III] \geq 0.23$  the activation energy increases, however, still deviates for high gallium content from the trend given by the CdS references.

Similar observations are made for the activation energies derived from dark measurements

(fig. 4.22b). Therefore, a major effect of the illumination on the dominant recombination mechanism can be excluded. The activation energies for the as deposited, annealed and CdS reference devices are summarized in table 4.7 together with the ideality factor at 300 K and the average and minimum band gap of the absorber.

**Table 4.7:** Overview of the of the absorber's band gap, the activation energy and the diode ideality factor of the samples 1-8. The values of the samples with dominant recombination in the interface region are in italics and the corresponding corrected barrier height for the holes at the interface  $\phi_p^f$  is in bold.

Sample	as deposited		130'@200 °C		CdS reference			
	$E_g^{XRF}$ [eV]	$E_g^{EQE}$ [eV]	$E_a^{JscVoc}$ [eV]	$A$	$E_a^{JscVoc}$ [eV]	$A$	$E_a^{JscVoc}$ [eV]	$A$
1	1.19	1.13	<b>0.90</b>	1.88	<b>1.07</b>	1.28	1.17	1.58
2	1.16	1.11	<b>0.86</b>	2.09	<b>1.03</b>	1.36	1.16	1.63
3	1.14	1.10	<b>0.85</b>	2.10	<b>1.11</b>	1.29	1.14	1.41
4	1.13	1.08	<b>0.92</b>	1.87	<b>1.08</b>	1.30	1.14	1.33
5	1.12	1.08	1.11	1.58	1.14	1.27	1.12	1.40
6	1.11	1.07	1.14	1.43	1.12	1.22	1.13	1.35
7	1.09	1.05	1.14	1.45	1.07	1.28	1.09	1.29
8	1.07	1.04	1.12	1.31	1.09	1.15	1.08	1.18
	$E_g^{average}$	$E_g^{min}$	$E_g^{minSCR}$ or $\phi_p^f$		$E_g^{minSCR}$ or $\phi_p^f$		$E_g^{minSCR}$	

Comparing the activation energies of the as deposited devices with USP-In<sub>2</sub>S<sub>3</sub> buffer layer with the average and minimum band gap of the absorber it is possible to distinguish between interface or SCR dominated recombination. The activation energy of the samples 1-4 ( $[Ga]/[III] \geq 0.23$ ) is significantly smaller than the minimum band gap of the absorber. In this case the activation energy represents the corrected barrier height for holes at the interface and the recombination is dominated by interface recombination (cf. figure 2.4). In this case the  $V_{OC}$  is given by equation 2.16 and mainly limited by the barrier height (surface inversion of the absorber or band gap widening at the surface) and the recombination velocity at the interface. For the samples 5-8 the activation energy is comparable with the average band gap and the ideality factor is greater than unity, i.e. in this case the losses are dominated by recombination in the SCR. The  $V_{OC}$  for the samples 5-8 is given by equation 2.15 and mainly limited by the diffusion constant and length of the minority charge carriers and the shallow net acceptor density in the absorber.

With the annealing treatment of the devices with USP-In<sub>2</sub>S<sub>3</sub> buffer layer the activation energy of the samples 1-4 approach the minimum band gap of the absorber. Only small changes in the activation energy due to the annealing are observed for the samples 5-8. The difference to the CdS reference devices are within the measurement error which is estimated from error propagation to be  $\pm 0.03$  eV. The ideality factor of all samples 1-8



decreases with the annealing treatment and reaches an almost constant value of about 1.3 with the exception of the sample with the lowest gallium content where a value of 1.15 is measured after annealing. The dependency of the ideality factor at 300 K on the gallium content is also shown in figure 4.23a.

Figure 4.23b shows the activation energy divided by the ideality factor at 300 K. In case of interface dominated recombination this yields the barrier height for holes at the buffer-absorber interface at zero bias according to equation 2.17. Values between 0.4 and 0.5 eV are obtained for the as deposited samples 1-4. This indicates a weak surface inversion of the CIGS layer in the as deposited device with USP- $\text{In}_2\text{S}_3$  buffer layer. After annealing the obtained values are considerably higher and due to the low ideality factor even exceed the values obtained for the CdS references. However, the ratio  $E_a/A$  has only a physical meaning if interface recombination is dominant.

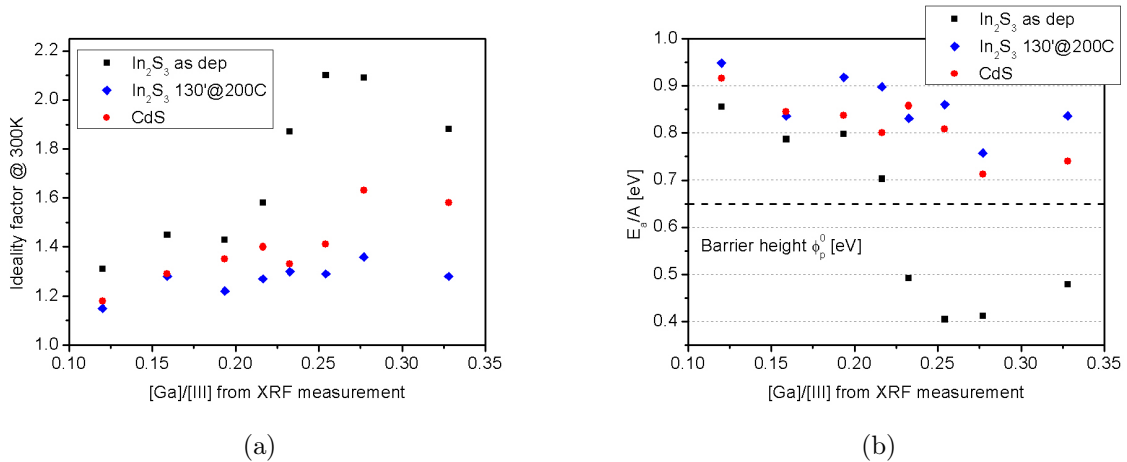


**Figure 4.23:** (a) Ideality factor  $A$  of CIGS solar cells with USP- $\text{In}_2\text{S}_3$  buffer layer before and after device annealing compared to the CBD-CdS reference. (b)  $E_a$  from figure 4.22a divided by the ideality factor. In case interface recombination is dominant, this value yields the barrier height for holes at the interface at zero bias (cf. fig. 2.4 and equ. 2.16).

The temperature dependence of the ideality factor for the as deposited and annealed device with USP- $\text{In}_2\text{S}_3$  buffer layer and the CBD-CdS reference is shown in figure 4.24. The ideality factor of the as deposited samples 1-4 has a strong temperature dependency. Already close to room temperature the measured values are above 2. This indicates that the interface recombination is enhanced by tunneling not only for low temperatures but also contributes to the losses at 300 K (cf. equation 2.24 and dashed arrows for path C in figure 2.4). For the samples 5-8 the ideality factor is almost independent on the temperature and stays well below 2 even for low temperatures except for sample 5 at very low temperatures.

After annealing a reduced temperature dependency of the samples 1-4 is observed as shown in figure 4.24b. At temperatures above 250 K almost no temperature dependency is observed and the curves obtained for samples 1-8 coincide. Below 250 K the ideality factor of

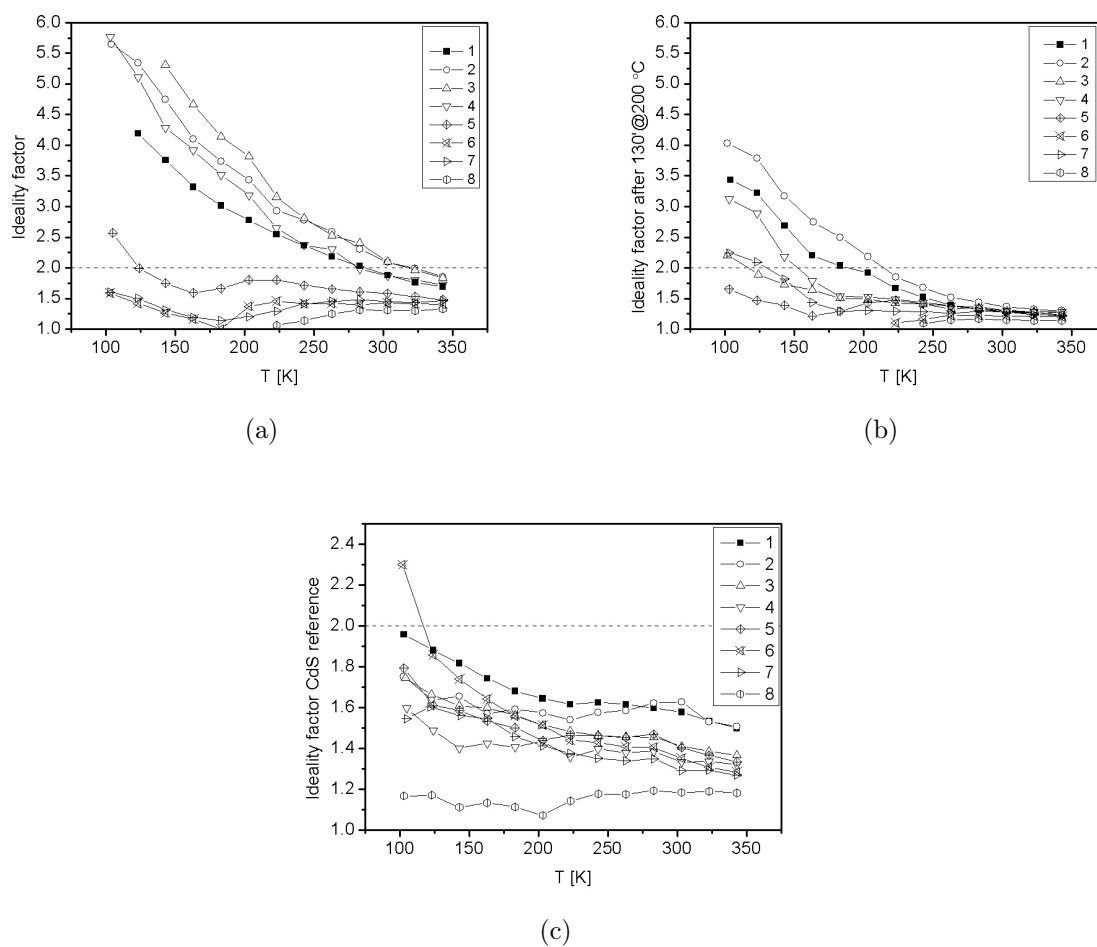


**Figure 4.24:** Ideality factor of samples 1-8 with USP-In<sub>2</sub>S<sub>3</sub> buffer layer as deposited (a), after 130 min air annealing at 200°C (b) and the CBD-CdS references (c).

sample one, two and four significantly exceed the value 2. Figure 4.24c shows the temperature behavior of the ideality factor of the CBD-CdS reference devices (note the different scale). It can be observed here that the ideality factor increases with increasing gallium content and that it is only weakly temperature dependent.

The increase of the  $V_{OC}$  after annealing for the samples with  $[Ga]/[III] \geq 0.23$  as observed in figure 4.17a can be explained by the increase of the activation energy and the shift of the  $V_{OC}$  for all samples after 130 min at 200 °C results from the decrease in the ideality factor (cf. equation 2.15). Reconsulting equation 2.9, the reduced ideality factor also explains the increase of the fill factor with device annealing shown in figure 4.17c.

The difference in the  $V_{OC}$  for the two different buffer layers is discussed in section 4.3.3 on page 83. Differences in surface type inversion of the absorber and diffusion of  $Cu^+$  ions from the surface region into the bulk of the absorber are identified as possible reasons for the differences in the  $V_{OC}$ . Figure 4.25 shows the apparent doping density of as deposited and air annealed sample 6 with USP- $In_2S_3$  buffer layer compared to the CBD-CdS reference cell. The doping concentration of the p-type absorber with  $In_2S_3$  buffer layer before annealing is  $1.7 \cdot 10^{15} \text{ cm}^{-3}$  and decreases to  $1.4 \cdot 10^{15} \text{ cm}^{-3}$  after 130 min air annealing at 200 °C. A doping concentration of  $3 \cdot 10^{15} \text{ cm}^{-3}$  is measured for the CBD-CdS reference device of absorber 6. The lower doping concentration of the device with  $In_2S_3$  buffer layer is consistent with the diffusion of positive copper ions into the bulk of the absorber which is even more pronounced after annealing. Two conclusions can be drawn: (i) the observed increase of the  $V_{OC}$  after annealing does not result from improved doping concentration; (ii) the difference in the doping concentration of the USP- $In_2S_3$  and CBD-CdS buffered absorbers is not the only reason for the difference of 70 mV in the open circuit voltage (cf. equ. 2.15). This indicates that the differences in surface type inversion of the absorber caused by oxygenation is the main reason for the lower  $V_{OC}$  of the USP- $In_2S_3$  buffered cells.

The following two questions still remain to answer: (i) why is there a step in the activation energy between  $[Ga]/[III]$  ratio of 0.22 and 0.23? (ii) why does the activation energy increases for  $[Ga]/[III] \geq 0.23$  with device annealing?

Alloying  $CuInSe_2$  with gallium increases the band gap of the semiconductor by shifting the conduction band upwards whilst the position of the valence band remains constant [124]. Assuming that the valence band offset between the  $CuIn_{1-x}Ga_xSe_2$  and the USP- $In_2S_3$  remains constant with gallium alloying, then it is obvious from figure 2.4 that the conduction band offset  $\Delta E_C$  will change the sign at a certain gallium composition, i.e. changing from spike to cliff. A cliff would result in increased availability of electrons at the buffer-absorber interface and thus, increase the probability for interface recombination. Since the change from SCR dominated to interface dominated recombination happens between  $[Ga]/[III]$  ratio between 0.22-0.23 it can be assumed that a cliff in the conduction band forms for  $[Ga]/[III] \geq 0.23$ .

There are two possible explanations for the observed annealing induced increase of the

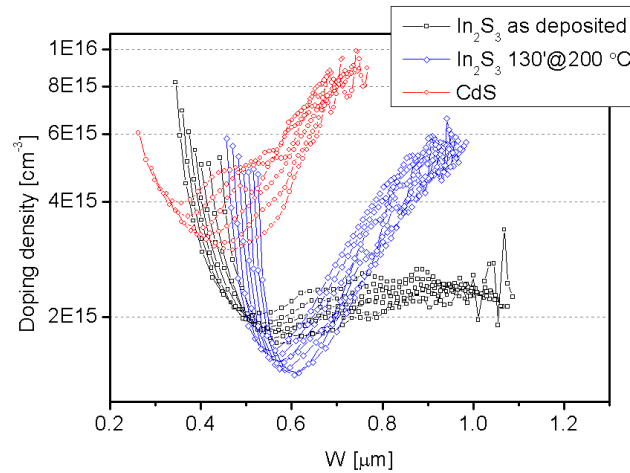


**Figure 4.25:** Apparent doping density of as deposited and air annealed CIGS device with USP- $\text{In}_2\text{S}_3$  buffer layer is compared to the CBD-CdS reference. The measurements were performed between 120 and 300 K at a frequency of 300 kHz. Plotted are only the curves obtained for the temperatures which are not affected by the capacitance changing defect.

activation energy of the samples with  $[\text{Ga}]/[\text{III}] \geq 0.23$ :

(i) Pinning of the Fermi level close to the conduction band with positive interface charges and thus amplification of the surface inversion of the absorber; a possible mechanism for the recovery of the positive surface charges is the partial exchange of oxygen which occupies selenium valencies at the interface with sulfur from the buffer layer driven by the thermal energy provided during the annealing. The effect on the net positive surface charge of the substitution of sulfur for oxygen is described in section 4.3.1 on page 72 and is based on the findings of [115]. By increasing the positive interface charges the energy distance between the Fermi level and the conduction band of the absorber at the interface is reduced. Simultaneously, this results in an increase of the barrier height for holes at the interface. As described in section 3.5.4 a substitution of oxygen for sulfur in the  $\text{In}_2\text{S}_3$  layer increases the energy band gap. However, due to the small concentration changes induced by the interdiffusion of oxygen and sulfur no significant change in the band gap is expected (see also [86]).

(ii) Band gap widening of the absorber at the interface due to copper depleted surface region; copper diffusion away from the CIGS surface region either into the buffer layer driven by the thermal energy and the chemical potential difference and/or onto the CIGS bulk driven by the thermal energy and the built in electric field results in a copper depleted surface region. The off-stoichiometry in the near surface region results in a surface defect layer (SDL) [117, 123] with an increased energy band gap [125–127]. An internal valence band offset close to the CIGS surface and no conduction band offset is assumed [117, 123]. The valence band offset indicated in figure 4.20 provides a direct increase of the barrier height for holes at the interface (cf. fig. 2.4).

Both of the above described mechanisms can explain the increase of the activation energy. In case of increased surface inversion a shift of the position of the N1 defect state towards lower values in the CIGS would be expected [42, 128]. Figure 4.26 shows the density of states derived from C-f measurements as described in [68] of the sample 6 with USP-In<sub>2</sub>S<sub>3</sub> buffer layer before and after device annealing and the CBD-CdS reference. The derived energy values are 0.235 and 0.280 eV for the as deposited and annealed device, respectively. The annealing increases the energy level of the N1 defect of sample 2. An improved surface inversion or Fermi level pinning due to device annealing can be excluded. For the CBD-CdS reference of sample 6 the peak of the density of states is found at 0.180 eV which is significantly lower compared to the USP-In<sub>2</sub>S<sub>3</sub> buffered devices.

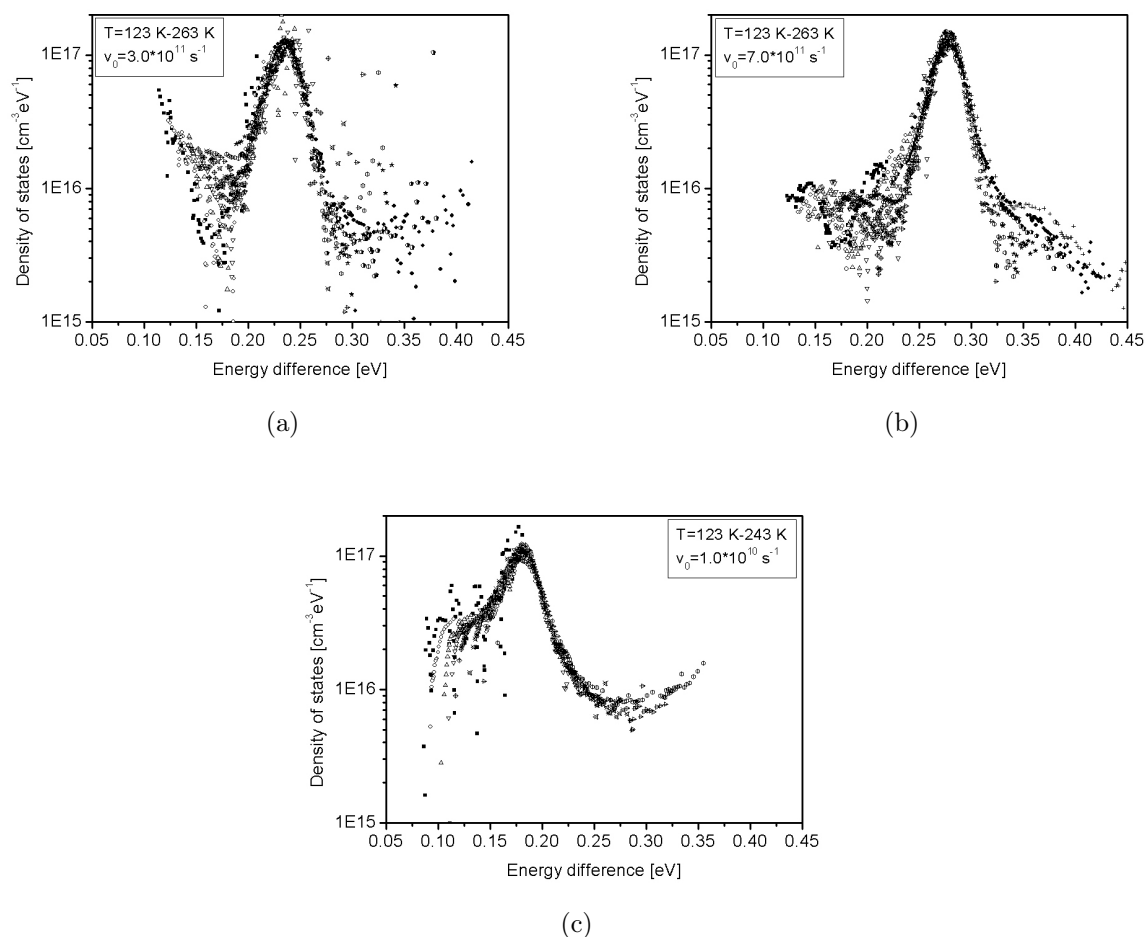


**Figure 4.26:** Density of states derived from the C-f measurement of as deposited (a) and annealed (b) with USP-In<sub>2</sub>S<sub>3</sub> buffer layer and the CdS reference (c) of sample 6 for temperatures between 123 and 263 K at zero bias voltage.

Rau et al. proposed that the energy level of N1 is determined by the energy difference between the Fermi level and the conduction band of the absorber at the interface [42].

Therefore, it can be concluded that the surface type inversion or Fermi level pinning of the absorber layer is not amplified with the annealing treatment and the increase of the activation energy results from a band gap widening due to copper depletion.

### 4.3.5 Partial electrolyte treatment

In this section the effect of cadmium ions at the absorber-buffer-contact interfaces is investigated and discussed. After the deposition of the indium sulfide buffer layers on the CIGS/Mo/SLG stack, a chemical surface treatment was applied. The  $\text{In}_2\text{S}_3/\text{CIGS}/\text{Mo}/\text{SLG}$  layer stack was immersed in an aqueous solution containing 0.0018 mol/l cadmium acetate, 1.32 mol/l ammonia, and 0.02 mol/l thiourea for two minutes, whereas the bath was heated from room temperature to 45 °C. After the treatment, the samples were rinsed with high purity de-ionized water and finished to a solar cell devices.

The J-V characteristics of CIGS solar cells with treated and untreated USP- $\text{In}_2\text{S}_3$  layer are compared in figure 4.27a. The corresponding photovoltaic characteristic values are summarized in Table 4.8. Solar cells with sprayed  $\text{In}_2\text{S}_3$  buffer layer and  $\text{CuIn}_{1-x}\text{Ga}_x\text{Se}_2$  absorber layers with  $x \geq 0.3$  grown with copper excess of 20-25% in the second stage generally show very low PV performance. The effect of a chemical surface treatment after the buffer layer deposition, as described above, is illustrated in figure 4.27a. A considerable increase of the  $J_{\text{SC}}$  to a value comparable to the CBD-CdS reference cell is observed. Also  $V_{\text{OC}}$  and FF increase with the chemical treatment.

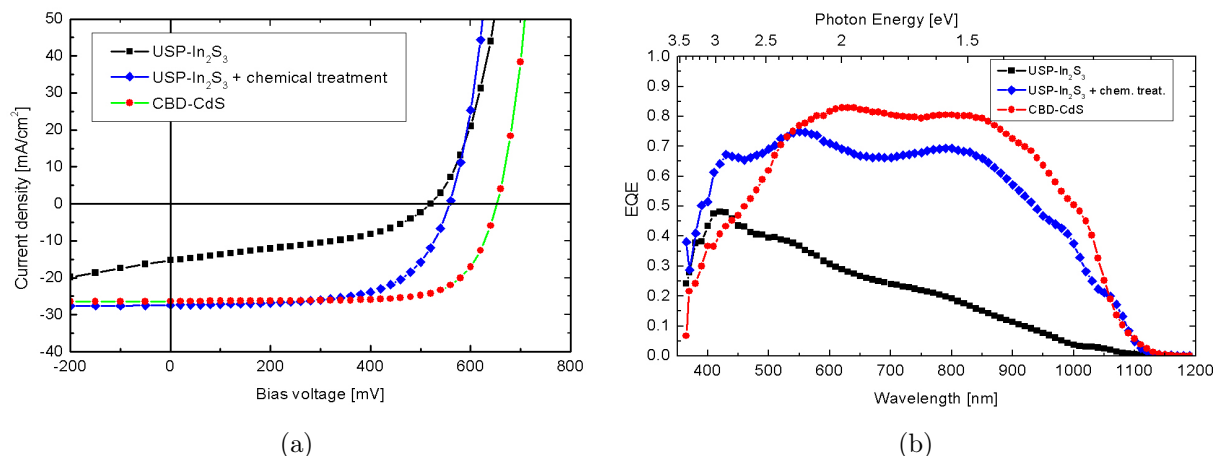


**Figure 4.27:** (a) J-V characteristics of solar cells with sprayed  $\text{In}_2\text{S}_3$  buffer layer; sprayed  $\text{In}_2\text{S}_3$  buffer layer and surface chemical treatment of the buffer layer after deposition; and CdS buffer layer deposited by CBD. (b) Corresponding external quantum efficiency of the solar cells shown in (a).

External quantum efficiency measurements of the cells reveal that the current increases over the entire spectrum due to the chemical surface treatment of the buffer layer in the Cd containing solution (fig. 4.27b). The EQE curves also demonstrate the reduced parasitic absorption of high energy photons for sample with the  $\text{In}_2\text{S}_3$  buffer layer compared to the CBD-CdS reference.

Solar cells with USP- $\text{In}_2\text{S}_3$  on absorbers with lower gallium content and copper excess show an improved  $V_{\text{OC}}$  and FF after the chemical treatment as shown in figure 4.28 but

**Table 4.8:** *PV characteristic values of solar cells with sprayed  $\text{In}_2\text{S}_3$  buffer layer without and with 2 min surface chemical treatment (CT) and of the corresponding CBD-CdS reference cell.*

Sample	$\eta$ [%]	$V_{OC}$ [mV]	$J_{SC}$ [mA/cm <sup>2</sup> ]	FF [%]
USP- $\text{In}_2\text{S}_3$	3.4	519	15.2	42
USP- $\text{In}_2\text{S}_3$ +CT	9.6	558	27.1	63
CBD-CdS	12.6	652	26.3	73

no increase of  $J_{SC}$ .

The growth of an uniformly covering CdS layer on the indium sulfide surface after 2 min in the bath at solution temperature between 25 °C and 45 °C is very unlikely since the deposition reaction takes several minutes to initiate and is in the order of 30 min at 45 °C [43].

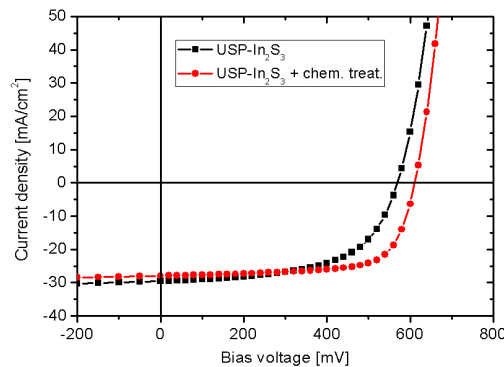


**Figure 4.28:** *Effect of chemical treatment on J-V characteristics of a device with USP- $\text{In}_2\text{S}_3$  buffer and absorber layer with reduced gallium content ( $x=0.13$ ) and copper excess (10%).*

The Cd concentration in the buffer layer and at the CIGS-buffer interface was investigated by means of conventional TEM and STEM analysis with a high angular annular dark field detector (HAADF) coupled with EDX. Neither in the bulk material nor at the buffer layer interfaces any Cd could be detected within the detection limits of these techniques. However, we need to understand the diffusion of Cd ions through the buffer and CIGS.

A previous study on the so called Cd partial electrolyte treated CIGS solar cells, where the CIGS absorbers were immersed in an aqueous bath with 0.0015 mol/l  $\text{CdSO}_4$  and 1.5 mol/l  $\text{NH}_4\text{OH}$ , showed a beneficial effect for the cell performance [94]. This effect was attributed by the authors to the ability of Cd to produce n-type doping or a strong inver-



sion of the surface region of the CIGS absorber. Diffusion of Cd during the CBD process into the CIGS layer approximately 10 nm from the interface boundary was reported by T. Nakada [129] suggesting that Cd substitutes Cu atoms in the CIGS, resulting in conversion from p to n type conduction. This implies that the pn-junction is buried in the CIGS absorber layer which could be the explanation for the improved  $J_{SC}$  of the Cd-treated cells as illustrated in figure 4.27.

Studies of Cd and Zn diffusion in  $CuInSe_2$  single crystals demonstrated that these elements are efficient n-type dopants [130]. Cd diffusion could lead to defect passivation at the buffer layer interfaces or in the bulk materials. A reduction of the recombination sites for charge carriers can increase the  $V_{OC}$  of the solar cell, as shown in figure 4.28. As proposed by Ramanathan et al. [94] shifting the peak of the electric field away from the absorber/buffer interface due to Cd diffusion into the CIGS can reduce the interface recombination. This could explain the improvement of the  $V_{OC}$  of the treated cells.

The chemical treatment of the as-deposited  $In_2S_3$  buffer layer on CIGS for 2 min showed an improvement of the solar cell performance. Two distinct effects were observed: an increase of the  $V_{OC}$  and FF for cells with low gallium content in the absorber. For cells with high gallium content additionally an increase in the  $J_{SC}$  is observed. EQE measurements suggest that the collection of charge carriers is drastically improved if the buffer layer is chemically treated in Cd containing solution. A similarity of this treatment with the Cd partial electrolyte treatment of CIGS thin film buffer free solar cells is observed, with the difference that the presented treatment is applied on the buffer layer.

## 4.4 Summary and conclusion

Based on XPS measurements of bare CIGS absorber and argumentations presented in section 4.2 a completely copper depleted metal terminated surface layer of the CIGS with net positive surface charge and  $(2V_{Cu}^- + In_{Cu}^{2+})^0$  defect clusters is assumed.

With ultrasonic spray pyrolysis it is possible to grow stoichiometric tetragonal- $In_2S_3$  layers with low impurity concentration on CIGS absorbers with conformal substrate coverage. A microcrystalline  $In_2S_3$  structure is favorable for buffer layer application to avoid spikes which could lead to deteriorate ZnO.

Diffusion of copper from the absorber layer into the USP- $In_2S_3$  buffer layer was detected qualitatively by EDX mapping in transmission electron microscopy. XPS measurements of  $In_2S_3$  layers deposited at different substrate temperatures onto CIGS absorbers yielded quantitative results of copper diffusion into the  $In_2S_3$  layer.

With increasing deposition temperature an increased copper concentration in the buffer layer was found and simultaneously an upwards shift of the valence band maximum was

observed. This confirms that copper incorporation rather than sodium incorporation dominates the modifications of the electronic properties of  $\text{In}_2\text{S}_3$  deposited on CIGS absorbers. The USP deposition of  $\text{In}_2\text{S}_3$  onto the absorber at substrate temperatures of about  $200^\circ\text{C}$  yields single phase material with copper impurities. Increasing the temperature to  $250^\circ\text{C}$  and above results in a coexistence of the  $\text{In}_2\text{S}_3$  and  $\text{CuIn}_5\text{S}_8$  phases.

The application of the spray deposition temperature profile to the absorber layer before CBD-CdS deposition showed that the elevated temperature necessary for the deposition of USP- $\text{In}_2\text{S}_3$  amplifies oxygenation of the CIGS surface, i.e. selenium valencies are filled with oxygen and the type inversion of the CIGS surface is reduced. Minimizing the oxygenation of the CIGS surface is mandatory in order to achieve highly efficient solar cells.

The degree of copper excess in the 2<sup>nd</sup> stage of the absorber deposition has a direct influence on the performance of the CIGS solar cells with USP- $\text{In}_2\text{S}_3$  buffer layer. The copper excess affects predominantly the fill factor. For CIGS samples with 20% or higher copper excess a fill factor higher than 65% was not achieved. Decreasing the copper excess to 10% and below resulted in a significant increase of the fill factor.

An explanation for the strong dependency of the device performance on the copper excess can be the shift of the gallium dip (band gap minimum) driven by the degree of copper excess (cf. [116]). The lower the copper excess the further is the band gap minimum shifted towards the surface of the absorber. This influences the maximum achievable band gap at the surface which in turn affects the diode ideality and recombination mechanisms (cf. section 4.3.4).

Modifications of absorber finishing showed that copper-poor grow conditions are necessary in order to minimize recombination losses of CIGS solar cells with USP- $\text{In}_2\text{S}_3$  buffer layers. Also the reduction of gallium concentration towards the surface of the absorber proved to be necessary for good device performance.

The variation of the gallium content in CIGS layers grown with minimum copper excess and copper-poor finish revealed a change of the dominant recombination mechanism for a  $[\text{Ga}]/[\text{III}]$  ratio between 0.22 and 0.23. Assuming that the valence band offset between the CIGS and the USP- $\text{In}_2\text{S}_3$  buffer layer remains constant with gallium alloying, then the conduction band offset  $\Delta E_C$  will change sign at a certain gallium concentration, i.e. it changes from spike to cliff. A cliff results in increased availability of electrons at the buffer absorber interface and thus increase the probability for interface recombination. Since the change from SCR dominated to interface dominated recombination happens between  $[\text{Ga}]/[\text{III}]$  ratio between 0.22-0.23 it can be concluded that a cliff in the conduction band forms for  $[\text{Ga}]/[\text{III}] \geq 0.23$ .

A significant increase of the  $V_{OC}$  and the FF is observed for CIGS solar cells with USP- $\text{In}_2\text{S}_3$  buffer layer after device annealing at  $200^\circ\text{C}$  in air. This improvement results from an increase of the activation energy caused by a band gap widening of the surface region

of the absorber due to copper depletion.

An partial electrolyte Cd treatment of the as-deposited  $\text{In}_2\text{S}_3$  buffer layer on CIGS for 2 min showed an improvement of the solar cell performance. Two distinct effects were observed: (i) an increase of the  $V_{\text{OC}}$  and FF. This increase can be explained by reduced recombination losses originating from recovered surface inversion of the absorber due to cadmium atoms occupying copper vacancies [115]. (ii) For cells with high gallium content additionally an increase in the  $J_{\text{SC}}$  is observed. EQE measurements suggest that the collection of charge carriers is drastically improved if the buffer layer is chemically treated in Cd containing solution. A similarity of this treatment with the Cd partial electrolyte treatment of CIGS thin film buffer free solar cells is observed, with the difference that the presented treatment is applied on the buffer layer.

Highest total area efficiency of 13.4% was achieved with USP- $\text{In}_2\text{S}_3$  buffer layer on a CIGS absorber with  $[\text{Ga}]/[\text{III}]$  ratio of 0.14 and a gallium finish. However, the procedure of the gallium finish failed in terms of reproducibility. Minimum copper excess, copper-poor finish and gallium reduction in the 3<sup>rd</sup> stage proved to be a CIGS absorber deposition procedure yielding reproducible results with USP- $\text{In}_2\text{S}_3$  buffer layer. With this process highest total area efficiency of 13.1% was achieved corresponding to 13.7% of the CBD-CdS reference device. With the application of a  $\text{MgF}_2$  anti-reflection coating, the total area efficiency of this CIGS solar cells is increased to 14.2% and the active area efficiency is 15.0%.



## 5 Application in CIGSSe thin film solar cells

This chapter is in part based on the following publication:

S. Buecheler, D. Corica, D. Guettler, A. Chirila, R. Verma, U. Müller, T.P. Niesen, J. Palm, A.N. Tiwari, "Ultrasonically sprayed indium sulfide buffer layers for Cu(In,Ga)(S,Se)<sub>2</sub> thin-film solar cells", *Thin Solid Films*, Volume **517**, Issue 7, 2 February 2009, Pages 2312-2315.

The application of USP-In<sub>2</sub>S<sub>3</sub> as buffer layer in solar cells with sulfur containing chalcopyrite absorbers supplied from the pilot production line of a company was investigated and the results are presented in this chapter. The Cu(In,Ga)(S,Se)<sub>2</sub> (CIGSSe) were deposited on molybdenum coated soda line glass by sputtering of the metals with subsequent rapid thermal processing in selenium and sulfur containing ambient. In table 5.1 the elemental compositions as measured by EDX of the absorbers from different batches are summarized. The gallium content of the absorber layers is relatively low. SEM images show that the thickness of the absorber layer is approximately 2 μm and the information depth of the EDX measurement is approximately 1.3 μm (20 kV accelerating voltage for the scanning electrons). It is expected that gallium is only present at the back of absorber and it can be neglected at the interface to the buffer layer. The ratio between sulfur and selenium determines the energy band gap of the absorber at the buffer-absorber interface.

**Table 5.1:** *Composition as measured by EDX of Cu(In,Ga)(S,Se)<sub>2</sub> from the different batches (1-5) which were investigated in this work. The values given are averages from three measurements at different spots on the same sample. The standard deviation for all values is below ±1%.*

	Cu	In	Ga	Se	S	[Ga]/[III]	[Cu]/[III]	[S]/[Se+S]	[M]/[Se+S]
1	22.3%	29.1%	1.2%	41.5%	5.9%	0.04	0.74	0.12	1.11
2	21.7%	29.4%	1.0%	39.3%	8.6%	0.03	0.71	0.18	1.09
3	21.8%	29.8%	1.0%	41.7%	5.7%	0.03	0.71	0.12	1.11
4	22.1%	29.6%	0.8%	41.9%	5.7%	0.03	0.73	0.12	1.1
5	22.3%	29.2%	1.2%	42.2%	5.1%	0.04	0.74	0.1	1.1

All absorbers are extremely copper poor which means that a segregation of  $\text{Cu}_2\text{Se}$  or  $\text{Cu}_2\text{S}$  on the surface are not likely [131] but an indium terminated  $\{112\}$  facet is expected [80]. The absorbers from the batch no. 2 differ from the other in terms of  $[\text{S}]/[\text{Se}+\text{S}]$  ratio. The sulfur content of that absorber is significantly higher. The different sulfur concentration influences the band gap of the absorber, as well as the position of the conduction and valence band relative to the Fermi level [124]. With the EDX measurement the yielded composition is an average over the information volume. Inferences about the quantitative composition at the interface are not possible, since a composition grading can not be excluded.

## 5.1 Morphology and interdiffusion in CIGSSe devices

Figure 5.1 shows cross section images obtained with SEM of finished devices with CIGSSe absorbers from batch no. 1 and USP- $\text{In}_2\text{S}_3$  buffer layers. The  $\text{In}_2\text{S}_3$  layer was deposited with varying In/S ratio (1:1, 1:2, 1:3, and 1:4) in the precursor solution. The amorphous or microcrystalline structure of the layer deposited with sulfur deficiency compared to the stoichiometry of  $\text{In}_2\text{S}_3$  (fig. 5.1a) and the polycrystalline structure of the layers sprayed with sulfur excess (fig. 5.1b-d) is visible.

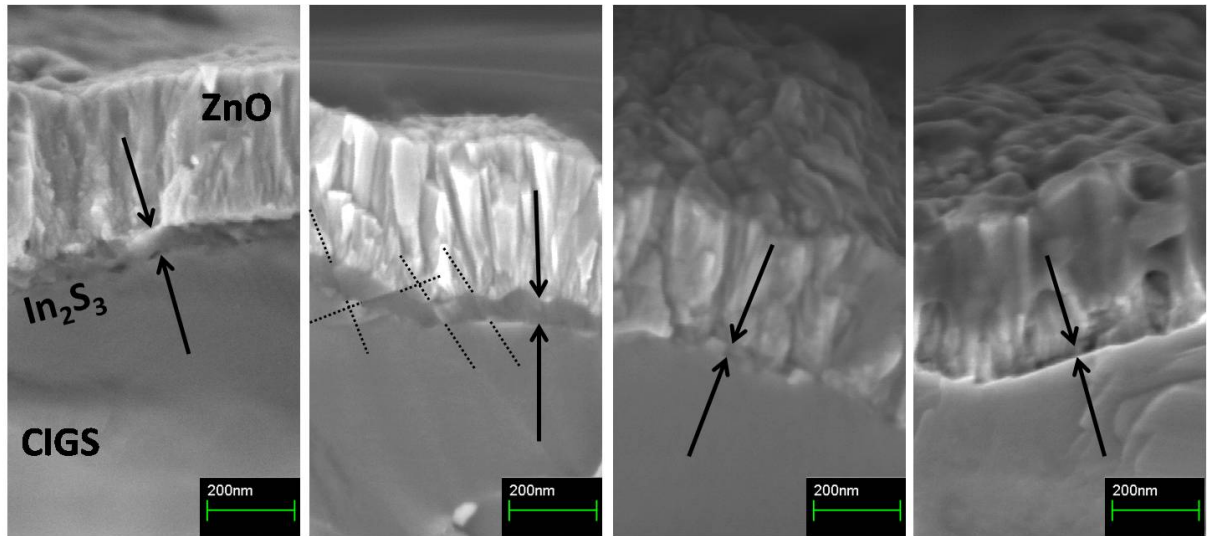


**Figure 5.1:** SEM cross section of finished devices with  $\text{Cu}(\text{In},\text{Ga})(\text{S},\text{Se})_2$  absorbers and USP- $\text{In}_2\text{S}_3$  buffer layers sprayed with sulfur deficiency  $\text{In}/\text{S}=1:1$  (a), and sulfur excess  $\text{In}/\text{S}=1:2$  (b),  $\text{In}/\text{S}=1:3$  (c), and  $\text{In}/\text{S}=1:4$  (d).

As a guide for the reader's eye some edges of the crystalline grains in the  $\text{In}_2\text{S}_3$  layer are indicated by the dotted lines in figure 5.1b. The  $\text{In}_2\text{S}_3$  layers in Figure 5.1c+d are also polycrystalline, however, the layer thickness and grain size is reduced. The deposition temperature was kept constant in this set of experiments to expose all samples at elevated temperature to the ambient for the same time. Therefore, the decrease in layer thickness from fig. 5.1a to d reflects again the decrease of growth rate with increasing degree of

sulfur excess as discussed in section 3.4.

Figure 5.2 illustrates elemental depth profiles of AZO/i-ZnO/ $\text{In}_2\text{S}_3$ / $\text{Cu}(\text{In,Ga})(\text{S,Se})_2$  interfaces. In the measured samples, the buffer layers were deposited with indium to sulfur ratio of 1:3 at  $200^\circ\text{C}$  on absorber from batch no. 2. With profilometer and SEM cross section calibration measurements the  $\text{In}_2\text{S}_3$  layer thickness is expected to be 30 nm for the investigated samples. For obtaining the depth profile, the stacks are stepwise plasma etched with 4 keV argon ions.

As described in section 3.5.3 no standards of the different elemental sputter yields were available for the analyzed structure, therefore, the given concentrations in the y-axis are not the absolute atomic concentrations of the material. Also possible forward sputtering across the interfaces has to be taken into account in the analysis of elemental interdiffusion.

The measurement area of the XPS measurement is  $1\text{ mm}^2$ ; hence, the obtained signal is a superposition of elemental profiles over many CIGS single grains. The average absorber surface roughness is more than twice the  $\text{In}_2\text{S}_3$  layer thickness, i.e. the interfaces are not two dimensional but three dimensional which is even more pronounced with the  $\text{Cu}(\text{In,Ga})(\text{S,Se})_2$  absorbers with high surface roughness. For the XPS depth profile, this means that the measurement is blurred at the interfaces and the width of the  $\text{In}_2\text{S}_3$  signal, in the following referred to as  $\text{In}_2\text{S}_3$  region, is also influenced by the absorber roughness and not only by the layer thickness.

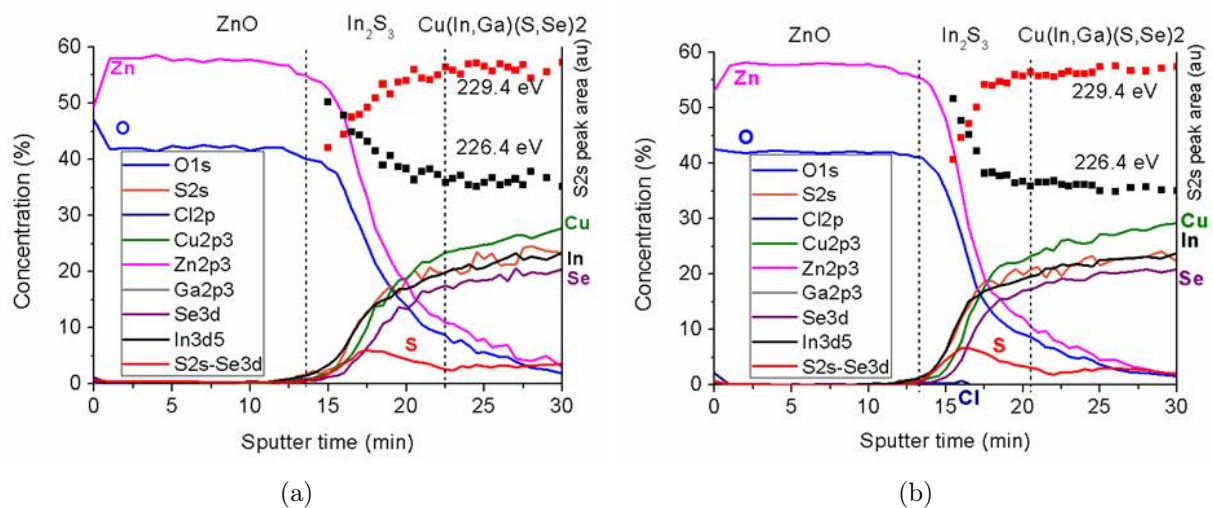


**Figure 5.2:** Elemental depth profile as obtained with XPS measurements including stepwise Ar etching. (a) shows the  $\text{ZnO}$ - $\text{In}_2\text{S}_3$ - $\text{Cu}(\text{In,Ga})(\text{S,Se})_2$  interfaces of an as deposited sample and (b) the same sample after air annealing at  $200^\circ\text{C}$  for 5 min.

The  $\text{In}_2\text{S}_3$  region in Figure 5.2 is defined by the  $\text{S}2s$  signal at 226.4 eV (see the black data points and the y-axis at the right hand side). The peak at 229.4 eV is a superposition of a weak  $\text{S}2s$  signal and a strong  $\text{Se}3s$  signal. Therefore, the  $\text{S}2s$  data line in the CIGS region

does not represent sulfur but selenium plus sulfur.

To get an idea of the sulfur distribution itself, the Se3d signal was subtracted from the S2s signal. Such obtained sulfur distribution (represented as red line in fig. 5.2) of the as deposited device shows a broad peak in the  $\text{In}_2\text{S}_3$  region (fig. 5.2a) with a shallow slope on both sides, starting together with the In signal at the ZnO interface. The Cu signal appears before the Se signal, indicating copper diffusion from the absorber into the  $\text{In}_2\text{S}_3$  layer.

After device annealing at 200 °C for 5 min the width of the  $\text{In}_2\text{S}_3$  region is decreased (Fig. 5.2b), apparent by the steeper slopes of all elemental depth distributions. Also in the annealed device copper is detected in the buffer layer but no increased interdiffusion is observed due to the annealing. To some extent, the strong broadening of the interfaces in the as deposited device is likely to originate from sputter damages during ZnO deposition. The annealing treatment provides thermal energy to the material to restructure resulting in more abrupt interfaces. This effect is reflected in an increase in efficiency by 2% absolute.

## 5.2 Photovoltaic properties with CIGSSe absorbers

The effect of basic deposition parameters of the ultrasonic spray pyrolysis on the device performance are presented in this section. The impact of the deposition temperature, solvent used for the transport of the precursors to the substrate, the precursor ratio and the use of additives were investigated.

### 5.2.1 Impact of the deposition temperature

The absorber used in the investigation of the deposition temperature of the USP- $\text{In}_2\text{S}_3$  buffer layer is from the batch no. 1 and the elemental composition is given in table 5.1.

The PV performance of CIGSSe solar cells with USP- $\text{In}_2\text{S}_3$  buffer layer were investigated for different substrate temperatures during spray pyrolysis. The  $\text{In}_2\text{S}_3$  layers were sprayed from a methanol based solution containing 0.01 mol/l  $\text{InCl}_3$  and an In/S ratio of 1:3. The deposition was terminated after 30 minutes. Figure 5.3 shows the average  $V_{\text{OC}}$  and FF for the temperature range between 190 and 220 °C. The current density is not shown since no change with temperature is observed. Given are always the substrate surface temperatures, however, measured were the temperatures near the surface of the hot plate directly below the sample. Calibration measurements performed under simulated spray conditions are then used to derive the surface temperature of the sample. The temperature values given throughout this work are therefore comparable, however, care must be taken when the values are compared with temperatures measured in other setups or laboratories.

The average open circuit voltage and the fill factor have a maximum at a deposition temperature of 200 °C. At lower temperature the layer thickness is probably not sufficient for



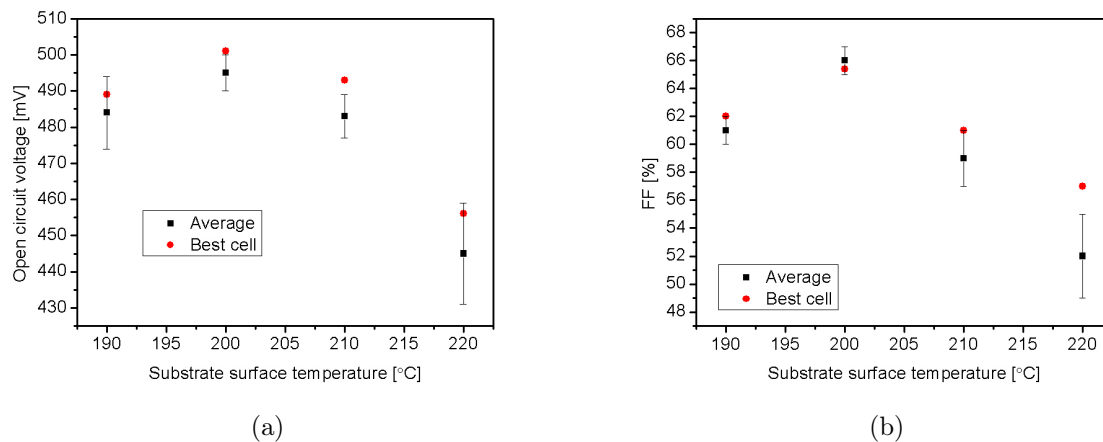


**Figure 5.3:** *Open circuit voltage (a) and fill factor (b) of CIGSSe solar cells with USP  $\text{In}_2\text{S}_3$  buffer layer sprayed at different substrate temperatures. Given are average values of cells on one sample, the standard deviation and the values for the best cell on the corresponding sample.*

a compact layer formation on the absorber. A possible explanation for the decrease of the electronic properties above 200 °C is that the inter-diffusion of copper and indium between the CIGSSe and the  $\text{In}_2\text{S}_3$  layer is enhanced with the detrimental effect as described in section 4.2.

### 5.2.2 Influence of the solvent and additives

Parts of this section were gathered during the master thesis of Rodrigo Lopes Sauaia [132].

The absorber used in the investigation of different solvent and additives is from the batch no. 5 and the composition is given in table 5.1. For the investigation of different solvents  $\text{In}_2\text{S}_3$  buffer layers were grown by USP on  $\text{Cu}(\text{In,Ga})(\text{S,Se})_2$  absorber with an area of  $2.5 \times 2.5 \text{ cm}^2$ . The following solvents were investigated: methanol (reference), methanol: $\text{H}_2\text{O}$  (1:1), ethanol, acetone and acetonitrile. Additionally, one sample was prepared with methanol on an absorber which was etched with 10% KCN in aqueous solution for 10 seconds prior to the buffer deposition. The deposition parameters used for the buffer layer were similar to those used for the layers on SLG which were discussed in section 3.5.2. A pre-spray step was used during heating of the absorber to the desired substrate temperature, as an attempt to minimize oxygenation of the absorber layer. The pre-spray solutions used with all solvents contained 0.002 mol/l  $\text{InCl}_3$ . Additionally, a set of solar cells sprayed with acetone and acetonitrile replacing  $\text{InCl}_3$  by 0.002 mol/l thiourea in the pre-spray solution was also prepared. The spraying time was adjusted for each solvent in order to obtain an  $\text{In}_2\text{S}_3$  layer thickness of 30-50 nm: 920 seconds for methanol and methanol: $\text{H}_2\text{O}$ ; 1610 seconds for ethanol; and 1840 seconds for acetone and acetonitrile. The buffer layer thickness was verified by profilometer measurements on soda lime glass

dummy samples sprayed alongside the absorber. The J-V measurements of the finished devices are presented in figure 5.4.

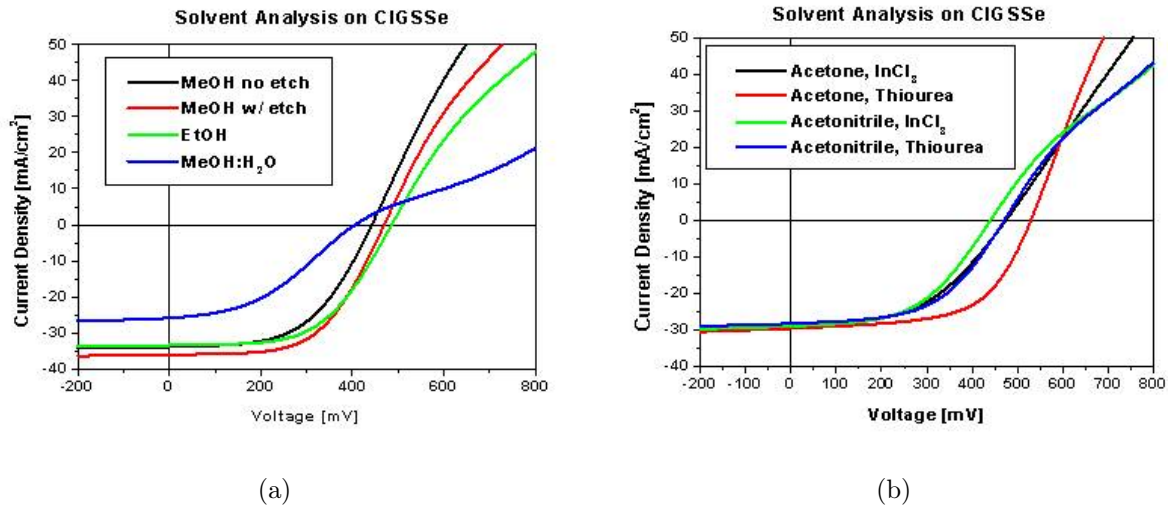


**Figure 5.4:** (a) *J-V characteristics for CIGSSe solar cells with USP-In<sub>2</sub>S<sub>3</sub> buffer layers using different solvents during deposition.* (b) *Modification of the pre-spray solution.*

The USP method proved to be robust with different solvents. The PV parameters of the solar cells are homogeneously distributed over the whole absorber area, and standard deviations of the photovoltaic parameters are well below 10%.

Comparing the performance of solar cells sprayed with methanol with and without KCN etching of the absorber prior to the buffer deposition one can note the beneficial effect of the etching procedure. The  $V_{OC}$  of etched samples was on average 20 mV higher than those of non-etched ones, indicating a reduced recombination of carriers after impurities and oxides on the absorber surface were removed. The etching also improved the FF of the solar cells slightly, reduced series resistances and improved parallel resistances. As a consequence, average efficiencies are considerably higher. The KCN of the absorber etching was then set as standard before the USP-In<sub>2</sub>S<sub>3</sub> deposition on absorbers from batch no. 5.

Samples sprayed with methanol:H<sub>2</sub>O have considerably lower PV parameters when compared to samples prepared with other solvents. The need for higher spraying temperatures for this solvent (260 °C) enhances oxygenation of the absorber surface. This leads to oxygen incorporation on the surface of the absorber, resulting in passivation of selenium vacancies and reducing the type-inversion of the absorber surface [42]. Furthermore, the increased deposition temperature might result in the formation of a secondary CuIn<sub>5</sub>S<sub>8</sub>. The detrimental effects of such a phase are described in section 4.2. Morphology investigations of In<sub>2</sub>S<sub>3</sub> layers deposited on soda lime glass from methanol:H<sub>2</sub>O solution showed that the film is not continuous. A high density of voids are found in the In<sub>2</sub>S<sub>3</sub> layer. It can be

concluded that methanol:H<sub>2</sub>O (1:1) is not a suitable solution for the deposition of In<sub>2</sub>S<sub>3</sub> as buffer layers in CIGS thin film solar cells.

Also for ethanol as solvent the deposition temperature needs to be increased in order to guarantee complete solvent evaporation. For this experiment the temperature was set to 245 °C on the surface. Solar cells produced with ethanol show comparable V<sub>OC</sub> and FF values, slightly higher than the values obtained with KCN-etched methanol, and comparable efficiencies to the reference solvent. SEM images of films deposited with ethanol indicate the formation of a uniform mesh of polycrystalline In<sub>2</sub>S<sub>3</sub> (see section 3.5.2). This layer covered the absorber quite uniformly, but the porosity of the polycrystalline mesh still exposes the absorber layer to undesired effects (e.g. oxidation, sputtering damage).

With acetone as solvent the obtained V<sub>OC</sub> is comparable with the methanol reference, however FF and J<sub>SC</sub> are lower. Changing the pre-spray solutions from InCl<sub>3</sub> to thiourea results in an increase of the average V<sub>OC</sub> by 57 mV (see table 5.2). Thiourea can act as an antioxidant and pre-spraying the absorber surface with a thiourea-containing solution might avoid oxidation of the material during the heating phase, before the deposition starts, or even reduce the amount of oxidized sites present on the absorber surface (cf. section 4.3.1). SEM images of films deposited with acetone show the formation of a continuous, dense and relatively uniform layer of In<sub>2</sub>S<sub>3</sub>, with small holes or voids of approximately 50 nm size (fig. 3.7). This is in agreement with the higher V<sub>OC</sub> and FF values obtained for solar cells, indicating the formation of a more uniform and well distributed p-n heterojunction throughout the device, with less current leakages or shunted regions.

**Table 5.2:** Average and best cell PV parameters of CIGSSe solar cells with In<sub>2</sub>S<sub>3</sub> deposited using acetone and acetonitrile and solvents.

Sample		$\eta$ [%]	V <sub>OC</sub> [mV]	J <sub>SC</sub> [mA/cm <sup>2</sup> ]	FF [%]	R <sub>p</sub> [ $\Omega$ cm <sup>2</sup> ]
acetone	average	6.6 ± 0.2	461 ± 16	28.5 ± 0.5	45 ± 3	307 ± 23
InCl <sub>3</sub>	best cell	6.7	474	28.5	50	341
acetone	average	8.4 ± 0.5	518 ± 11	27.7 ± 0.9	57 ± 3	272 ± 15
TU	best cell	9.2	529	29.4	59	261
acetonitrile	average	6.1 ± 0.3	432 ± 11	29.1 ± 0.5	49 ± 1	291 ± 21
InCl <sub>3</sub>	best cell	6.5	440	29.3	51	323
acetonitrile	average	6.8 ± 0.5	451 ± 17	28.5 ± 0.7	51 ± 2	272 ± 21
TU	best cell	7.1	470	28.4	53	314

As shown in figure 3.7 the layers obtained with acetonitrile as solvent are similar to the ones sprayed from acetone. However, the PV performance of devices with In<sub>2</sub>S<sub>3</sub> buffer layer sprayed from acetonitrile is lower. The substrate temperature used for the deposition from acetonitrile solution reaches with 240 °C already values where copper diffusion and CuIn<sub>5</sub>S<sub>8</sub> phase formation can deteriorate the device performance (cf. section 4.2 and

5.2.1).

Figure 5.5 shows the J-V characteristics of devices with  $\text{In}_2\text{S}_3$  buffer layers deposited using different combinations of citric acid additive corresponding to the samples listed in table 5.3.

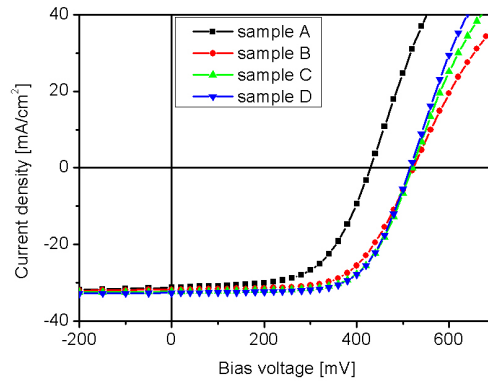


**Figure 5.5:** *J-V characteristics of CIGSSe solar cells with  $\text{In}_2\text{S}_3$  buffer layer deposited with different combinations of citric acid additives (cf. table 5.3).*

The solar cells on the device produced with a high citric acid concentration during the layer deposition (sample A) have a low average  $V_{OC}$  and FF of  $413 \pm 11$  mV and  $59 \pm 1\%$ , respectively. Reducing the citric acid concentration in the precursor solution (sample B-D) yields devices with improved average  $V_{OC}$  and FF (see table 5.3). The considerable increase of about 100 mV in the  $V_{OC}$  is also illustrated in figure 5.5 for the best cells of each sample. Remarkable are also the small deviations from the average value shown in table 5.3 for samples with citric acid as additive.

**Table 5.3:** *Average and best cell PV parameters of CIGSSe solar cells with  $\text{In}_2\text{S}_3$  deposited using different combinations of citric acid additives.*

Sample		$\eta$ [%]	$V_{OC}$ [mV]	$J_{SC}$ [mA/cm <sup>2</sup> ]	FF [%]	$R_p$ [ $\Omega\text{cm}^2$ ]
Sample A	average	$7.8 \pm 0.3$	$413 \pm 11$	$32.0 \pm 0.5$	$59 \pm 1$	$559 \pm 94$
	best cell	8.0	429	31.2	60	304
Sample B	average	$10.5 \pm 0.2$	$516 \pm 6$	$32.1 \pm 0.4$	$63 \pm 1$	$1191 \pm 251$
	best cell	10.8	522	31.8	63	1149
Sample C	average	$10.8 \pm 0.2$	$515 \pm 4$	$31.8 \pm 0.3$	$66 \pm 1$	$1500 \pm 254$
	best cell	11.1	520	32.3	66	1403
Sample D	average	$11.3 \pm 0.1$	$514 \pm 3$	$33.1 \pm 0.3$	$66 \pm 1$	$1097 \pm 251$
	best cell	11.5	516	33.5	67	1242

As discussed in section 3.5.2, almost no  $\text{In}_2\text{S}_3$  layer is obtained when using high concen-

tration of citric acid in the precursor solution. This explains the large difference in the voltage between sample A and B-D. Sample A has almost no buffer layer and the junction is formed directly between the ZnO bilayer of the front contact and the CIGSSe absorber.

The PV performance of samples B, C and D are promising also if compared to the devices sprayed without citric acid (figure 5.4b). The average  $V_{OC}$  is similar compared to the samples prepared with acetone and thiourea without citric acid but the  $J_{SC}$  and the FF values are higher.

### 5.2.3 Impact of the In to S ratio in the solution

In the investigation of the In to S ratio in the precursor solution for the USP- $In_2S_3$  buffer layer deposition absorber from the batch no. 1 were used. The elemental composition of the  $Cu(In,Ga)(S,Se)_2$  layers is given in table 5.1.

Figure 5.6 shows the external quantum efficiency curves of  $Cu(In,Ga)(S,Se)_2$  solar cells with USP- $In_2S_3$  buffer layers sprayed with In/S ratio of 1:1, 1:3 and 1:4. Not only the In/S ratio variation but also the different layer thicknesses have to be considered in the discussion on the current density. From calibration experiments of sprayed layers on SLG and Si substrate the buffer layer thicknesses from the cells in figure 5.6 are estimated to be 80 nm (1:1), 50 nm (1:3) and 40 nm (1:4). Transmittance and reflectance measurements of  $In_2S_3$  on SLG revealed that beside the absorption also the reflectance is thickness dependent for very thin layers (see section 3.5.4).

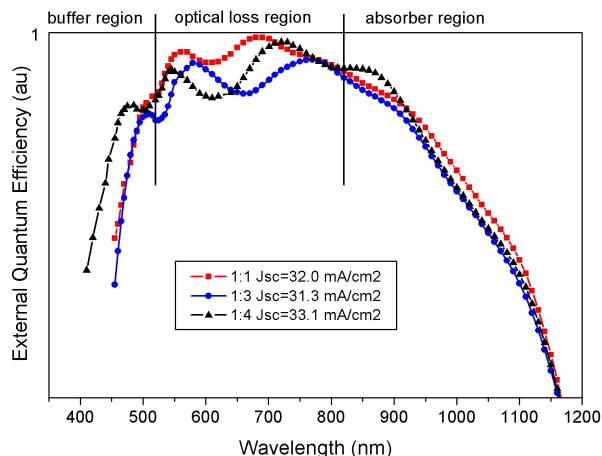


**Figure 5.6:** Normalized External Quantum Efficiency of CIGS solar cells with USP- $In_2S_3$  buffer layer sprayed with different In/S ratios in the precursor solution. The effect of the In/S ratio on the EQE is overlapping with the impact of different layer thicknesses. The given  $J_{SC}$  are derived from the area under the corresponding curve.

The difference in the optical loss region between the quantum efficiency curves for ratios of 1:3 and 1:4 can be attributed to the larger thickness of the  $In_2S_3$  layer sprayed with 1:3

solution, as the interference peaks shift towards longer wavelengths with increasing film thickness. In the buffer region (see fig. 5.6) the difference is due to increased absorption in the thicker layer, overlapped by interference effects. However, the EQE of the 1:1 sample shows a different behavior. Here, the additional chlorine in the buffer layer reduces reflection losses which can be seen in the optical loss region in figure 5.6. In the absorber region only minor differences are observed. Transmittance measurements of the corresponding buffer layers on SLG showed a shift of the absorption edge of the 1:1 sample towards lower wavelengths indicating a change in the absorption coefficient of the layer with high Cl content (see section 3.5.4).

## 5.2.4 Impact of device light soaking and annealing

### 5.2.4.1 Light soaking

For Light-soaking the sample were illuminated with white light and sample temperature was kept constant at 80 °C. No significant effects were observed with standard SLG/Mo/Cu(In,Ga)(S,Se)<sub>2</sub>/In<sub>2</sub>S<sub>3</sub>/i-ZnO/AZO devices as shown in figure 5.7. The used absorbers are from batch no. 4.

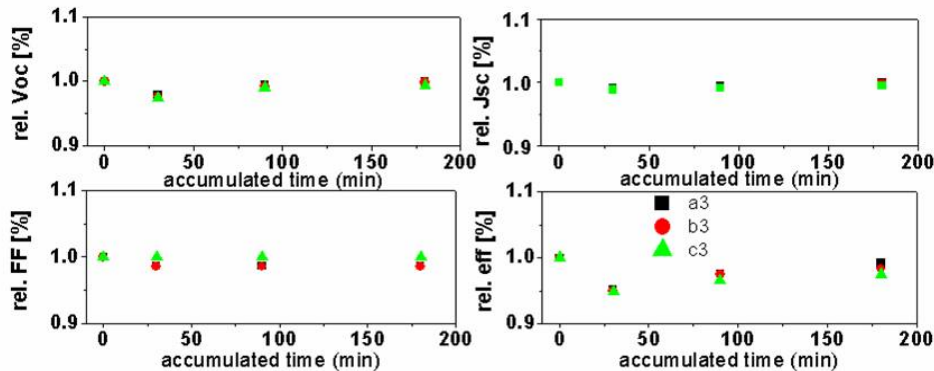


**Figure 5.7:** Relative change of the PV parameters due to light-soaking of standard devices with USP-In<sub>2</sub>S<sub>3</sub> buffer layer. The samples were subsequently light soaked for 30 min, 60 min and 90 min. After each period J-V characteristics were measured and the light soaking was immediately started again. The x-axis shows the accumulated time.

Due to band alignment considerations, also devices without i-ZnO between the buffer and the front contact layers were investigated (see also section 1.4). The initial solar cell performance of those devices was comparable to devices with i-ZnO layer, but efficiency degraded rapidly due to losses in  $V_{OC}$  and FF (fig. 5.8). Already after 5 min of light-soaking under abovementioned conditions, the  $V_{OC}$  and FF decreased below 90% of the initial values and decrease further below 70% for devices with thinner In<sub>2</sub>S<sub>3</sub> and even below 60% for devices with the thicker In<sub>2</sub>S<sub>3</sub> after 180 min of accumulated light soaking. The data points at times higher 200 min are the performances after one day in dark.  $V_{OC}$  and FF of the devices without i-ZnO partly recover but by far do not reach the initial values. The devices with i-ZnO layer do not show any light soaking effect in  $V_{OC}$ , the FF

of the cells with thinner  $\text{In}_2\text{S}_3$ , however, also decreases to about 70% of the initial value after 180 min but recovers almost completely after one day in dark.

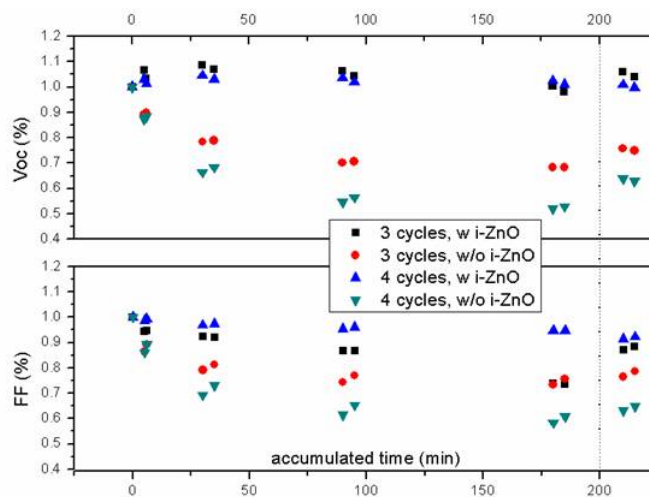


**Figure 5.8:** Relative change of the PV parameters due to light-soaking of devices with and without  $i\text{-ZnO}$  ( $i\text{-ZnO}$ ) and different  $\text{In}_2\text{S}_3$  layer thicknesses. The values given above 200 min are the PV parameters after keeping the samples one day in dark.

#### 5.2.4.2 Device annealing

Figure 5.9 shows the effect of air annealing treatment performed at  $200^\circ\text{C}$  for 5 min on the finished solar cell devices with  $\text{Cu}(\text{In,Ga})(\text{S,Se})_2$  absorbers from batch no. 1. The  $\text{In}_2\text{S}_3$  buffer layer was sprayed from precursor solutions with varying In/S ratios. Average parameters of nine cells of small area on one substrate and the corresponding standard deviations in each case are plotted.

The annealing step showed only minor improvements in the  $V_{\text{OC}}$  with exception for an In/S ratio of 1:4, at which it increases by 25 mV. After the annealing step the cell efficiency is about 10% and the  $V_{\text{oc}}$  above 500 mV, irrespective of the In/S ratio in the solution. The as-deposited devices show highest FF of 67% for a ratio of 1:3, but after annealing highest FF (67%) is observed with an In/S ratio of 1:2. Starting from an In/S ratio of 1:1 and increasing the sulfur amount the short circuit current density ( $J_{\text{SC}}$ ) first decreases but then again increases in case of a ratio of 1:4. Annealing increases the  $J_{\text{SC}}$  by 6-10%, irrespective of the In/S ratio.

An increase of 1-3  $\text{mA}/\text{cm}^2$  is observed for all investigated absorber batches with USP- $\text{In}_2\text{S}_3$  buffer layer. A change in the  $V_{\text{OC}}$  and FF is only observed after aging of the absorber. However, if the absorbers are etched with KCN prior to the buffer deposition, the as deposited  $V_{\text{OC}}$  and FF are already relatively high and do not change after device annealing at  $200^\circ\text{C}$  for 5 min.

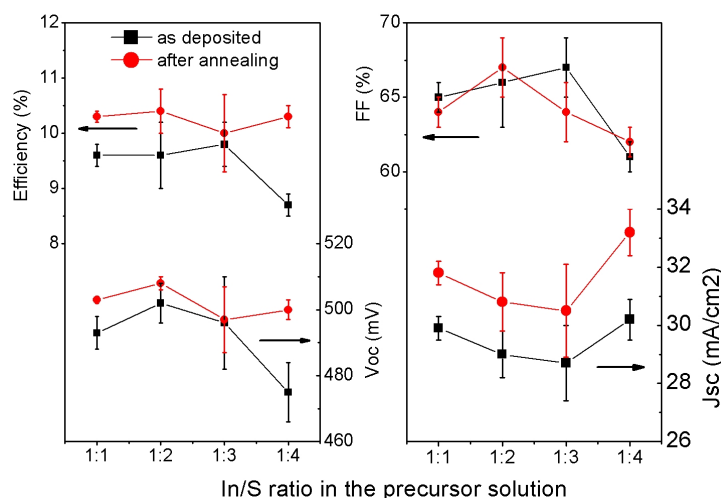


**Figure 5.9:** Impact of the In/S ratio in the precursor solution and annealing treatment at 200°C for 5 min on the PV-parameters of solar cells with  $\text{In}_2\text{S}_3$  buffer layers deposited at 200°C. For the sake of clarity the data points are connected.

PV parameters of a CIGSSe solar cell as deposited and annealed with absorber from batch 2 are presented in table 5.4. The depth profile of this sample is shown in figure 5.2.

**Table 5.4:** PV parameters of CIGSSe solar cells with  $\text{In}_2\text{S}_3$  as deposited and after device annealing at 200°C for 5 min. The depth profile of these cells is shown in figure 5.2

Sample	$\eta$ [%]	$V_{OC}$ [mV]	$J_{SC}$ [mA/cm <sup>2</sup> ]	FF [%]
as-dep	8.9	481	29	64
5'@200°C	10.7	512	30.3	69

### 5.3 Performance with reference to CdS buffer layer

In order to compare the device performance of CIGSSe solar cells with USP- $\text{In}_2\text{S}_3$  buffer layer with state-of-the-art technology and also to determine the absorbers quality of the different batches, CBD-CdS reference devices were prepared.

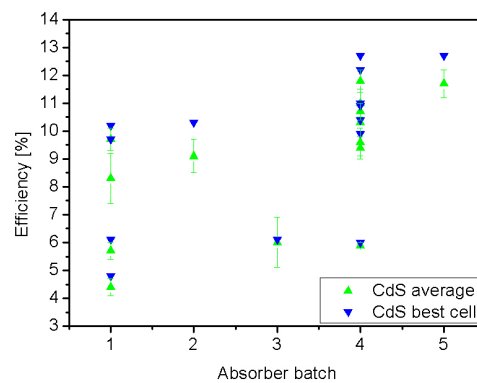
#### 5.3.1 Definition of the CdS reference

Figure 5.10 shows the average and best cell efficiencies of CIGSSe solar cells with CBD-CdS buffer layers for the investigated batches. The efficiency varies strongly between different batches but also within the single batches and the variation is not consistent with applied surface treatments before buffer deposition. Best performance for batch 1 was obtained after etching the absorber surface in KCN (10%) for 10 seconds whereas for batch 2 surface



etching was detrimental.

The impact of different surface etching as well as the history of the absorber was investigated more closely with batch no. 4. Figure 5.11 illustrates the PV parameters for different pre-treatment procedures. The CdS buffer layer of the first two devices was deposited by the industrial partner before sending the samples. The bare absorber of sample 3 was resent to the industrial partner for CdS deposition in order to investigate the effect of transport. The CdS buffer layer of samples 4-7 was deposited in-house with the standard recipe used for highly efficient CIGS solar cells. For those samples different etching treatments were applied. The front contact of all samples was deposited identically in our research laboratory.



**Figure 5.10:** Conversion efficiency of CIGSSe solar cells with absorbers from different batches and CBD-CdS buffer layer.

The data of the samples 1-3 indicate that the history of the absorber does not adversely affect the performance if the CBD-CdS procedure of the industrial partner is used. The deposition procedure especially the application of a surface cleaning before the CdS layer deposition used by the industrial partner is not known. The performance data in figure 5.11 show that a surface treatment of the absorber from batch 4 is mandatory if the CdS is not deposited by the industrial partner. Best results are obtained with a KCN (10%) etching for 10 seconds at room temperature. However, also ammonia (1 mol/l) etching for 2 min at room temperature already yields a significant increase of  $V_{OC}$  and FF. This indicates the importance for removing surface oxides before the buffer deposition of batch no. 4. With this absorber batch best efficiency of 12.7% was obtained with CBD-CdS deposited by the industrial partner and 10.9% with in-house CBD after KCN etching. In contrast, with batch no. 5 best efficiency of 12.7% was achieved with in-house CBD without any surface treatment of the absorber.

This shows that the definition of a simple reference procedure which is valid for all batches is not possible. In the following section always the best CdS reference obtained with in-house CBD for each batch is used to compare with the performance of the alternative

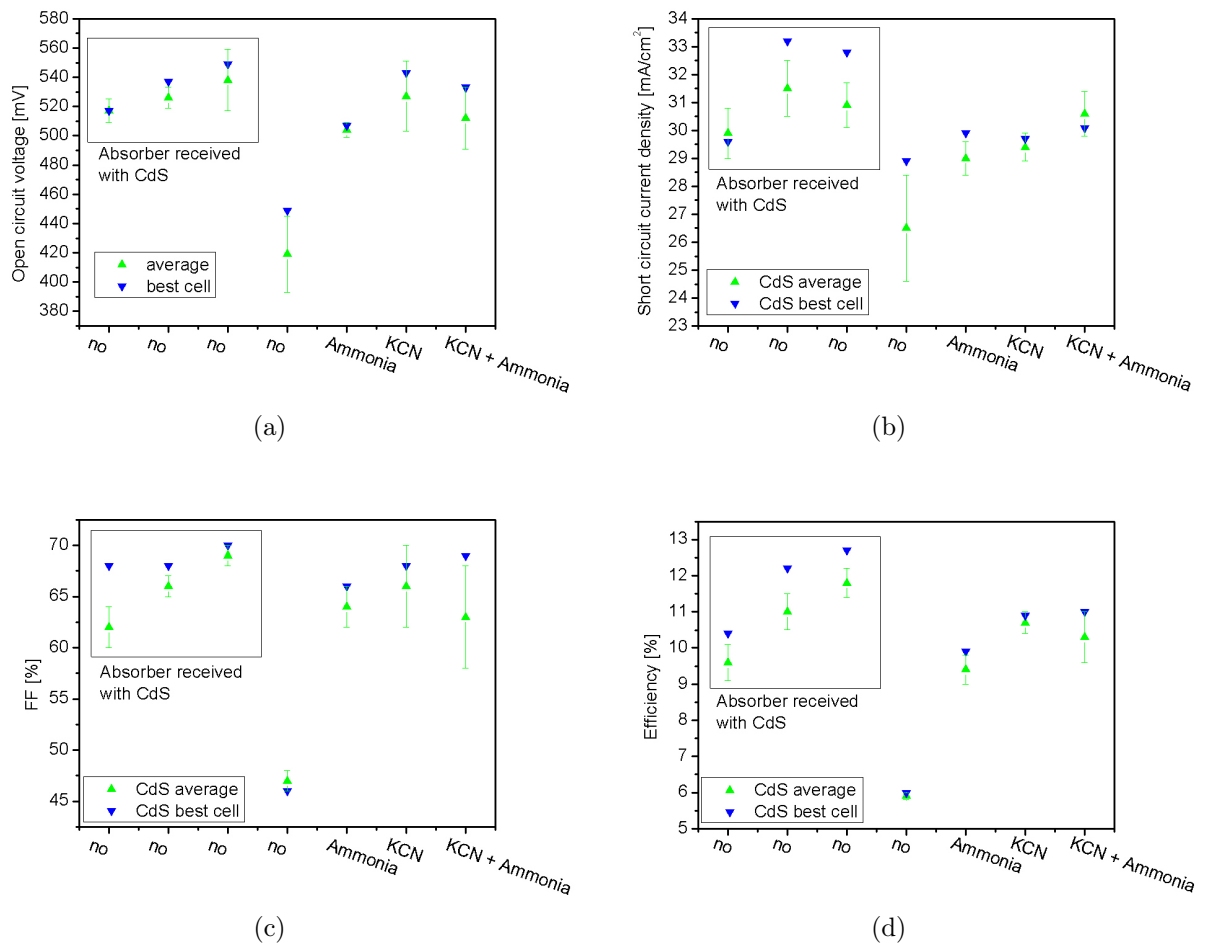


**Figure 5.11:** Comparison of different surface treatments prior to the chemical bath deposition on the absorber of the batch number 4. Additionally, the effect of shipping of absorbers and the CBD procedure itself are investigated.

buffer layers.

### 5.3.2 PV performance

Figure 5.12 compares the PV parameters of CIGSSe thin film solar cells with USP- $\text{In}_2\text{S}_3$  and CBD-CdS buffer layer. With batch no. 3 high efficiency was not obtained, irrespective of the buffer layer material. Therefore it is ignored in the following. The  $V_{\text{OC}}$  of the devices with USP- $\text{In}_2\text{S}_3$  stays 500 and 520 mV for all batches. The  $V_{\text{OC}}$  of the CdS buffered cells is up to 36 mV higher and reaches an value of 552 mV for batch no. 5. The USP- $\text{In}_2\text{S}_3$  buffered device from batch no. 2 yields highest  $J_{\text{SC}}$  ( $34.7 \text{ mA/cm}^2$ ) and FF (71%) and with the  $V_{\text{OC}}$  of 502 mV this results in 12.4% efficiency. This corresponds to 120% if compared to the CBD-CdS reference cell of the same batch and to 98% if compared to the best CBD-CdS reference cell from all batches.

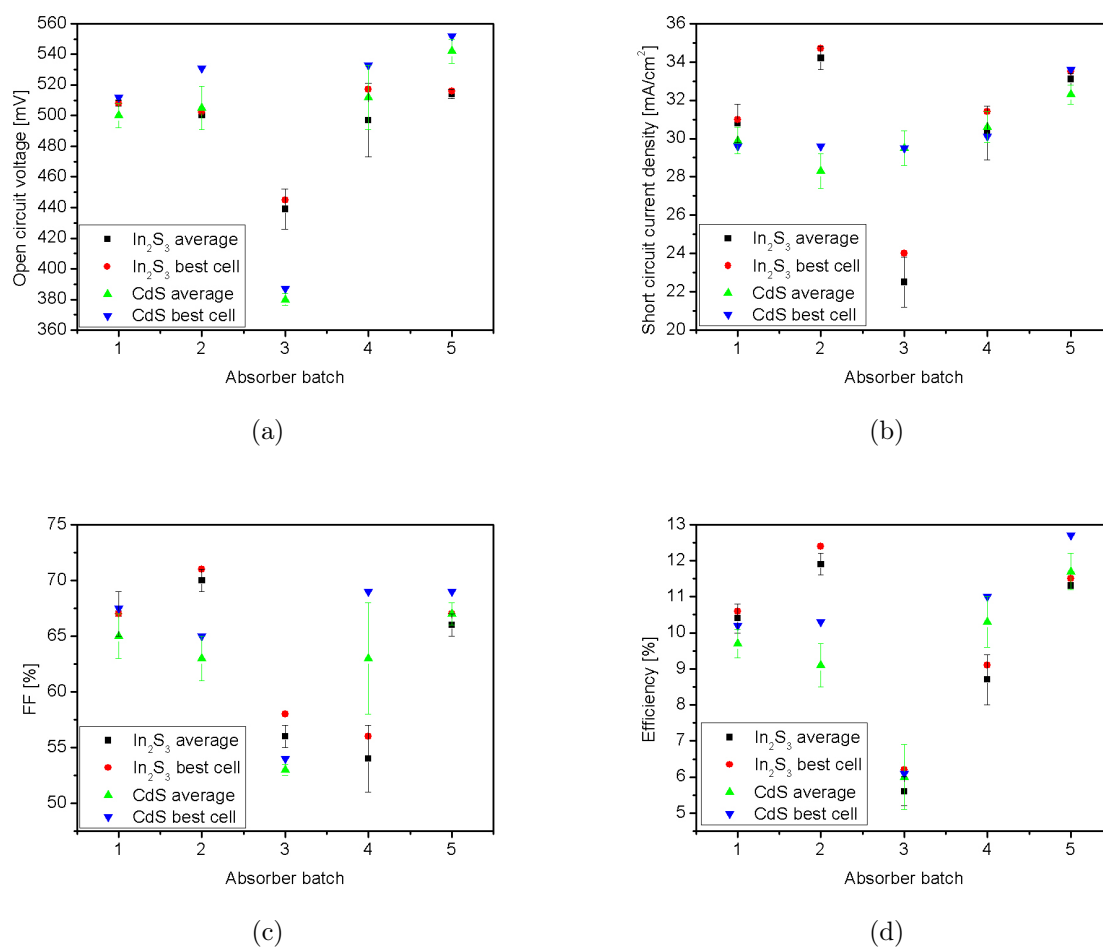


**Figure 5.12:** PV performance of CIGSSe thin film solar cells with USP- $\text{In}_2\text{S}_3$  buffer layers on different absorber batches. Also shown are the selected CBD-CdS references.

Also the efficiency of the cells with USP-In<sub>2</sub>S<sub>3</sub> buffer layer on absorber from batch no. 1 and 5 are close to the corresponding reference with 104% and 91%, respectively.

Of the investigated batches the absorbers from batch no. 2 have an exceptional high sulfur content resulting in a [S]/[Se+S] ratio of 0.18 (see table 5.1). The increased sulfur content and with this the widening of the band gap at the surface of the absorber by down shifting of the valence band [124] can affect the junction formation beneficially. However, only one batch with increased sulfur content was supplied and investigated. Thus, considering also the irreproducibility of the CBD-CdS references an ultimate conclusion on the influence of the [S]/[Se+S] ratio is not possible.

## 5.4 Summary and conclusion

Sulfur containing CIGSSe absorber grown by rapid thermal processing have a high surface roughness. With the USP method is possible to cover those rough surfaces with a compact In<sub>2</sub>S<sub>3</sub> layer. Even though the CIGSSe absorbers are extremely copper-poor, copper diffusion from the absorber into the buffer layer is detected with XPS depth profiling. After device annealing at 200 °C for 5 min the width of the In<sub>2</sub>S<sub>3</sub> region in the XPS depth profile is decreased indicating a reconstruction of the interface region due to provided thermal energy during the annealing treatment.

The optimum deposition temperature for the USP-In<sub>2</sub>S<sub>3</sub> layer onto the absorber was found to be 200 °C. Acetone and methanol proved to be best solvents for ideal In<sub>2</sub>S<sub>3</sub> layer growth. Citric acid and thiourea were found to be suitable antioxidant agents in order to reduce the surface oxygenation of the absorber layer during buffer layer deposition.

Variation of sulfur deficiency in the precursor solution is a tool for the optical absorption properties of the In<sub>2</sub>S<sub>3</sub> buffer layer by introducing chlorine. Furthermore reflection losses can be reduced with this parameter. Sulfur excess variation mainly influences the layer growth and absorber surface by adding more sulfur. Best cell efficiency of 12.4% was obtained with a CIGSSe absorber and USP-In<sub>2</sub>S<sub>3</sub> buffer layer sprayed with sulfur excess.

No significant effects of white light soaking at 80 °C on the device performance were observed with standard SLG/Mo/CIGSSe/In<sub>2</sub>S<sub>3</sub>/i-ZnO/AZO devices. Omitting the i-ZnO layer, the initial solar cell performance of is comparable to devices with i-ZnO layer, but the efficiency degraded rapidly during light soaking due to losses in V<sub>OC</sub> and FF.

Post-deposition device annealing in air at 200 °C for 5 min yields an increase of 1-3 mA/cm<sup>2</sup> for all investigated absorber batches with USP-In<sub>2</sub>S<sub>3</sub> buffer layer. A change in the V<sub>OC</sub> and FF is only observed after aging of the absorber. However, if the absorbers are etched with KCN prior to the buffer deposition, the as deposited V<sub>OC</sub> and FF are already relatively high and do not change after device annealing.

---

The highest total area efficiency of 12.4% was achieved with CIGSSe absorber from batch no. 2 with highest [S]/[Se+S] ratio in this investigation. This corresponds to 120% if compared to the CBD-CdS reference cell of the same batch and to 98% if compared to the best CBD-CdS reference cell from all batches.



## 6 Other alternative buffer layers

Parts of this chapter were gathered during the diploma thesis of Carolin Fella [121].

Zinc sulfide is a semiconductor material with a wide direct band gap of about 3.6 eV. Due to its physical properties, e.g. high refractive index and large band gap energy, it has a potential for applications in chalcopyrite solar cells as buffer layer. In this chapter the application of ZnS as buffer layer deposited with ultrasonic spray pyrolysis in Cu(In,Ga)(S,Se)<sub>2</sub> solar cells is investigated.

### 6.1 Deposition of ZnS films

For the deposition of ZnS layers the precursor chemicals zinc chloride hydrate ( $\text{ZnCl}_2(\text{H}_2\text{O})$ , 99.999% from Alfa Aesar) and thiourea ( $\text{CS}(\text{NH}_2)_2$ , 99.0% from Fluka) were used.

The effect of the Zn to S ratio in the precursor solution (1:1 and 1:2) and of the deposition temperature on the layer properties and the PV parameters are discussed in this section. Acetone is used as solvent with 0.1 mol/l thiourea. The concentration of  $\text{ZnCl}_2$  in the solution is 0.05 mol/l and 0.1 mol/l, respectively. ZnS layers are sprayed on glass substrates heated to 180°C, 230°C, 280°C and 330°C for various spraying times.

The transmission and reflection spectra of ZnS layers deposited on soda lime glass at different substrate temperatures are shown in figure 6.1. The transmittance decreases with increasing substrate temperature for both Zn/S ratios. This decrease in transmittance results mainly from an increased reflectance.

Rutherford backscattering spectroscopy (RBS) was used in order to determine the elemental composition of the grown ZnS layers. For the RBS measurement ZnS layers were deposited on silicon wafers with the same spray parameters as before. The RBS spectra are presented in figure 6.2. Three peaks are measured for all investigated layers which can clearly be identified with the elements zinc, sulfur and chlorine. The calculated compositions are given in table 6.1. These calculations suggest that the sprayed layers are composed of stoichiometric ZnS with chlorine impurities.

The amount of chlorine impurity decreases with increasing deposition temperature and increasing amount of sulfur available during reaction. The same behavior was also observed for chlorine impurities in USP-In<sub>2</sub>S<sub>3</sub> (see section 3.5.3). From the width of the peaks in

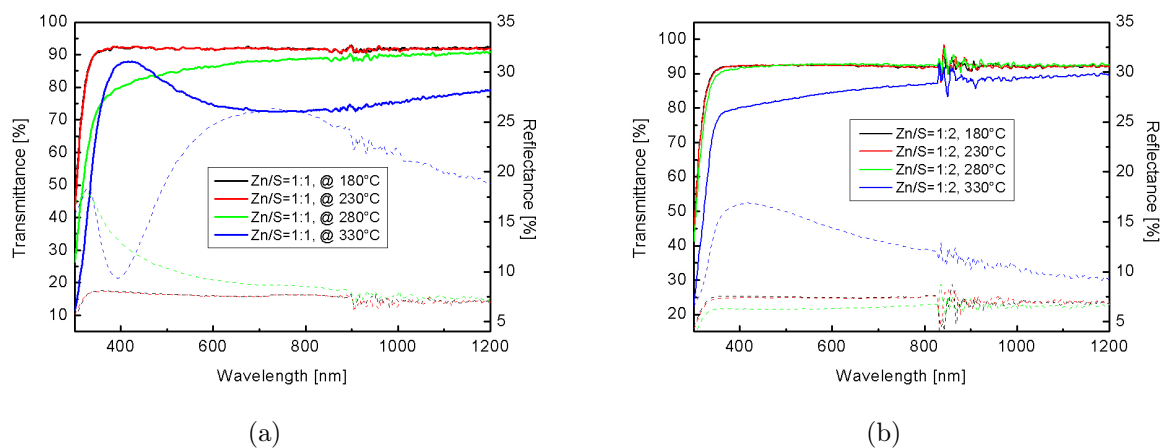


**Figure 6.1:** Transmission and reflection spectra of thin ZnS films obtained from solution B1 and C2 after 30 minutes spray time. Continuous lines show the transmission and dotted lines the reflectance. The same color corresponds to samples with a certain deposition temperatures.

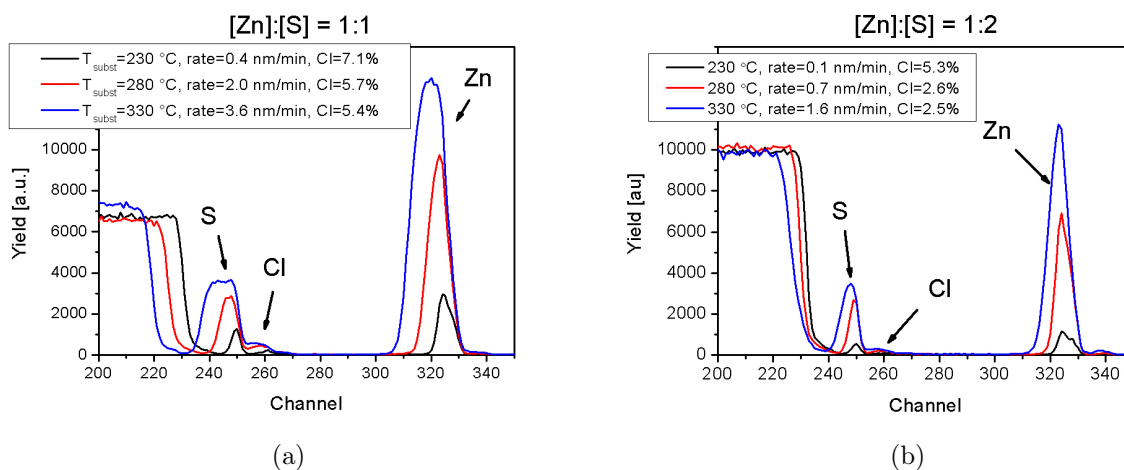


**Figure 6.2:** RBS data for thin ZnS films depending on the precursor ratios  $Zn/S = 1:2$  and  $1:1$  and the deposition temperature.



the RBS spectra the growth rate of the ZnS layer is estimated. For this estimation the density of the layer is assumed to be the one of pure ZnS. The values for the growth rate are also given in table 6.1. The dependence of the growth rate on the temperature and the precursor ratio are the same as observed for the USP-In<sub>2</sub>S<sub>3</sub> layers described in section 3.4.

**Table 6.1:** Chemical composition of USP-ZnS layers deposited at different substrate temperatures and precursor ratios.

Temp [°C]	In/S=1:1				In/S=1:2			
	Zn [%]	S [%]	Cl [%]	rate [nm/min]	Zn [%]	S [%]	Cl [%]	rate [nm/min]
230	47.6	45.2	7.1	0.4	48.5	46.1	5.3	0.1
280	47.8	46.4	5.7	2	51.3	46.2	2.6	0.7
330	49.3	45.3	5.4	3.6	50.0	47.5	2.5	1.5

## 6.2 Photovoltaic performance with ZnS buffer layer

Solar cells were prepared with Cu(In,Ga)(S,Se)<sub>2</sub> absorbers from batch F. The best CBD-CdS reference fabricated on this batch reached an efficiency of 11.4%. Prior to the buffer layer deposition the Cu(In,Ga)(S,Se)<sub>2</sub> absorbers were chemically etched for 2 minutes in aqueous solution with 1 mol/l NH<sub>4</sub>OH and rinsed with de-ionized water finally dried with pure nitrogen. Before placing the absorber layer on the hot plate the quasi closed chamber below the funnel is saturated with the precursor chemical mist and the inert nitrogen carrier gas causing a minimum of oxygen present. The samples are then placed onto the hot plate directly in the saturated atmosphere and the zinc sulfide deposition is started immediately.

In first set of experiments the deposition temperature was set to 170°C, 220°C, 270°C and 320°C while the spray time was kept constant at 15 min. The effect of the Zn/S ratio on the finished solar cell devices with Cu(In,Ga)(S,Se)<sub>2</sub> absorbers is illustrated in figure 6.3. The best cell out of nine cells on 2.5x2.5cm<sup>2</sup> substrates, the best reference CBD-CdS cell and a cell without buffer layer are plotted.

The substrate temperature has a significant influence on all PV parameters. The as-deposited devices show highest PV parameters at 220°C. Irrespective of the substrate temperature the performance of devices with ZnS buffer layer sprayed from solution with 1:1 zinc to sulfur ratio is higher than those with ZnS sprayed from 1:2 ratio. A possible explanation could be that the layer grown from the solution with 1:1 ratio covers the absorber completely while the other does not. As expected, the short circuit current is higher for cells with USP-ZnS than for cells with CBD-CdS buffer layer due to the higher transmission in the blue wavelength region, provided that the deposition temperature is

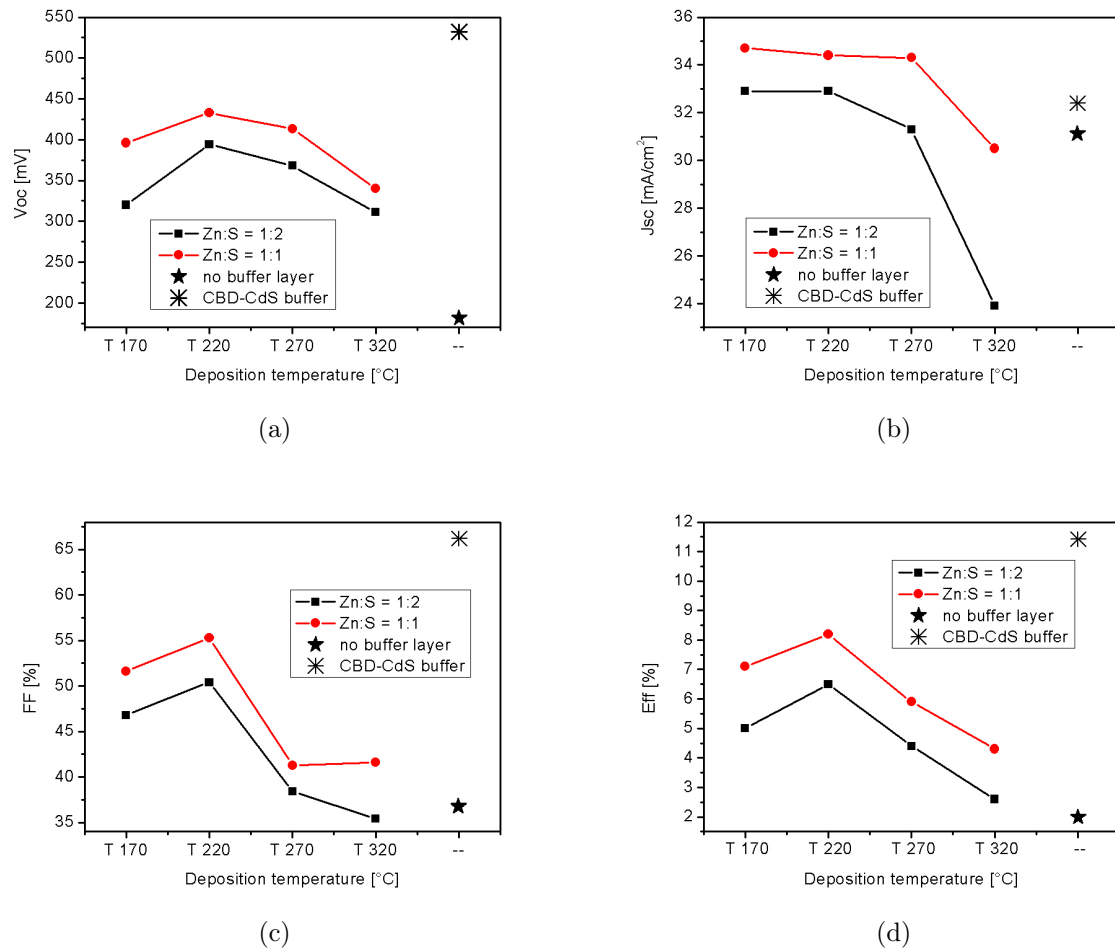


**Figure 6.3:** PV parameters of  $\text{Cu(In,Ga)(S,Se)}_2$  solar cells with USP-ZnS buffer layer sprayed with Zn/S ratios 1:2 and 1:1 deposited at different temperatures for a deposition time of 15 minutes. Also indicated are the PV parameters for a solar cell without buffer layer and the CBD-CdS reference cell. For the sake of clarity the data points are connected.

not too high. All the other parameters of the as-deposited samples are below the CBD-CdS reference. Obvious reasons for the poor FF of the USP-ZnS cells are large series and small shunt resistances. The poor  $V_{OC}$  could stem from higher recombination in the ZnS-absorber interface.

Light soaking experiments under 1 sun at  $80^\circ\text{C}$  for 21 hours did not show any reversible or irreversible changes of the PV parameters. To investigate the influence of the layer thickness, the spray time was varied at constant temperatures of  $170^\circ\text{C}$  and  $220^\circ\text{C}$  and with Zn/S ratio of 1:1. Figure 6.4 shows the PV parameters of CIGSSe solar cells with USP-ZnS buffer layers deposited at  $220^\circ\text{C}$  before (0 minutes) and after air-annealing treatment at  $200^\circ\text{C}$  of the completed device. Similar effects are observed with USP-ZnS layers deposited at  $170^\circ\text{C}$  (cf. the J-V characteristics in fig. 6.5a).

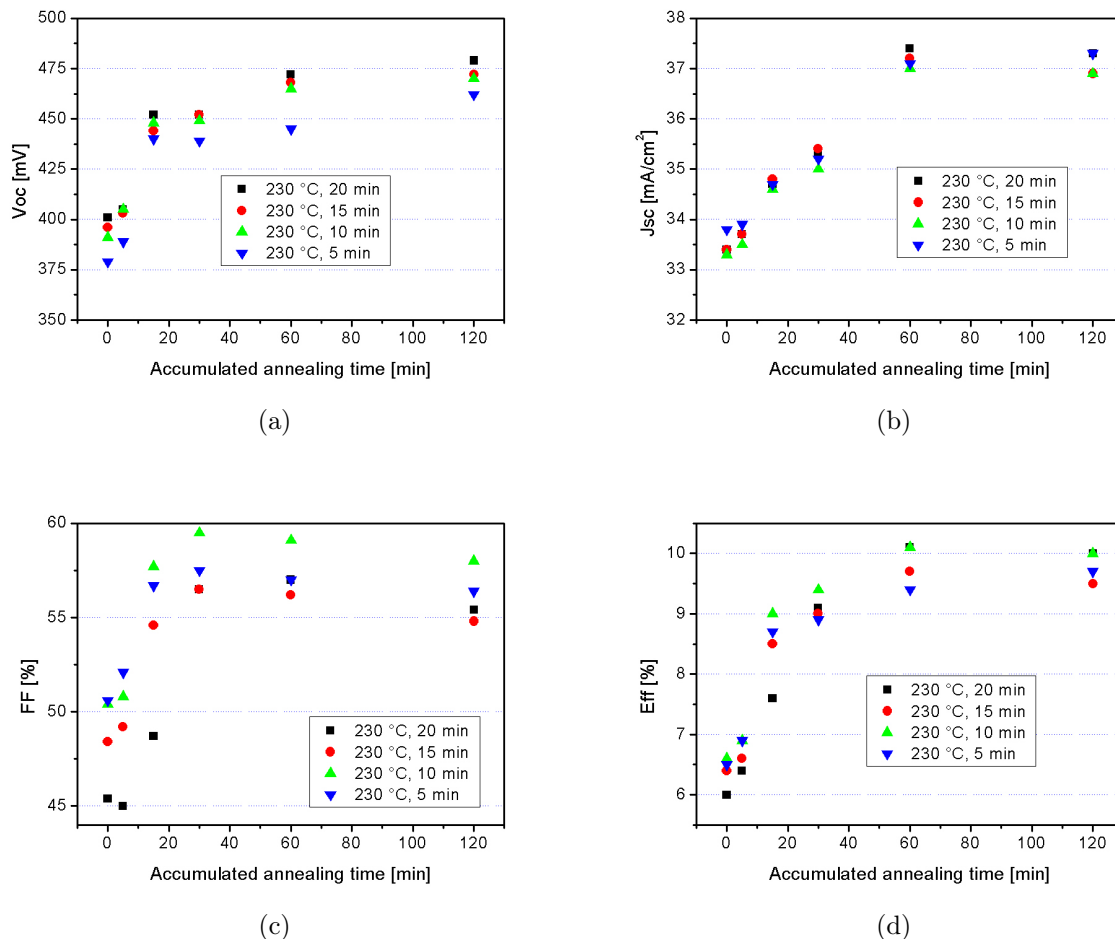


**Figure 6.4:** PV parameters of CIGSSe solar cells with USP-ZnS buffer layer sprayed with Zn/S ratio 1:1 deposited at  $T = 220^\circ\text{C}$  for deposition times ranging from 5 to 20 minutes. The effect of a post-deposition air-annealing of the finished device at  $200^\circ\text{C}$  is indicated by the x-axis showing the accumulated annealing time.

The effect of device annealing on the PV performance can be divided into two steps irrespective of the ZnS deposition temperature and layer thickness. In a first step the  $V_{OC}$  and FF considerably increase after 20 min of accumulated annealing time. In a second step a further increase in the  $V_{OC}$  is observed along with a significant increase in the  $J_{SC}$  after 60 min of accumulated annealing time.

Possible mechanisms during the annealing treatment are: (i) interdiffusion of zinc at the buffer - absorber interface into the  $Cu(In,Ga)(S,Se)_2$  resulting in n-type Zn doping of the absorber. Depending on how far the zinc diffuses into the absorber this could form a buried junction in the CIGS. The zinc could occupy copper valencies in the at the CIGS surface resulting net positive interface charges. This would pin the Fermi-level close to the conduction band at the interface. (ii) Intermixing of ZnS and ZnO is expected to form a  $Zn(O,S)$  buffer layer what would enhance the band alignment between the absorber and the buffer layer.

In the quantum efficiency plot in figure 6.5b the increase of the current density after 60 min air annealing is shown as a function of the wavelength. The quantum efficiency increases in the high energy region and decreases in the low energy region. The increase for higher energies suggests that the optical properties of the ZnO-ZnS bilayer change after sufficient air annealing. Also shown in figure 6.5b is the quantum efficiency of the CBD-Cds reference device. The advantage of reduced parasitic absorption of the zinc based buffer layer is obvious.

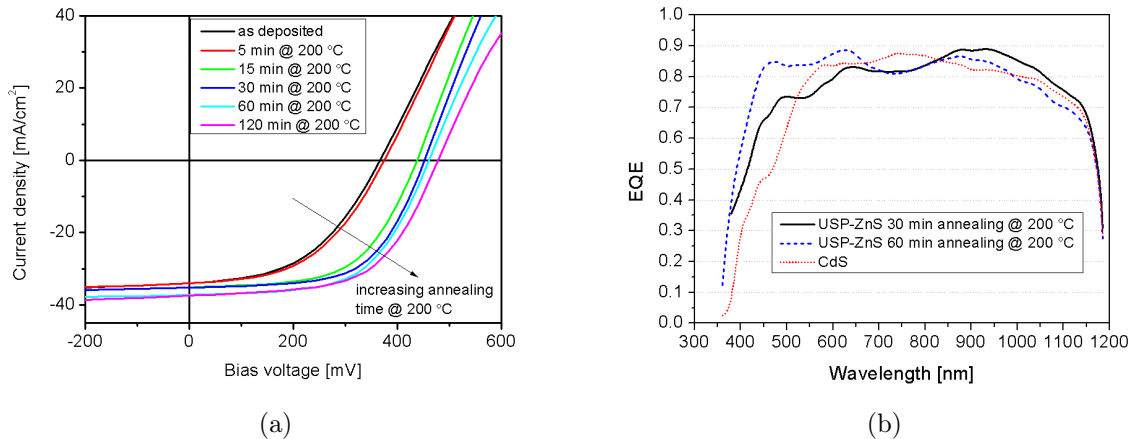


**Figure 6.5:** (a)  $J$ - $V$  characteristics of the best CIGSSe based solar cells with USP-ZnS buffer layer grown from 1:1 solution at  $170^\circ\text{C}$  for a spraying time of 20 minutes. The effects of annealing treatment are shown. (b) External quantum efficiency of the same solar cells; the air-annealing effect after between 30 and 60 minutes is shown. For comparison the curve of the CBD-CdS reference solar cell is also plotted.

A conversion efficiency of 10.8% is reached after 120 minutes air-annealing at  $200^\circ\text{C}$ . The corresponding efficiency of the CBD-CdS reference cell is 11.4%. The  $J$ - $V$  characteristics

are compared in figure 6.6. The current density of the USP-ZnS cell is 5.6 mA higher as the corresponding CdS reference, but FF and also  $V_{OC}$  of the CdS reference are higher. Table 6.2 summarizes the PV parameters of the best USP-ZnS device and the CBD-CdS reference.

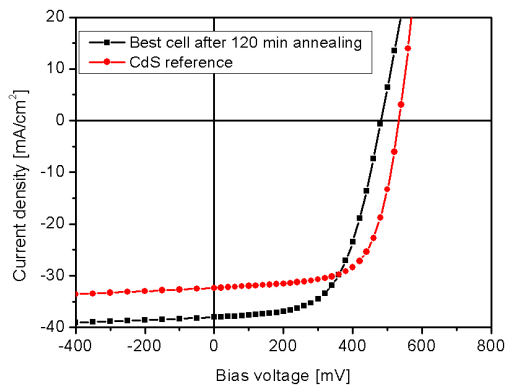


**Figure 6.6:** Comparison of the  $J$ - $V$  characteristics of CIGSSe devices with USP-ZnS and CBD-CdS buffer layer.

**Table 6.2:** PV parameter of the best USP-ZnS solar cell before and after 120 minutes air-annealing compared to the CBD-CdS reference

Sample	$\eta$ [%]	$V_{OC}$ [mV]	$J_{SC}$ [mA/cm <sup>2</sup> ]	FF [%]
USP-ZnS	5.4	331	34.5	47.1
as-dep				
USP-ZnS	10.8	482	38	59.2
annealed				
CBD-CdS	11.4	533	32.4	66.2

### 6.3 Summary and conclusion

With USP method stoichiometric ZnS layers can be grown from zinc chloride and thiorea precursors dissolved in acetone. Chlorine impurities are found in the sprayed ZnS layers. The amount of chlorine impurity decreases with increasing deposition temperature and increasing amount of sulfur available during reaction. The same behavior was also observed for chlorine impurities in USP-In<sub>2</sub>S<sub>3</sub> layers.

A temperature variation of the CIGSSe substrate showed that best performance is obtained with about 220 °C deposition temperature. The same temperature dependency was found for USP-ZnS layers sprayed with Zn/S ratio of 1:1 and 1:2, whereas the layers

sprayed with 1:1 showed slightly superior performance.

A significant increase of all PV parameters of CIGSSe solar cells with USP-ZnS buffer layer is observed after device annealing in air at 200 °C. The effect of device annealing on the PV performance can be divided into two steps irrespective of the ZnS deposition temperature and layer thickness. In a first step the  $V_{OC}$  and FF considerably increase after 20 min of accumulated annealing time. In a second step a further increase in the  $V_{OC}$  is observed along with a significant increase in the  $J_{SC}$  after 60 min of accumulated annealing time caused by a modification of the optical properties of the ZnO-ZnS layer stack.

Highest total area efficiency of 10.8% is obtained with USP-ZnS buffer layer on CIGSSe absorbers, however with major losses in  $V_{OC}$  and FF compared to the CdS reference with an efficiency of 11.4%. The losses result from an unfavorable band alignment of the ZnO/ZnS/CIGSSe stack. Partial substitution of oxygen for the sulfur in ZnS should yield an optimized band alignment and thus improve the device performance.

## 7 Outlook and closing remarks

Ultrasonic spray pyrolysis is a suitable method for buffer layer deposition in chalcopyrite based solar cells. Homogeneous and compact  $\text{In}_2\text{S}_3$  and  $\text{ZnS}$  layers with continuous substrate coverage are obtained within this work from methanol or acetone based solutions at deposition temperature around  $200^\circ\text{C}$ . Impurities of extrinsic elements such as chlorine and oxygen can be minimized by increasing the temperature and amount of sulfur excess in the solution. However, the experiments showed that the elevated temperature which is necessary for the USP deposition amplifies oxygenation of the CIGS surface, i.e. selenium vacancies are filled with oxygen and with this positive surface charges of the CIGS are reduced. This effect can be minimized by oxygen control and additional partial electrolyte treatment. By further exploration of in-situ surface treatments of the CIGS absorber during the spray process such as aerosol assisted etching prior to the deposition more positive surface charges should be restored resulting in improved device performance.

Systematic variation of the gallium concentration, i.e. the position of the conduction band, in the CIGS absorber indicated a transition of the conduction band alignment from spike to cliff if the  $[\text{Ga}]/[\text{III}]$  ratio is increased above 22%. Furthermore, the analysis of the dominant recombination mechanism before and after device annealing suggest the formation of a copper depleted resulting in a band gap widening in the surface region of the CIGS absorber. Measuring the valence band offset by Ultraviolet Photoelectron Spectroscopy (USP) or X-ray Photoelectron Spectroscopy (XPS) and/or the conduction band offset by Inverse Photoelectron Spectroscopy (IPES) would give clarity about the band alignment in the system. However, measuring a depth profile of the bands in the buffer-absorber stack requires stepwise sputtering of the material. Sputtering of  $\text{In}_2\text{S}_3$ ,  $\text{ZnS}$ , and CIGS results in significant changes of the composition and with this also in the band structure due to sulfur or selenium depletion. Using non-destructive synchrotron based photoelectron spectroscopy, where the information depth can be tuned by the energy of the synchrotron radiation, should yield a direct proof of the proposed band alignments.

The USP- $\text{In}_2\text{S}_3$  buffer layer works well CIS and CIGS based solar cells with low gallium content. Equal or even superior efficiencies should be obtained with USP- $\text{In}_2\text{S}_3$  compared to CBD- $\text{CdS}$  buffer layers in CIGS solar cells up to a  $[\text{Ga}]/[\text{III}]$  ratio of 22%. Increasing the  $[\text{Ga}]/[\text{III}]$  ratio above 22% results in increased charge carrier recombination as well as FF and  $J_{\text{SC}}$  limitations due to unfavorable conduction band alignment. This means that USP- $\text{In}_2\text{S}_3$  as buffer layer in CIGS thin film solar cells has its limitations for very high efficiency devices since the band gap of the absorber can not be increased to the optimum

value for conversion of AM1.5G spectrum. Further improving the tradeoff between the short circuit current density and the open circuit voltage in the device by fixing the band gap of the CIGS surface region such that the conduction band alignment between the absorber and buffer is flat and optimizing the minimum band gap in the CIGS would yield the highest efficiency with USP-In<sub>2</sub>S<sub>3</sub> buffer layer.



# Acknowledgment

First of all I thank Prof. Dr. Ayodhya Nath Tiwari, head of the Laboratory for Thin Films and Photovoltaics at Empa, and Prof. Dr. Danilo Pescia, Head of the Microstructure Research Group, Laboratory for Solid State Physics, ETH Zürich for their support, advice, and supervision of my PhD thesis.

Further I thank Prof. Dr. Marc Burgelman, Electronics and Information Systems, University of Gent, for being external examiner of this thesis, his motivation, fruitful discussions, and access to his laboratory. I also thank Koen Decock for support and discussions.

Special thanks go to Adrian Chirila for continuous supply of CIGS absorbers, to the semester, master and diploma students Thomas Uehlinger, Dario Corica, Rodrigo Lopes Sauaia, Simon Haenni, Fabian Pianezzi, and Carolin Fella for their help and good results and to all the other former and current members and academic guests of the research group: Alessandro Romeo, Daniel Abou-Ras, Dominik Rudmann, Marc Kaelin, David Bremaud, Kaja Ernits, Chris Hibberd, Sonya Calnan, Maxim Ganchev, Osvaldo Moreira, Dominik Guettler, Shiro Nishiwaki, Rajneesh Verma, Sigi Seyrling, Julian Perrenoud, Yaroslav Romanyuk, Patrick Ploesch, Lukas Kranz, Alexander Uhl. I also thank our secretaries Rosemarie Lacher and Chantal Haenni and all current and former technicians: Jachen Daescher, Oliver Meier, Rudi Flueck, Reto Balz, Stefan Siegrist, Thomas Kämpfer and Michael Leopold.

I would also like to thank PD Dr. Hans Zogg, head of Thin Film Physics Group, Laboratory for Solid State Physics, ETH Zürich, for the opportunity to work in his group as well as Martin Arnold, Ferdinand Felder, Mohamed Rahim and Matthias Fill for all the entertaining discussions.

Furthermore, I thank Dr. Elisabeth Müller (Electron Microscopy Center, ETH Zürich) for her support in TEM sample preparation and TEM investigation, Prof. Dr. L. Gauckler (Nonmetallic Inorganic Materials Group, ETH Zürich) for access to XRD, DTA/TG, and SEM instruments, Dr. Ulrich Müller (Empa) for XPS measurements, and Dr. Max Döbeli (Ion Beam Physics, ETH Zürich) for RBS and ERDA measurements.

Last but not least I would like to thank my family and especially my wife Denise Buecheler for their support during the whole time.



# Abbreviations and Symbols

AFM	Atomic force microscopy
ALD	Atomic layer deposition
AM1.5G	Reference global spectrum at air mass 1.5
AZO	Aluminum doped ZnO
CBD	Chemical bath deposition
C-f	Capacitance-frequency
CGS	CuGaSe <sub>2</sub>
CiAc	Citric acid
CIGS	CuIn <sub>1-x</sub> Ga <sub>x</sub> Se <sub>2</sub>
CIGSSe	CuIn <sub>1-x</sub> Ga <sub>x</sub> Se <sub>2-2z</sub> S <sub>2z</sub>
CIS	CuInSe <sub>2</sub>
CT	Chemical treatment
C-V	Capacitance-voltage
EB	Ethylene glycol monobutyl ether
EDX	Energy dispersive X-ray spectroscopy
EQE	External quantum efficiency
ERDA	Elastic recoil detection analysis
HAADF	High angular annular dark field detector
HAX-PES	Hard X-ray photoelectron spectroscopy
HR-TEM	High resolution transmission electron microscopy
HTR	Highly transparent and resistive layer
ILGAR	Ion layer gas reaction
InTu <sub>3</sub> Cl <sub>3</sub>	Complex formed by indium(III)chloride and thiourea
IQE	Internal quantum efficiency
i-ZnO	Zinc oxide without extrinsic doping
J-V	Current density - voltage
ODC	Ordered defect compound
Oh	Octahedral site in the spinel structure
OVC	Ordered vacancy compound
PV	Photovoltaic
PVD	Physical vapor deposition
QNR	Quasi neutral region
RBS	Rutherford backscattering spectroscopy
SCR	Space charge region

---

SDL	Surface defect layer
SEM	Scanning electron microscopy
SIMS	Secondary ion mass spectroscopy
SLG	Soda-lime glass (float glass)
STC	Standard test conditions
STEM	Scanning transmission electron microscopy
TC	Texture coefficient of polycrystalline layer
TCO	Transparent conductive oxide
TEM	Transmission electron microscopy
Th	Tetrahedral site in the spinel structure
TU	Thiourea
USP	Ultrasonic spray pyrolysis
XPS	X-ray photoelectron spectroscopy
XRD	X-ray diffraction
XRF	X-ray fluorescence
XTEM	Cross section sample for TEM

Symbol	Description	Unit
[III]	Sum of group three elements	
$A$	Ideality factor	
$A_0$	Device area	[cm <sup>2</sup> ]
$\alpha$	Absorption coefficient	[cm <sup>-1</sup> ]
$BP$	Boiling point of the solvent	[°C]
$C$	Capacity	[F]
$D$	Average grain size	[nm]
$d$	Droplet diameter	[μm]
$D_e$	Diffusion coefficient	[cm <sup>2</sup> /s]
$\Delta E_C$	Conduction band offset	[eV]
$E_{00}$	Characteristic tunneling energy	[eV]
$E_a$	Activation energy of the saturation current density	[eV]
$E_C$	Energy level of the conduction band	[eV]
$\eta$	Conversion efficiency	[%]
$E_g$	Energy band gap	[eV]
$E_g^{average}$	Average energy band gap	[nm]
$E_g^{EQE}$	Energy band gap determined by EQE measurement	[eV]
$E_g^{interface}$	Energy band gap of the absorber at the interface to the buffer layer	[eV]
$E_g^{interface}$	Modified interface energy band gap due to Cu depletion	[eV]
$E_g^{min}$	Minimum energy band gap	[eV]
$E_g^{min.SCR}$	Minimum energy band gap in the SCR	[eV]
$E_{max}$	Maximum electric field in the SCR	[V/m]
$\epsilon_0$	Permittivity of the vacuum	[F/m]
$\epsilon_s$	Dielectric constant	
$E_V$	Energy level of the valence band	[eV]
$FF$	Fill factor	[%]
$h\nu$	Photon energy	[eV]
$J_0$	Saturation current density	[mA/cm <sup>2</sup> ]
$J_{00}$	Weakly temperature dependent prefactor	[mA/cm <sup>2</sup> ]
$J_L$	Leakage current density	[mA/cm <sup>2</sup> ]
$J_{Ph}$	Photogenerated current density	[mA/cm <sup>2</sup> ]
$J_{rec}$	Recombination current density	[mA/cm <sup>2</sup> ]
$J_{SC}$	Short circuit current density	[mA/cm <sup>2</sup> ]
$k$	Extinction coefficient	
$kT^*$	Characteristic energy	[eV]
$\lambda$	Wavelength	[nm]
$L_e$	Diffusion length	[nm]
$N_a$	Shallow acceptor concentration	[cm <sup>-3</sup> ]
$N_C$	Effective density of states in the conduction band	[cm <sup>-3</sup> ]
$N_d$	Shallow donor concentration	[cm <sup>-3</sup> ]
$N_t(E_\omega)$	Energy distribution of defects	[cm <sup>-3</sup> eV <sup>-1</sup> ]
$\nu_0$	Attempt to escape frequency	[Hz]
$N_V$	Effective density of states in the valence band	[cm <sup>-3</sup> ]

$\phi_p^f$	Corrected barrier for holes at the buffer-absorber interface	[eV]
$\phi_p^0$	Barrier height for holes at the buffer-absorber interface at zero bias	[nm]
$P_i$	Incident irradiation power density	[mW/cm <sup>2</sup> ]
$P_{MPP}$	Maximum power point power density	[W/cm <sup>2</sup> ]
$q$	Elemental charge	[C]
$\rho$	Solvent density	[g/ml]
$R_p$	Parallel resistance (also called shunt resistance)	[ $\Omega\text{cm}^2$ ]
$r_p$	Normalized parallel resistance	
$R_s$	Series resistance	[ $\Omega\text{cm}^2$ ]
$r_s$	Normalized series resistance	
$\sigma$	Standard deviation of the texture coefficient	
$\sigma$	Surface tension of the solvent	[mN/m]
$t$	Layer thickness	[m]
$\Theta$	Diffraction angle	[°]
$\Delta\Theta$	FWHM of the diffraction peak	[°]
$T_S$	Substrate surface temperature	[°C]
$T_{sbp}$	Solvent boiling point	[°C]
$V_{bi}$	Built in voltage of the pn junction	[V]
$V_{OC}$	Open circuit voltage	[mV]
$v_{OC}$	Normalized open circuit voltage	
$VP$	Vapor pressure of the solvent	[mbar]
$W$	Width of the SCR	[m]
$w_p$	Depletion width on the p-side of the SCR	[m]
$w'_p$	Modified depletion width on the p-side of the SCR	[m]
$x$	Gallium concentration ([Ga]/[III])	
$y$	Copper concentration ([Cu]/[III])	

# Curriculum Vitae

## Stephan Friedrich Buecheler

Date of birth: 12 May 1977  
Place of birth: Waldshut-Tiengen, Germany  
Nationality: German

- Apr. 2007 - present    PhD student at the Thin Film Physics Group,  
Lab. for Solid State Physics, ETH Zurich, Switzerland;  
now Laboratory for Thin Films and Photovoltaics,  
Empa, Switzerland.
- Apr 2005 - Feb 2007    Technical and scientific assistant in the  
Thin Film Physics Group, Lab. for Solid State Physics,  
ETH Zurich, Switzerland.
- Sep 2002 - Feb 2007    Studies of Physics at ETH Zurich, Switzerland;  
Diploma thesis on CIGS Thin Film Solar Cells;  
graduated as Dipl. Phys. ETH.
- Sep 1999 - Jun 2002    'Abitur' at Technischen Oberschule Freiburg, Germany  
and 'Mittlere Reife' at the Berufsoberschule  
Bad Säckingen, Germany.
- Nov 1998- Sep 2000    Motor mechanic at Autohaus Schmidt,  
Titisee-Neustadt, Germany.
- Jan 1998 - Okt 1998    Military service at Kraftfahrausbildungszentrum  
Pfullendorf, Germany.
- Feb 1997 - Dez 1997    Motor mechanic at Autohaus Schmidt,  
St.Blasien, Germany.
- Sep 1994 - Jan 1997    Apprenticeship as motor mechanic at Autohaus Schmidt,  
St.Blasien, Germany.





# Publications

## Journal publications

S. Buecheler, F. Pianezzi, C. Fella, A. Chirila, K. Decock, M. Burgelman and A.N. Tiwari, "Interface formation between  $\text{CuIn}_{1-x}\text{Ga}_x\text{Se}_2$  absorber and  $\text{In}_2\text{S}_3$  buffer layer", submitted to *Thin Solid Films*, Special Issue, Proc. of E-MRS Spring Meeting 2010.

J. Perrenoud, L. Kranz, S. Buecheler, F. Pianezzi and A.N. Tiwari, "The use of aluminium doped ZnO as transparent conductive oxide for CdS/CdTe solar cells", submitted to *Thin Solid Films*, Special Issue, Proc. of E-MRS Spring Meeting 2010.

A. Chirila, P. Bloesch, S. Seyrling, A. Uhl, S. Buecheler, F. Pianezzi, D. Guettler, S. Nishiwaki, Y. Romanyuk, G. Bilger, D. Brémaud, and A. N. Tiwari, "Cu(In,Ga)Se<sub>2</sub> Solar Cell Grown on Flexible Polymer Substrate with Efficiency exceeding 17%", revised manuscript submitted to *Progress in Photovoltaics: Research and Application*.

A. Chirila, S. Seyrling, S. Buecheler, D. Guettler, S. Nishiwaki, Y. Romanyuk, G. Bilger and A.N. Tiwari, "Influence of High Growth Rates on evaporated Cu(In,Ga)Se<sub>2</sub> Layers and Solar Cells", submitted to *Progress in Photovoltaics: Research and Application*.

N. Naghavi, D. Abou-Ras, N. Allsop, N. Barreau, S. Buecheler, A. Ennaoui, C.-H. Fischer, C. Guillen, D. Hariskos, J. Herrero, R. Klenk, K. Kushiya, D. Lincot, R. Menner, T. Nakada, C. Platzer-Bjoerkman, S. Spiering, A.N. Tiwari, T. Toerndahl, "Buffer layers and transparent conducting oxides for chalcopyrite Cu(In,Ga)(S,Se)<sub>2</sub> based thin film photovoltaics: present status and current developments", *Prog. Photovolt: Res. Appl.* (accepted for publication).

S. Buecheler, D. Corica, D. Guettler, A. Chirila, R. Verma, U. Müller, T.P. Niesen, J. Palm, A.N. Tiwari, "Ultrasonically sprayed indium sulfide buffer layers for Cu(In,Ga)(S,Se)<sub>2</sub> thin-film solar cells", *Thin Solid Films*, Volume 517, Issue 7, 2 February 2009, Pages 2312-2315.

S. Calnan, H.M. Uphadhyaya, S. Buecheler, G. Khrypunov, A. Chirila, A. Romeo, R. Hashimoto, T. Nakada, A.N. Tiwari, "Application of high mobility transparent conductors to enhance long wavelength transparency of the intermediate solar cell in multi-junction

solar cells", *Thin Solid Films*, Volume **517**, Issue 7, 2 February 2009, Pages 2340-2343.

S. Seyrling, S. Calnan, S. Bücheler, J. Hüpkes, S. Wenger, D. Brémaud, H. Zogg, A.N. Tiwari, "CuIn<sub>1-x</sub>Ga<sub>x</sub>Se<sub>2</sub> photovoltaic devices for tandem solar cell application", *Thin Solid Films*, Volume **517**, Issue 7, 2 February 2009, Pages 2411-2414.

A. Romeo, S. Buecheler, M. Giarola, G. Mariotto, A.N. Tiwari, N. Romeo, A. Bosio, S. Mazzamuto, "Study of CSS- and HVE-CdTe by different recrystallization processes", *Thin Solid Films*, Volume **517**, Issue 7, 2 February 2009, Pages 2132-2135.

K. Ernits, D. Brémaud, S. Buecheler, C.J. Hibberd, M. Kaelin, G. Khrypunov, U. Müller, E. Mellikov, A.N. Tiwari, "Characterisation of ultrasonically sprayed In<sub>x</sub>S<sub>y</sub> buffer layers for Cu(In,Ga)Se<sub>2</sub> solar cells", *Thin Solid Films*, Volume **515**, Issue 15, 31 May 2007, Pages 6051-6054.

## Conference proceedings

J.Perrenoud, S.Buecheler, L.Kranz, C. Fella, J.Skarp, A.N.Tiwari, "The application of  $\text{ZnO}_{1-x}\text{S}_x$  as buffer layer in CdTe solar cells", *Photovoltaic Specialists Conference (PVSC), 2010 35th IEEE*, Hawaii, USA, June 21-25, 2010.

C. Fella, S. Buecheler, D. Guettler, J. Perrenoud, A. Uhl and A.N. Tiwari, "Ultrasonically Sprayed Zinc Sulfide Buffer Layers for  $\text{Cu}(\text{In,Ga})(\text{S,Se})_2$  Solar Cells", *Photovoltaic Specialists Conference (PVSC), 2010 35th IEEE*, Hawaii, USA, June 21-25, 2010.

S. Buecheler, R.L. Sauaia, D. Corica, C. Fella, R. Verma, A. Chirila, Y.E. Romanyuk and A.N. Tiwari, "Deposition process of ultrasonically sprayed  $\text{In}_2\text{S}_3$  buffer layers for  $\text{Cu}(\text{In,Ga})\text{Se}_2$  thin film solar cells", *Proc. 24th European Photovoltaic Solar Energy Conference and Exhibition*, Hamburg, Germany, 2009

S. Buecheler, D. Corica, A. Chirila, D. Güttler, F. Pianezzi, R. Verma, K. Decock and A.N.Tiwari, "Influence of the absorber composition in  $\text{CuIn}_{1-x}\text{Ga}_x\text{Se}_2$  solar cells with sprayed  $\text{In}_2\text{S}_3$  buffer layers on the dominant recombination mechanism", *Proc. 24th European Photovoltaic Solar Energy Conference and Exhibition*, Hamburg, Germany, 2009

J. Perrenoud, S. Buecheler, A.N. Tiwari, "Flexible CdTe solar cells and modules: challenges and prospects", *Proceedings of the SPIE - The International Society for Optical Engineering*, Thin Film Solar Technology, San Diego, CA USA, Pages: 74090L (5 pp.) Published: 2009.

A. Chirila, D. Guettler, D. Bremaud, S. Buecheler, R. Verma, S. Seyrling, S. Nishiwaki, S. Haenni, G. Bilger, A.N. Tiwari, "CIGS solar cells grown by a three-stage process with different evaporation rates", *Photovoltaic Specialists Conference (PVSC), 2009 34th IEEE*, Digital Object Identifier: 10.1109/PVSC.2009.5411161, Publication Year: 2009 , Pages: 000812-000816.

J. Perrenoud, S. Buecheler, A.N. Tiwari, "Flexible CdTe solar cells with high photovoltaic conversion efficiency", *Photovoltaic Specialists Conference (PVSC), 2009 34th IEEE*, Digital Object Identifier: 10.1109/PVSC.2009.5411573, Publication Year: 2009 , Pages: 000695-000699.

S. Buecheler, R. Chati, J. Perrenoud, A.N. Tiwari, "Low temperature processed CdTe thin film solar cells with reduced CdS thickness", (submitted to proceedings of E-MRS spring meeting 2009, to be published in *Physics Procedia*).

R. Verma, S. Buecheler, D. Corica, A. Chirila, S. Seyrling, J. Perrenoud, D. Guettler, C. J. Hibberd and A. N. Tiwari, " $\text{Cu}(\text{In,Ga})\text{Se}_2$  Solar Cells with  $\text{In}_2\text{S}_3$  Buffer Layers grown by Vacuum Evaporation and Chemical Spray Methods", *Proc. 23rd European Photovoltaic*

*Solar Energy Conference and Exhibition*, Valencia, Spain, Sept. 1-5, 2008, p. 2315-2319.

D. Corica, S. Buecheler, D. Guettler, A. Chirila, S. Seyrling, R. Verma and A.N. Tiwari, "Indium Sulfide Buffer Layer for Cu(In,Ga)Se<sub>2</sub> Thin-Film Solar Cells Deposited by Ultrasonic Spray Pyrolysis", *Proc. 23rd European Photovoltaic Solar Energy Conference and Exhibition*, Valencia, Spain, Sept 1-5, 2008.

R. Verma, D. Bremaud, S. Buecheler, S. Seyrling, H. Zogg, A.N. Tiwari, "Physical vapor deposition of In<sub>2</sub>S<sub>3</sub> buffer on Cu(In,Ga)Se<sub>2</sub> absorber: optimization of processing steps for improved cell performance", *Proc. 22nd European Photovoltaic Solar Energy Conference and Exhibition*, Milan, Italy, Sept 3-7, 2007.

# Bibliography

- [1] Deutsche Bank, Solar Photovoltaics Technology and Economics: Thin Films and Crystalline Silicon, 2007.
- [2] I. Repins, M. Contreras, B. Egaas, C. DeHart, J. Scharf, C. Perkins, B. To, and R. Noufi, 19.9%-efficient ZnO/CdS/CuInGaSe<sub>2</sub> solar cell with 81.2% fill factor, *Prog. Photovolt: Res. Appl.* **16**, 235 (2008).
- [3] I. Repins, S. Glynn, J. Duenow, T. Coutts, W. Metzger, and M. Contreras, Required Material Properties for High-Efficiency CIGS Modules, in *Proceedings of the SPIE - The International Society for Optical Engineering, San Diego, CA USA*, 2009.
- [4] T. Maeda, T. Takeichi, and T. Wada, Systematic studies on electronic structures of CuInSe<sub>2</sub> and the other chalcopyrite related compounds by first principle calculations, *Phys. Stat. Sol. A* **203**, 2634 (2005).
- [5] M. Kaelin, *Low-cost Cu(In,Ga)Se<sub>2</sub> absorber from nanosized precursor materials for thin-film solar cells*, PhD thesis, ETH Zurich, 2005, Dissertation ETH No. 15877.
- [6] H. M. Upadhyaya, T. M. Razykov, and A. N. Tiwari, Thin Film PV Technology, in *CRC Handbook of Energy Conservation and Renewable Energy*, edited by F. Kreith and D. Y. Goswami, CRC Press.
- [7] D. Bremaud, *Investigation and Development of CIGS Solar Cells on Flexible Substrates and with Alternative Electrical Back Contacts*, PhD thesis, ETH Zurich, 2009, Dissertation ETH No. 18194.
- [8] D. Rudmann, *Effects of sodium on growth and properties of Cu(In,Ga)Se<sub>2</sub> thin films and solar cells*, PhD thesis, ETH Zurich, 2004, Dissertation ETH No. 15576.
- [9] S. M. Sze, *Physics of Semiconductor Devices* (John Wiley and Sons, Inc., 1981).
- [10] A. Klein, F. Saeuberlich, B. Spaeth, T. Schulmeyer, and D. Kraft, Non-stoichiometry and electronic properties of interfaces, *J Mater. Sci.* **42**, 1890 (2007).
- [11] R. Klenk, Characterization and modelling of chalcopyrite solar cells, *Thin Solid Films* **387**, 135 (2001).
- [12] U. Rau and M. Schmidt, Electronic properties of ZnO/CdS/Cu(In,Ga)Se<sub>2</sub> solar cells - aspects of heterojunction formation, *Thin Solid Films* **387**, 141 (2001).

- [13] N. Naghavi *et al.*, Buffer layers and transparent conducting oxides for chalcopyrite  $\text{Cu}(\text{In,Ga})(\text{S,Se})_2$  based thin film photovoltaics: present status and current developments, *Prog. Photovolt: Res. Appl.*, accepted for publication.
- [14] S. Gall, N. Barreau, F. Jacob, S. Harel, and J. Kessler, Influence of sodium compounds at the  $\text{Cu}(\text{In,Ga})\text{Se}_2/(\text{PVD})\text{In}_2\text{S}_3$  interface on solar cell properties, *Thin Solid Films* **515**, 6076 (2007).
- [15] P. Pistor, R. Caballero, D. Hariskos, V. Izquierdo-Roca, R. Waechter, S. Schorr, and R. Klenk, Quality and stability of compound indium sulfide as source material for buffer layers in  $\text{Cu}(\text{In,Ga})\text{Se}_2$  solar cells, *Sol. Energy Mater. Sol. Cells* **93**, 148 (2009).
- [16] D. Hariskos, R. Menner, S. Spiering, A. Eicke, and M. Powalla,  $\text{In}_2\text{S}_3$  buffer layer deposited by magnetron sputtering for  $\text{Cu}(\text{In,Ga})\text{Se}_2$  solar cells, in *Proceedings of 19th European Photovoltaic Solar Energy Conference*, 2004.
- [17] D. Hariskos, R. Menner, E. Lotter, S. Spiering, and M. Powalla, Indium sulfide as buffer layer in  $\text{Cu}(\text{In,Ga})\text{Se}_2$ -based solar cells, in *Proceedings of 20th European Photovoltaic Solar Energy Conference*, 2005.
- [18] N. Naghavi, S. Spiering, M. Powalla, B. Cavana, and D. Lincot, High-efficiency copper indium gallium diselenide (CIGS) solar cells with indium sulfide buffer layers deposited by atomic layer chemical vapor deposition (ALCVD), *Prog. Photovolt: Res. Appl.* **11**, 437 (2003).
- [19] S. Buecheler, D. Corica, A. Chirila, D. Güttler, F. Pianezzi, R. Verma, K. Decock, and A.N.Tiwari, Influence of the absorber composition in  $\text{CuIn}_{1-x}\text{Ga}_x\text{Se}_2$  solar cells with sprayed  $\text{In}_2\text{S}_3$  buffer layers on the dominant recombination mechanism, in *Proceedings of 24th European Photovoltaic Solar Energy Conference and Exhibition*, 2009.
- [20] R. Bhattacharya, M. Contreras, and G. Teeter, Copper indium gallium diselenide (CIGS) devices using single-layer chemical-bath-deposited  $\text{ZnS}(\text{O,OH})$ , *Japanese J. Appl. Phys.* **43**, L1475 (2004).
- [21] U. Zimmermann, M. Ruth, and M. Edoff, Cadmium-free CIGS mini-modules with ALD-grown  $\text{Zn}(\text{O,S})$ -based buffer layers, in *Proceedings of 21st European Photovoltaic Solar Energy Conference*, 2006.
- [22] A. Hultquist, C. Platzer-Bjoerkman, T. Toerndahl, M. Ruth, and M. Edoff, Optimization of i-ZnO window layers for  $\text{Cu}(\text{In,Ga})\text{Se}_2$  solar cells with ALD buffers, in *Proceedings of 22nd European Photovoltaic Solar Energy Conference*, 2007.
- [23] N. Allsop, A. Haensel, S. Visbeck, T. Niesen, M. Lux-Steiner, and C.-H. Fischer, Spray ILGAR Indium Sulfide Buffers for  $\text{Cu}(\text{In,Ga})(\text{S,Se})_2$  Solar Cells, *Prog. Photovolt: Res. Appl.* **13**, 607 (2005).

- [24] S. Buecheler, D. Corica, D. Guettler, A. Chirila, R. Verma, U. Müller, T. Niesen, J. Palm, and A. Tiwari, Ultrasonically sprayed indium sulfide buffer layers for Cu(In,Ga)(S,Se)<sub>2</sub> thin-film solar cells, *Thin Solid Films* **517**, 2312 (2009).
- [25] R. Saez-Araoz, A. Ennaoui, T. Kropp, E. Veryaeva, T. Niessen, and M. Lux-Steiner, Use of different Zn precursors for the depositoin of Zn(O,S) buffer layers by chemical bath for chalcopyrite based Cd-free thin-film solar cells, *Physica Status Solidi (a)* **205**, 2330 (2008).
- [26] T. Glatzel, H. Steigert, R. Klenk, M. Lux-Steiner, T. Niesen, and S. Visbeck, Zn<sub>1-x</sub>Mg<sub>x</sub>O as a window layer in completely Cd-free Cu(In,Ga)(S,Se)<sub>2</sub> based thin film solar cells, in *Technical Digest of the International PVSEC-14, Bangkok*, 2004.
- [27] W. Shafarman and L. Stolt, Cu(In,Ga)Se<sub>2</sub> Solar Cells, in *Handbook of Photovoltaic Science and Engineering*, edited by A. Luque and S. Hegedus, John Wiley & Sons, Ltd.
- [28] Crystal structures and bulk lattice parameters of materials quoted in the volume, in *Landolt-Börnstein - Group III Condensed Matter Numerical Data and Functional Relationships in Science and Technology*, edited by G. Chiarotti, chap. 24c: Interaction of Charged Particles and Atoms with Surfaces, SpringerMaterials - The Landolt-Börnstein Database, DOI: 10.1007/100860666.
- [29] R. Nomura, K. Konishi, and H. Matsuda, Single-source organometallic chemical vapour deposition process for sulphide thin films: introduction of a new organometallic precursor Bu<sup>n</sup>In(SPr<sup>i</sup>)<sub>2</sub> and preparation of In<sub>2</sub>S<sub>3</sub> thin films, *Thin Solid Films* **198**, 339 (1991).
- [30] N. Barreau, A. Mokrani, F. Couzinie-Devy, and J. Kessler, Bandgap properties of the indium sulfide thin-films grown by co-evaporation, *Thin Solid Films* **517**, 2316 (2009).
- [31] C. White and H.Okamoto, *Phase Diagramms of Indium Alloys and Their Engineering Applications* (ASM International, 1992), .
- [32] B. Predel, In-S (Indium-Sulfur), in *Landolt-Börnstein - Group IV Physical Chemistry Numerical Data and Functional Relationships in Science and Technology*, edited by O. Madelung, chap. 5G: Hg-Ho - La-Zr, SpringerMaterials - The Landolt-Börnstein Database, DOI: 10.1007/105066261758.
- [33] T. Goedecke and K. Schubert, On the phase diagram InS, *Z. Metallkde.* **76**, 358 (1985).
- [34] A. Thompson, M. Stubbs, and J. Schuffle, Thermodynamics of the In-In<sub>2</sub>S<sub>3</sub> System, *J. Am. Chem. Soc.* **76**, 341 (1954).
- [35] W. Duffin and J. Hogg, Crystalline Phases in the System In-In<sub>2</sub>S<sub>3</sub>, *Acta Crystallogr.* **20**, 566 (1966).

- [36] G. King, The Space Group of  $\beta$ - $\text{In}_2\text{S}_3$ , *Acta Crystallogr.* **15**, 512 (1962).
- [37] A. Likforman, M. Guittard, A. Tomas, and J. Flahaut, Mise ´evidence d’une solution solide de type spinelle dans le diagramme de phase du systeme In-S, *J. Solid State Chem.* **34**, 353 (1980).
- [38] H. Hahn and W. Klingler, Ueber die Kristallstrukturen des  $\text{In}_2\text{S}_3$  and  $\text{In}_2\text{Te}_3$ , *Z. anorg. Chem.* **260**, 97 (1949).
- [39] S. Siebentritt, Alternative buffers for chalcopyrite solar cells, *Solar Energy* **77**, 767 (2004).
- [40] D. Hariskos, S. Spiering, and M. Powella, Buffer layers in  $\text{Cu}(\text{In,Ga})\text{Se}_2$  solar cells and modules, *Thin Solid Films* **480-481**, 99 (2005).
- [41] J. Kessler, K. O. Velthaus, M. Ruckh, R. Laichinger, H. W. Schock, D. Lincot, R. Ortega, and J. Vedel, Chemical Bath Deposition of CdS on CIS, etching effects and growth kinetics, in *Int. Photovoltaic Science and Engineering Conference*, 1992.
- [42] U. Rau, D. Braunger, R. Herberholz, H. Schock, J. Guillemoles, L. Kronik, and D. Cahen, Oxygenation and air-annealing effects on the electronic properties of  $\text{Cu}(\text{In,Ga})\text{Se}_2$  films and devices, *J Appl. Phys.* **86**, 497 (1999).
- [43] R. Ortega-Borges and D. Lincot, Mechanism of Chemical Bath Deposition of Cadmium Sulfide Thin Films in the Ammonia-Thiourea System, *J. Electrochem. Soc.* **140**, 3464 (1993).
- [44] R. Chamberlin and J. Skarman, Chemical spray deposition process for inorganic films, *J. Electrochem. Soc.* **113**, 36 (1966).
- [45] A. P. R. Rajan, Correlations to predict droplet size on ultrasonic atomisation, *Ultrasonics* **39**, 235 (2001).
- [46] R. Lang, Ultrasonic Atomization of Liquids, *J. Acoust. Soc. Am.* **34**, 6 (1962).
- [47] S. Tsai, Y. Song, C. Tsai, Y. Chou, and C. Cheng, Ultrasonic atomization using MHz silicon-based multiple-Fourier hon nozzles, *Applied Physics Letters* **88**, 014102 (2006).
- [48] A. Lozano, H. Amaveda, F. Barreras, X.Jordà, and M. Lozano, High-Frequency Ultrasonic Atomization with Pulsed Excitation, *Journal of Fluids Engineering* **125**, 941 (2003).
- [49] C. Wohlfarth and B. Wohlfarth, Pure Liquids: Data, in *Landolt-Börnstein - Group IV Physical Chemistry Numerical Data and Functional Relationships in Science and Technology*, edited by M. D. Lechner, chap. Volume 16: Surface Tension of Pure Liquids and Binary Liquid Mixtures, SpringerMaterials - The Landolt-Börnstein Database, DOI: 10.1007/105601912.



- [50] D. R. Lide, editor, *CRC Handbook of Chemistry and Physics*, 87 ed. (CRC press, 2006).
- [51] C. Barret and T. Massalskie, *Structure of Metals* (Pergamon, Oxford, 1980).
- [52] Powder diffraction data are taken from the Joint Committee for Powder Diffraction Standard (JCPDS).
- [53] D. Abou-Ras, *Structural and chemical analysis of buffer layers in Cu(In,Ga)Se<sub>2</sub> thin-film solar cells*, PhD thesis, ETH Zurich, 2005, Dissertation ETH No. 16424.
- [54] C. Kottler, *Duennschichtanalyse mittels Vorwaertsstreuung bei tiefer Energie*, PhD thesis, ETH Zurich, 2005, Dissertation ETH No. 16079.
- [55] U. Rau and H. Schock, Cu(In,Ga)Se<sub>2</sub> solar cells, in *Clean electricity from photovoltaics*, edited by M. Archer and R. Hill, Imperial College Press, London, 2001.
- [56] M. Green, *Solar Cells: Operating Principles, Technology and System Applications* (University of New South Wales, Sydney, 1986).
- [57] U. Rau and H. Schock, Electronic properties of Cu(In,Ga)Se<sub>2</sub> heterojunction solar cells—recent achievements, current understanding, and future challenges, *Appl. Phys. A* **69**, 131 (1999).
- [58] U. Rau, Tunneling-enhanced recombination in Cu(In,Ga)Se<sub>2</sub> heterojunction solar cells, *Applied Physics Letters* **74**, 111 (1999).
- [59] S. Hegedus and W. Shararman, Thin-film solar cells: device measurements and analysis, *Prog. Photovolt: Res. Appl.* **12**, 155 (2004).
- [60] J. Verschraegen, M. Burgelman, and J. Penndorf, Temperature dependence of the diode ideality factor in CuInS<sub>2</sub>-on-Cu-tape solar cells, *Thin Solid Films* **480-481**, 307 (2005).
- [61] T. Walter, R. Menner, C. Koeble, and H. Schock, in *Proceedings of 12th European Photovoltaic Energy Conference*, edited by R. Hill, W. Palz, and P. Helm, 1994.
- [62] F. Padovani and R. Stratton, Field and thermionic-field emission in Schottky barriers, *Solid-State Electronics* **9**, 695 (1966).
- [63] M. Burgelman, Cadmium telluride thin film solar cells, in *Thin film solar cells: fabrication, characterization, and application*, edited by J. Poortmans and V. Arkhipov, John Wiley and Sons Ltd., 2006.
- [64] V. Nadenau, U. Rau, A. Jasenek, and H. Schock, Electronic properties of CuGaSe<sub>2</sub>-based heterojunction solar cells. Part I. Transport analysis, *J. Appl. Phys.* **87**, 584 (2000).
- [65] F. Pianezzi, Analysis of Recombination Mechanisms in Thin-Film CIGS Solar Cells, Master's thesis, ETH Zurich, 2009, Performed in the Laboratory for Thin Films and Photovoltaics at Empa, under the supervision of S. Buecheler.

- [66] For absolute measurement, please refer to the international standard IEC 60904-8 ed2.0 or ASTM international E 1021-06.
- [67] D. Schroder, *Semiconductor material and device characterization* (John Wiley and Sons, Inc., 2006).
- [68] T. Walter, R. Herberholz, C. Mueller, and H. Schock, Determination of defect distributions from admittance measurements and application to Cu(In,Ga)Se<sub>2</sub> based heterojunctions, *J. Appl. Phys.* **80**, 4411 (1996).
- [69] T. Kodas and M. Hampden-Smith, *Aerosol Processing of Materials* (Wiley-VCH, 1999).
- [70] D. Beckel, *Thin Film Cathodes for Micro Solid Oxide Fuel Cells*, PhD thesis, ETH Zurich, 2007, Dissertation ETH No. 17206.
- [71] A. Carty and D. Tuck, The Coordination Chemistry of Indium, *Progress in Inorg. Chem.* **19**, 243 (1975).
- [72] A. Carty and D. Tuck, Co-ordination Compounds of Indium. Part IV. Adducts of Indium(III)Chloride, Bromide, and Iodide with Neutral Donors, *J. Chem. Soc. A* , 1081 (1966).
- [73] J. Madarasz and G. Pokol, Comparative evolved gas analysis on thermal degradation of thiourea by coupled TG-FTIR and TG/DTA-MS instruments, *J. Therm. Analys. Cal.* **88**, 329 (2007).
- [74] D. Corica, S. Buecheler, D. Guettler, A. Chirila, S. Seyrling, R. Verma, and A. Tiwari, Indium Sulfide buffer layer for Cu(In,Ga)Se<sub>2</sub> thin film solar cells deposited by ultrasonic spray pyrolysis, in *Proc. of 23rd European Photovoltaic Solar Energy Conference and Exhibition*, 2008.
- [75] P. Eckerlin and H. Kandler, HoS - InSn, in *Landolt-Börnstein - Group III Condensed Matter Numerical Data and Functional Relationships in Science and Technology*, edited by K.-H. Hellwege and A. M. Hellwege, chap. 6: Structure Data of Elements and Intermetallic Phases, SpringerMaterials - The Landolt-Börnstein Database, DOI: 10.1007/1020145451.
- [76] W. Pies and A. Weiss, a2282, I.2.1 Simple chlorides and their solid solutions, in *Landolt-Börnstein - Group III Condensed Matter Numerical Data and Functional Relationships in Science and Technology*, edited by K.-H. Hellwege and A. M. Hellwege, chap. 7a: Key Elements: F, Cl, Br, I, SpringerMaterials - The Landolt-Börnstein Database, DOI: 10.1007/1020145451.
- [77] Card 25-0390, in *Powder Diffraction File*, Joint Committee on Powder Diffraction Standards.
- [78] Card 05-0731, in *Powder Diffraction File*, Joint Committee on Powder Diffraction Standards.

- [79] S. Zhang and S. Wei, Reconstruction and energetics of the polar (112) and ( $\bar{1}\bar{1}2$ ) versus the non polar (220) surfaces of CuInSe<sub>2</sub>, *Physical Review B* **65**, 081402 (2002).
- [80] S. Siebentritt, N. Papathanasiou, J. Albert, and M. Lux-Steiner, Stability of surfaces in the chalcopyrite system, *Appl. Phys. Lett.* **88**, 151919 (2006).
- [81] Y. Strzhemechny, P. Smith, S. Bradley, D. Liao, A. Rockett, K. Ramanathan, and L. Billson, Near-surface electronic defects and morphology of CuIn<sub>1-x</sub>Ga<sub>x</sub>Se<sub>2</sub>, *J. Vac. Sci. Technol.* **20**, 2441 (2002).
- [82] J. I. Pankove, *Optical Processes in Semiconductors* (Dover Publications, Inc., New York, NY).
- [83] N. Allsop, A. Schoenmann, A. Belaidi, H.-J. Muffler, B. Mertesacker, W. Bohne, E. Strub, J. Roehrich, M. Lux-Steiner, and C.-H. Fischer, Indium sulfide thin films deposited by the spray ion layer gas reaction technique, *Thin Solid Films* **513**, 52 (2006).
- [84] J. Sterner, J. Malmstroem, and L. Stolt, Study on ALD In<sub>2</sub>S<sub>3</sub>/Cu(In,Ga)Se<sub>2</sub> Interface Formation, *Prog. Photovolt: Res. Appl.* **13**, 179 (2005).
- [85] N. Barreau, Indium sulfide and relatives in the world of photovoltaics, *Solar Energy* **83**, 363 (2009).
- [86] R. Robles, N. Barreau, A. Vega, S. Marsillac, J. Bernede, and A. Mokrani, Optical properties of large band gap  $\beta$ -In<sub>2</sub>S<sub>3-3x</sub>O<sub>3x</sub> compounds obtained by physical vapour deposition, *Optical Materials* **27**, 647 (2005).
- [87] N. Barreau, J. Bernede, and S. Marsillac, Study of the new  $\beta$ -In<sub>2</sub>S<sub>3</sub> containing Na thin films. Part II: Optical and electrical characterization of thin films, *J. Cryst. Growth* **241**, 51 (2002).
- [88] N. Barreau and M. Tessier, Characterization of Indium Sulfide Thin Films Containing Copper, in *Thin-Film Compound Semiconductor Photovoltaics — 2009*, edited by A. Yamada, C. Heske, M. Contreras, M. Igalson, and S. Irvine, pp. 1165–M08–21, Mater. Res. Soc. Symp. Proc. Volume 1165, Warrendale, PA, 2009.
- [89] N. Barreau, C. Deudon, A. Lafond, S. Gall, and J. Kessler, A study of bulk Na<sub>x</sub>Cu<sub>1-x</sub>In<sub>5</sub>S<sub>8</sub> and its impact on the Cu(In,Ga)Se<sub>2</sub>/In<sub>2</sub>S<sub>3</sub> interface of solar cells, *Sol. Energy Mat. Sol. Cells* **90**, 1840 (2006).
- [90] M. Gloeckler, A. Fahrenbruch, and J. Sites, Numerical Modeling of CIGS and CdTe solar cells: setting the baseline, in *Proceedings of 3rd World Conference on Photovoltaic Energy Conversion*, 2003.
- [91] AM1.5G spectrum from IEC 60904-4 Ed.2.

- [92] A. Strohm, L. Eisenmann, R. Gebhardt, A. Harding, T. Schloetzer, D. Abou-Ras, and H. Schock, ZnO/In<sub>x</sub>S<sub>y</sub>/Cu(In,Ga)Se<sub>2</sub> solar cells fabricated by coherent heterojunction formation, *Thin Solid Films* **480-481**, 162 (2005).
- [93] Q. Nguyen, K. Orgassa, I. Koetschau, U. Rau, and H. Schock, Influence of heterointerfaces on the performance of Cu(In,Ga)Se<sub>2</sub> solar cells with CdS and In(OH<sub>x</sub>,S<sub>y</sub>) buffer layers, *Thin Solid Films* **431-432**, 330 (2003).
- [94] K. Ramanathan, F. Hasoon, S. Smith, A. Mascarenhas, H. Al-Thani, J. Alleman, H. Ullal, J. Keane, P. Johnson, and J. Sites, Properties of Cd and Zn partial electrolyte treated CIGS solar cells, in *Proceedings of 29th IEEE Photovoltaic Specialists Conference*, 2002.
- [95] U. Rau, K. Taretto, and S. Siebentritt, Grain boundaries in Cu(In,Ga)(Se,S)<sub>2</sub> thin-film solar cells, *Appl Phys A* **96**, 221 (2009).
- [96] D. Schmid, M. Ruckh, F. Grunwald, and H. Schock, Chalcopyrite/defect chalcopyrite heterojunction on the basis of CuInSe<sub>2</sub>, *J. Appl. Phys* **73**, 2902 (1993).
- [97] J. Tuttle, D. Albin, and R. Noufi, Thoughts on the microstructure of polycrystalline thin film CuInSe<sub>2</sub> and its impact on material and device performance, *Solar cells* **30**, 21 (1991).
- [98] R. Herberholz, U. Rau, H. Schock, T. Haalboom, T. Goedecke, F. Ernst, C. Beilharz, K. Benz, and D. Cahen, Phase segregation, Cu migration and junction formation in Cu(In,Ga)Se<sub>2</sub>, *Eur. Phys. J. AP* **6**, 131 (1999).
- [99] S. Zhang, S. Wei, and A. Zunger, Stabilization of Ternary Compounds via Ordered Arrays of Defect Pairs, *Physical Review Letters* **78**, 4059 (1997).
- [100] A. Niemegeers, M. Burgelman, R. Herberholz, U. Rau, D. Hariskos, and H. Schock, Model for electronic transport in Cu(In,Ga)Se<sub>2</sub> solar cells, *Prog. Photovolt. Res. Appl.* **6**, 407 (1998).
- [101] M. Burgelman, P. Nollet, and S. Degraeve, Modelling polycrystalline semiconductor solar cells, *Thin Solid Films* **361-362**, 527 (2000).
- [102] H. Moenig, C. Fischer, R. Caballero, C. Kaufmann, N. Allsop, M. Gorgoi, R. Klenk, H. Schock, S. Lehmann, M. Lux-Steiner, and I. Laueremann, Surface Cu depletion of Cu(In,Ga)Se<sub>2</sub> films: An investigation by hard X-ray photoelectron spectroscopy, *Acta Materialia* **57**, 3645 (2009).
- [103] F. Py, M. Womes, J. Durand, J. Olivier-Fourcade, J. Jumas, J. Esteva, and R. Karnatak, Copper in In<sub>2</sub>S<sub>3</sub>: a study by X-ray diffraction, diffuse reflectance and X-ray absorption, *J. Alloy. Comp.* **178**, 297 (1992).
- [104] C. Guillot-Deudon, S. Harel, A. Mokrani, A. Lafond, N. Barrau, V. Fernandez, and J. Kessler, Electronic structure of Na<sub>x</sub>Cu<sub>1-x</sub>In<sub>5</sub>S<sub>8</sub> compounds: X-ray photoemission spectroscopy study and band structure calculations, *Physical Review B* **78**, 235201 (2008).

- [105] N. Barreau, S. Marsillac, J. C. Bernede, and L. Assmann, Evolution of the band structure of  $\beta\text{-In}_2\text{S}_{3-3x}\text{O}_{3x}$  buffer layer with its oxygen content, *J. Appl. Phys.* **93**, 5456 (2003).
- [106] N. Barreau, J. Bernede, C. Deudon, L. Brohan, and S. Marsillac, Study of the new  $\beta\text{-In}_2\text{S}_3$  containing Na thin films. Part II: Synthesis and structural characterization of the material, *J. Cryst. Growth* **241**, 4 (2002).
- [107] D. Schmid, M. Ruckh, and H. Schock, Photoemission studies on  $\text{Cu}(\text{In,Ga})\text{Se}_2$  thin films and related binary selenides, *Applied Surface Science* **103**, 409 (1996).
- [108] A. Lavrent'ev, N. Safontseva, V. Dubeiko, B. Gabrel'yan, and I. Nikiforov, Electronic band structures of  $\text{In}_2\text{S}_3$  and  $\text{CdIn}_2\text{S}_4$  semiconductor spinels from the data of x-ray spectroscopy and theoretical calculations, *Phys. Solid. State* **42**, 2047 (2000).
- [109] E. Domashevskaya, V. Terekhov, L. Marshakova, Y. Ugai, V. Nefedov, and N. Sergushin, Participation of d-electrons of metals of group I, II, and III in chemical bonding with sulphur, *Electron Spec. Rel. Phenom.* **9**, 261 (1976).
- [110] V. Tomashik, Cu-In-S (Copper-Indium-Sulfur), in *Landolt-Börnstein - Group IV Physical Chemistry Numerical Data and Functional Relationships in Science and Technology*, edited by G. Effenberg and S. Ilyenko, chap. 11C1: Non-Ferrous Metal Systems. Part 1, SpringerMaterials - The Landolt-Börnstein Database, 10.1007/1091598124.
- [111] D. Abou-Ras, D. Rudmann, G. Kostorz, S. Spiering, M. Powalla, and A. Tiwari, Microstructural and chemical studies of interfaces between  $\text{Cu}(\text{In,Ga})\text{Se}_2$  and  $\text{In}_2\text{S}_3$  layers, *J. Appl. Phys.* **97**, 084908 (2005).
- [112] D. Abou-Ras, G. Kostorz, D. Hariskos, R. Menner, M. Powalla, S. Schorr, and A. Tiwari, Structural and chemical analyses of sputtered  $\text{In}_x\text{S}_y$  buffer layers in  $\text{Cu}(\text{In,Ga})\text{Se}_2$  thin-film solar cells, *Thin Solid Films* **98**, 2792 (2009).
- [113] D. Abou-Ras, G. Kostorz, A. Strohm, H. Schock, and A. Tiwari, Interfacial layer formations between  $\text{Cu}(\text{In,Ga})\text{Se}_2$  and  $\text{In}_x\text{S}_y$  layers, *J. Appl. Phys.* **98**, 123512 (2005).
- [114] D. Cahen and R. Noufi, Surface passivation of polycrystalline, chalcogenide based photovoltaic cells, *Solar Cells* **30**, 53 (1991).
- [115] L. Kronik, U. Rau, J. Guillemoles, D. Braunger, H. Schock, and D. Cahen, Interface redox engineering of  $\text{Cu}(\text{In,Ga})\text{Se}_2$  - based solar cells: oxygen, sodium, and chemical bath effects, *Thin Solid Films* **361-362**, 353 (2000).
- [116] A. Chirila, D. Guettler, D. Brémaud, S. Buecheler, R. Verma, S. Seyrling, S. Nishiwaki, S. Haenni, G. Bilger, and A. N. Tiwari, CIGS solar cells grown by a three-stage process with different evaporation rates, in *Proceedings of 34th IEEE Photovoltaic Specialists Conference*, 2009.

- [117] Dullweber, G. Hanna, U. Rau, and H. Schock, A new approach to high-efficiency solar cells by band gap grading in  $\text{Cu}(\text{In,Ga})\text{Se}_2$  chalcopyrite semiconductors, *Solar Energy Mat. Solar Cells* **67**, 145 (2001).
- [118] S.-H. Wei and A. Zunger, Band offsets and optical bowings of chalcopyrites and Zn-based II-VI alloys, *J. Appl. Phys.* **78**, 3846 (1995).
- [119] S.-H. Wei, S. B. Zhang, and A. Zunger, Effects of Ga addition to  $\text{CuInSe}_2$  on its electronic, structural, and defect properties, *Appl. Phys. Lett.* **72**, 3199 (1998).
- [120] F. Jacob, N. Barreau, S. Gall, and J. Kessler, Performance of  $\text{CuIn}_{1-x}\text{Ga}_x\text{Se}_2/(\text{PVD})\text{In}_2\text{S}_3$  solar cells versus gallium content, *Thin Solid Films* **515**, 6028 (2007).
- [121] C. Fella, Interface investigation of buffer layers on CIGS solar cells, Master's thesis, Friedrich-Alexander-Universitaet Erlangen-Nuernberg, 2010, Performed in the Laboratory for Thin Films and Photovoltaics at Empa, under the supervision of S. Buecheler.
- [122] U. Rau, Electronic properties of  $\text{Cu}(\text{In,Ga})\text{Se}_2$  thin-film solar cells - an update, *Adv. in Solid State Phys.* **44**, 27 (2004).
- [123] M. Turcu and U. Rau, Fermi level pinning at  $\text{CdS}/\text{Cu}(\text{In,Ga})(\text{Se,S})_2$  interfaces: effect of chalcopyrite alloy composition, *J. Phys. Chem. Solids* **64**, 1591 (2003).
- [124] M. Turcu and U. Rau, Compositional trends in defect energies, band alignments, and recombination mechanism in the  $\text{Cu}(\text{In,Ga})(\text{Se,S})_2$  alloy system, *Thin Solid Films* **431-432**, 158 (2003).
- [125] D. Schmid, M. Ruchh, F. Grunwald, and H. Schock, Chalcopyrite/defect chalcopyrite heterojunction on the basis of  $\text{CuInSe}_2$ , *J. Appl. Phys.* **73**, 2902 (1993).
- [126] M. Romero, K. Jones, A. J. Y. Yan, M. Al-Jassim, and R. Noufi, Surface-layer band gap widening in  $\text{Cu}(\text{In,Ga})\text{Se}_2$  thin films, *Appl. Phys. Lett.* **83**, 4731 (2003).
- [127] M. Contreras, H. Wiesner, D. Niles, K. Ramanathan, R. Matson, J. Tuttle, J. Keane, and R. Noufi, Defect chalcopyrite  $\text{Cu}(\text{In}_{1-x}\text{Ga}_x)_3\text{Se}_5$  materials and high-Ga-content  $\text{Cu}(\text{In,Ga})\text{Se}_2$ -based solar cells, in *Proceedings of 25th Photovoltaic specialist conference, Washington, D.C., USA*, 1996.
- [128] M. Igalson, A. Urbaniak, and M. Erdoff, Reinterpretation of defect levels derived from capacitance spectroscopy of CIGSe solar cells, *Thin Solid Films* **517**, 2153 (2009).
- [129] T. Nakada, Nano-structural investigations on Cd-doping into  $\text{Cu}(\text{In,Ga})\text{Se}_2$  thin films by chemical bath deposition process, *Thin Solid Films* **361-362**, 346 (2000).
- [130] P. Migliorato, J. Shay, H. Kasper, and S. Wagner, Analysis of the electrical and luminescent properties of  $\text{CuInSe}_2$ , *J. Appl. Phys.* **46**, 1777 (1975).
- [131] Private communication with manufacturer, 2008.

- [132] R. Saaia, Development and Characterisation of  $\text{Cu}(\text{In,Ga})(\text{S,Se})_2$  Thin Film Solar Cells with  $\text{In}_2\text{S}_3$  Buffer Layers Deposited by Ultrasonic Spray Pyrolysis, Master's thesis, CREST, Loughborough University, Loughborough, United Kingdom, 2008, Performed in the group of Thin Film Physics at ETH Zuerich, under the supervision of S. Buecheler.